

# Nuclear Structure Near Doubly Magic Nuclei

**I n a u g u r a l d i s s e r t a t i o n**

zur

Erlangung des akademischen Grades eines  
Doktors der Naturwissenschaften (Dr. rer. nat.)

der

Mathematisch-Naturwissenschaftlichen Fakultät

der

Universität Greifswald

vorgelegt von

Lukas Nies

geboren am 17.07.1995

in Schotten, Hessen

24. Juli, 2023



Dekan:	Prof. Dr. Gerald Kerth
1. Gutachter:	Prof. Dr. Lutz Schweikhard
2. Gutachter:	Prof. Dr. Michael Block
3. Gutachter:	Prof. Dr. Georg Bollen
Tag der Disputation:	15. Dezember 2023

# Contents

<b>List of Figures</b>	<b>III</b>
<b>Nomenclature</b>	<b>VII</b>
<b>1 Introduction</b>	<b>1</b>
<b>2 Nuclear Structure</b>	<b>5</b>
2.1 Nuclear Models . . . . .	5
2.2 Observables . . . . .	8
2.2.1 Nuclear Binding Energies . . . . .	8
2.2.2 Nuclear Moments, Isotope Shift and Hyperfine Structure . . . . .	13
2.2.3 Nuclear Deformation . . . . .	17
<b>3 Production of Radioactive Ion Beams</b>	<b>19</b>
3.1 Isotope Separator Online Device . . . . .	20
3.2 Targets and Ion Sources . . . . .	22
<b>4 Experimental Methods</b>	<b>27</b>
4.1 Mass Spectrometry With Trapped Ions . . . . .	27
4.1.1 Penning Trap Mass Spectrometry . . . . .	28
Buffer gas cooling . . . . .	29
Ion-cyclotron resonance techniques . . . . .	30
4.1.2 Multi-Reflection Time-of-Flight Mass Spectrometry . . . . .	33
4.2 The ISOLTRAP mass spectrometer at ISOLDE/CERN . . . . .	35
4.3 Technical Developments at ISOLTRAP . . . . .	36
4.3.1 A new offline ion source . . . . .	37
4.3.2 MR-ToF MS Improvements . . . . .	38
4.3.3 MR-ToF MS data analysis . . . . .	40
4.4 Laser Spectroscopy . . . . .	42
4.4.1 Collinear Laser Spectroscopy . . . . .	42
4.4.2 Resonance Ionization Spectroscopy . . . . .	43
<b>5 Conclusion and outlook</b>	<b>47</b>
<b>6 Bibliography</b>	<b>49</b>
<b>7 Cumulative thesis articles</b>	<b>73</b>
7.1 Author contributions . . . . .	73
7.2 Charge radii, moments, and masses of mercury isotopes across the $N = 126$ shell closure . . . . .	75
7.3 Isomeric excitation energy for $^{99}\text{In}^m$ from mass spectrometry reveals constant trend next to doubly magic $^{100}\text{Sn}$ . . . . .	95
7.4 Further evidence for shape coexistence in $^{79}\text{Zn}^m$ near doubly-magic $^{78}\text{Ni}$ . . . . .	105

## *Contents*

<b>8</b>	<b>Eigenständigkeitserklärung</b>	<b>115</b>
<b>9</b>	<b>Peer-reviewed publications</b>	<b>117</b>
<b>10</b>	<b>Acknowledgments</b>	<b>119</b>
<b>A</b>	<b>Appendix</b>	<b>121</b>
A.1	Note on the atomic mass unit . . . . .	121

# List of Figures

1.1	Chart of nuclides . . . . .	2
2.1	Valence space for $^{79}\text{Zn}$ calculations . . . . .	7
2.2	Binding energy per nucleon for the stable nuclei . . . . .	10
2.3	Binding energies for elements with magic proton number . . . . .	11
2.4	Mass filter comparison . . . . .	12
2.5	Hyperfine structure transitions in $^{203}\text{Hg}$ . . . . .	16
2.6	Visualization of the Hill-Wheeler coordinate space for quadrupole deformation with associated shapes . . . . .	18
3.1	Nuclear reactions for ISOL RIB production . . . . .	20
3.2	Schematic of ISOLDE facility . . . . .	21
3.3	Yields at ISOLDE for the $^{100}\text{Sn}$ region . . . . .	24
3.4	Release of zinc from an $\text{UC}_x$ target . . . . .	25
4.1	3D Motion of a trapped charged particle in a Penning trap . . . . .	29
4.2	Time-of-flight ion-cyclotron resonance spectra for $^{206}\text{Hg}$ and $^{207}\text{Hg}$ . . .	31
4.3	Ion spots on the position-sensitive detector after ejection from the Penning trap for different measurement steps . . . . .	32
4.4	Multi-Reflection Time-of-Flight Mass Spectrometer of ISOLTRAP . . .	34
4.5	ISOLTRAP mass spectrometer as of 2021 . . . . .	35
4.6	Annotated CAD drawing of the combined surface and laser-ablation ion source . . . . .	37
4.7	Time-of-Flight spectrum of laser-ablated carbon cluster ions . . . . .	38
4.8	Relative voltage deviation for the MR-ToF MS mirror voltage stabilization	39
4.9	Mains power phase dependence of the ion time-of-flight . . . . .	39
4.10	Time-of-Flight correction of data for the $m/q = 99$ isobaric beam from experiment IS661 . . . . .	40
4.11	Multi-component probability density function to fit asymmetric peak shape of the ToF spectra . . . . .	41
4.12	Schematic of the experimental setups for the in-source resonance ionization spectroscopy of rare mercury isotopes . . . . .	44
5.1	Follow-up mass measurements at ISOLTRAP . . . . .	48
A.1	Relations of the base units with physical constants in the 2018 redefinition of the SI units . . . . .	122



# Nomenclature

## Acronyms

AME .....	atomic mass evaluation
CEC .....	charge exchange cell
CERN .....	European Organization for Nuclear Research
CLS .....	collinear laser spectroscopy
DFT .....	density functional theory
EBIS .....	electron beam ion source
FEBIAD .....	forced electron beam induced arc discharge
FT-ICR .....	Fourier-transform ion-cyclotron-resonance
FWHM .....	full width at half maximum
GPS .....	general purpose separator
HRS .....	high resolution separator
IGISOL .....	ion guide isotope separator online
ISOL .....	isotope separator online
LAIS .....	laser-ablation ion source
MCP .....	multichannel plate
MCSM .....	Monte-Carlo shell model
MR-ToF MS ....	multi-reflection time-of-flight mass spectrometer
PI-ICR .....	phase-imaging ion-cyclotron-resonance
PI-LIST .....	perpendicularly-illuminated laser ion source trap
PSB .....	proton synchrotron booster
PTMS .....	Penning trap mass spectrometry
RF .....	radio frequency
RFQ-cb .....	radiofrequency quadrupole cooler-buncher

## Nomenclature

RIB	radioactive ion beam
RILIS	resonant laser ionization ion source
RIS	resonance ionization spectroscopy
SM	shell model
TDC	time-to-digital converter
VADIS	versatile arc discharge ion source
VS-IMSRG	valence space in-medium similarity renormalization group

## Symbols

$\Delta m$	mass difference
$\delta m$	mass defect
$\Delta t$	temporal width of an ion bunch
$\delta\nu^{AA'}$	isotopic shift
$\Delta_{\text{Ref}}$	difference of square roots of reference masses
$\lambda$	photon wavelength
$\langle r_c^2 \rangle$	root mean square charge radius
$\mu$	magnetic dipole moment
$\nu_+$	reduced cyclotron frequency of a trapped ion
$\nu_-$	magnetron frequency of a trapped ion
$\nu_c$	cyclotron frequency of a trapped ion
$\nu_z$	axial frequency of a trapped ion
$\Sigma_{\text{Ref}}$	sum of square roots of reference masses
$A$	mass number
$B_e$	electron binding energy
$C_{\text{TOF}}$	experimental observable for two-reference MR-ToF mass measurements
$E$	nuclear binding energy
$E_{\text{kin}}$	kinetic energy
$I$	isospin quantum number

$l$ .....	anugular momentum quantum number
$m$ .....	mass
$M_A$ .....	atomic mass
$m_{\text{ref}}$ .....	reference mass
$N$ .....	neutron number
$n$ .....	major quantum number
$Q$ .....	electric quadrupole moment
$q$ .....	ion charge
$R$ .....	mass resolving power
$s$ .....	spin quantum number
$S_{2n,p}$ .....	two-neutron, proton separation energy
$S_{n,p}$ .....	single-neutron, proton separation energy
$t$ .....	flight time
$v$ .....	velocity
$Z$ .....	proton number



# 1 Introduction

Research into nuclear physics has enjoyed a long and rich history since the earliest experiments began investigating atomic constituents. The discovery of the atomic nucleus in the early 20<sup>th</sup> century has started a complex field of research that has undergone many transformations with the advancements of modern technology. Today, atomic nuclei are not only studied to advance our understanding of the strong force but also to gain more information on the synthesis of elements in the universe, to exploit nuclear decay to investigate the weak interaction, and to search for physics beyond the standard model.

In this work, we will study the strong force in atomic nuclei, i.e. the way nucleons (protons and neutrons) arrange themselves in a many-body system governed by the repulsive Coulomb interaction and the attractive strong interaction. Figure 1.1 shows the nuclear chart of all observed nuclear isotopes, which are atoms consisting of nuclei with the same proton number  $Z$  (same chemical element) but different neutron number  $N$ . For heavier nuclei, starting after  $N = Z = 20$ , all stable nuclei show an excess in neutrons with respect to their protons. This is caused by the long-range repulsive Coulomb interaction between the protons, which requires an even larger amount of neutrons for compensation by the short-range attractive strong interaction, leading to an imbalance between neutron and proton numbers.

In particular, we will focus on nuclear structure near nuclei with a “magic number” of  $Z$  protons and  $N$  neutrons, so-called doubly-magic nuclei, exhibiting a particularly stable configuration with respect to neighboring nuclei [1]. Within the nuclear shell model, similar to the atomic shells, the magic numbers indicate shell closures accompanied by energy gaps. Nuclei at double-shell closures and their direct vicinity provide an important playground to benchmark nuclear theories and models that aim to predict the intricate interplay of the nucleons that lead to enhanced nuclear binding energies, significant changes in charge radii and transition strengths, etc. Of particular interest are nuclear isomers, long-lived excited states, in which the nucleon configuration with respect to its ground state is altered, resulting in a modification of their properties despite having the same number of protons and neutrons.

The first section of Chapter 2 will provide a brief overview of some of the many different nuclear models that have been developed over the decades, comparing empirical models, such as the liquid drop model, the Fermi gas model, and the shell model, to energy density functional theory and *ab initio* approaches. In the second section of Chapter 2, nuclear observables are introduced, for brevity limited to ground state properties, namely nuclear binding energies, electromagnetic moments, charge radii, and nuclear deformation.

Many of the doubly-magic nuclei are stable or exhibit a very long half-life, such as  ${}^4_2\text{He}_2$ ,  ${}^{16}_8\text{O}_8$ ,  ${}^{40}_{20}\text{Ca}_{20}$ ,  ${}^{48}_{28}\text{Ca}_{28}$ , and  ${}^{208}_{82}\text{Pb}_{126}$ . Other nuclei that are predicted to be doubly-magic, such as  ${}^{56}_{28}\text{Ni}_{28}$ ,  ${}^{78}_{28}\text{Ni}_{50}$ ,  ${}^{100}_{50}\text{Sn}_{50}$ , and  ${}^{132}_{50}\text{Sn}_{82}$ , have to be produced artificially, as they are

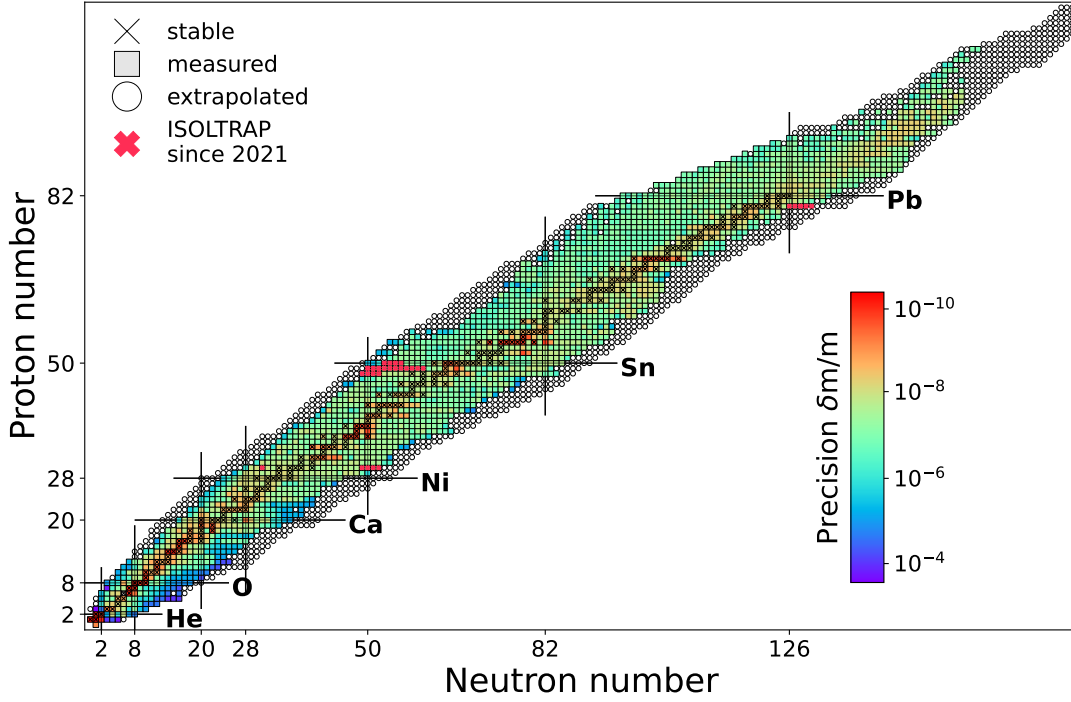


**Figure 1.1:** Chart of nuclides. The colored boxes represent measured masses with the color code depicting the measurement uncertainty. The open boxes represent extrapolated values. The data is taken from [2]. The figure was generated using code from [3].

radioactive with half-lives ranging from days to milliseconds. Chapter 3 will give a short introduction to the production of radioactive isotopes with a focus on accelerator-based techniques using a high-energy, high-intensity proton beam on a thick target, producing radioactive reaction products through nuclear fission, spallation, and fragmentation. Different target and ion-source types are discussed in this context, and the radioactive ion beam facility ISOLDE at CERN, Switzerland, is introduced.

Different experimental methods at facilities like ISOLDE are employed to extract nuclear observables of radioactive isotopes. Binding energies can be deduced from the atomic mass using high-precision mass spectrometers that measure masses of charged radioisotopes using ion-trapping techniques. To measure electromagnetic moments and relative charge radii, the atomic hyperfine structure is probed using laser spectroscopy on the atomic shell of the radioisotope. These two methods will be explained in Chapter 4 followed by a short description of technical improvements on the ISOLTRAP mass spectrometer at ISOLDE/CERN.

Chapter 5 will provide a brief overview of binding energy measurements that were not included in this thesis and which are yet to be published, as well as future measurements and technical improvements. The introductory part of this cumulative thesis is concluded with the bibliography in Chapter 6.

The main part of this work consists of three publications, reprinted in Chapter 7,

which report on nuclear structure investigations through mass measurements and laser spectroscopy near the doubly magic nuclei  $^{78}_{28}\text{Ni}_{50}$ ,  $^{100}_{50}\text{Sn}_{50}$ , and  $^{208}_{82}\text{Pb}_{126}$ . The nuclides investigated in this work include neutron-deficient indium isotopes, neutron-rich zinc isotopes, and neutron-rich mercury isotopes. In Fig. 1.1, masses measured with the ISOLTRAP setup since the end of the CERN Long Shutdown in 2021 are highlighted, also including the aforementioned isotopes. The predicted and confirmed doubly-magic nuclei are indicated through the intersecting black lines.

Near doubly-magic  $^{208}_{82}\text{Pb}_{126}$ , the mercury chain with  $Z = 80$  offers insight into the behavior of nuclei located just two protons away from the  $Z = 82$  shell closure. On the neutron-deficient side, a unique and localized odd-even staggering in charge radii was found, resulting from monopole and quadrupole interactions [4], while on the neutron-rich side, a kink in charge radius at  $N = 126$  was observed [5]. **Article I** reports on a laser spectroscopy experiment that followed up investigating this kink, combined with high-precision mass measurements. The measurements are compared to covariant density functional theory, illuminating the influence of the occupancy of neutrons in certain orbitals and their energies.

The experimental campaign around **Article II** was motivated by high-precision mass measurements of neutron-deficient indium isotopes with  $Z = 49$  close to doubly-magic  $^{100}_{50}\text{Sn}_{50}$ , reported in [6]. The mass measurements of  $^{99-101}\text{In}$  in this predecessor experiment could indirectly reduce the mass uncertainty on  $^{100}\text{Sn}$  through its  $Q_\beta$ -value to  $^{100}\text{In}$  and was able to compare the results with *ab initio* calculations, that were performed for the first time for an odd- $Z$  isotopic chain close to  $^{100}\text{Sn}$ . In the proposed follow-up campaign, ISOLDE experiment IS661 [7], the  $1/2^-$  isomeric states in  $^{99,101}\text{In}$  were measured precisely, the results of which are reported in **Article II**. Only one proton away from  $^{100}\text{Sn}$ , the two long-lived states in  $^{99}\text{In}_{50}$  are particularly interesting as their excitation-energy difference directly reflects single proton-hole states in  $^{100}\text{Sn}$  itself. The experimental results for the nuclear binding energies in combination with electromagnetic moments from literature are compared to large-scale shell model, DFT, and *ab initio* calculations and reflect a major benchmark of these state-of-the-art calculations.

Being located close to doubly-magic  $^{78}_{28}\text{Ni}_{50}$ , isotones (nuclei with the same neutron number) with  $N = 49$  have been of great interest for the study of intruder configurations (nucleon configuration for which one or more nucleons are excited across a large shell gap, often found near magic nuclei). Shape coexistence (spherical and deformed states at similar excitation energies) has been observed near doubly-magic nuclei and was investigated in the vicinity of  $^{78}\text{Ni}$ . While some experiments could find an indication of shape coexistence [8], other experiments yielded contradicting results [9]. A significantly larger charge radius within the  $5/2^+$  isomer with respect to its ground state was found in  $^{79}_{30}\text{Zn}_{49}$  [10], but could not unambiguously be attributed to a deformed state. For **Article III**, different high-precision mass-measurement techniques were applied independently at two radioactive ion beam facilities. Penning-trap mass spectrometry was performed in Jyväskylä, Finland, while multi-reflection time-of-flight mass spectrometry was used at ISOLDE/CERN to measure the excitation energy of this state. Using large-scale shell model calculations, binding energies, charge radii, and the deformation of the ground and isomeric states were assessed and compared to the experimental findings.



## 2 Nuclear Structure

The theoretical description of the atomic nucleus as a complex many-body system made of a few to some hundreds of nucleons has been a great challenge since its discovery by Ernest Rutherford in 1911 [11]. Over the last decades, many models have emerged that try to explain observables such as nuclear decay, binding energies, charge radii, nuclear electromagnetic moments, etc. Of particular interest are features of the nuclear landscape that seem to appear near certain “magic” numbers of nucleons. In this chapter, a range of nuclear models and observables, as well as a discussion of the emergence and disappearance of magic numbers and the role of doubly-magic nuclei will be presented.

### 2.1 Nuclear Models

After discovering the atomic nucleus and Rutherford’s identification of hydrogen nuclei as protons in 1920 [12], it was suggested that the total amount of charged constituents in a nucleus only accounts for roughly half of its atomic mass [13]. With the discovery of the neutron in 1932 [14], the building blocks of the atomic nucleus consisting of  $A$  nucleons ( $Z$  protons and  $N$  neutrons) was quickly developed. One of the first models describing the nucleus was the **liquid drop model** developed by George Gamow [15] and was used by Carl Friedrich von Weizsäcker to approximate a semi-empirical formula [16] for calculating the nuclear binding energy (see Section 2.2.1). This model describes the nucleus as a drop of incompressible nuclear fluid of protons and neutrons, held together by the strong interaction.

Within the **Fermi-gas model** [17], the protons and neutrons are treated as two separate, non-interacting systems of Fermions (particles with half-integer spin). The free-moving Fermions move in a common, constant potential inside the nuclear volume  $V$  and they obey the Pauli principle [18], which excludes two or more particles with the same quantum number from occupying the same quantum state. The potential depths between the neutrons and protons are different, as the Coulomb repulsion of the protons leads to an overall decrease in their binding strength.

One of the most successful models yet to describe nuclear structure is the **nuclear shell model**, developed independently in the 1940s by Eugene Paul Wigner and Maria Goeppert-Mayer as an alternative to the liquid drop model, earning them a share in the 1963 Nobel prize in physics [19]. Within this model, the nucleons populate energy levels obeying the Pauli principle and move within a common **mean field**  $U(i)$  generated by all  $A$  nucleons. The dynamics of the  $A$  nucleons can be described through the Schrödinger

equation

$$\hat{H}\Psi(1, \dots, A) = E\Psi(1, \dots, A) \quad (2.1)$$

$$\hat{H} = \sum_{i=1}^A \left[ -\frac{\hbar^2}{2m} \Delta_i + U(i) \right] + \sum_{i < j=1}^A W(i, j) - \sum_{i=1}^A U(i) = \hat{H}^0 + \hat{V} \quad (2.2)$$

where  $\Psi$  is the nuclear wave function and  $\hat{H}$  is the Hamiltonian with

$$\hat{H}^0 = \sum_{i=1}^A \left[ -\frac{\hbar^2}{2m} \Delta_i + U(i) \right] \equiv \sum_{i=1}^A \hat{h}(i) \quad (2.3)$$

containing two-body interactions  $W(i, j)$ , the mean-field  $U(i)$  and the residual interaction  $\hat{V}$ . The mean field  $U(i)$  is chosen to minimize the total energy, while the solutions for  $\hat{h}(i)$  are used to construct a basis for  $\hat{V}$ . The single-particle wave functions  $\psi(i)$ , which make up the nuclear wave function  $\Psi$ , can be separated into a spherical part  $Y_l^m(\theta, \phi)$  and a radial part  $R_{nl}(r)$ .

Similar to the atomic shell described in Section 2.2.2, spin and momentum quantum numbers are assigned to the wave functions: the principle quantum number  $n$ , the angular momentum quantum number  $l$  ( $0 \leq l \leq n-1$ ,  $l$  is denoted using letters where  $l = s, p, d, f, g, h, \dots = 0, 1, 2, 3, 4, 5, \dots$ ), and the magnetic quantum number  $m$  ( $-l \leq m \leq +l$ ). A quantum state at  $nl$  can accommodate  $2(2l+1)$  different nucleons, where  $(2l+1)$  is the number of possible configurations for  $m$ , multiplied by a factor 2 for the two different spin states. For atomic shells, Hund's rule dictates how they are filled with electrons (first,  $nl$  sub-shells are filled with electrons of a certain spin, after which electrons with opposite spin are added). Due to the net attractive force between the nucleons caused by the strong interaction, this does not apply to atomic nuclei.

The choice of potential  $U(i)$  dictates the efficiency of solving the many-body problem of the Schrödinger equation. For light nuclei, the harmonic oscillator  $U(r) = m\omega^2 r^2/2$  Ansatz can be analytically solved through diagonalization and normalization, resulting in the eigenvalues for the energy levels. In heavier nuclei, this approach is no longer valid; centrifugal forces  $l \cdot l$  and spin-orbit interactions  $s \cdot l$  modify the harmonic oscillator potential. The quantum number for the total angular momentum  $j$  is introduced, which can assume values for  $l-1/2 \leq j \leq l+1/2$ . The  $nl$  state now degenerates into sub-states  $nl_j$  described by the total angular momentum, where the number of nucleons per state is given by  $2j+1$ . Large energy gaps between certain shells and sub-shells give rise to the magic proton and neutron numbers 2, 8, 20, 50, 82, 126. Another quantum number, the nuclear spin  $I$ , is assigned to the nucleons to distinguish between protons and neutrons.

To solve the Schrödinger equation of Eq. (2.2), the single-particle wavefunctions are used to construct a basis to diagonalize the Hamiltonian. Common bases are the m-scheme base built from Slater determinants, normalized and symmetrized products of  $A$  single-particle wave functions occupying  $A$  different states, and the  $J(T)$ -coupled base, which is constructed from a linear combination of antisymmetrized and normalized products of single-particle wave functions to yield good angular momenta  $J$  and isospin  $T$ . A more recent development, used in **Article III**, is utilizing a non-orthogonal basis in combination with beyond-mean field techniques [20].

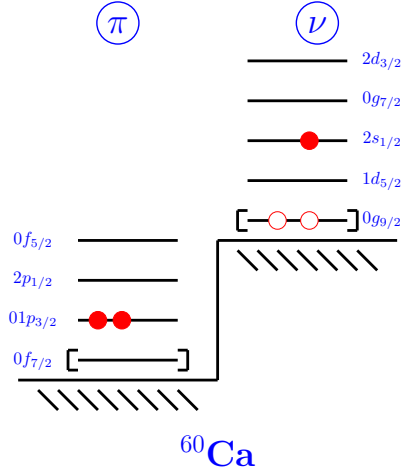


**Figure 2.1:** Valence space for the  $^{79}\text{Zn}$  calculations of **Article III**. In this work, it was found that the neutron  $2s_{1/2}$  level falls below the neutron  $1d_{5/2}$  in  $^{79}\text{Zn}$ .

Fig. 2.1 shows the PFSDG-U valence space [21] used in **Article III** for the shell-model calculations. An inert  $^{60}_{20}\text{Ca}_{40}$  core was used for these, while the valence space was spanned using the proton  $pf$  and neutron  $sdg$  shells. This approach was chosen to cope with the problem of large dimensions. In the traditional m-scheme, the dimension  $d$  of the valence space can be estimated as the number of possible proton and neutron configurations using the product of the two binomial coefficients  $\binom{\Sigma_\pi}{Z}$  and  $\binom{\Sigma_\nu}{N}$ , where  $\Sigma_\pi$  and  $\Sigma_\nu$  are the numbers of available proton and neutron states in the valence space. The proton  $\pi f$  shell ( $l = 3$ ), for example, can accommodate  $2(2 \times 3 + 1) = 14$  protons, split into the  $\pi f_{5/2}$  (6 protons) and the  $\pi f_{7/2}$  (8 protons) sub-shells, while  $\pi p$  can accommodate 6 protons.

In a simplified model,  $^{79}_{30}\text{Zn}_{49}$  is described with a full  $\pi f_{7/2}$  shell and two protons in the  $\pi p_{3/2}$  shell, while the neutron  $\nu g_{9/2}$  shell has two neutron holes and one neutron in the  $\nu s_{1/2}$  shell. For the PFSDG-U space, this would result in a valence space dimension of  $d = \binom{20}{10} \binom{30}{9} \approx 2.6 \times 10^{12}$ . More accurately, the shell-model calculations yield partial occupancies for the different sub-shells, providing an average number of nucleons per sub-shell. Withing the calculations of **Article III** (Tab. II) it was found that, on average, about 8.5 neutrons occupy the  $\nu g_{9/2}$ , while the residual 0.5 neutrons are distributed over the other four sub-shells of the neutron valence space.

Another way to handle large dimensions  $d$  is the **Monte-Carlo Shell Model**, in which the implementation of an auxiliary field reduces the two-particle Hamiltonian to a form of one-particle fields, after which a sub-set of random basis states are selected until energy convergence is reached [22].

A different approach to solving the Hamiltonian is the **Energy Density Functional Theory** (DFT), which maps the many-body problem onto a one-body problem based on the Hohenberg-Kohn theorem. This states that a many-body system's ground state density  $\rho(r)$  determines its ground state energy [23]. Here the Hamiltonian is expressed in terms of kinetic energy, the sum of external potentials, and the nucleon-nucleon interaction. The expectation value of the energy is split into the ground state density with external potential and into a functional, which is independent of the external potential. The ground-state energy is calculated by minimizing the energy expectation

value with respect to the density.

Early functionals within the Hartree-Fock framework were developed by T. Skyrme [24], which are based on effective interactions with two- and three-body forces being expanded at short ranges using a number of effective parameters that are adjusted to experimental observables such as binding energies and nuclear radii. Further work was done by D. Gogny and colleagues [25] by expanding to finite-range two-body interactions, also including pairing interactions by introducing quasi-particles to retain the single-particle description of the Hartree-Fock-Bogolyubov method [26].

The need to describe effects that go beyond single-particle-single-hole excitations was accommodated by using methods such as the particle vibration coupling [27] or the generator coordinate method [28]. The latter was used in **Article III** to find a different basis for diagonalizing the Hamiltonian within the Discrete Non-Orthogonal Shell Model method [20].

Enabled through advancements in computational power, *ab initio* methods have gained much attention in the last decade. In this approach, nuclear properties are deduced from first principles: the Hamiltonian is diagonalized in the full model space (no inert core) and is expanded until the results converge. Furthermore, the effective interactions are directly derived from realistic nucleon-nucleon scattering experiments, as well as from the properties of bound two- and three-particle states, e.g.  $^2\text{H}$  and  $^3\text{He}$ . The specific method used in **Article II** to deduce binding energies of ground and isomeric states in neutron-deficient odd-even indium isotopes is the Valence Space In-Medium Similarity Renormalization Group (VS-IMSRG) method [29]. A generic many-body Hamiltonian is diagonalized by using a unitary transformation with unitary operator  $U^\dagger(s)$  and flow parameter  $s$ . The Hamiltonian is renormalized by splitting into diagonal and off-diagonal elements. Higher order operators of the SRG are evolved in-medium using only the realistic two and three body interactions. Effective interactions generated in this way are used in a valence space to calculate ground-state properties and excited states of closed-shell and open-shell nuclei. For the presented article, the 1.8/2.0(EM) [30,31] and  $\Delta\text{NNLO}_{GO}$  [32] effective interactions were benchmarked against the reported experimental results.

## 2.2 Observables

### 2.2.1 Nuclear Binding Energies

During the process of establishing the proton and neutron as constituents of the atomic nuclei and the advent of ever more precise mass spectrographs, it was found that the “whole number rule”, attributing mass to atoms as multiple integers of the hydrogen mass, was not applicable [33]. This so-called “mass defect”

$$\delta m = Zm_p + Nm_n - M_N(Z, N) = -E(Z, N)/c^2 \quad (2.4)$$

where  $c$  is the speed of light in vacuum, and the nuclear mass  $M_N(Z, N)$  is smaller than the sum of its constituents, i.e.  $Z$  proton masses  $m_p$  and  $N$  neutron masses  $m_n$ . This mass defect is equivalent to the binding energy  $E(Z, N)$  (carrying a minus sign as the binding energy itself is a negative quantity) using Einstein’s relativistic mass-energy equivalence principle  $E = mc^2$  and is used to test its validity directly [34].

The atomic mass  $M_A(Z, N)$  of a neutral atom can be calculated from the nuclear mass

$$M_N(Z, N) = M_A(Z, N) - Zm_e + B_e(Z) \quad (2.5)$$

using the well-known electron mass  $m_e$  [35] and the electron binding energy  $B_e(Z)$ .

As described at the beginning of Section 2.1, the semi-empirical mass formula can be used to estimate the nuclear binding energy  $E(Z, N)$ . First proposed based on the liquid drop model by Bethe and Weizsäcker [16, 36], the formula consists of several components and can be written as [37]:

$$-E(Z, N) = a_V A - a_s A^{2/3} - a_C \frac{(Z-1)Z}{A^{1/3}} - a_{\text{sym}} \frac{(N-Z)^2}{A} - \delta A^{-1/2}, \quad (2.6)$$

where  $a_V (\approx 16 \text{ MeV}) A$  is the volume including the short-range strong interaction for nucleons interacting with the nearest neighbor;  $a_s (\approx 20 \text{ MeV}) A^{2/3}$  is the surface term which is negative as the nucleons at the surface have fewer neighbors to interact with;  $a_C (\approx 0.75 \text{ MeV}) \frac{(Z-1)Z}{A^{1/3}}$  is the Coulomb term which is negative as the Coulomb force is repulsive between protons;  $a_{\text{sym}} (\approx 21 \text{ MeV}) \frac{(N-Z)^2}{A}$  is the asymmetry term which is negative as the Pauli exclusion principle forbids two Fermions (e.g. protons and neutrons) to be in the same quantum state; and  $\delta A^{-1/2}$  is the pairing term that describes the pairing energy between two like nucleons with  $\delta = -11.2 \text{ MeV}$  (even-even nuclei),  $\delta = 0 \text{ MeV}$  (odd-even nuclei), and  $\delta = 11.2 \text{ MeV}$  (odd-odd nuclei). In practice, the atomic mass is conveniently given as a mass-excess

$$M_E(Z, N) = M(Z, N) - (Z + N)u, \quad (2.7)$$

where  $u$  is the unified atomic mass unit, equivalent to one Dalton Da and “1/12 of the mass of a free carbon 12 atom, at rest and in its ground state” [38]<sup>1</sup>, thus defining carbon-12 as the absolute atomic mass reference.

Historically, the nuclear binding energy per nucleon

$$E(N, Z)/A = [ZM_A(^1\text{H}) + Nm_n - M_A(N, Z)]/A \quad (2.8)$$

$$= [M_E(N, Z) - Z \cdot M_E(^1\text{H}) - N \cdot M_E(n)]/A \quad (2.9)$$

has been used to highlight the binding energy trend along stable nuclei up to Uranium [39]. From Fig. 2.2, it can be seen that the maximum binding energy per nucleon is reached close to  $^{56}\text{Fe}$ . The fusion of lighter nuclei releases some of the binding energy, enabling nuclear fusion processes. Similarly, the fission of heavier nuclei releases binding energy as well.

The nuclear binding energy, as the lowest Eigenvalue of the Hamiltonian, is usually the quantity determined by theoretical calculations. As these calculations are complex many-body problems, perfectly accurate results are rare and not achieved on large parts of the nuclear chart. Instead, the binding energies of neighboring and next-to-neighboring nuclei in isotopic (same  $Z$ ) and isotonic (same  $N$ ) chains are compared.

---

<sup>1</sup>For a note on fundamental constants and the atomic mass unit see Appendix A.

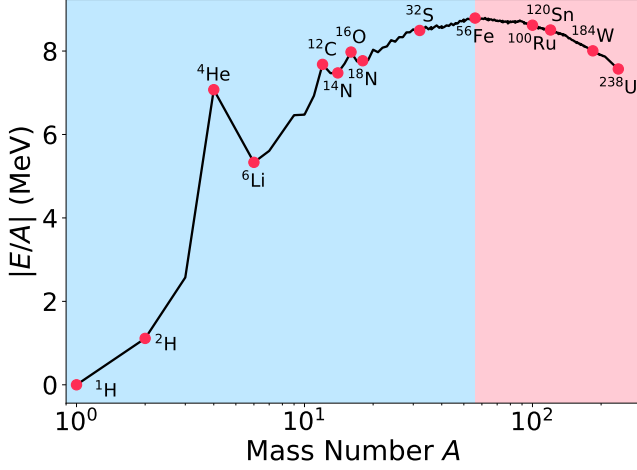


**Figure 2.2:** Binding energy per nucleon for the stable nuclei. Data is taken from the AME2020 [2]. Note that the absolute binding energy is plotted. The blue and red areas indicate regions of fusion and fission, respectively.

Binding energy differences, so-called empirical *mass filters*, are calculated to highlight microscopic and macroscopic nuclear properties. Proton (neutron) separation energies are used to estimate single-particle energies. The simplest, the single-nucleon separation energy

$$S_p(N, Z) = E(Z - 1, N) - E(Z, N) \quad (2.10)$$

$$S_n(N, Z) = E(Z, N - 1) - E(Z, N), \quad (2.11)$$

is used to directly compare neighboring nuclei and the effect of removing one nucleon from the nucleus. This quantity is plotted for different isotopic chains of elements with magic proton numbers Fig. 2.3 (second panel), compared to their total binding energy Fig. 2.3 (first panel). While the absolute value of the total binding energy gradually increases with the number of nucleons in the nucleus on the scale of several tens to hundreds of MeV over the isotopic chain, significant variations in the order of few MeV become visible when applying the  $S_n$  filter. This odd-even staggering is a direct consequence of nucleon-pairing. Sudden drops indicate the completion of a shell and the beginning of a new shell, highlighting the main shell closures at the well-established magic numbers.

To bring more subtle effects to the fore and to avoid mixing single-particle and pairing effects, the so-called two-nucleon separation energy

$$S_{2p}(N, Z) = E(Z - 2, N) - E(N, Z) \quad (2.12)$$

$$S_{2n}(N, Z) = E(Z, N - 2) - E(Z, N) \quad (2.13)$$

is used. The third panel in Fig. 2.3 shows this quantity, and the sudden changes are much more visible. Approaching a magical number  $N_0$ , the variation in  $S_{2n}$  is very flat. Crossing into the new shell, it takes two more neutrons to reach a more flat evolution again. To investigate the strength of these drops, the evolution of the changes in  $S_{2p}$

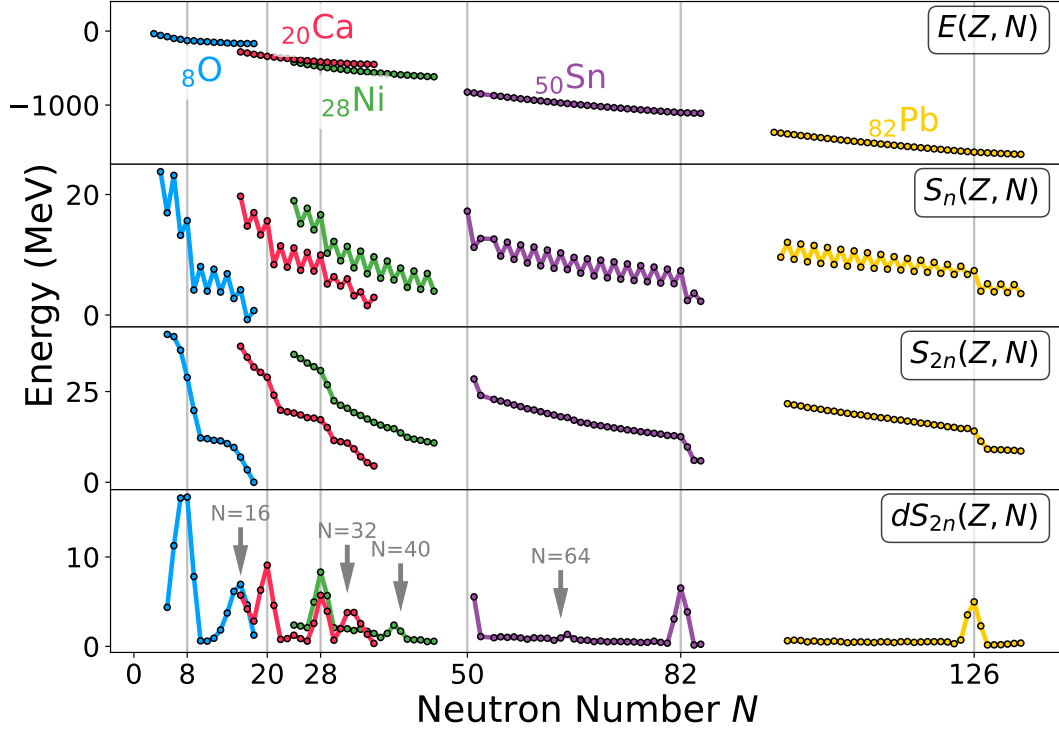


**Figure 2.3:** Binding energies for elements with magic proton number using data from the AME2020 [2]. First panel: total binding energy. Second panel: neutron separation energy. Third panel: Two-neutron separation energy. Fourth panel: evolution of two-neutron separation energy differences.

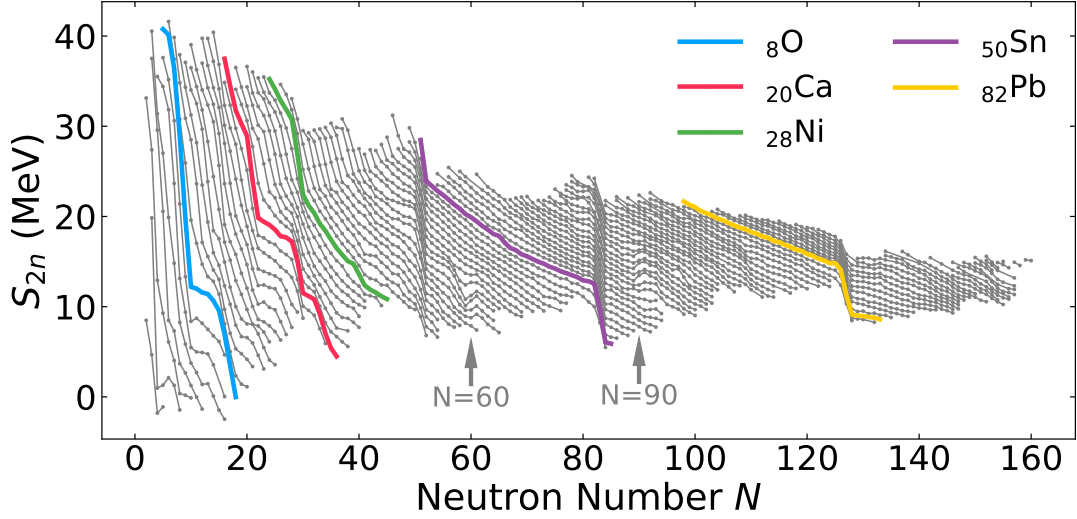
and  $S_{2n}$  can be written as

$$\begin{aligned} dS_{2p}(Z, N) &= S_{2p}(Z, N) - S_{2p}(Z + 2, N) \\ &= E(Z - 2, N) - 2E(Z, N) + E(Z + 2, N) \end{aligned} \quad (2.14)$$

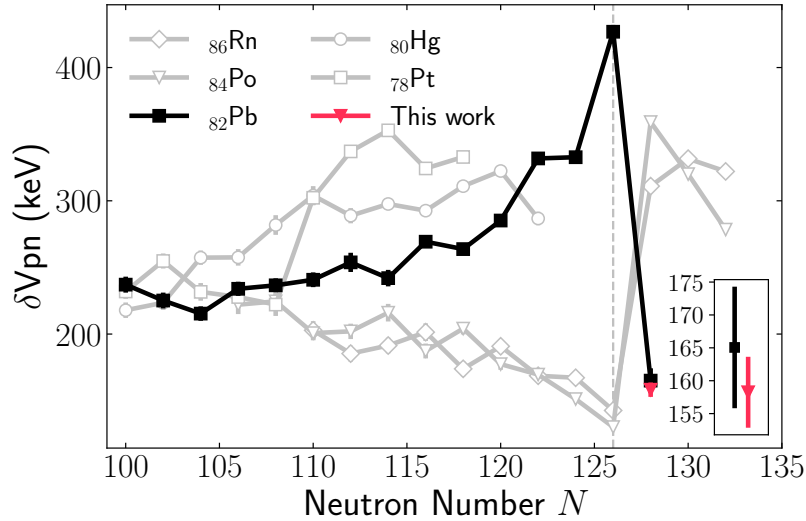
$$\begin{aligned} dS_{2n}(Z, N) &= S_{2n}(Z, N) - S_{2n}(Z, N + 2) \\ &= E(Z, N - 2) - 2E(Z, N) + E(Z, N + 2). \end{aligned} \quad (2.15)$$

This filter visualizes the smallest changes from linearity and gives great insight into nuclear structures far from stability. As shown in the fourth panel in Fig. 2.3, the rare n-rich oxygen isotopes near the drip line indicate the existence of an additional shell closure at  $N = 16$ , supported by neutron knock-out studies [40, 41] and mass measurements and proton knock-out studies of n-rich calcium isotopes have confirmed a shell closure at  $N = 32$  [42–44]. A similar indication from mass measurements around  $N = 40$  could only be confirmed for  $Z = 28$  in the nickel chain [45, 46], but was not observed in changes in the mean square charge radii measurements [47]. The small bump at  $N = 64$  for the tin isotopic chain is expected to be caused by a weak sub-shell closure [1].

Other features besides (sub-)shell closures can also be found employing the  $S_{2n}$  filter. Figure 2.4(a) shows the  $S_{2n}$  values compiled for all known masses evaluated in the



(a) Two-neutron separation energy for all known masses as compiled in the AME2020 [2].

(b) Mass filter for residual proton-neutron interaction with data from **Article I** and the AME2020 [2].**Figure 2.4:** Mass filter comparison.

AME2020 [2]. Local minima and maxima (valleys and ridges) are clearly visible around neutron numbers  $N \approx 60$  and  $N \approx 90$  for elements that are located roughly halfway between magic proton numbers. These islands of deformation are caused by collective effects, such as nucleon excitations and shape coexistence [48], as well as shape-phase transitions [49] that lead to modifications in binding energies and result in deviations from the otherwise linear trends. Isotopes with  $A \approx 100$  in the  $N \approx 60$  region have been intensely studied, including  $^{36}\text{Kr}$  [50],  $^{37}\text{Rb}$  [51],  $^{38}\text{Sr}$  [52],  $^{39}\text{Y}$  [53],  $^{40}\text{Zr}$  [54],  $^{41}\text{Nb}$  [55], with  $^{96}\text{Kr}_{96}$  being identified as the low- $Z$  boundary [56]. Similarly,  $^{148}\text{Ce}_{90}$  was identified

as the low- $Z$  boundary [57] for a region of shape phase transition around  $N \approx 90$  [58, 59].

A thorough analysis of the single- and two-nucleon separation energies and their implications on nuclear structure can be found in [60].

Moving away from single- and two-particle energy estimators, the so-called  $\delta V_{pn}$  mass-filter provides empirical information about the average proton-neutron interaction for the  $(Z - 1, Z)$  protons with the  $(N - 1, N)$  neutrons [61]. Defined for even-even nuclei as

$$\delta V_{pn}(Z, N) = \frac{1}{4} [E(Z, N) + E(Z - 2, N - 2) - E(Z, N - 2) - E(Z - 2, N)], \quad (2.16)$$

this and similar filters were discussed extensively on a global scale, including a large variety of isotopic chains [62–64]. Near doubly magic nuclides, this filter plays an important role in investigating residual interactions across the shell gaps.

An important  $\delta V_{pn}$  value was added to the chart after the first direct mass measurement of  $^{208}\text{Hg}$  by *Chen et al.* [65], which was the last of four required masses to calculate the  $^{210}\text{Pb}$   $\delta V_{pn}$  value. It highlights the interaction between the two neutrons above the gap and the last two protons in the  $Z = 50 - 82$  valence space. In Figure 2.4(b) the improved value from the mass measurement of **Article I** to the  $\delta V_{pn}$  value for  $^{210}\text{Pb}$  is compared with the *Chen et al.* measurement used in the AME2020 evaluation. Following the argumentation of *Chen et al.*, the trend of  $\delta V_{pn}$  for different isotopic chains close to doubly magic nuclei can be explained by the degree of spatial overlap of the proton on neutron orbits. For  $N \leq 126$  and  $Z > 82$ , e.g.  $^{84}\text{Po}$  and  $^{86}\text{Rn}$ , the last two protons populate low  $n$ -high  $j$  orbits in a new shell while the corresponding neutrons populate high  $n$ -low  $j$  orbits. This results in poor overlapping of orbits and a small pn-interaction. Transiting to  $N > 126$ , however, neutrons also occupy high- $j$  orbits, suddenly increasing the interaction strength. For  $Z \leq 82$ , e.g.  $^{78}\text{Pt}$ ,  $^{80}\text{Hg}$  and  $^{82}\text{Pb}$ , the opposite behavior can be observed. When  $N \leq 126$ , the two last protons and neutrons populate low  $j$ -high  $n$  orbits with high overlap, thus resulting in a strong proton-neutron interaction. Adding two neutrons to the new shell above  $N = 126$ , the overlap of the protons and neutrons suddenly decreases, as demonstrated by *Chen et al.* and independently confirmed in this work. The  $\delta V_{pn}$  value for  $^{210}\text{Pb}$  is an important validation for our understanding of the pn-interaction strength across the  $N = 126$  shell gap since no other value for  $N > 126$  and  $Z \leq 82$  will be provided in the near future due to the challenges of producing the isotopes needed for computing the value.

### 2.2.2 Nuclear Moments, Isotope Shift and Hyperfine Structure

Apart from the mass of a nucleus, electromagnetic properties are of great interest in the study of nuclear structure. Like the extraction of nuclear binding energies through atomic mass measurements, the atom carries information about nuclear electromagnetic properties. The interaction of the orbiting electrons with spin angular  $s$  and orbital angular momentum  $l$  leads to the fine structure splitting of the electron orbit  $nl$  into the fine structure electron configuration  $nl_J$ , where  $n$  is the major quantum number, and  $J$  is the total angular momentum with values  $|l - s| \leq J \leq |l + s|$  in integer steps. The interaction between the nuclear spin  $I$  and the electron angular momentum  $J$  leads

to further degeneration of the atomic states, the so-called hyperfine structure. Each fine structure state splits into different hyper-fine levels with a total angular momentum  $F$  and a range of  $|I - J| \leq F \leq |I + J|$ .

Due to the finite size of the nucleus, the electronic wave functions have a non-zero probability of overlapping with the nucleus itself, which leads to a slight shift of the atomic levels with respect to the calculation of a point charge. This furthermore leads to energy differences in isotopes of the same element, the so-called isotopic shift

$$\delta\nu^{AA'} = \nu^{A'} - \nu^A, \quad (2.17)$$

where  $\nu^A$  is the transition energy for the considered level in an isotope with mass number  $A$  and another with mass number  $A'$ .

The isotope shift has two different contributions. The field shift results from the change in nuclear charge radius between isotopes. The finite size of the nucleus results in a more shallow potential as compared to the pure Coulomb potential of a point-like charge. The electrons with an overlapping wave function thus feel less attraction to the extended nuclear volume. The energy shift for the finite nucleus is linearly proportional to the mean square charge radius

$$\langle r_c^2 \rangle = \int_0^\infty r^2 \rho_c(r) dr, \quad (2.18)$$

with  $\rho_c(r)$  being the nuclear charge density. Usually, differences in mean square charge radii

$$\delta\nu_{\text{FS}}^{AA'} \equiv F \delta \langle r_c^2 \rangle^{AA'} \quad (2.19)$$

are studied, with  $F$  being the field shift factor.

The second contribution to the overall isotope shift, the relative difference in mass shift

$$\delta\nu_{\text{MS}}^{AA'} \equiv K \frac{M_{A'} - M_A}{M_{A'} M_A} = K (\tilde{M}^{AA'})^{-1} \quad (2.20)$$

from one isotope with mass  $M_A$  to another with mass  $M_{A'}$  including mass shift factor  $K$ , results solely from the motion of the nucleus within the center-of-mass frame of the atom. Similar to Eq. (2.18), the mass shift is costly to compute when multiple orbiting electrons must be considered. The total isotope shift is thus given as the sum of the two individual components

$$\delta\nu^{AA'} = F \times \delta \langle r_c^2 \rangle^{AA'} + K \times (\tilde{M}^{AA'})^{-1} \quad (2.21)$$

$$\Rightarrow \delta\nu_{\text{mod}}^{AA'} = F \times \delta \langle r_c^2 \rangle_{\text{mod}}^{AA'} + K, \quad (2.22)$$

where  $\delta\nu_{\text{mod}}^{AA'} = \delta\nu^{AA'} \times \tilde{M}^{AA'}$  and  $\delta \langle r_c^2 \rangle_{\text{mod}}^{AA'} = \delta \langle r_c^2 \rangle^{AA'} \times \tilde{M}^{AA'}$ . It can be seen that the isotope shift between two isotopes depends linearly on the mean square charge radius difference between them.

In case the isotope shift  $\delta\nu_{i,\text{mod}}^{AA'}$  of transition  $i$  and the differences in mean square charge radius  $\delta \langle r_c^2 \rangle^{AA'} \times \tilde{M}^{AA'}$  are known for at least two different isotopes with same

reference isotope, then the parameters  $F_i$  and  $K_i$  can be extrapolated from a linear regression of the two data points, where  $F_i$  is the slope and  $K_i$  is the intercept with the vertical axis. This so-called King-plot analysis [66] usually requires precise measurements of at least three isotopes, usually from muonic spectroscopy or high-precision atomic spectroscopy of stable isotopes. This linear relationship also holds for two different electronic transitions  $i$  and  $j$  in the same atom. By dividing Eq. (2.22) for the two different transitions, the difference in charge radius cancels out and one arrives at

$$\delta\nu_{i,\text{mod}}^{AA'} = \frac{F_i}{F_j} \times \delta\nu_{j,\text{mod}}^{AA'} + K_i - \frac{F_i}{F_j}, \quad (2.23)$$

where the field shift and mass shift parameters are determined through the slope  $\kappa = F_i/F_j$  and the intercept  $K_i - F_i/F_j$ . It has recently been shown that this type of analysis can also be applied to radioactive molecules [67].

The electric properties of the finite nucleus with  $Z$  protons can be described in terms of a multipole expansion of the potential  $V$  at a location  $\mathbf{r}$  that is generated due to the positive charge that the  $i$ -th proton in the nucleus carries

$$V(\mathbf{r}) = \sum_i \frac{q_i}{|\mathbf{r}|} + \frac{\hat{\mathbf{r}} \cdot \mathbf{p}}{r^2} + \frac{1}{2} \frac{\sum_{mn} Q_{mn} \hat{n}_m \hat{n}_n}{r^3} + \dots, \quad (2.24)$$

where  $\hat{\mathbf{r}}$  and  $\hat{n}_{m,n}$  are unit vectors in respect to charge  $q_i$ , with  $m, n$  denoting Cartesian coordinates (following the notation of [26]). The first term, the electric monopole, represents the Coulomb term for a point-like particle. The second term, the electric dipole moment  $\mathbf{p}$ , results from a difference in the center-of-mass and the center-of-charge. The nuclear EDM is assumed to be near zero and prospects of a direct measurement with today's technologies are slim as the electric dipoles are shielded against an external electric field [68]. The third term, the intrinsic electric quadrupole moment

$$Q_{mn}(\mathbf{r}) = \sum_i q_i (3r_{mi}r_{ni} - |\mathbf{r}_i|^2 \delta_{mn}) \quad (2.25)$$

is used to quantify the deviation of the nuclear charge density  $\rho(\mathbf{r})$  from sphericity. The nuclear quadrupole moment measured in the lab frame is called the spectroscopic quadrupole moment

$$Q_s(I) = \sqrt{\frac{I - 1/2}{2(2I + 1)(2I + 3)(I + 1)}} \langle I || Q_{zz} || I \rangle \quad (2.26)$$

and is the expectation value of  $Q_{zz}$  component from Eq. (2.25) [69]. It can be seen that for  $I = 1/2$  nuclei, the spectroscopic quadrupole moment vanishes.

From [70], for heavy, axially symmetric nuclei it can be written as

$$Q_s = \frac{3K^2 - I(I - 1)}{(I + 1)(2I + 3)} Q_0, \quad (2.27)$$

where  $K^2$  is the projection of the nuclear spin along the symmetry axis of the nucleus, and  $Q_0$  is the intrinsic quadrupole moment. The latter can be split into a single-particle part and a core part [70]: the single-particle part quadrupole moment

$$Q_{\text{s.p.}} = -e_j \frac{2j - 1}{2j + 2} \langle r_j^2 \rangle \quad (2.28)$$

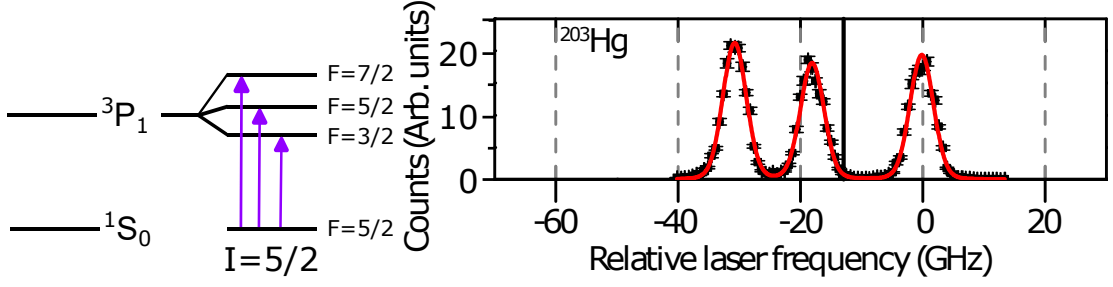


**Figure 2.5:** Left: Observed hyperfine structure transitions in  $^{203}\text{Hg}$  from **Article I**. Right: Measured hyperfine structure of  $^{203}\text{Hg}$  through in-source resonance ionization spectroscopy.

of a nucleon with orbital spin  $j$  depends on its mean square charge radius  $\langle r_j^2 \rangle$  and the effective charge  $e_j$  ( $e_j^\pi = 1$  for a free proton and  $e_j^\nu = 0$  for a free neutron). The sign of  $e_j$  flips if a hole instead of a particle is considered. Due to particle-core and residual interactions, as well as configuration mixing, the free nucleon charges are replaced by effective charges ( $e_j^\pi = 1.5$ ,  $e_j^\nu = 0.95$ ) [69]. The core part can be expressed in terms of the liquid drop model (see Section 2.1)

$$Q_{\text{core}} = \frac{3}{\sqrt{5}\pi} eZR^2\beta_2 \left[ 1 + \pi^2(a_s/R)^2 + 2\sqrt{5}/7\sqrt{\pi}\beta_2 \right], \quad (2.29)$$

with  $R = 1.2 \text{ fm} \cdot A^{1/3}$  and  $a_s$  being the nuclear radius and the surface correction term from Eq. (2.6) and  $\beta_2$  being the nuclear deformation parameter (see Section 2.2.3).

The magnetic properties of the nucleus are mainly defined through the magnetic dipole moment. The magnetic dipole moment  $\mu$  is generated through the movement of the protons inside the nucleus together with the intrinsic spin of the nucleus

$$\mu = \frac{g}{\hbar} I \mu_N, \quad (2.30)$$

where  $g$  is the gyromagnetic factor relating the spin angular momentum  $I$  to the nuclear magneton  $\mu_N = \frac{e\hbar}{2m_p} \approx 3.152 \times 10^{-8} \text{ eV T}^{-1}$  [35]. Free nucleons carry the so-called Schmidt moments  $\mu_p \approx 2.792\mu_N$  and  $\mu_n = -1.913\mu_N$ . Classically one would expect  $\mu_n = 0$ , but due to the quark structure of the neutron,  $\mu_n$  is non-zero. Schmidt values for nuclei are the values of magnetic dipole moments calculated for single nucleons with a total angular momentum  $j$ . As the nucleons inside an atomic nucleus are influenced by the other nucleons, polarization effects and meson exchange current corrections have to be considered and are very important for single particles orbiting a doubly magic nucleus [69]. The dipole moment is not sensitive to second-order core polarization effects, which leads to a constancy of g-factors over a long range of nucleons. Still, it is very sensitive to 1p-1h excitations which are the major contribution to deviations from single-particle g-factors, which requires the introduction of effective g-factors [69].

The hyperfine splitting level scheme for the  $5d^{10}6s^2 \ ^1S_0 \rightarrow 5d^{10}6s6p \ ^3P_1$  transition at 253.65 nm in mercury used in **Article I** is shown in Fig. 2.5 (left). The  $I^\pi = 5/2^-$  nuclear spin couples to the total angular  $J$  momentum, splitting the  $^3P_1$  state into three

hyperfine states. In Fig. 2.5 (right), the ion signal from resonant laser ionization is plotted versus the excitation frequency (energy).

The shift in the energy of the hyperfine state has two contributions. The magnetic component is caused, to first degree, by the interaction of the nuclear magnetic dipole moment  $\mu$  with the magnetic field  $B_e(0)$  created by the electrons

$$\Delta\nu_{\text{mag}} = \frac{A}{2}(F(F+1) - J(J+1) - I(I+1)) \equiv \frac{A}{2}C \quad A = \frac{\mu B_e(0)}{\hbar I J}. \quad (2.31)$$

The magnetic moment can be deduced by dividing factor  $A$  by a known reference  $A_{\text{ref}}$ . Taking into account the finite size of the nucleus, resulting in the Breit-Rosenthal effect (finite distribution of the nuclear charge density  $\rho(r)$ ) [71] and the Bohr-Weisskopf effect (finite distribution of the nuclear magnetic moment) [72] causes a slight shift from one isotope to another, the so-called hyperfine anomaly

$$\frac{A}{A_{\text{ref}}} = \frac{g}{g_{\text{ref}}}(1 + {}^1\Delta^2), \quad (2.32)$$

with  ${}^1\Delta^2$  modifying the ratio on a percent level. For a more detailed description of the Breit-Rosenthal and Bohr-Weisskopf contributions to the total hyperfine anomaly, see Appendix A of **Article I**.

The second contribution to the energy shift of a hyperfine state is due to the interaction of the electric quadrupole moment  $Q_s$  from Eq. (2.27) with the electric field of the electronic shell  $V_z$  along the symmetry axis. It is most pronounced in heavy, deformed nuclei. The energy shift can be written as

$$\Delta\nu_{\text{el}} = B \frac{\frac{3}{4}C(C+1) - I(I+1)J(J+1)}{2I(2I-1)J(2J-1)} \quad B = \frac{eQ_s}{\hbar} \left. \frac{\partial^2 V}{\partial z^2} \right|_{r=0}. \quad (2.33)$$

Experimental methods to determine the hyperfine parameters  $A$  and  $B$  to deduce the magnetic dipole moment and the electric quadrupole moment, as well as the isotope shift and the mean square charge radius, are presented in Section 4.4.

### 2.2.3 Nuclear Deformation

As was presented in Eq. (2.29), the electric quadrupole moment can be connected to nuclear deformation. Within the liquid drop model, the surface of the nucleus can be parameterized using spherical harmonic functions  $Y_l^m(\theta, \phi)$  to express the nuclear surface with an angle-dependent radius

$$R(\theta, \phi) = R_0 \left( 1 + \sum_{l,m} \alpha_l^m Y_l^m(\theta, \phi) \right), \quad (2.34)$$

where  $R_0$  is the radius at spherical equilibrium and  $\alpha_l^m$  being expansion parameters defining the multidimensional surface [73]. In the following, only quadrupolar degrees of freedom ( $l = 2$ ) are considered, as they are the most fundamental type of deformation<sup>2</sup> leading to ellipsoidal shapes. Since  $l \leq m \leq l$ , five different radial contributions to Eq. (2.34) exist. The angular orientation and degree of extension are

<sup>2</sup>Higher degrees of freedom exist, such as the  $l = 4$  octupolar deformation (“going pear-shaped”) [74].

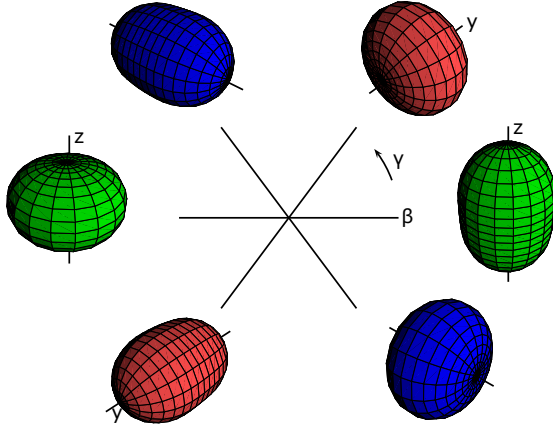


**Figure 2.6:** Visualization of the Hill-Wheeler coordinate space for quadrupole deformation with associated shapes. Figure from [73] reproduced with permission from Springer Nature.

thus described by a set of five independent parameters  $\{\alpha_{2,m}\} \rightarrow \{a_0, a_2, \theta_1, \theta_2, \theta_3\}$  spanning a five-dimensional configuration space. Hill and Wheeler introduced a coordinate transformation [75], using  $\{\beta_2, \gamma_2, \theta_i\}$  as a coordinate space where  $\{\beta_2, \gamma_2\}$  define a two-dimensional polar coordinate system in the five-dimensional quadrupolar deformation space with  $a_0 = \beta_2 \cos(\gamma_2)$  and  $a_2 = (\beta_2/\sqrt{2}) \sin(\gamma_2)$ . Three radii are associated with  $\beta_2$  and  $\gamma_2$ :

$$R_k = R_0 \left( 1 + \frac{5}{4\pi} \beta_2 \cos\left(\gamma_2 - \frac{2}{3}\pi k\right) \right), k = 1, 2, 3. \quad (2.35)$$

In Fig. 2.6, the Hill-Wheeler polar coordinate space is shown with different quadrupolar shape deformations [73]. For  $\beta_2 = 0$ , the nucleus has a spherical shape, while for  $\beta_2 \neq 0$ , the nucleus has an ellipsoidal shape (prolate for  $\beta_2 > 0$ , oblate for  $\beta_2 < 0$ ). Larger values for  $\beta_2$  thus result in a stronger ellipsoidal deformation. For  $\gamma_2 = n\frac{\pi}{3}, n \in \mathbb{Z}$  (thick lines in Fig. 2.6), two of the three axes have the same length. All other values inside the triangles result in a certain degree of triaxiality with axes as defined in Eq. (2.35). For cases where triaxiality does not play a role, i.e. when  $\gamma$  is small, Eq. (2.35) can be simplified and expressed in terms of the mean square charge radii

$$\langle r_c^2 \rangle^A = \langle r_c^2 \rangle_0^A \left( 1 + \frac{5}{4\pi} \langle \beta_2 \rangle^2 \right), \quad (2.36)$$

where  $\langle r_c^2 \rangle_0^A$  is the mean square charge radius deduced from the liquid drop model [76]. The shell-model calculations in **Article III** use the Hill-Wheeler coordinate space to represent the potential energy surface together with the degree of deformation for the examined nuclear states, demonstrating different degrees of deformation for the  $9/2^+$  ground state and the  $1/2^+$  isomeric state in  $^{79}\text{Zn}$ .

### 3 Production of Radioactive Ion Beams

With the discovery of the atomic nucleus and the early experiments studying nuclei of different stable elements, research soon expanded to unstable isotopes. Still, this was often limited by the half-lives and availability via suitable production schemes. To study radioactive nuclei with short lifetimes, i.e. in the range of days to seconds and well below, radioisotopes have to be produced artificially before being investigated in experiments. Due to this, the production of radioisotopes and their investigation are often intertwined. An effective way of delivering short-lived nuclei proved to be in the form of ion beams. After their production, radioisotopes are transported as ions at beam energies of some keV to several MeV  $u^{-1}$ , which allows the study of isotopes (including isomeric states) with half-lives as low as few milliseconds.

Today, radioactive ion beam (RIB) facilities can be mainly divided into two categories: in-flight facilities that use a high-energy beam of stable ions on a thin target material and thick-target facilities that use a high-energy proton beam on an extended target, often several centimeters thick. In the thin-target facilities, the products have beam energies similar to the driver beam and must be thermalized for low-energy measurements. In the case of thick targets, the isotopes are created in the bulk material and are then extracted and ionized. In both cases, the high-energy driver beam creates radioactive isotopes through nuclear reactions, separated with respect to their mass-over-charge ratios by strong magnetic fields.

Different nuclear reactions can occur depending on the primary beam energy, its composition, the target material, and the target thickness [78]: In fission processes, the incoming beam induces nuclear fission in the target nucleus, splitting it into two fission products while freeing a large number of neutrons. In nuclear spallation, several nucleons are ejected from the target nucleus after being struck by a light primary beam projectile, producing lighter nuclei than the target material<sup>1</sup>. In target fragmentation, a light primary beam leads to the fragmentation of the heavy target nucleus, while in projectile fragmentation, both the target and projectile can fragment. Both fragmentation methods produce nuclei lighter than the target or projectile nucleus. In transfer reactions, a heavy projectile nucleus can transfer a few nucleons with a heavy target nucleus, producing predominantly nuclei near the target and projectile nuclei sizes. During fusion-evaporation processes in which the projectile and target fuse and evaporate a few nucleons, neutron-deficient isotopes of elements heavier than the reaction partners (e.g. super-heavy elements) can be produced. Finally, spontaneous fission of a heavy nucleus [80] or neutron-induced fission of a heavy target nucleus [81] can populate a vast region of neutron-rich isotopes below the fissioning target. Spallation, fragmentation, and fission processes are highlighted in Fig. 3.1. This chapter will focus on the ISOL

---

<sup>1</sup>Nuclei heavier than the target material can be produced through proton and neutron absorption, but their production cross-sections are small [79].

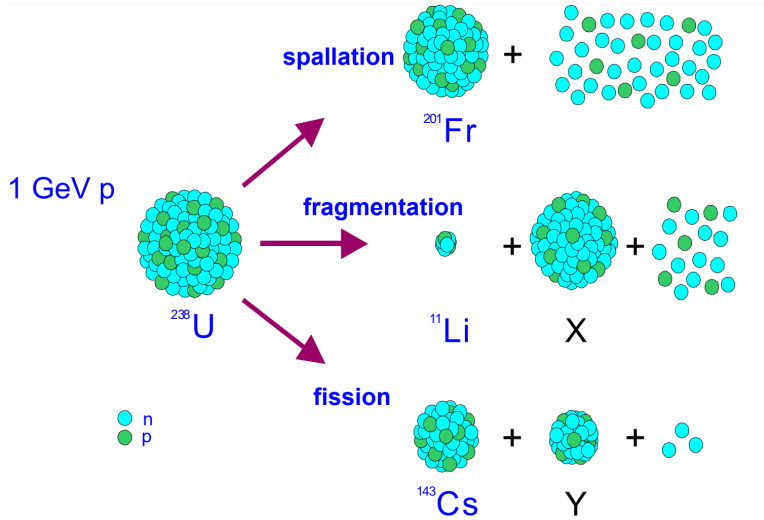


**Figure 3.1:** Nuclear reactions after high-energy protons hit a heavy nucleus. In this case, protons on a  $^{238}\text{U}$  nucleus. These are the main nuclear reactions that produce radioactive isotopes for ISOL beam production. Graphic taken from [77].

(isotope separator online) method, which uses a high-energy proton beam on a thick, heavy target.

### 3.1 Isotope Separator Online Device

The ISOL method relies on light, high-energy, and high-intensity projectiles to induce fission, spallation, and fragmentation processes in a thick target material. The reaction products are then extracted from the target before being ionized in an ion source and accelerated as an ion beam. The first demonstration of this method was performed in 1951 at the University of Copenhagen, where the fission products of neutron-induced fission of an uranium oxide target located close to a cyclotron accelerator were transported through a pipe to the nearby ion source, mass separator, and experimental station, allowing half-life measurements of short-lived krypton isotopes and their decay products [82]. In the decade that followed, research with this method commenced in Copenhagen before the cyclotron was moved to a different location, and the research community was searching for an alternative accelerator laboratory to continue the study of short-lived radio-isotopes [83].

In the mid-60s, it was decided to build a dedicated facility at the Synchro-Cyclotron (SC), an accelerator based at the European Organization for Nuclear Research (CERN) near Geneva, Switzerland, able to deliver protons at 600 MeV of beam energy. The Isotope Separator Online Device (ISOLDE) facility conducted its first experiments in 1967 and has been operating ever since. Naturally, many improvements and upgrades were performed in the almost 60-year history of the facility, with the most significant being the move from the SC to the Proton Synchrotron Booster (PSB) in 1990-1992, promising proton beam energies of 1 GeV at up to 2  $\mu\text{A}$  proton intensity [84].

Since the 90s, the facility has been expanded several times to accommodate the experimental needs of the ever-growing users community, including a post-accelerator that can re-accelerate radioactive ion beams to almost 10  $\text{MeV u}^{-1}$ . Today, ISOLDE consists of two target stations with individual mass separator magnets, a low-energy

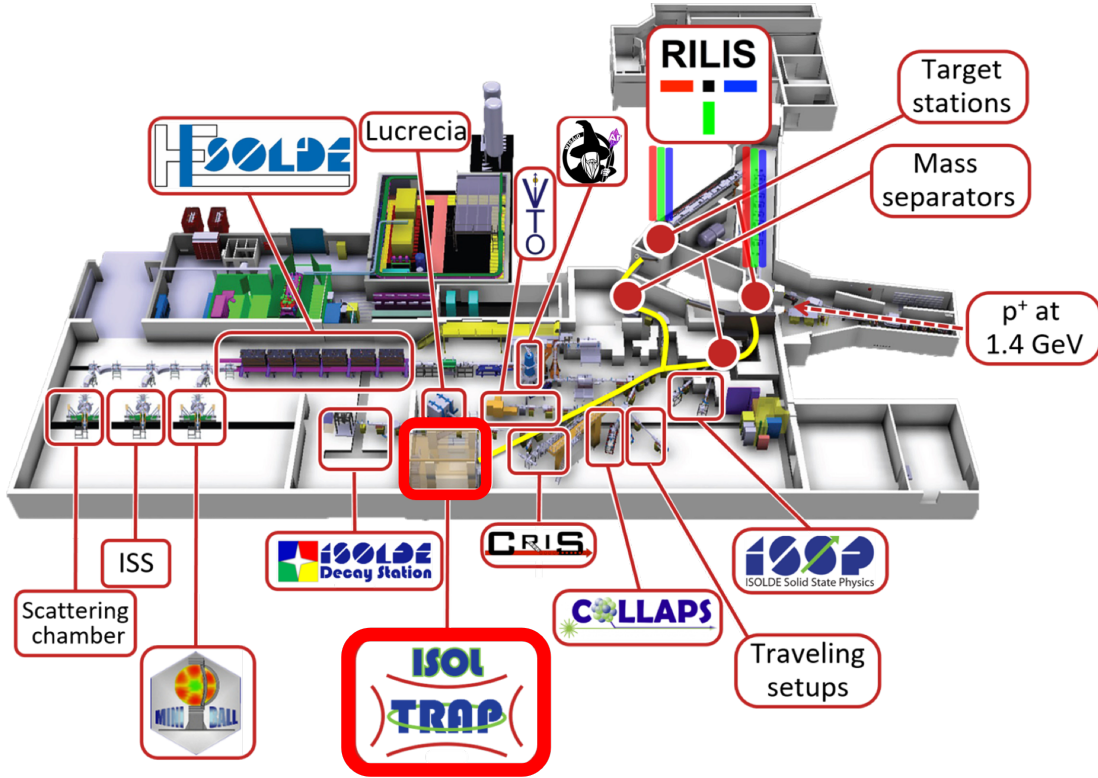


**Figure 3.2:** Schematic of ISOLDE facility as of 2023 with the location of the ISOLTRAP mass spectrometer highlighted. Graphic courtesy of the ISOLDE collaboration.

experimental area (RIBs up to 60 keV) with a number of collection areas, beam lines for visiting short-term experiments, and a number of long-term experiments that specialize in the measurement of different nuclear observables. With its superconducting post-accelerator, the high-energy part, HIE-ISOLDE, provides RIBs to several experiments. Currently, the beam dumps of both target stations are rated for up to  $3 \times 10^{13}$  protons per proton pulse with a maximum beam energy of 1.7 GeV. To make full use of the PSBs capabilities, the beam dumps are planned to be exchanged to handle a higher number of protons per proton pulse with energies up to 2 GeV, promising an overall increase in yield of up to a factor 3 to 4 [85].

Fig. 3.2 shows the layout of the ISOLDE facility as of 2023. The pulsed proton beam from the PSB is impinging on one of the two target stations. Each target has a dedicated electromagnetic separator magnet: the GPS (general purpose separator) magnet is a single electromagnet that can separate the produced RIBs with a resolving power  $R = m/\Delta m$  of up to 500, while the HRS (high-resolution separator) consists of two separate electromagnets that can yield resolving powers of up to  $R = 6000$ . Behind the HRS, a linear radiofrequency quadrupole Paul trap (ISCOOL) [86] can collect, cool, and bunch the continuous mass-separated beam to provide bunched beams to the downstream experiments.

Both beamlines of HRS and GPS are merged in the first segment of the central beamline, at which the ISOLDE tape station is located [87]. This device resembles a

large tape recorder that can transport radioactivity implanted on a tape to either a  $4\pi$  beta detector or a gamma detector used for yield measurements, beam composition studies, and target parameter optimization. Following this first section of the central beamline, the RIBs are distributed to the different low-energy experiments at ISOLDE (including the ISOLTRAP mass spectrometer, which is located at the end of the central beamline), or the beam is injected into the REX-EBIS for charge breeding and post-acceleration in the HIE-ISOLDE post-accelerator [88].

## 3.2 Targets and Ion Sources

Target containers at ISOLDE consists of a 20 cm long tantalum tube with a diameter of 2 cm that is heated to up to 2200 °C. Depending on the required radioactive beam, this tube is filled with metal foils (Ta, Ti, Nb), molten metals (Pb, Sn), or ceramic compounds such as oxides (zirconia, CaO) or carbides ( $UC_x$ ,  $Th_x$ ,  $La_x$ ). Proton pulses delivered by the PSB impinge on the target at a maximum of 1.2 s interval, depending on the general demand for protons at CERN (the PSB is part of the accelerator chain leading to the Large Hardon Collider). The proton beam can also be steered onto a solid tungsten cylinder near the target container, creating intense neutron fluences to favor the production of neutron-induced fission products over proton-induced spallation [89]. Each proton pulse consists of up to  $3 \times 10^{13}$  protons, divided into 20 short bunches within a 2.4  $\mu$ s time window. In a special staggered mode, the four PSB cyclotrons eject their proton bunches with a certain delay with respect to each other, resulting in four times five bunches with a time spacing of 5 to 500  $\mu$ s in-between. The target heating, in combination with the heating of the proton impact, leads to diffusion and effusion of the produced radioisotopes into the transfer line. The simple version is usually made of tungsten or tantalum and has an inner diameter of 3 mm, connecting the target container with an ion source.

Different ways to ionize neutral radioactive atoms have been developed over the decades at ISOL facilities. The most straightforward method is the surface ionization of atoms in the hot cavity of the transfer line. The degree of ionization  $\alpha_s \sim n_{\text{ions}}/n_{\text{atoms}}$  on a hot surface is described through the Saha-Langmuir equation and depends on  $\exp((\Phi_{\text{sur}} - W_i)/k_B T)$ , where  $\Phi_{\text{sur}}$  is the work function of the surface material,  $W_i$  is the ionization energy that is needed to remove the outermost electron from the atom, and  $k_B T$  is the temperature of the surface [90]. Elements with  $W_i \lesssim 6$  eV, such as the alkali metals and some lanthanides and actinides, are well ionized in this way. In many cases, surface-ionized elements contribute significantly to the contamination of the desired element. Thus, materials with a low work function would be preferable [91]. In practice, however, with the need to operate at high temperatures to promote diffusion into the ion source, metals with a high melting point, such as tungsten and tantalum, are chosen, which have work functions around 4 eV to 5 eV. To circumvent this problem, a piece of quartz located in a temperature-controlled transfer line can trap alkali ions by significantly delaying their diffusion into the ion source [92, 93].

An element-insensitive way of ionization is the Forced Electron Beam Induced Arc Discharge (FEBIAD) type ion source [94, 95]. In this ion source, the atoms diffuse out of the transfer line through the holes of a cathode into a discharge chamber formed by

a cylindrical electrode (anode). By applying a voltage between the cathode and the anode, electrons emitted through thermionic emission by the cathode are accelerated into the discharge chamber, ionizing the neutral atoms inside. A noble gas is let into the chamber to facilitate the ionization process, creating a plasma. An electromagnet surrounds the anode for the confinement of the plasma. At ISOLDE, the volume of the discharge chamber of this FEBIAD-style ion source is enlarged to increase the active plasma volume. This so-called Versatile Arc Discharge Ion Source (VADIS) has a factor 3-20 better ionization efficiency compared to the FEBIAD ion source [96], which enabled the discovery of the until then unobserved radon-229 isotope using the ISOLTRAP mass spectrometer [97]. The VADIS can be coupled to different types of transfer lines, i.e. to a hot transfer line (VD5) or to a water-cooled transfer line (VD7) which delivers very clean radioactive beams of volatile species, including molecules, and noble gases.

Finally, resonant laser ionization is an element-selective way to ionize radioisotopes. The Resonant Laser Ionization Ion Source (RILIS) uses lasers at different wavelengths to selectively excite and finally to ionize a certain element inside the hot cavity between the transfer line and extraction electrode [98]. Section 4.4.2 introduces the concept of resonant laser ionization and the laser spectroscopy that can be applied inside the hot cavity of this ion source. While performing laser ionization, surface ionized contamination can be reduced by employing the LIST, the Laser Ion Source and Trap [99, 100], by spatially separating the parasitic surface ionization and the laser ionization. A LIST decouples the laser ionization from the hot cavity by using a repeller and an RFQ ion guide: surface ionized elements are repelled by the repeller potential while other elements, still neutral, diffuse through the repeller into the RFQ structure, in which the element of interest is selectively laser ionized and guided through the RF guiding field towards the extraction electrode. The LIST mode of operation can yield contamination suppression factors of several orders of magnitude while sacrificing the part of the atoms that are laser ionized in the hot cavity and thus blocked by the repeller. This loss factor is usually in the order of 5-20 and, in many cases, a good trade-off in terms of efficiency versus background suppression.

For **Article I**, a molten lead target (target number #511) was coupled to a hot VD5 plasma ion source with RILIS laser ionization inside the anode cavity, the so-called “VADLIS” mode [101]. This target and the ion-source combination were, in parts, chosen for the production of mercury isotopes since the mercury vapor pressure promises good release from the molten lead target material while the production of contamination, such as francium, is suppressed due to their release characteristics from the target and due to the small blocking potential provided by the ion source cathode (which in this way acts similar to the blocking potential of the LIST). The RILIS ionization scheme for mercury is detailed in Section 2.2.2. In this configuration, both n-deficient and n-rich mercury isotopes were produced with minimal background.

To produce neutron-deficient indium isotopes in the  $^{100}\text{Sn}$  region for **Article II**, a lanthanum-carbide target (target number #732) in combination with ionization by the standard RILIS MK1 was used. The neutron-deficient isotopes around  $^{100}\text{Sn}$  are mostly produced through spallation processes and are selectively ionized through laser ionization. For indium, a two-level scheme was used, with the first step resonantly driving the  $5s^25p\ ^2P_1 \rightarrow 5s^25d\ ^2D_{3/2}$  transition at 304.023 nm, followed by a non-resonant high-power step at 532 nm (“Blaze”). Yields in the central beamline CA0 extracted from

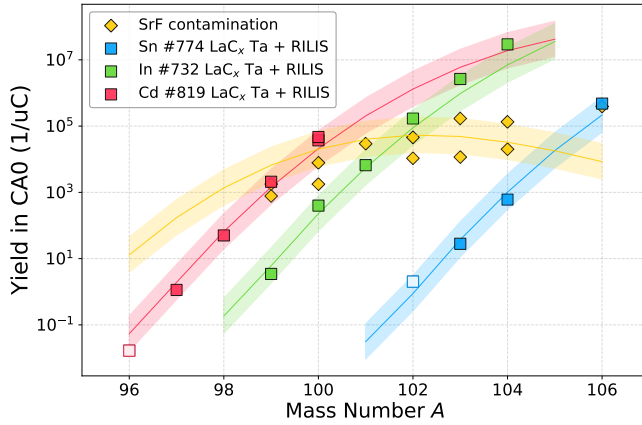


**Figure 3.3:** Measured (solid symbols) and estimated (solid line and shaded bands) yields for neutron deficient isotopes in the  $^{100}\text{Sn}$  region from a  $\text{LaC}_x$  target with laser ionization. The open symbols are upper limits based on the absence of counts per observation time window. The solid lines and shaded bands are scaled yield estimations based on EPAX V3 empiric fragmentation cross-section calculations [103] (see text for explanations).

MR-ToF MS measurements for this and two other target units used to produce neutron-deficient tin, indium, and cadmium isotopes are shown in Fig. 3.3. The measured yields are augmented by fragmentation cross-section calculations using the empirical EPAX V3 parameterization (solid lines and shaded bands). The fragmentation yields are scaled by factors of 0.5, 1.0, 0.1, and 0.0001 for tin, indium, cadmium, and strontium, respectively. These factors were chosen to match the observed yields and to provide a rough extrapolation for other rare isotopes along the different chains. Please note that this estimation does not consider half-lives and release characteristics, which are two major influences on observed yields in the central beamline, making the use of adjustment factors necessary. The open symbols for tin and cadmium are upper limits based on the non-observation of the isotopes within the observation time window. The most dominant radioactive contamination in the region was strontium in the form of the strontium-fluoride molecule, here highlighted in gold, which proved to be a serious obstacle in measuring  $^{102}\text{Sn}$  and  $^{101}\text{Sn}$  for experiment IS719 [102].

The zinc beam of **Article III** was produced at ISOLDE from a uranium-carbide target (target number #758) in combination with a quartz transfer line for suppression of surface ionized contaminants, such as rubidium, and RILIS laser ionization inside the hot tantalum tube that connects the quartz towards the extraction electrode. The laser scheme used three steps: The first and second steps drove resonantly the  $4s^2\ ^1S_0 \rightarrow 4s4p\ ^1P_1 \rightarrow 4s4d\ ^1D_2$  transition at 213.925 nm and 636.41 nm, respectively. The third step was again non-resonant at 532 nm (“Blaze”). Pure zinc beams were thus delivered, starting to suffer from rubidium contamination only for  $A > 81$ . It should be noted that this laser scheme coincidentally also ionizes iron very efficiently, which is a problem on masses  $A = 56 - 58$ , where stable iron from the target and ion source container results in very strong contamination. A release curve was measured to most effectively capture and measure the laser-ionized zinc isotopes (see Fig. 3.4). Due to the rather quick release of zinc, the experimental cycle was synchronized to the proton impact and the ISOLDE beam gate was open only when zinc was released from the target and ion source, i.e. 150 ms to 600 ms after proton impact.

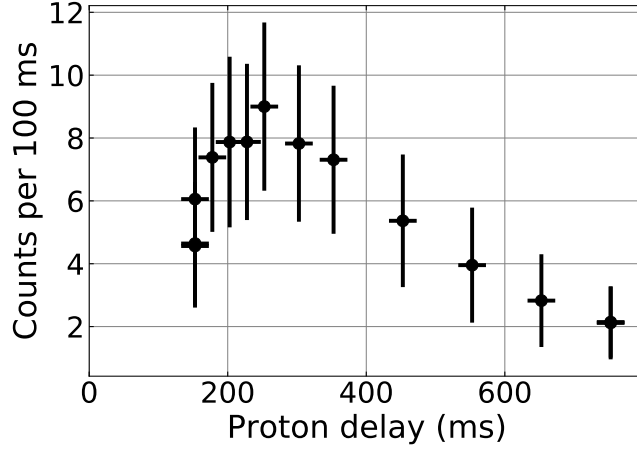


**Figure 3.4:** Release of zinc from an  $\text{UC}_x$  target with neutron converter and quartz line (target number #758) during the experiment for **Article III**. Note the delay of almost 200 ms after proton impact.

The Penning trap experiment of **Article III** was performed at the Ion Guide Isotope Separator Online (IGISOL) facility at the University of Jyväskylä, Finland [104]. In this method, a proton beam or a heavy ion beam produces proton-induced fission or fusion evaporation reactions in a thin target. The reaction products, usually in a high charge state, are stopped in a helium-filled stopping cell in which most of the products end up singly charged [105]. These ions are then guided to an extraction electrode using an RF sextupole, after which they are accelerated and separated with respect to their mass-over-charge ratio.



## 4 Experimental Methods

Experiments at radioactive ion beam facilities for nuclear structure investigations can be divided into low energy (beam energies of  $< 100$  keV), medium energy (up to  $15 \text{ MeV u}^{-1}$ ), and high energy (up to several hundreds of  $\text{MeV u}^{-1}$ ). Experiments at low energies perform measurements mostly on ground state and isomeric state properties with stopped beams, trapped beams, or in-flight techniques. Decay spectroscopy experiments stop radioactive ions on catcher foils near radiation detectors to detect the particles that are emitted during the decay of the radioactive ions. Other experiments trap RIB in ion traps to perform mass and half-life measurements or perform laser spectroscopy, the latter can also be done in-flight. At medium energies, Coulomb excitation experiments below the Coulomb barrier ( $3 - 4 \text{ MeV u}^{-1}$ ) probe nuclear collectivity and transfer reaction experiments ( $5 - 10 \text{ MeV u}^{-1}$ ) investigate highly excited nucleon orbits. At high energies, usually in storage rings at energies ranging around  $10 - 500 \text{ MeV u}^{-1}$ , mass, lifetime, and in-ring transfer reaction experiments are performed. Following the present work, this chapter will focus on nuclear structure experiments at low energies, namely with trapped ions and with laser spectroscopy of low-energy beams.

### 4.1 Mass Spectrometry With Trapped Ions

Mass spectrometry of stored radioactive ions for nuclear and weak interaction physics has a long history [106]. The most established types of spectrometers today include Paul traps (radiofrequency and electrostatic fields), Penning traps (electrostatic fields with strong magnetic field), and Multi-Reflection Time-of-Flight devices (electrostatic fields). Other types of spectrometers, such as storage rings [107], radiofrequency transmission spectrometers [108], time-of-flight spectrometers [109], or cyclotrons [110] are used as well but will not be discussed here.

Mass spectrometry with trapped ions at low energy is performed at many RIB facilities worldwide, namely ISOLTRAP/ISOLDE-CERN (Switzerland, see Section 4.2) [111], TITAN/ISAC-TRIUMF (Canada) [112], JYFLTRAP/IGISOL-Jyvaskyla (Finland) [113], LEBIT/FRIB (USA) [114], SHIPTRAP/GSI (Germany) [115], and ZD MRTOF/RIBF-RIKEN (Japan) [116]. Most of these setups consist of a radiofrequency trap or stopping cell to accumulate, cool, and bunch the RIB in combination with one or more of the abovementioned spectrometer types.

In the following, the two most important techniques for this work, i.e. Penning Trap Mass Spectrometry (PTMS) and Multi-Reflection Time-of-Flight Mass Spectrometry (MR-ToF MS), will be introduced based on the example of the ISOLTRAP setup.

### 4.1.1 Penning Trap Mass Spectrometry

Initially built by Dehmelt and Van Dyck to measure the properties of the electron, the Penning trap was quickly adapted to other fields of research, benefiting from the highly controllable environment in which charged particles can be trapped inside the device. Coined by Dehmelt after the dutch Physicist Frans Penning, who studied electric discharges at low pressures, the Penning trap uses the electric field  $\mathbf{E}$  generated by a ring electrode in between two end-cap electrodes in combination with a strong homogeneous magnetic field  $\mathbf{B}$  to confine charged particles. The electric potential, providing the axial confinement, can be written as

$$\phi = U_0(2z^2 - x^2 - y^2)/d^2 = U_0(2z^2 - \rho^2)/d^2, \quad (4.1)$$

where  $U_0$  is the difference between the electric potentials of the end-caps and the ring electrode,  $d^2 = (z_0^2 + \rho_0^2/2)/2$  is the characteristic dimension of the electrodes with  $z_0$  being the distance between the trap center from the end-caps and  $\rho_0$  being the radius of the ring electrode,  $x$ ,  $y$ , and  $z$  being the Cartesian coordinates with respect to the trap center, and  $\rho^2 = x^2 + y^2$  being the radial dimension for cylinder coordinates. The homogeneous magnetic field along the  $z$ -axis provides radial confinement through the Lorentz force  $\mathbf{v} \times \mathbf{B}$  resulting in a cyclotron motion with an  $\mathbf{E} \times \mathbf{B}$  drift resulting in a magnetron motion. Both these circular motional modes lead to the combined radial trajectory of the charged particles. In addition, the ions follow a harmonic oscillation in the  $z$ -direction, i.e. between the end-cap electrodes (see Fig. 4.1).

In the non-relativistic case, the motion of the charged particle with mass  $m$  and charge  $q$  can be expressed as a simple harmonic oscillator and can be determined by solving the equations of motion  $\mathbf{F} = m\ddot{\mathbf{r}} = q(-\nabla\phi + \dot{\mathbf{r}} \times \mathbf{B})$ . By choosing a generic oscillator Ansatz  $f(t) = A \exp(i\omega t)$ , three different oscillation frequencies can be found:

$$\nu_z = \frac{1}{2\pi} \sqrt{\frac{qU_0}{md^2}} \quad \nu_{\pm} = \frac{\nu_c}{2} \pm \sqrt{\frac{\nu_c^2}{4} - \frac{\nu_z^2}{2}} \Rightarrow \nu_c = \nu_+ + \nu_- \quad (4.2)$$

where  $\nu_c = qB/m$  is the cyclotron frequency for the trapped charged particle,  $\nu_z$  is the frequency of the axial motion, and  $\nu_{\pm}$  are those of the reduced cyclotron and magnetron motions, respectively. From these equations, it follows that  $\nu_c > \nu_+ \gg \nu_z > \nu_-$  for heavy, singly-charged radioactive ions in a strong magnetic field of some Tesla.

The resulting motion is thus a superposition of the three different solutions to the differential equations and is visualized in Fig. 4.1(a). From the abovementioned equations, it can be seen that the motion is highly dependent on the mass of the stored particle and the magnetic field. Brown and Gabrielse have shown that, to first order, the sum of all squared eigenfrequencies is equal to the square of the cyclotron frequency even in the presence of small electric field imperfections  $\epsilon$  and electrode misalignment  $\theta$  with respect to the magnetic field [118]. This invariance theorem enables either the direct measurement of  $\nu_c$  or to infer  $\nu_c$  by measuring the eigenfrequencies independently. By measuring the frequency ratio

$$R = \frac{\nu_{c,\text{ioi}}}{\nu_{c,\text{ref}}} = \frac{m_{\text{ref}}}{m_{\text{ioi}}}, \quad (4.3)$$

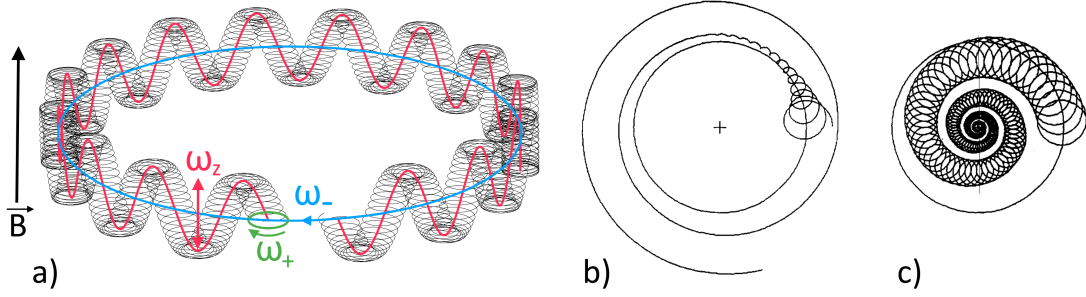


**Figure 4.1:** 3D Motion of a trapped charged particle in a Penning trap (a). Radial motion of a particle with buffer gas collisions without (b) and with (c) resonant quadrupolar excitation at  $\nu_c$ . Figures (b) and (c) from [117] reproduced with permission from Elsevier.

for a reference ion with mass  $m_{\text{ref}}$  and cyclotron frequency  $\nu_{c,\text{ref}}$ , and the frequency  $\nu_{\text{ioi}}$  of the ion of interest, then the magnetic field  $B$  cancels out and the mass  $m_{\text{ioi}}$  of the ion of interest can be calculated.

### Buffer gas cooling

Both axial and radial motions of the charged particle can be manipulated through the application of an alternating electric dipole field superposed onto the static trapping potential. The amplitude of the axial motion can be, for example, dampened or excited by applying a radiofrequency voltage on the end-cap electrodes at the eigenfrequency  $\nu_z$ . Segmenting the ring electrode into two separated pieces enables the manipulation of the two radial motions in the same way. While the magnetron motion is only weakly mass-dependent, resonant excitation of the reduced cyclotron motion removes particles with unwanted masses from the trap by applying a dipolar excitation at  $\nu_+$  to increase the reduced cyclotron radius  $\rho_+$  until the particles are driven into the electrodes. A four-fold segmentation of the ring electrode in combination with an rf voltage applied to opposite segments at the cyclotron frequency  $\nu_c$  generates a quadrupolar rf field which can periodically convert the magnetron motion into the reduced cyclotron motion and vice-versa.

The inter-conversion of energy stored in the radial motion is used in the so-called mass-selective buffer gas cooling technique [117]. The presence of residual gas inside the Penning trap leads to particle-gas collisions in which the stored particles transfer parts of their potential energy to the buffer gas. This effectively increases the magnetron radius  $\rho_-$  since the energy potential of the magnetron motion has a maximum in the trap center. To avoid loss of the particles, a quadrupolar rf voltage at  $\nu_c$  is applied, which converts the magnetron motion into the reduced cyclotron motion, which has an energy potential minimum at the trap center, leading to a mass-selective cooling of the stored particles into the trap center. A short conversion pulse at larger amplitudes leads to a fast, broad-band interconversion, while a long pulse with a small amplitude has a larger mass resolving power but requires longer storage times. The particle motion in the presence of a buffer gas without and with an rf drive at  $\nu_c$  is shown in Fig. 4.1(b)

and Fig. 4.1(c).

To measure the mass of a trapped charged particle in a Penning trap means measuring its cyclotron frequency. The cyclotron frequency can be determined indirectly by measuring the different eigenfrequencies through image currents induced on the electrodes (non-destructive) or directly through time-of-flight and phase-imaging techniques (destructive). Since radioactive isotopes can have short half-lives, direct and fast measurements are usually employed at radioactive ion beam facilities to determine  $\nu_c$ . In the following, the two state-of-the-art methods are described.

### Ion-cyclotron resonance techniques

As described earlier, the two radial motions can be interconverted using a quadrupolar electric rf voltage on resonance with the cyclotron frequency of the charged particle. Hence, resonant excitation of the trapped particle at  $\nu_c$  has been the main tool for determining the cyclotron frequency. Historically used to determine the proton electron mass ratio [119], the time-of-flight-based technique utilizes the time-of-flight dependency of the particle's energy stored in the cyclotron motion to detect resonantly excited ions.

Consider an ion with initial total energy  $E_0$  moving in a magnetic field  $B(z)$  and an electric field generated by the electric potential  $U(z)$  with  $z$  being the coordinate axis along the trap's symmetry axis. The ion's magnetic moment  $\mu_z(\nu_{rf}, z) = E_r(\nu_{rf})/B(z)$  can then be expressed in terms of the energy stored in the radial motion  $E_r$  (depending on quadrupole excitation  $\nu_{rf}$ ) and the external magnetic field along the  $z$  axis. The interaction of the magnetic moment with the external magnetic field creates potential energy  $E_{\text{pot}}(\nu_{rf}, z) = -\mu(\nu_{rf}, z)B(z)$  with force  $F_z(\nu_{rf}, z) = -\mu(\nu_{rf}, z)\frac{\partial B(z)}{\partial z}$  along the  $z$  axis. Thus, ions with their magnetron motion fully converted into reduced cyclotron motion ( $\nu_{rf} = \nu_c$ ) experience a stronger force along the  $z$  axis when moving through a magnetic field gradient as compared to ions with residual magnetron motion, leading to a reduction in the ions' time-of-flight after the pulsed release from the trap to the detector in the fringe field of the magnet.

Following the analytic expression of [120], the effective time-of-flight can be expressed as

$$T(\nu_{rf}) = \int_{z_0}^{z_1} \sqrt{\frac{m}{2 * [E_0 - qU(z) - \mu(\nu_{rf}, z)B(z)]}} dz. \quad (4.4)$$

Starting with a pure magnetron motion, the radial kinetic energy  $E_r \sim \sin^2(\nu_b T_{rf})/\nu_B^2$  can be expressed in terms of the length  $T_{rf}$  of the excitation pulse and a modified ion frequency  $\nu_B$  that contains information about dampening through rest gas collisions and the initial magnetron radius. The equation shows that precise knowledge of the electric and magnetic field along the  $z$  axis between start-point  $z_0$  and point of measurement  $z_1$  is needed, accessible through simulations and measurements.

In practice, the time-of-flight of a stored ion after some excitation time  $T_{rf}$  onto a time-of-flight detector is measured for different excitation frequencies  $\nu_{rf}$ , resulting in a time-of-flight spectrum that can be analytically understood using Eq. (4.4). Typically, single pulses are used for the quadrupole excitation, leading to a resonance spectrum with a main fringe and several side fringes in the frequency domain, which corresponds to the Fourier transformation of a single rectangular pulse. For a single excitation

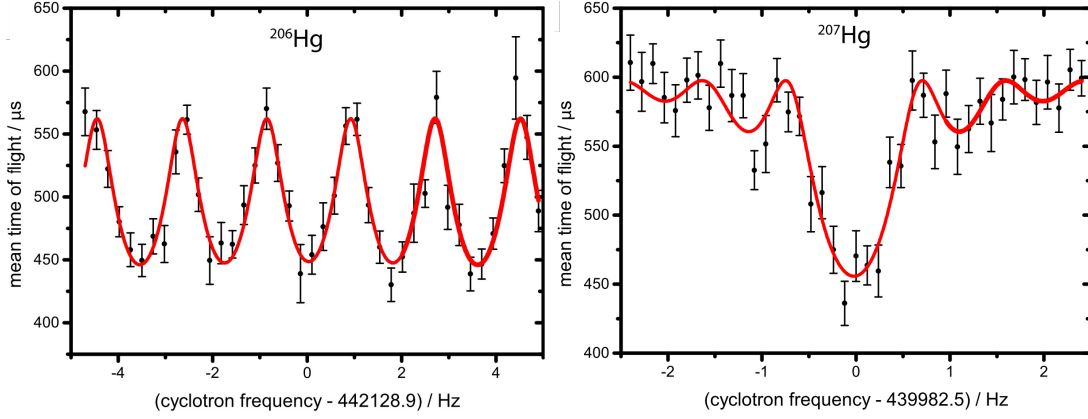


**Figure 4.2:** Time-of-flight ion-cyclotron resonance spectra for  $^{206}\text{Hg}$  and  $^{207}\text{Hg}$  from **Article I** with excitation times of 600 ms and 1.2 s, respectively.

pulse, the full-width-at-half-maximum  $\Delta\nu_{\text{FWHM}} \sim 0.8/T_{\text{rf}}$  can be estimated through tailor-expanding  $E_r$  and determines the intrinsic mass resolution of the technique since  $\nu_c \sim 1/m$ . For a two-pulse Ramsey-type excitation ( $T_{\text{rf}} = T_{\text{rf, on}} + T_{\text{rf, off}} + T_{\text{rf, on}}$ ), the full-width-at-half-maximum can be reduced by 30% while the statistical improvement yields almost a factor of three in precision on determining  $\nu_c$  for the same excitation time and amount of measured ions as compared to the single-pulse excitation scheme [121, 122].

In Fig. 4.2 the time-of-flight ion-cyclotron resonance (ToF-ICR) spectra for  $^{206}\text{Hg}$  and  $^{207}\text{Hg}$  from **Article I** are shown [123]. The spectrum for  $^{206}\text{Hg}$  was measured using a two-pulse excitation scheme with  $T_{\text{rf}} = 60 \text{ ms} - 480 \text{ ms} - 60 \text{ ms}$  (on-off-on), resulting in several pronounced ToF maxima and minima. The spectrum for  $^{207}\text{Hg}$  was measured with  $T_{\text{rf}} = 1.2 \text{ s}$  resulting in one minimum with small side fringes. Comparing both resonances, considering the overall factor two in excitation time difference, the center fringe for the Ramsey-type excitation scheme is slightly narrower as compared to the single-pulse excitation.

As discussed in the previous paragraph, the intrinsic resolution of this method is limited by the excitation time  $T_{\text{rf}}$ . Furthermore, several data points at different excitation frequencies must be taken. To circumvent these limitations, a non-scanning technique relying on measuring phase differences using a position-sensitive time-of-flight detector has been introduced recently [124, 125]: as shown in Fig. 4.3, the ions start at the trap center (position 1). Following, the radial motion (either  $\nu_+$  or  $\nu_-$ ) is excited with a dipole pulse to position (2), after which the ions revolve freely around the trap center for a phase-accumulation time  $t$ . During this time, the ions accumulate an absolute phase  $\Phi + 2\pi n = 2\pi\nu t$  at position (3), where  $\Phi$  is the phase angle between position (2) and (3),  $n$  is the total number of revolutions and  $\nu$  is the frequency of the radial motion. The radial frequency can thus be written as

$$\nu = \frac{\Phi + 2\pi n}{2\pi t}. \quad (4.5)$$

The cyclotron frequency is calculated through independent measurements of  $\nu_-$  and  $\nu_+$  (see Eq. (4.2)) by ejecting the ions out of the trap onto the position-sensitive detector for

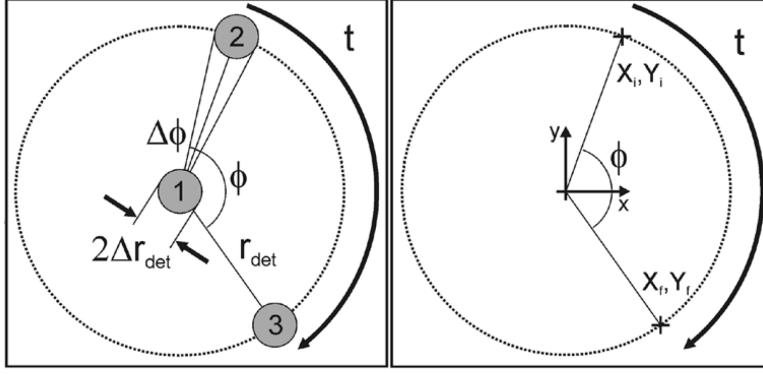


**Figure 4.3:** Ion spots on the position-sensitive detector after ejection from the Penning trap for different measurement steps. Figure from [125] reproduced with permission for Springer Nature.

positions (1-3). Due to the diverging magnetic field near the exit of the solenoidal field, the projection of the ions at the position of the trap onto the on-axis detector outside the magnet is magnified by a magnification factor  $G$ . The resolution of this technique is then dependent on the spot size (radius  $r$  in Cartesian coordinates or phase distribution  $\Delta\Phi$  in polar coordinates) and the spatial separation in phase  $\Phi$  after time  $t$ .

The cyclotron frequency  $\nu_c$  can, however, be measured directly. To do so, two different alternating excitation patterns are performed. Both patterns share the first two steps and only differ in step 3:

- 1 After capturing the ions in the trap, the ions are brought into the trap center by applying a  $180^\circ$  phase-shifted dipole pulse at  $\nu_-$  to effectively reduce the magnetron radius  $\rho_-$
- 2 Excitation of the ions to a large  $\rho_+$  by applying an in-phase dipole pulse at  $\nu_+$
- 3a Either conversion to slow magnetron motion through quadrupolar excitation at  $\nu_c$ , then phase accumulation  $\Phi_- + 2\pi n_-$  for  $t_1$
- 3b Or phase accumulation  $\Phi_+ + 2\pi n_+$  for  $t_2$  at fast reduced cyclotron motion, then conversion to pure magnetron motion through quadrupole excitation at  $\nu_c$
- 4 Extraction of the ions and projection onto the detector

If  $t_1 = t_2 = t$ , then the excess phases  $\Phi_-$  and  $\Phi_+$  accumulated after  $n_-$  and  $n_+$  revolutions in steps 3a and 3b, respectively, can be summed, resulting in a phase difference

$$\Phi_c = \Phi_- + \Phi_+ = 2\pi\nu_c t - 2\pi(n_+ + n_-) \quad (4.6)$$

from which  $\nu_c$  can be calculated [125]. For a so-called center-spot reference (position 1), the ions are quickly ejected out of the trap after step 1, effectively projecting the location of the trap center onto the position-sensitive detector.

This so-called phase-imaging ion-cyclotron resonance (PI-ICR) technique has the advantage over ToF-ICR that no frequency scan has to be performed and that fewer ion counts are needed to extract  $\nu_c$ . Due to the spatial resolution of the detector and the separation of the phases, PI-ICR increases the measurement precision by a factor of 5 and the resolving power by a factor of 40 compared to the same measurement conditions with ToF-ICR [125].

### 4.1.2 Multi-Reflection Time-of-Flight Mass Spectrometry

The time-of-flight technique described in the following relies fully on the fact that, starting with the same kinetic energy, a bunch of ions with different masses is separated over a long flight distance as heavier ions travel slower than lighter ions.

For the non-relativistic case, the mass  $m$  of an ion moving with a velocity  $v$  can be expressed through its kinetic energy  $E_{\text{kin}} = 1/2 \cdot m \cdot v^2$ , where  $v = s/t$  is the time  $t$  the ion needs to travel a certain distance  $s$ . When the kinetic energy and the flight distance are known and the flight-time  $t$  is measured, then the ion's mass can be calculated. The mass-resolving power

$$R = m/\Delta m = t/2\Delta t_{\text{FWHM}} \quad (4.7)$$

is a quantity determining how well the signals of ions with different masses can be separated with a certain flight time  $t$  and a time focus given a Full-Widht-Half-Maximum time spread of  $\Delta t_{\text{FWHM}}$ . Thus, the resolving power scales linearly with the absolute ToF provided the time spread remains constant.

Single-pass spectrometers with short flight times date back to the 1940s [126] and are used for cases where masses with vastly different mass numbers need to be resolved, e.g. for applications in biology and chemistry. Ways to increase the flight time without increasing the overall device size include static electrodes to reflect ions within the device [127]. Using electrodes for multiple reflections has been demonstrated to lead to exceptionally long flight times [128–130] and therefore yields high resolving powers.

Today, many such multi-reflection devices are used at RIB facilities worldwide for purification [131], identification [79, 132], and mass spectrometry [133–136], exploiting high mass resolving powers in excess of  $10^5$  and competing with PTMS for cases, where the ion's half-life is too short to allow for long excitation times ( $< 50$  ms) [137]. Furthermore, performing collinear laser spectroscopy (see Section 4.4) within an MR-ToF device promises greatly enhanced sensitivity with respect to the conventional single-pass method as the number of interactions between the laser light and the ions is many orders of magnitude higher [138–140].

In practice, the kinetic energy  $E_{\text{kin}}$  and the total flight path  $s$  are usually not known with high precision. The mass  $m$  of the ion of interest is therefore extracted from its measured time of flight (ToF)  $t$ , compared to two reference masses  $m_1$  and  $m_2$  with flight times  $t_1$  and  $t_2$ , respectively:

$$m^{1/2} = C_{\text{ToF}}\Delta_{\text{Ref}} + \Sigma_{\text{Ref}}/2, \quad (4.8)$$

where  $\Delta_{\text{Ref}} = \sqrt{m_1} - \sqrt{m_2}$ ,  $\Sigma_{\text{Ref}} = \sqrt{m_1} + \sqrt{m_2}$  and  $C_{\text{ToF}} = (2t - t_1 - t_2)/[2(t_1 - t_2)]$  [42]. The mass difference between two species stored in an MR-ToF device can be expressed through a ToF difference, particularly when the masses are very similar. This is especially interesting for extracting Q-values or isomeric excitation energies. For example, the excitation energy

$$E = \left[ \left( \frac{\Delta t}{t_0} \right)^2 + 2 \frac{\Delta t}{t_0} \right] m_0 c^2, \quad (4.9)$$

of an isomeric state can be directly related to the ToF difference  $\Delta t$  with respect to its ground state of mass  $m_0$  and ToF  $t_0$ , with  $c$  being the speed of light in vacuum. This

## 4 Experimental Methods

reduces to  $E \approx 2 \frac{\Delta t}{t_0} m_0 c^2$  for  $\Delta t \ll t_0$ , where the ratio  $\frac{\Delta t}{t_0}$  is in the order of  $10^{-5}$ , typical for singly charged ions and trapping times of several milliseconds.

A typical MR-ToF device for mass spectrometry is shown in Fig. 4.4. A drift region with a single, long electrode separates two stacks of mirror electrodes consisting of up to six individual electrodes. The mirror electrodes are usually designed to form a complex electrostatic potential, in which the ions are decelerated, focused, and effectively reflected by 180 degrees back into the drift region. There are different ways to load and unload ion bunches into the device. The first method requires certain electrodes in the mirrors to be switched to a lower potential to allow the ion bunch to enter and exit the device. The second method uses a potential slightly lower than the beam energy and captures or ejects the ion bunch by pulsing the potential of the drift electrode in the drift region.

Ion bunches loaded into the device tend to disperse due to the initial non-zero energy spread, slightly different trajectories inside the device, and the Coulomb interaction between the ions, especially at the turning points where the space-charge density is highest. This has to be considered for choosing the proper mode of operation for one's application.

The device can be operated in three different modes, characterized by the rate of change  $\partial T / \partial E_{\text{kin}}$  in revolution period  $T$  with the kinetic energy  $E_{\text{kin}}$  [141, 142]. In dispersive mode ( $\partial T / \partial E_{\text{kin}} < 0$ ), a rather steep mirror potential leads to a strong correlation between the faster and slower ions through Coulomb interaction, where slower ions are not reflected as quickly as fast ions, leading to an overall increase in the initial dispersion. In self-bunching mode ( $\partial T / \partial E_{\text{kin}} > 0$ ), the opposite effect can be found. Momentum exchange between ions with different velocities increases accumulation around the center-of-mass of the ion bunch. In the transition between both modes ( $\partial T / \partial E_{\text{kin}} \sim 0$ ), initial non-uniformities in trajectories and energies are compensated. In this isochronous mode, ions with larger velocities penetrate the mirror potentials deeper and thus travel a larger distance than ions with slower velocities, leading to a sustained bunch character inside the device. For mass spectrometry, the third mode with a very small ion load is desired since, similar to PTMS, even the smallest space-charge effects can already lead to strong systematic mass shifts [143].

Due to electrode imperfections, drifting electric fields, and other perturbations, the mass-resolving power does not rise linearly for long flight times as Eq. (4.7) would suggest but rather flattens and slowly decreases due to residual dispersion of the ion

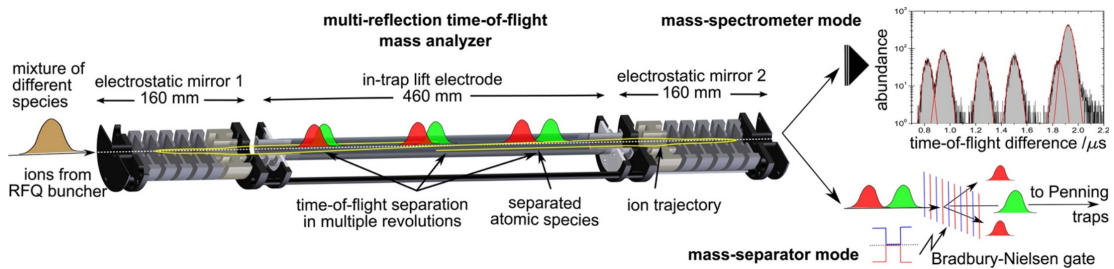


**Figure 4.4:** Multi-Reflection Time-of-Flight Mass Spectrometer of ISOLTRAP. Graphic from [133] reproduced with permission for Elsevier.

bunch. Depending on the initial bunch conditions, this so-called aberration limit is typically reached after the first few hundred to a few thousand revolutions.

## 4.2 The ISOLTRAP mass spectrometer at ISOLDE/CERN

The ISOLTRAP mass spectrometer at ISOLDE/CERN has pioneered Penning trap mass spectrometry at RIB facilities since the early 1990s [111, 144, 145]. Initially consisting of the tandem Penning trap system, the spectrometer was extended with a Radiofrequency Quadrupole Cooler-Buncher (RFQ-cb) [146] for cooling and bunching the quasi-continuous RIB, and a Multi-Reflection Time-of-Flight mass spectrometer [133, 147].

A typical measurement scheme is visualized in Fig. 4.5. The laser-ionized [98] and mass-separated RIB [86] is injected into the RFQ-cb, which is floated to a high voltage of typically 30 kV to 60 kV to match the RIB beam energy. Helium buffer gas is let into the vacuum chamber of the RFQ-cb to provide buffer-gas cooling through ion-gas collisions. The radial confinement by the RF field is tuned in amplitude and frequency through an adjustable RLC circuit to match the  $m/q$  of the stored ions, mixed with a DC potential along the trap axis, allowing stable confinement in the trapping region. After trapping times of several milliseconds, the ion bunch is ejected and brought to a beam energy of 3.2 keV.

Using the in-trap pulsed electrode [148], the ion bunch is then captured in between the electrostatic mirrors of the MR-ToF MS. Depending on the desired separation power, beam intensity, and half-life, the ions are trapped for a few tens to up to several thousands of revolutions, leading to kilometer-long flight paths. The optimal ToF focus on a ToF detector for a chosen number of revolutions is set by adjusting the kinetic

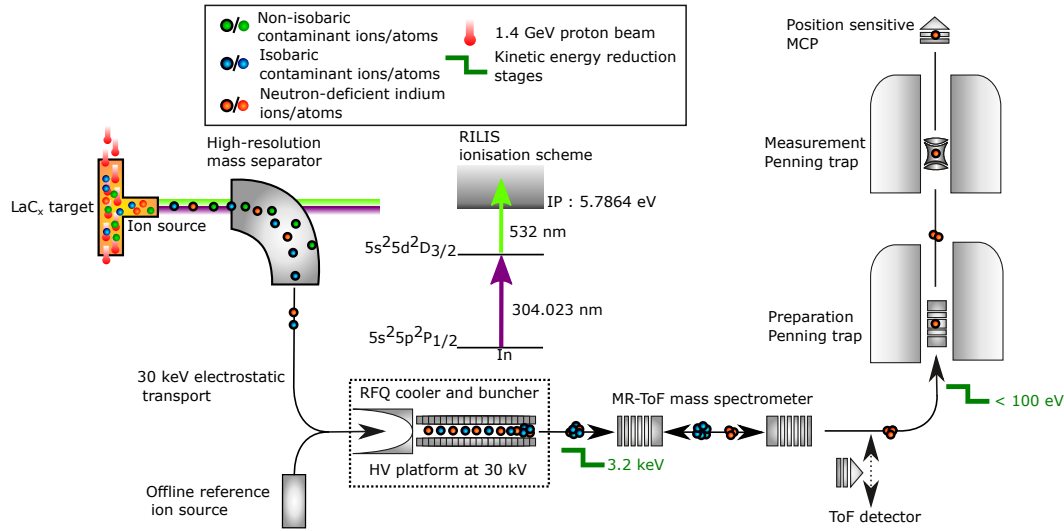


**Figure 4.5:** ISOLTRAP mass spectrometer as of 2021. The spectrometer comprises the RFQ-cb, the MR-ToF MS and the tandem Penning trap system. Graphic amended from [6].

energy of the bunch inside the MR-ToF MS during the capture of the ions. Typical beam energies during trapping are  $\sim 2$  keV, varying by  $\pm 50$  eV depending on the number of revolutions and the ion mass.

Following, the ion bunch is ejected using the lift electrode, raising the beam energy back to 3.2 keV. If used as a mass spectrometer, the ions are immediately implanted on a MagneToF<sup>®</sup> single-ion detector from *ETP ion detect*<sup>TM</sup>, situated downstream of the device. The raw signal is fed into a TDC from *FAST ComTec GmbH*, and the data is pre-binned into 800 ps bins.

If the device is used as an isobar separator for beam purification, the lift electrode is pulsed for some hundreds of nanoseconds only to eject the isotope of interest, suppressing isobaric contamination [149]. The purified ion bunch is then guided through a 90-degree bender into the vertical part of the setup, after which the beam energy is reduced to less than 100 eV. The beam is then captured by the cylindrical Preparation Penning trap [150], which is located inside a 4.7 T superconducting magnet. Here, the mass-selective buffer gas cooling technique [117] as discussed in Section 4.1.1 is employed to further improve the ion bunch emittance. If the half-life of the ion is not limiting the storage time, the cooling lasts several hundred milliseconds. Otherwise, the helium pressure in the trap can be increased, and the amplitudes and excitation times of the RF excitations can be adjusted to reduce the cooling times to a few tens of milliseconds.

The cooled ions are then ejected and transported to the hyperbolic Measurement Penning trap, which is housed in a 5.6 T superconducting magnet [151]. The cyclotron frequency of the stored ions is measured by employing either the ToF-ICR or PI-ICR technique as described in Section 4.1.1. To mitigate the effect of systematic drifts of the electric and magnetic fields, a higher-order magnetic field correction is applied using the magnetic field produced by room-temperature coils [152]. The ToF of the ions after ejection is measured by an MCP with delay lines from *RoentDek Handels GmbH* providing a sub-millimeter spatial and sub-nanosecond temporal resolution needed for both measurement techniques.

An offline ion source providing stable or long-lived radioactive isotopes can be used for various applications. For both MR-ToF MS and PTMS, reference masses are needed either to calculate the mass of interest from the measured ToF (see Eq. (4.8)) or cyclotron frequency (see Eq. (4.3)). To avoid mass-dependent systematic uncertainties, the mass difference between the mass of interest and the reference mass,  $(m - m_{\text{ref}})$ , should be minimized<sup>1</sup>. Furthermore, reference masses are used to calibrate the MR-ToF MS or the Penning traps to estimate the ToFs or resonance frequencies of unknown masses. Lastly, stable or long-lived radioactive isotopes provided by the offline ion source can be used to measure masses with high precision and statistics, independent of the experimental schedule of an online facility [154] or at offline labs [155, 156].

### 4.3 Technical Developments at ISOLTRAP

In this thesis, several technical developments at the ISOLTRAP setup have been performed. In the following, the design and commissioning of a new offline ion source

<sup>1</sup>For the ToF-ICR method at ISOLTRAP, for example, this uncertainty was determined to be  $-1.6(4) \times 10^{-10}/u \times (m - m_{\text{ref}})$  [153]

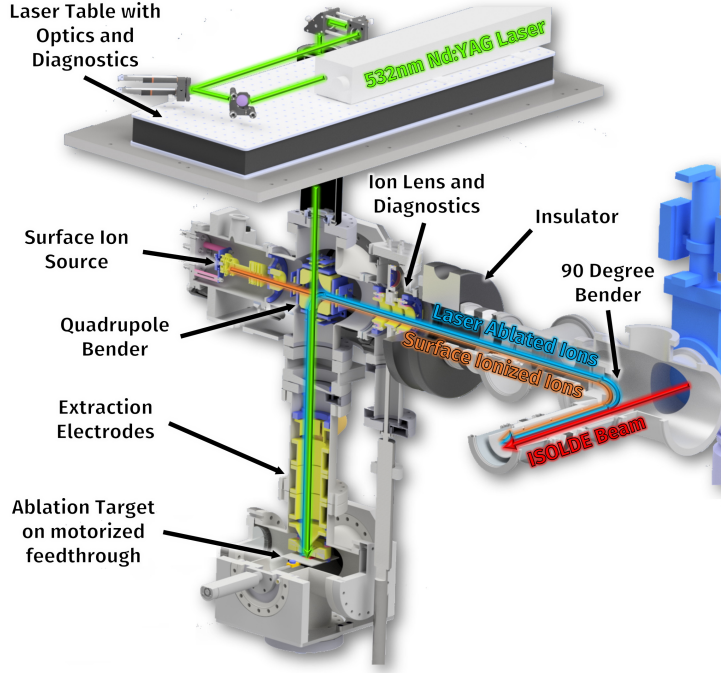


**Figure 4.6:** Annotated CAD drawing of the combined surface and laser-ablation ion source. The laser beam path is highlighted in green, the surface ion beam in orange, the laser-ablated ion beam in blue, and the ISOLDE RIB in red.

will be presented, followed by technical improvements leading to a 2.5-fold increase in mass resolving power with the MR-ToF MS.

#### 4.3.1 A new offline ion source

Over the years, many different ion-source types have been used at ISOLTRAP, including plasma, surface, magnetron, and laser-ablation sources. The latter type is particularly suitable, as the laser ablation from solid targets can produce reference ions from various elements, most prominently carbon ions and carbon cluster ions for absolute mass measurements [157–161]. Due to a remodeling of the beamline and the implementation of the MR-ToF MS, a new combined ion source was developed and commissioned in the framework of this doctoral thesis.

Now situated in front of the RFQ-cb, the new ion-source setup combines a surface ion source with a laser-ablation ion source (LAIS), see Fig. 4.6. Design considerations included high beam energies (up to 60 keV), small footprint ( $< 1 \text{ m}^2$ ), stringent laser safety rules, a motorized target that is easily exchangeable, and reliability. The driving laser, a frequency-doubled pulsed Nd:YAG laser with nanosecond pulse lengths and several millijoules of pulse energy, is located on top of a high-voltage cage inside an enclosure. The high-voltage cage houses the ion-source vacuum chambers, which are floated to a potential of 30 kV to 60 kV, and necessary equipment. The laser beam is guided through a set of motorized mirrors and a motorized telescope into the vertical part of the vacuum chamber, where it impinges on an ablation target that is mounted on a motorized linear feedthrough. Laser-ablated ions are accelerated and focused through two sets of 90-degree benders into the main ISOLTRAP beamline. A movable Faraday cup is located between the two sets of benders and serves for beam tuning and

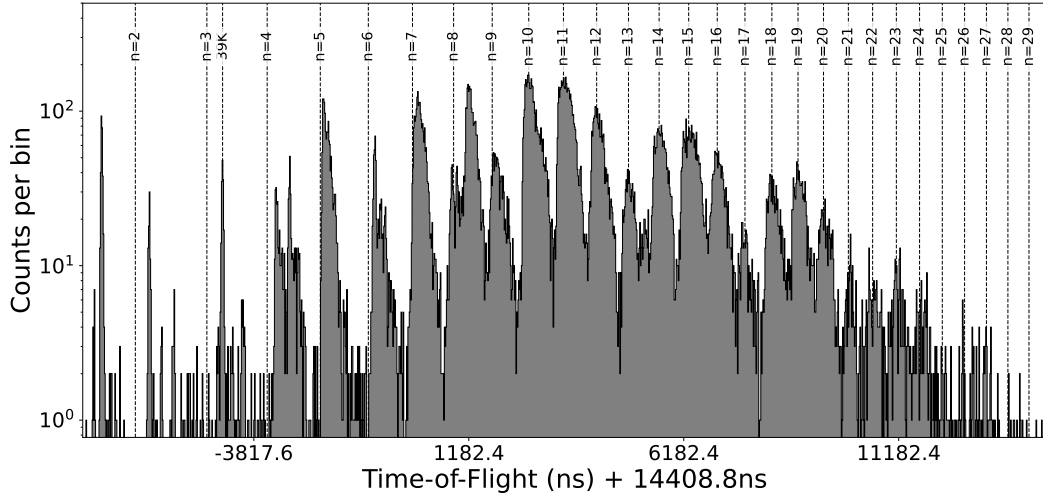


**Figure 4.7:** Time-of-Flight spectrum at 30 keV beam energy measured shooting through the MR-ToF MS without trapping.)

characterization.

The first commissioning work has been performed using a glassy carbon target [162], commercially available as *Sigradur*. Carbon targets are useful as they provide single atoms and atomic clusters from cluster sizes from  $n = 2$  to  $n > 60$  [158, 163], thus covering the whole mass range of the nuclear chart. A first cluster ToF spectrum from the commissioning is shown in Fig. 4.7, shooting the cooled and bunched 30 keV beam through the MR-ToF MS without trapping. It can be seen that heavier clusters up to  $n = 27$  are produced. Several contaminants are also visible, of which  $^{39}\text{K}$  was most easily identified.

#### 4.3.2 MR-ToF MS Improvements

Initially, the mass resolving power  $R$  of the ISOLTRAP MR-ToF MS rarely exceeded  $2 \times 10^5$  during online experiments and was dictated by the aberration limit of the device (see Section 4.1.2). To tackle one of the main causes of residual ion dispersion, an extended mirror-voltage electrode-stabilization system based on Refs. [164, 165] was implemented. The absolute voltage stability of single-pass electrodes such as steerers or lenses is less influential as compared to the electrodes forming the mirror potentials of the device, which are passed by the ion bunch many hundreds and thousands of times. Fluctuations in the voltages applied to the mirror electrodes are a major contribution to short and long-term fluctuations of the time-of-flight of stored ions which subsequently leads to a worsening of the overall performance. Various approaches to stabilize electrode voltages are employed at time-of-flight spectrometers, including passive filtering of high-frequency components through low-pass filters and active voltage regulation using feedback loops. These two measures have now been implemented for five of the six mirror electrodes of the device.

The choice of which mirrors to stabilize is based on the simulated and measured

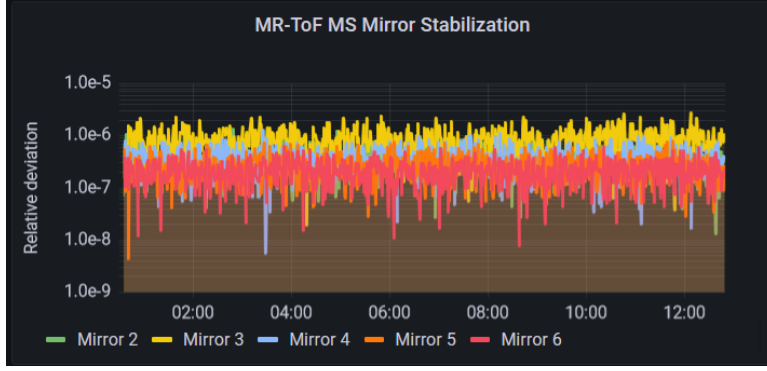


**Figure 4.8:** Relative voltage deviation from the set value over the course of 12 hours. For the most crucial mirrors, this deviation ranges in the millivolt region.

sensitivity of the ion ToF to small variations of the applied voltages [147]. The most sensitive mirror electrode, M5, forms the part of the potential where the turn-around point of the ion bunch is located. In this region, the ions are slowed down significantly and change their direction of velocity, which makes them most sensitive to voltage fluctuations, translating into the modification of the ion energy and, consequently, a modification of the time-of-flight. The relative voltage deviation  $U_{rel}(t) = |U_{set} - U(t)| / U_{set}$ , where  $U_{set}$  is the set voltage and  $U(t)$  is the measured voltage at time  $t$ , is shown in Fig. 4.8 for the five actively and passively stabilized mirrors. For the 2 kV to 4 kV mirrors, this ranges in the low  $10^{-7}$  region, translating to few millivolts in deviation.

The second direct way to improve the MR-ToF MS performance is to improve the initial ion bunch emittance. After the device was installed, the ejection out of the RFQ-cb had to be adjusted for the acceptance of the MR-ToF MS [133]. It was found that the necessary steeper potential increased the sensitivity of the ion bunch to the phase of the RF ( $\sim 1$  MHz) at the time of ejection [164]. Following up on this idea, the ejection potential out of the RFQ-cb was further increased from  $\pm 100$  V to up to  $\pm 250$  V to study the impact on the performance. Expectedly, stronger potentials lead

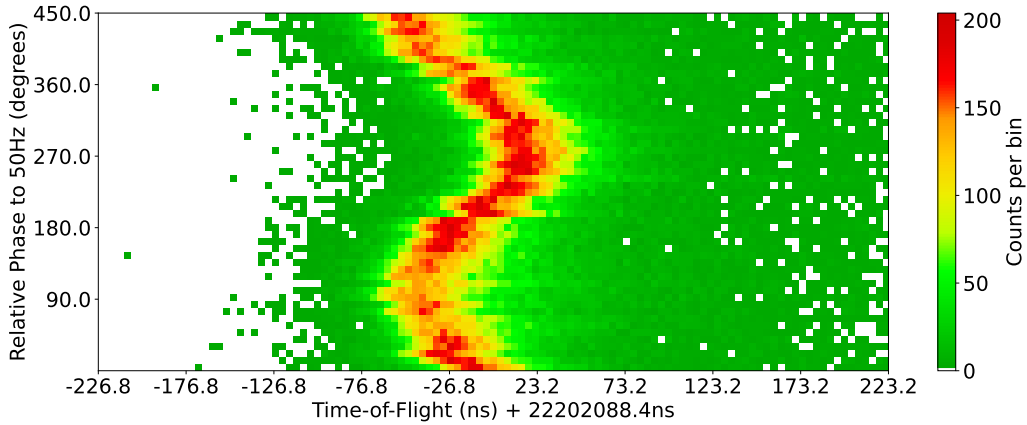


**Figure 4.9:** Mains power phase dependence of the ion time-of-flight. The start of the experimental cycle was scanned in 0.5 ms to probe the full 20 ms period of one 50 Hz power cycle.

to stronger sensitivity to the phase. A compromise between sensitivity, absolute ToF, and ToF width was chosen, such that the delayed ejection after turning off the confining RF field [164] was still able to counteract the residual RF influence without losing too many ions due to the weakening of the confining field.

Furthermore, it was found that the ToF strongly depends on the absolute phase of the 50 Hz mains power. Randomizing the cycle execution over different phases leads to a broadening of the ToF peak. This can easily be shown by synchronizing the experimental cycle to the mains power and by always triggering on the same absolute phase (see Fig. 4.9) and then delaying the start of the cycle with respect to the chosen absolute phase.

### 4.3.3 MR-ToF MS data analysis

An object-oriented toolset for the analysis of the MR-ToF MS data has been developed [166] based on the `Python` programming language [167] and the CERN `Root` data analysis framework [168]. The main purpose of the code is divided into data processing and analysis. The main features of the analysis part are isotope identification based on time-of-flight, drift correction, and peak fitting. The latter two parts are discussed in more detail in the following.

Residual ToF drifts due to temperature fluctuations on the order of hours to days are difficult to account for on the hardware level and would require sophisticated temperature stabilization of the experiment and all of its hardware. These fluctuations can be removed during off-line data analysis using an algorithm to calculate rolling averages of the observed ToFs [169, 170] of either the ion-of-interest or suitable isobaric reference mass.

Figure Fig. 4.10 shows the ToF correction on the data for **Article II** which was taken

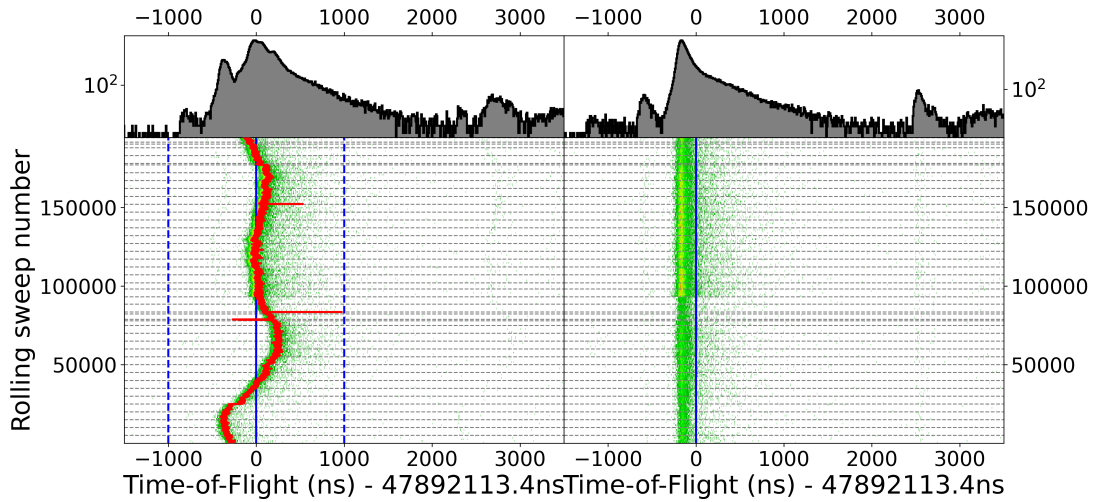


**Figure 4.10:** Time-of-Flight correction of data for the  $m/q = 99$  isobaric beam from experiment **Article II**. The raw data is plotted on the left with the rolling-average ToF for the SrF molecule highlighted in red. The corrected data is plotted on the right.

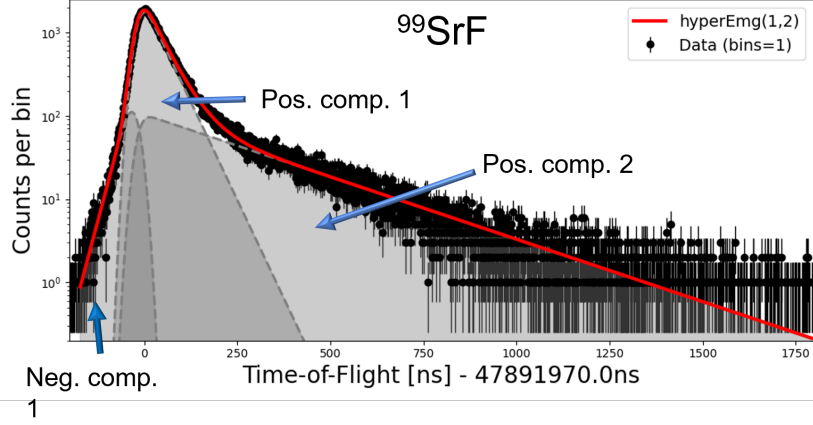


**Figure 4.11:** Multi-component probability density function to fit asymmetric peak shape of the ToF spectra. The data is from the  $m/q = 99$  beam from **Article II**. Here, one negative and two positive components fit the data best (red). The dashed lines indicate the individual components.

over the course of several days due to small production rates of less than 10 ions per second of the ion of interest. Using the dominating contamination, SrF, the rolling average ToF is calculated for a certain ToF window (dashed blue lines). The rolling correction factors are calculated in relation to a reference ToF (solid blue line) used to align all measured events. The choice of reference ToF is crucial when only the ion-of-interest is stored in the device since small shifts in ToF relative to the reference masses  $m_1$  and  $m_2$  (see Eq. (4.8)) yield rather large systematic mass shifts. If one of the reference masses is stored at the same time and is ToF corrected in the same way as the ion-of-interest, then the systematic mass shift is insignificant compared to the precision of the device (if only one ion is stored in the device on average to avoid space charge effects [143, 171]).

To extract the precise time-of-flight from the measured ToF spectra, a fitting routine using RooFit [172] to perform maximum likelihood estimation calculations was implemented. Due to the asymmetric shape of the ToF distribution, an asymmetric multi-component probability density function ("hyperEMG") was chosen [173]. This function is made from a superposition of several exponentially modified Gaussian distributions with positive and negative exponential components to account for the non-Gaussian tailing on either side of the distribution.

Figure Fig. 4.11 shows the best fit of a three-component hyperEMG function to the molecular contaminant  $^{99}\text{SrF}$  from **Article II**. The function consists of one negative component with a small decay constant, and two positive components with a short and a long decay constant (highlighted by the dashed lines). Note that the mean value of the Gaussian part does not indicate the maximum of the distribution and is offset by a small value. To extract the absolute ToFs for a ToF spectrum and the ToF differences between different species, all peaks were fitted simultaneously such that all fit parameters governing the shape of the ToF spectra (decay constants of exponential part, standard deviation of Gaussian part) were shared between the different peaks.

## 4.4 Laser Spectroscopy

As was shown in chapter Section 2.2.2, electromagnetic moments and charge radii are crucial observables for understanding nuclear structure. With the advent of modern laser systems, a large number of atomic transitions became accessible for studying the atomic hyperfine structure. Moving away from stable isotopes, laser-spectroscopy experiments naturally started investigating radioactive isotopes at radioactive ion beam facilities [174]. In the following, different laser-spectroscopy methods on radioactive ion beams, focussed on ISOL-type facilities, will be discussed.

### 4.4.1 Collinear Laser Spectroscopy

One of the first ever used online laser-spectroscopy methods utilizes collinear or anti-collinear overlapping of the laser beam with the radioactive ion beam to optically pump a short-lived atomic excited state and then to collect the fluorescence light produced by its decay [175]. With this method, due to the relative motion of the ion beam and the laser beam, the transition wavelengths  $\lambda_{\text{lab}}$  of the atomic transitions are Doppler-shifted in the stationary laboratory reference frame [176]:

$$\lambda_0 = \lambda_{\text{lab}} \gamma (1 + \beta \cos \theta) = \lambda_{\text{lab}} \frac{1 + \beta \cos \theta}{\sqrt{1 + \beta^2}}, \quad (4.10)$$

where  $\lambda_0$  is the observed wavelength,  $\gamma$  is the relativistic Lorentz-boost,  $\beta$  is the ratio of ion velocity  $v$  over speed of light  $c$ , and  $\theta$  is the angle between the ion beam and the laser light. Furthermore, the mass dependence of the electrostatic ion-beam acceleration at ISOL facilities, a “pseudo isotope shift” can be seen and must be considered.

Since transition wavelengths of atomic transitions in singly-charged ions are typically in the ultra-violet range, which is harder to reach with lasers and harder to detect, the ion beam is usually neutralized through a charge exchange cell (CEC). In such cells, alkali metals are heated to some hundreds of degrees Celcius to create an atomic vapor. Due to the low ionization potential of the alkali atoms in the vapor, the charge exchange of electrons with the passing ion beam is very efficient. After the CEC, the laser now interacts with the beam of neutral atoms in the optical detection region and creates fluorescence photons which are guided by mirrors and light guides to photomultiplier tubes. The CEC can be set to a potential to alter the ion beam energy and, thus, effectively shifts to transition frequency. This so-called voltage scanning of the transition frequency allows the laser to run at a fixed wavelength, which is usually more stable. This requires precise knowledge of the acceleration voltage to the  $10^{-4}$  level. Furthermore, the laser-atom-beam interaction has to be limited to the optical detection region to prevent the population of meta-stable “dark states” in which the atoms are then lost for further spectroscopy. To reduce the background of scattered laser light in the photomultiplier tubes, a three-level scheme can be chosen in which the excited state decays into a third short-lived state before decaying back to the ground state. This enables the usage of a filter that removes photons on the laser wavelength but allows the passage of fluorescence light.

Certain atomic levels show a large cross-section for charge exchange in a CEC or for collisional-induced ionization in a gas jet. These states can be used to gain sensitivity

while greatly reducing background. The ROC method (Radioactive detection of Optically pumped ions after state-selective Charge exchange) resonantly pumps an ion through a short-lived state into a meta-stable state which exhibits a large charge-exchange cross section [177]. After the ions in the beam are pumped into this state, they enter a CEC in which they are neutralized. The ion-to-atom ratio is measured for different potentials on the CEC to determine whether the optical pumping was resonant or not. To further reduce background, the atoms and ions are counted using two sets of scintillators to detect the beta and gamma particles from the characteristic decays of the isotope of interest.

The second method, state-sensitive ionization, relies on a similar effect [178]. First, the ion beam is neutralized in a CEC, leaving the atoms in a certain meta-stable state with a high ionization cross-section. A laser resonantly pumps the atoms from this meta-stable state into a short-lived excited state, from which the atoms decay into their ground state. Afterwards, the atom beam passes through a gas jet which selectively ionizes the atoms again, after which the ion-to-atom ratio is measured using decay spectroscopy or ion counting. This re-ionization [179] results in a large number of atoms only when the optical pumping is resonantly populating the ground state, which is not re-ionized.

#### 4.4.2 Resonance Ionization Spectroscopy

In contrast to fluorescence-detection, resonance ionization spectroscopy (RIS) relies on the step-wise excitation of an electron in the atomic shell, using pulsed lasers at different wavelengths, eventually ionizing the atom. The benefits of RIS are the detection of electrons or ions, which is more efficient than the detection of fluorescence photons, as well as the overall lower background. Commonly, two or three different excitation steps are used, differing only in the final step, which is usually the non-resonant excitation into the continuum, an auto-ionizing state, or a Rydberg state. In one of the latter two states, the overall efficiency of the ionization scheme is strongly enhanced, as the application of a weak electric field or the collisional ionization of such states are superior to the non-resonant excitation into the continuum.

Different RIS methods are applied at RIB facilities, depending on the production rate of the ion of interest and the levels of contamination. The first method, performed in the hot cavity of an ISOL target unit (see Section 3.2), utilizes the RILIS lasers by scanning one of the resonance steps of the laser scheme. Because of the high temperatures of the target container, the transfer line, and the hot cavity itself, the line widths of the atomic transition are broadened due to the Boltzmann-distributed velocities of the atom vapor. This Doppler-broadening can be written as

$$\Delta\nu = \nu \sqrt{\frac{8 \ln 2 kT}{mc^2}}, \quad (4.11)$$

where  $\nu$  is the transition frequency,  $k$  is the Boltzmann constant,  $T$  is the temperature of the atom vapor, and  $m$  is the mass of the atoms. For typical temperatures of  $T \approx 2300$  K and masses of about 200 u, the Doppler broadening is in the order of 1 GHz. The natural line width  $\nu_0$  of a transition is linked to the Heisenberg uncertainty principle where

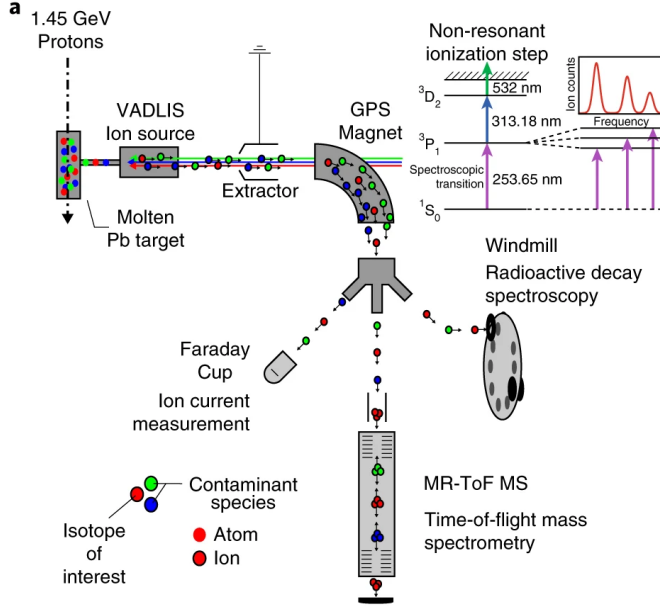


**Figure 4.12:** Schematic of the experimental setups for the in-source resonance ionization spectroscopy of rare mercury isotopes using the ISOLDE-RILIS and different ion detection techniques. Figure from [4] reproduced with permission from Springer Nature.

$\Delta E \Delta t \geq \frac{\hbar}{2}$ , resulting in

$$\nu_0 = \frac{1}{2\pi\tau}, \quad (4.12)$$

where  $\tau$  is the lifetime for the excited state. For the lifetime of the  $^3P_1$  state in mercury for **Article I**, with  $\tau = 122$  ns [180], a natural line width of about 1 MHz can be obtained. Even though the Doppler-broadening is clearly a resolution-limiting factor for in-source spectroscopy, for medium and heavy mass nuclei, the resolution of some GHz is sufficient to resolve isotope shifts and hyperfine structures while having high sensitivity which can range in the order of one ion per second or even lower.

Fig. 4.12 shows the setup for the experimental campaign to study rare mercury ions at ISOLDE. During the experiment, different detection techniques were employed to resolve the mercury isotopes from the isobaric background, i.e. decay spectroscopy and single-ion counting after high-resolution mass separation using the ISOLTRAP MR-ToF MS [4, 5, 123]. The resolution ranged in the GHz region, enough to resolve the HFS features, extract nuclear moments, and charge radii.

To improve the resolution of in-source RIS, a method was developed in which the spectroscopy laser of the multi-wavelength ionization scheme is overlapped perpendicular with the atom beam that effuses out of the hot cavity. In this so-called PI-LIST (perpendicularly-illuminated laser ion source and trap, see Section 3.2 for standard LIST mode) mode [181], only the lateral velocity component of the effusing conical atom beam contributes to the Doppler-broadening. This effect is further maximized by shining in the other lasers on the atom beam axis, which further reduces the effective lateral velocity phase space probed by the combination of the two lasers. While the sacrifice of large parts of the velocity phase space reduces the ionization efficiency by up to two orders of magnitude, line widths of as low as 200 MHz have been reported [181].

Resonance ionization spectroscopy can also be performed on fast ion beams with

collinear or anti-collinear lasers [182]. Similar to other CLS methods mentioned above, the ion beam is first neutralized in a CEC before several lasers on different wavelengths resonantly ionize the atoms in the beam. Afterward, the ions are deflected onto a single-ion detector or a decay spectrometer for counting.

While resonance ionization with RILIS was used in **Article II** and **Article III** to ionize indium and zinc isotopes and suppress unwanted contamination in the ISOLDE ion source, the laser wavelength was kept on resonance. For **Article I**, however, the laser wavelength was scanned to obtain the hyperfine spectra of the mercury isotopes.



## 5 Conclusion and outlook

This thesis reports on high-precision Penning trap and multi-reflection time-of-flight mass spectrometry and on in-cavity resonance ionization laser spectroscopy of short-lived radioactive isotopes near the doubly-magic nuclei  $^{78}\text{Ni}$ ,  $^{100}\text{Sn}$ , and  $^{208}\text{Pb}$ . The binding energy, magnetic moment, and nuclear charge radii measurements of rare indium, zinc, and mercury isotopes enabled the benchmarking of modern nuclear theory calculations and resulted in a better understanding of the forces at play in the many-body problem of the atomic nucleus. The isomeric excitation-energy measurements of  $^{99}\text{In}^m$  and  $^{79}\text{Zn}^m$  were enabled through technical improvements of the ISOLTRAP MR-ToF MS, which led to a factor 2-3 increase in mass-resolving power and long-term operation stability. Exploiting these upgrades in combination with newly implemented software tools to correct and analyze the data now supports mass measurements of isotopes with yields well below one ion per second over many consecutive days.

Yet to be analyzed and published mass measurements using the MR-ToF MS can be found in Fig. 5.1. Follow-up measurements near doubly-magic  $^{100}\text{Sn}$  for nuclear structure studies using the improved hardware have already been performed in the neutron-deficient cadmium chain, crossing the  $N = 50$  shell gap through the first direct measurement of  $^{97}_{48}\text{Cd}_{49}$  in its ground and high-spin isomeric state. This result will yield valuable information on the single-neutron separation energy and the correlated neutron gap, providing further input to shell-model calculations and motivating *ab initio* calculations in the neutron-deficient cadmium chain. Also, mass measurements of  $^{103}\text{Sn}$  were performed successfully, while measurements of  $^{101,102}\text{Sn}$  were still hindered by high levels of isobaric contamination.

Based on the expected production yields for  $^{101,102}\text{Sn}$  [102],  $^{98}\text{In}$  [7], and  $^{96}\text{Cd}$ , further high-precision mass measurements in the  $^{100}\text{Sn}$  region are feasible at ISOLDE but require efficiency improvements of the RFQ cooler-buncher and better isobaric contamination handling of the MR-ToF MS. A new RFQ is currently in the process of being implemented and tested to serve as a second Paul trap for mass-selective retrapping to improve contamination suppression, while a second such device could replace the main ISOLTRAP RFQ for improved efficiency in capturing the ions delivered by ISOLDE and preparing them for subsequent mass measurements.

Furthermore, neutron-rich mercury isotopes near doubly-magic  $^{208}\text{Pb}$  past  $N = 126$  were produced in a proof-of-principle experiment testing new target and ion-source settings. Using the MR-ToF MS,  $^{209}_{80}\text{Hg}_{129}$  and  $^{210}_{80}\text{Hg}_{130}$  were measured for the first time. With these new masses, a second  $\delta V_{pn}$  value above the shell gap, now at  $N = 130$ , can be calculated to probe residual  $pn$  interactions and to test nuclear structure calculations in that region of the nuclear chart. An experimental campaign to employ in-source laser spectroscopy, supported by MR-ToF MS and the ISOLDE decay station, is planned to systematically study the ground-state properties of these and more neutron-rich mercury isotopes in the near future.

## 5 Conclusion and outlook

The results of the data shown in Fig. 5.1 and the technical improvements presented in this chapter will be reported in upcoming scientific publications.

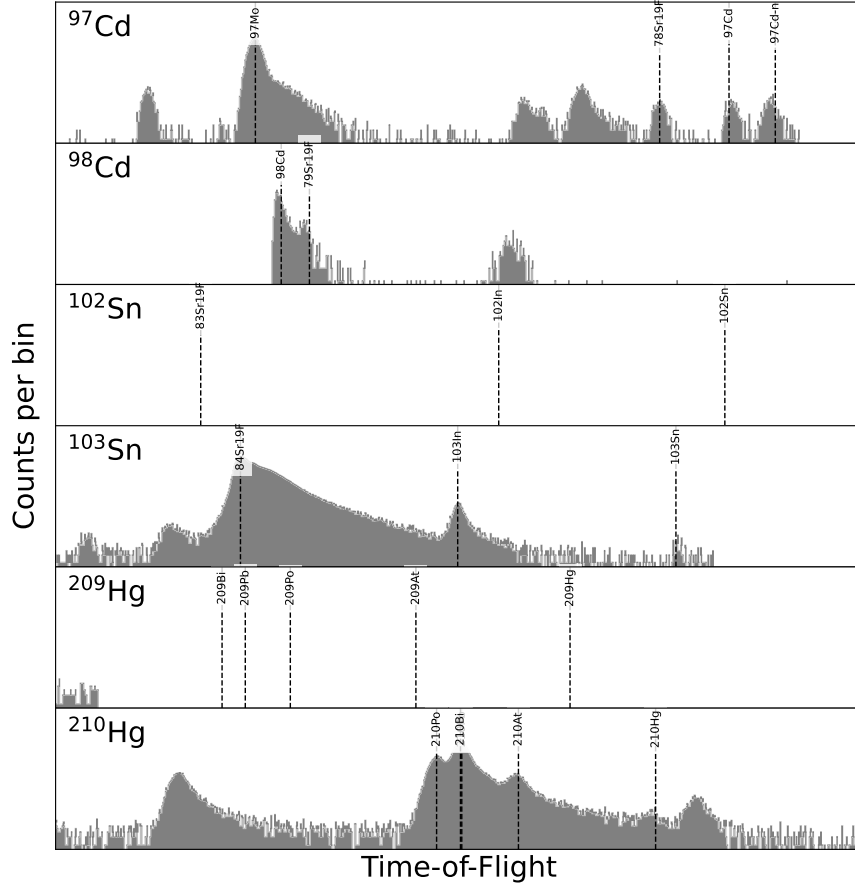


**Figure 5.1:** Follow-up mass measurements at ISOLTRAP from three different experimental campaigns. The cadmium and tin isotopes were produced from  $\text{LaC}_x$  targets with laser ionization, while the mercury isotopes were produced from an  $\text{UC}_x$  target with a cold transfer line and laser ionization.

## 6 Bibliography

- [1] O. Sorlin and M.-G. Porquet. Nuclear magic numbers: New features far from stability. *Progress in Particle and Nuclear Physics*, 61:602–673, 10 2008. URL: <https://linkinghub.elsevier.com/retrieve/pii/S0146641008000380>, doi: [10.1016/j.ppnp.2008.05.001](https://doi.org/10.1016/j.ppnp.2008.05.001).
- [2] Meng Wang, W.J. Huang, F.G. Kondev, G. Audi, and S. Naimi. The AME 2020 atomic mass evaluation (II). Tables, graphs and references\*. *Chinese Physics C*, 45:030003, 3 2021. doi: [10.1088/1674-1137/abddaf](https://doi.org/10.1088/1674-1137/abddaf).
- [3] Jonas Kartheim. Nuclear Chart Plotter. URL: <https://github.com/jonas-ka/nuclear-chart-plotter>.
- [4] B. A. Marsh, T. Day Goodacre, S. Sels, Y. Tsunoda, B. Andel, A. N. Andreyev, N. A. Althubiti, D. Atanasov, A. E. Barzakh, J. Billowes, K. Blaum, T. E. Cocolios, J. G. Cubiss, J. Dobaczewski, G. J. Farooq-Smith, D. V. Fedorov, V. N. Fedosseev, K. T. Flanagan, L. P. Gaffney, L. Ghys, M. Huyse, S. Kreim, D. Lunney, K. M. Lynch, V. Manea, Y. Martinez Palenzuela, P. L. Molkanov, T. Otsuka, A. Pastore, M. Rosenbusch, R. E. Rossel, S. Rothe, L. Schweikhard, M. D. Seliverstov, P. Spagnoletti, C. Van Beveren, P. Van Duppen, M. Veinhard, E. Verstraelen, A. Welker, K. Wendt, F. Wienholtz, R. N. Wolf, A. Zadvornaya, and K. Zuber. Characterization of the shape-staggering effect in mercury nuclei. *Nature Physics*, 14:1163–1167, 12 2018. URL: <https://www.nature.com/articles/s41567-018-0292-8>, doi: [10.1038/s41567-018-0292-8](https://doi.org/10.1038/s41567-018-0292-8).
- [5] T. Day Goodacre, A. V. Afanasjev, A. E. Barzakh, B. A. Marsh, S. Sels, P. Ring, H. Nakada, A. N. Andreyev, P. Van Duppen, N. A. Althubiti, B. Andel, D. Atanasov, J. Billowes, K. Blaum, T. E. Cocolios, J. G. Cubiss, G. J. Farooq-Smith, D. V. Fedorov, V. N. Fedosseev, K. T. Flanagan, L. P. Gaffney, L. Ghys, M. Huyse, S. Kreim, D. Lunney, K. M. Lynch, V. Manea, Y. Martinez Palenzuela, P. L. Molkanov, M. Rosenbusch, R. E. Rossel, S. Rothe, L. Schweikhard, M. D. Seliverstov, P. Spagnoletti, C. Van Beveren, M. Veinhard, E. Verstraelen, A. Welker, K. Wendt, F. Wienholtz, R. N. Wolf, A. Zadvornaya, and K. Zuber. Laser Spectroscopy of Neutron-Rich  $^{207,208}\text{Hg}$  Isotopes: Illuminating the Kink and Odd-Even Staggering in Charge Radii across the  $N = 126$  Shell Closure. *Phys. Rev. Lett.*, 126:032502, Jan 2021. URL: <https://link.aps.org/doi/10.1103/PhysRevLett.126.032502>, doi: [10.1103/PhysRevLett.126.032502](https://doi.org/10.1103/PhysRevLett.126.032502).
- [6] M. Mougeot, D. Atanasov, J. Kartheim, R. N. Wolf, P. Ascher, K. Blaum, K. Chrysalidis, G. Hagen, J. D. Holt, W. J. Huang, G. R. Jansen, I. Kulikov, Yu A. Litvinov, D. Lunney, V. Manea, T. Miyagi, T. Papenbrock, L. Schweikhard,

- A. Schwenk, T. Steinsberger, S. R. Stroberg, Z. H. Sun, A. Welker, F. Wienholtz, S. G. Wilkins, and K. Zuber. Mass measurements of  $^{99-101}\text{In}$  challenge ab initio nuclear theory of the nuclide  $^{100}\text{Sn}$ . *Nature Physics*, 17:1099–1103, 10 2021. doi:[10.1038/S41567-021-01326-9](https://doi.org/10.1038/S41567-021-01326-9).
- [7] L. Nies, K. Blaum, J. Kartheim, I. Kulikov, Yu. A. Litvinov, D. Lunney, V. Manea, M. Mougeot, W. J. Ong, H. Schatz, L. Schweikhard, A. Schwenk, F. Wienholtz, and K. Zuber. Mass measurement of the proton-rich  $^{99}\text{In}$  and self-conjugate  $^{98}\text{In}$  nuclides for nuclear and astrophysical studies. Technical report, CERN, Geneva, 2020. URL: <https://cds.cern.ch/record/2717873>.
- [8] A. Gottardo, D. Verney, C. Delafosse, F. Ibrahim, B. Roussière, C. Sotty, S. Roccia, C. Andreoiu, C. Costache, M.-C. Delattre, I. Deloncle, A. Etilé, S. Franchoo, C. Gaulard, J. Guillot, M. Lebois, M. MacCormick, N. Marginean, R. Marginean, I. Matea, C. Mihai, I. Mitu, L. Olivier, C. Portail, L. Qi, L. Stan, D. Testov, J. Wilson, and D. T. Yordanov. First Evidence of Shape Coexistence in the  $^{78}\text{Ni}$  Region: Intruder  $0_2^+$  State in  $^{80}\text{Ge}$ . *Phys. Rev. Lett.*, 116:182501, May 2016. URL: <https://link.aps.org/doi/10.1103/PhysRevLett.116.182501>, doi:[10.1103/PhysRevLett.116.182501](https://doi.org/10.1103/PhysRevLett.116.182501).
- [9] F. H. Garcia, C. Andreoiu, G. C. Ball, A. Bell, A. B. Garnsworthy, F. Nowacki, C. M. Petrache, A. Poves, K. Whitmore, F. A. Ali, N. Bernier, S. S. Bhattacharjee, M. Bowry, R. J. Coleman, I. Dillmann, I. Djianto, A. M. Forney, M. Gascoine, G. Hackman, K. G. Leach, A. N. Murphy, C. R. Natzke, B. Olaizola, K. Ortner, E. E. Peters, M. M. Rajabali, K. Raymond, C. E. Svensson, R. Umashankar, J. Williams, and D. Yates. Absence of Low-Energy Shape Coexistence in  $^{80}\text{Ge}$ : The Nonobservation of a Proposed Excited  $0_2^+$  Level at 639 keV. *Phys. Rev. Lett.*, 125:172501, Oct 2020. URL: <https://link.aps.org/doi/10.1103/PhysRevLett.125.172501>, doi:[10.1103/PhysRevLett.125.172501](https://doi.org/10.1103/PhysRevLett.125.172501).
- [10] X. F. Yang, C. Wraith, L. Xie, C. Babcock, J. Billowes, M. L. Bissell, K. Blaum, B. Cheal, K. T. Flanagan, R. F. Garcia Ruiz, W. Gins, C. Gorges, L. K. Grob, H. Heylen, S. Kaufmann, M. Kowalska, J. Kraemer, S. Malbrunot-Ettenauer, R. Neugart, G. Neyens, W. Nörtershäuser, J. Papuga, R. Sánchez, and D. T. Yordanov. Isomer shift and magnetic moment of the long-lived  $1/2^+$  isomer in  $^{49}\text{Zn}$ : Signature of shape coexistence near  $^{78}\text{Ni}$ . *Physical Review Letters*, 116:182502, 5 2016. URL: <https://journals.aps.org/prl/abstract/10.1103/PhysRevLett.116.182502>, doi:[10.1103/PHYSREVLETT.116.182502/FIGURES/4/MEDIUM](https://doi.org/10.1103/PHYSREVLETT.116.182502/FIGURES/4/MEDIUM).
- [11] E. Rutherford. LXXIX. The scattering of  $\alpha$  and  $\beta$  particles by matter and the structure of the atom. *The London, Edinburgh, and Dublin Philosophical Magazine and Journal of Science*, 21:669–688, 5 1911. URL: <https://www.tandfonline.com/doi/full/10.1080/14786440508637080>, doi:[10.1080/14786440508637080](https://doi.org/10.1080/14786440508637080).
- [12] E. Rutherford. LI. Collision of  $\alpha$  particles with light atoms I. Hydrogen. *The London, Edinburgh, and Dublin Philosophical Magazine and Journal of Science*, 37:537–561, 6 1919. doi:[10.1080/14786440608635916](https://doi.org/10.1080/14786440608635916).

- [13] Ernest Rutherford. Bakerian Lecture: Nuclear constitution of atoms. *Proceedings of the Royal Society of London. Series A, Containing Papers of a Mathematical and Physical Character*, 97:374–400, 7 1920. URL: <https://royalsocietypublishing.org/doi/10.1098/rspa.1920.0040>, doi:10.1098/rspa.1920.0040.
- [14] James Chadwick. Bakerian lecture.—The neutron. *Proceedings of the Royal Society of London. Series A, Containing Papers of a Mathematical and Physical Character*, 142:1–25, 10 1933. doi:10.1098/rspa.1933.0152.
- [15] George Gamow. Mass defect curve and nuclear constitution. *Proceedings of the Royal Society of London. Series A, Containing Papers of a Mathematical and Physical Character*, 126:632–644, 3 1930. doi:10.1098/rspa.1930.0032.
- [16] C. F. v. Weizsäcker. Zur Theorie der Kernmassen. *Zeitschrift für Physik*, 96:431–458, 7 1935. doi:10.1007/BF01337700.
- [17] E. Fermi. Zur Quantelung des idealen einatomigen Gases. *Zeitschrift für Physik*, 36:902–912, 11 1926. URL: <http://link.springer.com/10.1007/BF01400221>, doi:10.1007/BF01400221.
- [18] W. Pauli. The Connection Between Spin and Statistics. *Physical Review*, 58:716–722, 10 1940. URL: <https://link.aps.org/doi/10.1103/PhysRev.58.716>, doi:10.1103/PhysRev.58.716.
- [19] The 1963 Nobel Prize in Physics. *Physics Today*, 16(12):21–21, 12 1963. arXiv:[https://pubs.aip.org/physicstoday/article-pdf/16/12/21/8259438/21\\_1\\_online.pdf](https://pubs.aip.org/physicstoday/article-pdf/16/12/21/8259438/21_1_online.pdf), doi:10.1063/1.3050649.
- [20] D. D. Dao and F. Nowacki. Nuclear structure within a discrete nonorthogonal shell model approach: New frontiers. *Physical Review C*, 105:054314, 5 2022. URL: <https://link.aps.org/doi/10.1103/PhysRevC.105.054314>, doi:10.1103/PhysRevC.105.054314.
- [21] F. Nowacki, A. Poves, E. Caurier, and B. Bounthong. Shape Coexistence in  $^{78}\text{Ni}$  as the Portal to the Fifth Island of Inversion. *Physical Review Letters*, 117:272501, 12 2016. URL: <https://link.aps.org/doi/10.1103/PhysRevLett.117.272501>, doi:10.1103/PhysRevLett.117.272501.
- [22] T. Otsuka, M. Honma, T. Mizusaki, N. Shimizu, and Y. Utsuno. Monte Carlo shell model for atomic nuclei. *Progress in Particle and Nuclear Physics*, 47:319–400, 2001. URL: <https://linkinghub.elsevier.com/retrieve/pii/S0146641001001570>, doi:10.1016/S0146-6410(01)00157-0.
- [23] P. Hohenberg and W. Kohn. Inhomogeneous Electron Gas. *Physical Review*, 136:B864–B871, 11 1964. URL: <https://link.aps.org/doi/10.1103/PhysRev.136.B864>, doi:10.1103/PhysRev.136.B864.
- [24] T.H.R. Skyrme. The spin-orbit interaction in nuclei. *Nuclear Physics*, 9:635–640, 1 1958. URL: <https://linkinghub.elsevier.com/retrieve/pii/0029558258903468>, doi:10.1016/0029-5582(58)90346-8.

- [25] J. Dechargé and D. Gogny. Hartree-Fock-Bogolyubov calculations with the  $D1$  effective interaction on spherical nuclei. *Physical Review C*, 21:1568–1593, 4 1980. URL: <https://link.aps.org/doi/10.1103/PhysRevC.21.1568>, doi:10.1103/PhysRevC.21.1568.
- [26] Alexandre Obertelli and Hiroyuki Sagawa. *Modern Nuclear Physics*. Springer Singapore, 2021. URL: <https://link.springer.com/10.1007/978-981-16-2289-2>, doi:10.1007/978-981-16-2289-2.
- [27] C. Mahaux, P.F. Bortignon, R.A. Broglia, and C.H. Dasso. Dynamics of the shell model. *Physics Reports*, 120:1–274, 4 1985. URL: <https://linkinghub.elsevier.com/retrieve/pii/0370157385901000>, doi:10.1016/0370-1573(85)90100-0.
- [28] P.-G. Reinhard and K. Goeke. The generator coordinate method and quantised collective motion in nuclear systems. *Reports on Progress in Physics*, 50:1–64, 1 1987. URL: <https://iopscience.iop.org/article/10.1088/0034-4885/50/1/001>, doi:10.1088/0034-4885/50/1/001.
- [29] H. Hergert, S.K. Bogner, T.D. Morris, A. Schwenk, and K. Tsukiyama. The In-Medium Similarity Renormalization Group: A novel ab initio method for nuclei. *Physics Reports*, 621:165–222, 2016. Memorial Volume in Honor of Gerald E. Brown. URL: <https://www.sciencedirect.com/science/article/pii/S0370157315005414>, doi:10.1016/j.physrep.2015.12.007.
- [30] K. Hebeler, S. K. Bogner, R. J. Furnstahl, A. Nogga, and A. Schwenk. Improved nuclear matter calculations from chiral low-momentum interactions. *Physical Review C*, 83:031301, 3 2011. URL: <https://link.aps.org/doi/10.1103/PhysRevC.83.031301>, doi:10.1103/PhysRevC.83.031301.
- [31] J. Simonis, S. R. Stroberg, K. Hebeler, J. D. Holt, and A. Schwenk. Saturation with chiral interactions and consequences for finite nuclei. *Physical Review C*, 96:014303, 7 2017. URL: <http://link.aps.org/doi/10.1103/PhysRevC.96.014303>, doi:10.1103/PhysRevC.96.014303.
- [32] W. G. Jiang, A. Ekström, C. Forssén, G. Hagen, G. R. Jansen, and T. Papenbrock. Accurate bulk properties of nuclei from  $A = 2$  to  $\infty$  from potentials with  $\Delta$  isobars. *Physical Review C*, 102:054301, 11 2020. URL: <https://link.aps.org/doi/10.1103/PhysRevC.102.054301>, doi:10.1103/PhysRevC.102.054301.
- [33] F. W. ASTON. Atoms and their Packing Fractions<sup>1</sup>. *Nature*, 120:956–959, 12 1927. URL: <https://www.nature.com/articles/120956a0>, doi:10.1038/120956a0.
- [34] Simon Rainville, James K. Thompson, Edmund G. Myers, John M. Brown, Maynard S. Dewey, Ernest G. Kessler, Richard D. Deslattes, Hans G. Börner, Michael Jentschel, Paolo Mutti, and David E. Pritchard. A direct test of  $E = mc^2$ . *Nature*, 438:1096–1097, 12 2005. doi:10.1038/4381096a.
- [35] Eite Tiesinga, Peter J. Mohr, David B. Newell, and Barry N. Taylor. CODATA recommended values of the fundamental physical constants: 2018. *Reviews of*

*Modern Physics*, 93:025010, 6 2021. URL: <https://link.aps.org/doi/10.1103/RevModPhys.93.025010>, doi:10.1103/RevModPhys.93.025010.

- [36] H. A. Bethe and R. F. Bacher. Nuclear Physics A. Stationary States of Nuclei. *Reviews of Modern Physics*, 8:82–229, 4 1936. URL: <https://link.aps.org/doi/10.1103/RevModPhys.8.82>, doi:10.1103/RevModPhys.8.82.
- [37] Bogdan Povh, Klaus Rith, Christoph Scholz, and Frank Zetsche. *Teilchen und Kerne*. Springer Berlin Heidelberg, 1995. URL: <http://link.springer.com/10.1007/978-3-662-10282-4>, doi:10.1007/978-3-662-10282-4.
- [38] Bureau International des Poids et Mesures. The International System of Units 9th edition, 2019. URL: <https://www.bipm.org/en/publications/si-brochure/>.
- [39] W.J. Huang, Meng Wang, F.G. Kondev, G. Audi, and S. Naimi. The AME 2020 atomic mass evaluation (I). Evaluation of input data, and adjustment procedures\*. *Chinese Physics C*, 45:030002, 3 2021. URL: <https://iopscience.iop.org/article/10.1088/1674-1137/abddb0>, doi:10.1088/1674-1137/abddb0.
- [40] Takaharu Otsuka, Rintaro Fujimoto, Yutaka Utsuno, B. Alex Brown, Michio Honma, and Takahiro Mizusaki. Magic Numbers in Exotic Nuclei and Spin-Isospin Properties of the  $NN$  Interaction. *Physical Review Letters*, 87:082502, 8 2001. URL: <https://link.aps.org/doi/10.1103/PhysRevLett.87.082502>, doi:10.1103/PhysRevLett.87.082502.
- [41] C. R. Hoffman, T. Baumann, D. Bazin, J. Brown, G. Christian, P. A. DeYoung, J. E. Finck, N. Frank, J. Hinnefeld, R. Howes, P. Mears, E. Mosby, S. Mosby, J. Reith, B. Rizzo, W. F. Rogers, G. Peaslee, W. A. Peters, A. Schiller, M. J. Scott, S. L. Tabor, M. Thoennessen, P. J. Voss, and T. Williams. Determination of the  $N = 16$  Shell Closure at the Oxygen Drip Line. *Physical Review Letters*, 100:152502, 4 2008. URL: <https://link.aps.org/doi/10.1103/PhysRevLett.100.152502>, doi:10.1103/PhysRevLett.100.152502.
- [42] F. Wienholtz, D. Beck, K. Blaum, Ch. Borgmann, M. Breitenfeldt, R. B. Cakirli, S. George, F. Herfurth, J. D. Holt, M. Kowalska, S. Kreim, D. Lunney, V. Manea, J. Menéndez, D. Neidherr, M. Rosenbusch, L. Schweikhard, A. Schwenk, J. Simonis, J. Stanja, R. N. Wolf, and K. Zuber. Masses of exotic calcium isotopes pin down nuclear forces. *Nature*, 498:346–349, 6 2013. URL: <http://www.nature.com/articles/nature12226>, doi:10.1038/nature12226.
- [43] S. Michimasa, M. Kobayashi, Y. Kiyokawa, S. Ota, D. S. Ahn, H. Baba, G. P. A. Berg, M. Dozono, N. Fukuda, T. Furuno, E. Ideguchi, N. Inabe, T. Kawabata, S. Kawase, K. Kisamori, K. Kobayashi, T. Kubo, Y. Kubota, C. S. Lee, M. Matsushita, H. Miya, A. Mizukami, H. Nagakura, D. Nishimura, H. Oikawa, H. Sakai, Y. Shimizu, A. Stolz, H. Suzuki, M. Takaki, H. Takeda, S. Takeuchi, H. Tokieda, T. Uesaka, K. Yako, Y. Yamaguchi, Y. Yanagisawa, R. Yokoyama, K. Yoshida, and S. Shimoura. Magic Nature of Neutrons in  $^{52}\text{Ca}$ : First Mass Measurements of  $^{55-57}\text{Ca}$ . *Physical Review Letters*, 121:022506,

- 7 2018. URL: <https://link.aps.org/doi/10.1103/PhysRevLett.121.022506>, doi:10.1103/PhysRevLett.121.022506.
- [44] D. Steppenbeck, S. Takeuchi, N. Aoi, P. Doornenbal, M. Matsushita, H. Wang, H. Baba, N. Fukuda, S. Go, M. Honma, J. Lee, K. Matsui, S. Michimasa, T. Motobayashi, D. Nishimura, T. Otsuka, H. Sakurai, Y. Shiga, P.-A. Söderström, T. Sumikama, H. Suzuki, R. Taniuchi, Y. Utsuno, J. J. Valiente-Dobón, and K. Yoneda. Evidence for a new nuclear ‘magic number’ from the level structure of  $^{54}\text{Ca}$ . *Nature*, 502:207–210, 10 2013. URL: <http://www.nature.com/articles/nature12522>, doi:10.1038/nature12522.
- [45] C. Guénaut, G. Audi, D. Beck, K. Blaum, G. Bollen, P. Delahaye, F. Herfurth, A. Kellerbauer, H.-J. Kluge, J. Libert, D. Lunney, S. Schwarz, L. Schweikhard, and C. Yazidjian. High-precision mass measurements of nickel, copper, and gallium isotopes and the purported shell closure at  $N = 40$ . *Physical Review C*, 75:044303, 4 2007. URL: <https://link.aps.org/doi/10.1103/PhysRevC.75.044303>, doi:10.1103/PhysRevC.75.044303.
- [46] O. Sorlin, S. Leenhardt, C. Donzaud, J. Duprat, F. Azaiez, F. Nowacki, H. Grawe, Zs. Dombrádi, F. Amorini, A. Astier, D. Baiborodin, M. Belleguic, C. Borcea, C. Bourgeois, D. M. Cullen, Z. Dlouhy, E. Dragulescu, M. Górski, S. Grévy, D. Guillemaud-Mueller, G. Hagemann, B. Herskind, J. Kiener, R. Lemmon, M. Lewitowicz, S. M. Lukyanov, P. Mayet, F. de Oliveira Santos, D. Pantalica, Yu.-E. Penionzhkevich, F. Pougheon, A. Poves, N. Redon, M. G. Saint-Laurent, J. A. Scarpaci, G. Sletten, M. Stanoiu, O. Tarasov, and Ch. Theisen.  $^{68}\text{Ni}_{40}$  Magicity versus Superfluidity. *Physical Review Letters*, 88:092501, 2 2002. URL: <https://link.aps.org/doi/10.1103/PhysRevLett.88.092501>, doi:10.1103/PhysRevLett.88.092501.
- [47] S. Malbrunot-Ettenauer, S. Kaufmann, S. Bacca, C. Barbieri, J. Billowes, M. L. Bissell, K. Blaum, B. Cheal, T. Duguet, R. F. Garcia Ruiz, W. Gins, C. Gorges, G. Hagen, H. Heylen, J. D. Holt, G. R. Jansen, A. Kanellakopoulos, M. Kortelainen, T. Miyagi, P. Navrátil, W. Nazarewicz, R. Neugart, G. Neyens, W. Nörtershäuser, S. J. Novario, T. Papenbrock, T. Ratajczyk, P.-G. Reinhard, L. V. Rodríguez, R. Sánchez, S. Sailer, A. Schwenk, J. Simonis, V. Somà, S. R. Stroberg, L. Wehner, C. Wraith, L. Xie, Z. Y. Xu, X. F. Yang, and D. T. Yordanov. Nuclear Charge Radii of the Nickel Isotopes  $^{58-68,70}\text{Ni}$ . *Physical Review Letters*, 128:022502, 1 2022. URL: <https://link.aps.org/doi/10.1103/PhysRevLett.128.022502>, doi:10.1103/PhysRevLett.128.022502.
- [48] Paul E. Garrett, Magda Zielińska, and Emmanuel Clément. An experimental view on shape coexistence in nuclei. *Progress in Particle and Nuclear Physics*, 124, 5 2022. doi:10.1016/J.PPNP.2021.103931.
- [49] R. F. Casten. Shape phase transitions and critical-point phenomena in atomic nuclei. *Nature Physics*, 2:811–820, 12 2006. URL: <http://www.nature.com/articles/nphys451>, doi:10.1038/nphys451.

- [50] S. Naimi, G. Audi, D. Beck, K. Blaum, Ch. Böhm, Ch. Borgmann, M. Breitenfeldt, S. George, F. Herfurth, A. Herlert, M. Kowalska, S. Kreim, D. Lunney, D. Neidherr, M. Rosenbusch, S. Schwarz, L. Schweikhard, and K. Zuber. Critical-Point Boundary for the Nuclear Quantum Phase Transition Near  $A = 100$  from Mass Measurements of  $^{96,97}\text{Kr}$ . *Physical Review Letters*, 105:032502, 7 2010. URL: <https://link.aps.org/doi/10.1103/PhysRevLett.105.032502>, doi:10.1103/PhysRevLett.105.032502.
- [51] V. Manea, D. Atanasov, D. Beck, K. Blaum, C. Borgmann, R. B. Cakirli, T. Eronen, S. George, F. Herfurth, A. Herlert, M. Kowalska, S. Kreim, Yu. A. Litvinov, D. Lunney, D. Neidherr, M. Rosenbusch, L. Schweikhard, F. Wienholtz, R. N. Wolf, and K. Zuber. Collective degrees of freedom of neutron-rich  $A = 100$  nuclei and the first mass measurement of the short-lived nuclide  $^{100}\text{Rb}$ . *Physical Review C*, 88:054322, 11 2013. URL: <https://link.aps.org/doi/10.1103/PhysRevC.88.054322>, doi:10.1103/PhysRevC.88.054322.
- [52] E. Clément, M. Zielińska, A. Gorgen, W. Korten, S. Péru, J. Libert, H. Goutte, S. Hilaire, B. Bastin, C. Bauer, A. Blazhev, N. Bree, B. Bruyneel, P. A. Butler, J. Butterworth, P. Delahaye, A. Dijon, D. T. Doherty, A. Ekström, C. Fitzpatrick, C. Fransen, G. Georgiev, R. Gernhäuser, H. Hess, J. Iwanicki, D. G. Jenkins, A. C. Larsen, J. Ljungvall, R. Lutter, P. Marley, K. Moschner, P. J. Napiorkowski, J. Pakarinen, A. Petts, P. Reiter, T. Renstrøm, M. Seidlitz, B. Siebeck, S. Siem, C. Sotty, J. Srebrny, I. Stefanescu, G. M. Tveten, J. Van de Walle, M. Vermeulen, D. Voulot, N. Warr, F. Wenander, A. Wiens, H. De Witte, and K. Wrzosek-Lipska. Spectroscopic Quadrupole Moments in  $^{96,98}\text{Sr}$ : Evidence for Shape Coexistence in Neutron-Rich Strontium Isotopes at  $N = 60$ . *Physical Review Letters*, 116:022701, 1 2016. URL: <https://link.aps.org/doi/10.1103/PhysRevLett.116.022701>, doi:10.1103/PhysRevLett.116.022701.
- [53] B. Cheal, M.D. Gardner, M. Avgoulea, J. Billowes, M.L. Bissell, P. Campbell, T. Eronen, K.T. Flanagan, D.H. Forest, J. Huikari, A. Jokinen, B.A. Marsh, I.D. Moore, A. Nieminen, H. Penttilä, S. Rinta-Antila, B. Tordoff, G. Tungate, and J. Äystö. The shape transition in the neutron-rich yttrium isotopes and isomers. *Physics Letters B*, 645:133–137, 2 2007. URL: <https://linkinghub.elsevier.com/retrieve/pii/S037026930601608X>, doi:10.1016/j.physletb.2006.12.053.
- [54] Tomoaki Togashi, Yusuke Tsunoda, Takaharu Otsuka, and Noritaka Shimizu. Quantum Phase Transition in the Shape of Zr isotopes. *Physical Review Letters*, 117:172502, 10 2016. URL: <https://link.aps.org/doi/10.1103/PhysRevLett.117.172502>, doi:10.1103/PhysRevLett.117.172502.
- [55] B. Cheal, K. Baczynska, J. Billowes, P. Campbell, F. C. Charlwood, T. Eronen, D. H. Forest, A. Jokinen, T. Kessler, I. D. Moore, M. Reponen, S. Rothe, M. Rüffer, A. Saastamoinen, G. Tungate, and J. Äystö. Laser Spectroscopy of Niobium Fission Fragments: First Use of Optical Pumping in an Ion Beam Cooler Buncher. *Physical Review Letters*, 102:222501, 6 2009. URL: <https://link.aps.org/doi/10.1103/PhysRevLett.102.222501>, doi:10.1103/PhysRevLett.102.222501.

- [56] J. Dudouet, A. Lemasson, G. Duchêne, M. Rejmund, E. Clément, C. Michelagnoli, F. Didierjean, A. Korichi, G. Maquart, O. Stezowski, C. Lizarazo, R. M. Pérez-Vidal, C. Andreoiu, G. de Angelis, A. Astier, C. Delafosse, I. Deloncle, Z. Dombradi, G. de France, A. Gadea, A. Gottardo, B. Jacquot, P. Jones, T. Konstantinopoulos, I. Kuti, F. Le Blanc, S. M. Lenzi, G. Li, R. Lozeva, B. Million, D. R. Napoli, A. Navin, C. M. Petrache, N. Pietralla, D. Ralet, M. Ramdhane, N. Redon, C. Schmitt, D. Sohler, D. Verney, D. Barrientos, B. Birkenbach, I. Burrows, L. Charles, J. Collado, D. M. Cullen, P. Désesquelles, C. Domingo Pardo, V. González, L. Harkness-Brennan, H. Hess, D. S. Judson, M. Karolak, W. Korten, M. Labiche, J. Ljungvall, R. Menegazzo, D. Mengoni, A. Pullia, F. Recchia, P. Reiter, M. D. Salsac, E. Sanchis, Ch. Theisen, J. J. Valiente-Dobón, and M. Zielińska.  $^{96}_{36}\text{Kr}_{60}$  - Low- $Z$  Boundary of the Island of Deformation at Boundary at  $N = 60$ . *Physical Review Letters*, 118:162501, 4 2017. URL: <http://link.aps.org/doi/10.1103/PhysRevLett.118.162501>, doi:10.1103/PhysRevLett.118.162501.
- [57] P. Koseoglou, V. Werner, N. Pietralla, S. Ilieva, T. Nikšić, D. Vretenar, P. Alexa, M. Thürauf, C. Bernards, A. Blanc, A. M. Bruce, R. B. Cakirli, N. Cooper, L. M. Fraile, G. de France, M. Jentschel, J. Jolie, U. Köster, W. Korten, T. Kröll, S. Lalkovski, H. Mach, N. Mărginean, P. Mutti, Z. Patel, V. Pazi, Zs. Podolyák, P. H. Regan, J.-M. Régis, O. J. Roberts, N. Saed-Samii, G. S. Simpson, T. Soldner, C. A. Ur, W. Urban, D. Wilmsen, and E. Wilson. Low- $Z$  boundary of the  $N = 88 - 90$  shape phase transition:  $^{148}\text{Ce}$  near the critical point. *Physical Review C*, 101:014303, 1 2020. URL: <https://link.aps.org/doi/10.1103/PhysRevC.101.014303>, doi:10.1103/PhysRevC.101.014303.
- [58] R. F. Casten and N. V. Zamfir. Empirical Realization of a Critical Point Description in Atomic Nuclei. *Physical Review Letters*, 87:052503, 7 2001. URL: <https://link.aps.org/doi/10.1103/PhysRevLett.87.052503>, doi:10.1103/PhysRevLett.87.052503.
- [59] R. Krücken, B. Albanna, C. Bialik, R. F. Casten, J. R. Cooper, A. Dewald, N. V. Zamfir, C. J. Barton, C. W. Beausang, M. A. Caprio, A. A. Hecht, T. Klug, J. R. Novak, N. Pietralla, and P. von Brentano.  $B(E2)$  Values in  $^{150}\text{Nd}$  and the Critical Point Symmetry X(5). *Physical Review Letters*, 88:232501, 5 2002. doi:10.1103/PhysRevLett.88.232501.
- [60] Vladimir Manea. *Binding Energy of Strongly Deformed Radionuclides*. Springer International Publishing, 2015. URL: <https://link.springer.com/10.1007/978-3-319-20409-3>, doi:10.1007/978-3-319-20409-3.
- [61] J.-Y. Zhang, R. F. Casten, and D. S. Brenner. Empirical proton-neutron interaction energies. Linearity and saturation phenomena. *Physics Letters B*, 227:1–5, 1989. URL: <https://www.sciencedirect.com/science/article/pii/0370269389912732>, doi:10.1016/0370-2693(89)91273-2.
- [62] R. B. Cakirli, D. S. Brenner, R. F. Casten, and E. A. Millman. Proton-Neutron Interactions and the New Atomic Masses. *Phys. Rev. Lett.*, 94:92501, 3 2005. URL:

<https://link.aps.org/doi/10.1103/PhysRevLett.94.092501>, doi:10.1103/PhysRevLett.94.092501.

- [63] R. B. Cakirli and R. F. Casten. Direct Empirical Correlation between Proton-Neutron Interaction Strengths and the Growth of Collectivity in Nuclei. *Phys. Rev. Lett.*, 96:132501, 4 2006. URL: <https://link.aps.org/doi/10.1103/PhysRevLett.96.132501>, doi:10.1103/PhysRevLett.96.132501.
- [64] D. S. Brenner, R. B. Cakirli, and R. F. Casten. Valence proton-neutron interactions throughout the mass surface. *Phys. Rev. C*, 73:34315, 3 2006. URL: <https://link.aps.org/doi/10.1103/PhysRevC.73.034315>, doi:10.1103/PhysRevC.73.034315.
- [65] L. Chen, Yu. A. Litvinov, W. R. Plaß, K. Beckert, P. Beller, F. Bosch, D. Boutin, L. Caceres, R. B. Cakirli, J. J. Carroll, R. F. Casten, R. S. Chakrawarthy, D. M. Cullen, I. J. Cullen, B. Franzke, H. Geissel, J. Gerl, M. Górska, G. A. Jones, A. Kishada, R. Knöbel, C. Kozhuharov, S. A. Litvinov, Z. Liu, S. Mandal, F. Montes, G. Münzenberg, F. Nolden, T. Ohtsubo, Z. Patyk, Zs. Podolyák, R. Propri, S. Rigby, N. Saito, T. Saito, C. Scheidenberger, M. Shindo, M. Steck, P. Ugorowski, P. M. Walker, S. Williams, H. Weick, M. Winkler, H.-J. Wollersheim, and T. Yamaguchi. Schottky Mass Measurement of the  $^{208}\text{Hg}$  Isotope: Implication for the Proton-Neutron Interaction Strength around Doubly Magic  $^{208}\text{Pb}$ . *Phys. Rev. Lett.*, 102:122503, Mar 2009. URL: <https://link.aps.org/doi/10.1103/PhysRevLett.102.122503>, doi:10.1103/PhysRevLett.102.122503.
- [66] W. H. King. *Isotope Shifts in Atomic Spectra*. Springer US, Boston, MA, 1984. URL: <http://link.springer.com/10.1007/978-1-4899-1786-7>, doi:10.1007/978-1-4899-1786-7.
- [67] Michail Athanasakis-Kaklamanakis, Shane G. Wilkins, Alexander A. Breier, and Gerda Neyens. King-Plot Analysis of Isotope Shifts in Simple Diatomic Molecules. *Physical Review X*, 13(1):011015, 2 2023. URL: <https://link.aps.org/doi/10.1103/PhysRevX.13.011015>, doi:10.1103/PhysRevX.13.011015.
- [68] L. I. Schiff. Measurability of Nuclear Electric Dipole Moments. *Physical Review*, 132:2194–2200, 12 1963. URL: <https://link.aps.org/doi/10.1103/PhysRev.132.2194>, doi:10.1103/PhysRev.132.2194.
- [69] Gerda Neyens. Nuclear magnetic and quadrupole moments for nuclear structure research on exotic nuclei. *Reports on Progress in Physics*, 66:633–689, 4 2003. URL: <https://iopscience.iop.org/article/10.1088/0034-4885/66/4/205>, doi:10.1088/0034-4885/66/4/205.
- [70] H. Sagawa and A. Arima. Static and dynamic quadrupole moments of high-spin isomers in the Pb-region. *Physics Letters B*, 202(1):15–20, 2 1988. URL: <https://linkinghub.elsevier.com/retrieve/pii/0370269388908453>, doi:10.1016/0370-2693(88)90845-3.
- [71] Jenny E. Rosenthal and G. Breit. The Isotope Shift in Hyperfine Structure. *Physical Review*, 41:459–470, 8 1932. doi:10.1103/PhysRev.41.459.

- [72] Aage Bohr and V. F. Weisskopf. The Influence of Nuclear Structure on the Hyperfine Structure of Heavy Elements. *Physical Review*, 77:94–98, 1 1950. doi:[10.1103/PhysRev.77.94](https://doi.org/10.1103/PhysRev.77.94).
- [73] L. Fortunato. Solutions of the Bohr Hamiltonian, a compendium. *The European Physical Journal A*, 26:1–30, 10 2005. URL: <http://link.springer.com/10.1140/epjad/i2005-07-115-8>, doi:[10.1140/epjad/i2005-07-115-8](https://doi.org/10.1140/epjad/i2005-07-115-8).
- [74] L. P. Gaffney, P. A. Butler, M. Scheck, A. B. Hayes, F. Wenander, M. Albers, B. Bastin, C. Bauer, A. Blazhev, S. Bönig, N. Bree, J. Cederkäll, T. Chupp, D. Cline, T. E. Cocolios, T. Davinson, H. De Witte, J. Diriken, T. Grahn, A. Herzan, M. Huyse, D. G. Jenkins, D. T. Joss, N. Kesteloot, J. Konki, M. Kowalczyk, Th. Kröll, E. Kwan, R. Lutter, K. Moschner, P. Napiorkowski, J. Pakarinen, M. Pfeiffer, D. Radeck, P. Reiter, K. Reynders, S. V. Rigby, L. M. Robledo, M. Rudigier, S. Sambi, M. Seidlitz, B. Siebeck, T. Stora, P. Thoele, P. Van Duppen, M. J. Vermeulen, M. von Schmid, D. Voulot, N. Warr, K. Wimmer, K. Wrzosek-Lipska, C. Y. Wu, and M. Zielinska. Studies of pear-shaped nuclei using accelerated radioactive beams. *Nature*, 497:199–204, 5 2013. doi:[10.1038/nature12073](https://doi.org/10.1038/nature12073).
- [75] David Lawrence Hill and John Archibald Wheeler. Nuclear Constitution and the Interpretation of Fission Phenomena. *Physical Review*, 89:1102–1145, 3 1953. URL: <https://link.aps.org/doi/10.1103/PhysRev.89.1102>, doi:[10.1103/PhysRev.89.1102](https://doi.org/10.1103/PhysRev.89.1102).
- [76] D. Berdichevsky and F. Tondeur. Nuclear core densities, isotope shifts, and the parametrization of the droplet model. *Zeitschrift für Physik A Atoms and Nuclei*, 322:141–147, 3 1985. doi:[10.1007/BF01412027](https://doi.org/10.1007/BF01412027).
- [77] M. Lindroos. Review of the ISOL Method. Technical report, CERN, Geneva, 2004. revised version submitted on 2004-09-28 17:19:32. URL: <https://cds.cern.ch/record/793447>.
- [78] B. Blank, G. Canchel, F. Seis, and P. Delahaye. Evaluation of fusion-evaporation cross-section calculations. *Nuclear Instruments and Methods in Physics Research Section B: Beam Interactions with Materials and Atoms*, 416:41–49, 2 2018. URL: <https://linkinghub.elsevier.com/retrieve/pii/S0168583X17310054>, doi:[10.1016/j.nimb.2017.12.003](https://doi.org/10.1016/j.nimb.2017.12.003).
- [79] M. Au, M. Athanasakis-Kaklamanakis, L. Nies, R. Heinke, K. Chrysalidis, U. Köster, P. Kunz, B. Marsh, M. Mougeot, L. Schweikhard, S. Stegemann, Y. Vila Gracia, Ch. E. Düllmann, and S. Rothe. Production of neptunium and plutonium nuclides from uranium carbide using 1.4-GeV protons. *Physical Review C*, 107:064604, 6 2023. URL: <https://link.aps.org/doi/10.1103/PhysRevC.107.064604>, doi:[10.1103/PhysRevC.107.064604](https://doi.org/10.1103/PhysRevC.107.064604).
- [80] G. Savard, R. C. Pardo, S. Baker, C. N. Davids, A. Levand, D. Peterson, D. G. Phillips, T. Sun, R. Vondrasek, B. J. Zabransky, and G. P. Zinkann. CARIBU: a

new facility for the study of neutron-rich isotopes. *Hyperfine Interactions*, 199:301–309, 7 2011. URL: <http://link.springer.com/10.1007/s10751-011-0325-5>, doi:10.1007/s10751-011-0325-5.

- [81] J. McLain, C. A. Dickerson, M. Gott, J. Greene, J. Nolen, G. Savard, J. Song, and R. C. Vondrasek. nuCARIBU : An upgrade for the CARIBU facility at the Argonne Tandem Linac Accelerator System. *Journal of Physics: Conference Series*, 2244:012062, 4 2022. URL: <https://iopscience.iop.org/article/10.1088/1742-6596/2244/1/012062>, doi:10.1088/1742-6596/2244/1/012062.
- [82] O. Kofoed-Hansen and K. O. Nielsen. Short-Lived Krypton Isotopes and Their Daughter Substances. *Physical Review*, 82:96–97, 4 1951. URL: <https://link.aps.org/doi/10.1103/PhysRev.82.96.2>, doi:10.1103/PhysRev.82.96.2.
- [83] Gerhard John Krige. *History of CERN*. North-Holland, 1996.
- [84] Juha Äystö. CERN’s longest serving experimental facility. *Physics Reports*, 403-404:459–469, 12 2004. URL: <https://linkinghub.elsevier.com/retrieve/pii/S0370157304003412>, doi:10.1016/j.physrep.2004.08.030.
- [85] Sean Freeman. ISOLDE Consolidation and Improvements. Technical report, CERN, Geneva, 2023. URL: <https://cds.cern.ch/record/2846021>.
- [86] R. Catherall, W. Andreazza, M. Breitenfeldt, A. Dorsival, G. J. Focker, T. P. Gharsa, T. J. Giles, J.-L. Grenard, F. Locci, P. Martins, S. Marzari, J. Schipper, A. Shornikov, and T. Stora. The ISOLDE facility. *Journal of Physics G: Nuclear and Particle Physics*, 44:094002, 9 2017. URL: <https://iopscience.iop.org/article/10.1088/1361-6471/aa7eba>, doi:10.1088/1361-6471/aa7eba.
- [87] S. Stegemann, D. Atanasov, M. Au, E. Grenier-Boley, M. Butcher, M. Duffourg, E. Fadakis, T. Feniet, Y.N. Vila Gracia, T. Giles, J. Konki, L. Le, R. Lică, P. Martins, E. Matheson, C. Mihai, R. Martinez Muniz, C. Neacșu, G. Pascovici, K.A. Szczurek, S. Warren, and S. Rothe. The CERN-ISOLDE fast tape station. *Nuclear Instruments and Methods in Physics Research Section B: Beam Interactions with Materials and Atoms*, 541:169–172, 8 2023. URL: <https://linkinghub.elsevier.com/retrieve/pii/S0168583X23001465>, doi:10.1016/j.nimb.2023.04.018.
- [88] F. Wenander, B. Jonson, L. Liljeby, and G. H. Nyman. REXEBIS the Electron Beam Ion Source for the REX-ISOLDE project. Technical report, CERN, Geneva, 1998. URL: <http://cds.cern.ch/record/478399>.
- [89] R. Luis, J. G. Marques, T. Stora, P. Vaz, and L. Zanini. Optimization studies of the CERN-ISOLDE neutron converter and fission target system. *The European Physical Journal A*, 48:90, 6 2012. doi:10.1140/epja/i2012-12090-9.
- [90] R. Kirchner. On the thermoionization in hot cavities. *Nuclear Instruments and Methods in Physics Research Section A: Accelerators, Spectrometers, Detectors and Associated Equipment*, 292:203–208, 7 1990. URL: <https://>

[linkinghub.elsevier.com/retrieve/pii/S0168900290903771](https://linkinghub.elsevier.com/retrieve/pii/S0168900290903771), doi:10.1016/0168-9002(90)90377-I.

- [91] F. Schwellnus, R. Catherall, B. Crepieux, V.N. Fedosseev, B.A. Marsh, Ch. Mattoilat, M. Menna, F.K. Österdahl, S. Raeder, T. Stora, and K. Wendt. Study of low work function materials for hot cavity resonance ionization laser ion sources. *Nuclear Instruments and Methods in Physics Research Section B: Beam Interactions with Materials and Atoms*, 267(10):1856–1861, 2009. URL: <https://www.sciencedirect.com/science/article/pii/S0168583X09004054>, doi:10.1016/j.nimb.2009.02.068.
- [92] E. Bouquerel, R. Catherall, M. Eller, J. Lettry, S. Marzari, T. Stora, and ISOLDE Collaboration. Purification of a Zn radioactive ion beam by alkali suppression in a quartz line target prototype. *The European Physical Journal Special Topics*, 150:277–280, 11 2007. URL: <http://link.springer.com/10.1140/epjst/e2007-00323-4>, doi:10.1140/epjst/e2007-00323-4.
- [93] E. Bouquerel, R. Catherall, M. Eller, J. Lettry, S. Marzari, and T. Stora. Beam purification by selective trapping in the transfer line of an ISOL target unit. *Nuclear Instruments and Methods in Physics Research Section B: Beam Interactions with Materials and Atoms*, 266:4298–4302, 10 2008. URL: <https://linkinghub.elsevier.com/retrieve/pii/S0168583X08007246>, doi:10.1016/j.nimb.2008.05.060.
- [94] R. Kirchner and E. Roeckl. Investigation of gaseous discharge ion sources for isotope separation on-line. *Nuclear Instruments and Methods*, 133:187–204, 3 1976. URL: <https://linkinghub.elsevier.com/retrieve/pii/0029554X76906078>, doi:10.1016/0029-554X(76)90607-8.
- [95] S. Sundell and H. Ravn. Ion source with combined cathode and transfer line heating. *Nuclear Instruments and Methods in Physics Research Section B: Beam Interactions with Materials and Atoms*, 70:160–164, 8 1992. URL: <https://linkinghub.elsevier.com/retrieve/pii/S0168583X9295926I>, doi:10.1016/0168-583X(92)95926-I.
- [96] L. Penescu, R. Catherall, J. Lettry, and T. Stora. Development of high efficiency Versatile Arc Discharge Ion Source at CERN ISOLDE. *Review of Scientific Instruments*, 81:02A906, 2 2010. URL: <https://pubs.aip.org/aip/rsi/article/1071842>, doi:10.1063/1.3271245.
- [97] D. Neidherr, G. Audi, D. Beck, K. Blaum, Ch. Böhm, M. Breitenfeldt, R. B. Cakirli, R. F. Casten, S. George, F. Herfurth, A. Herlert, A. Kellerbauer, M. Kowalska, D. Lunney, E. Minaya-Ramirez, S. Naimi, E. Noah, L. Penescu, M. Rosenbusch, S. Schwarz, L. Schweikhard, and T. Stora. Discovery of  $^{229}\text{Rn}$  and the structure of the heaviest rn and ra isotopes from penning-trap mass measurements. *Phys. Rev. Lett.*, 102:112501, Mar 2009. URL: <https://link.aps.org/doi/10.1103/PhysRevLett.102.112501>, doi:10.1103/PhysRevLett.102.112501.

- [98] Valentin Fedosseev, Katerina Chrysalidis, Thomas Day Goodacre, Bruce Marsh, Sebastian Rothe, Christoph Seiffert, and Klaus Wendt. Ion beam production and study of radioactive isotopes with the laser ion source at isolde. *Journal of Physics G: Nuclear and Particle Physics*, 44:084006, 8 2017. URL: <https://iopscience.iop.org/article/10.1088/1361-6471/aa78e0>, doi:10.1088/1361-6471/aa78e0.
- [99] K. Blaum, C. Geppert, H.-J. Kluge, M. Mukherjee, S. Schwarz, and K. Wendt. A novel scheme for a highly selective laser ion source. *Nuclear Instruments and Methods in Physics Research Section B: Beam Interactions with Materials and Atoms*, 204:331–335, 5 2003. URL: <https://linkinghub.elsevier.com/retrieve/pii/S0168583X02019420>, doi:10.1016/S0168-583X(02)01942-0.
- [100] D.A. Fink, S.D. Richter, K. Blaum, R. Catherall, B. Crepieux, V.N. Fedosseev, A. Gottberg, T. Kron, B.A. Marsh, C. Mattolat, S. Raeder, R.E. Rossel, S. Rothe, F. Schwellnus, M.D. Seliverstov, M. Sjödin, T. Stora, P. Suominen, and K.D.A. Wendt. On-line implementation and first operation of the Laser Ion Source and Trap at ISOLDE/CERN. *Nuclear Instruments and Methods in Physics Research Section B: Beam Interactions with Materials and Atoms*, 344:83–95, 2 2015. URL: <https://linkinghub.elsevier.com/retrieve/pii/S0168583X14010222>, doi:10.1016/j.nimb.2014.12.007.
- [101] T. Day Goodacre, J. Billowes, R. Catherall, T.E. Cocolios, B. Crepieux, D.V. Fedorov, V.N. Fedosseev, L.P. Gaffney, T. Giles, A. Gottberg, K.M. Lynch, B.A. Marsh, T.M. Mendonça, J.P. Ramos, R.E. Rossel, S. Rothe, S. Sels, C. Sotty, T. Stora, C. Van Beveren, and M. Veinhard. Blurring the boundaries between ion sources: The application of the RILIS inside a FEBIAD type ion source at ISOLDE. *Nuclear Instruments and Methods in Physics Research Section B: Beam Interactions with Materials and Atoms*, 376:39–45, 6 2016. URL: <https://linkinghub.elsevier.com/retrieve/pii/S0168583X16002111>, doi:10.1016/j.nimb.2016.03.005.
- [102] L. Nies, K. Blaum, W. J. Huang, J. Kartheim, Yu. A. Litvinov, D. Lunney, V. Manea, M. Mougeot, S. Naimi, Ch. Schweiger, L. Schweikhard, A. Schwenk, and F. Wienholtz. Closing in on  $^{100}\text{Sn}$ : Mass Measurements of the Neutron Deficient N=51-53 Tin Isotopes. Technical report, CERN, Geneva, 2022. URL: <https://cds.cern.ch/record/2809461>.
- [103] K. Sümmerer. Improved empirical parametrization of fragmentation cross sections. *Physical Review C*, 86:014601, 7 2012. URL: <https://link.aps.org/doi/10.1103/PhysRevC.86.014601>, doi:10.1103/PhysRevC.86.014601.
- [104] I.D. Moore, T. Eronen, D. Gorelov, J. Hakala, A. Jokinen, A. Kankainen, V.S. Kolhinen, J. Koponen, H. Penttilä, I. Pohjalainen, M. Reponen, J. Rissanen, A. Saastamoinen, S. Rinta-Antila, V. Sonnenschein, and J. Äystö. Towards commissioning the new IGISOL-4 facility. *Nuclear Instruments and Methods in Physics Research Section B: Beam Interactions with Materials and Atoms*,

- 317:208–213, 12 2013. URL: <https://linkinghub.elsevier.com/retrieve/pii/S0168583X13007143>, doi:10.1016/j.nimb.2013.06.036.
- [105] A. Al-Adili, K. Jansson, M. Lantz, A. Solders, D. Gorelov, C. Gustavsson, A. Mattera, I. Moore, A. V. Prokofiev, V. Rakopoulos, H. Penttilä, D. Tarrío, S. Wiberg, M. Österlund, and S. Pomp. Simulations of the fission-product stopping efficiency in IGISOL. *The European Physical Journal A*, 51:59, 5 2015. URL: <http://link.springer.com/10.1140/epja/i2015-15059-2>, doi:10.1140/epja/i2015-15059-2.
  - [106] Klaus Blaum. High-accuracy mass spectrometry with stored ions. *Physics Reports*, 425(1):1–78, 3 2006. doi:10.1016/J.PHYSREP.2005.10.011.
  - [107] Y. H. Zhang, Yu. A. Litvinov, T. Uesaka, and H. S. Xu. Storage ring mass spectrometry for nuclear structure and astrophysics research. *Physica Scripta*, 91(7):073002, 7 2016. doi:10.1088/0031-8949/91/7/073002.
  - [108] M. D. Lunney, G. Audi, C. Borcea, M. Dedieu, H. Doubre, M. Duma, M. Jacotin, J. F. Képinski, G. Le Scornet, M. de Saint Simon, and C. Thibault. MISTRAL: A new program for precise atomic mass determinations of nuclides far from stability. *Hyperfine Interactions*, 99(1):105–114, 12 1996. doi:10.1007/BF02274914.
  - [109] L. Bianchi, B. Fernandez, J. Gastebois, A. Gillibert, W. Mittig, and J. Barrette. SPEG: An energy loss spectrometer for GANIL. *Nuclear Instruments and Methods in Physics Research Section A: Accelerators, Spectrometers, Detectors and Associated Equipment*, 276(3):509–520, 4 1989. doi:10.1016/0168-9002(89)90577-9.
  - [110] G. Auger, W. Mittig, A. Lépine-Szily, L.K. Fifield, M. Bajard, E. Baron, D. Bibet, P. Bricault, J.M. Casandjian, M. Chabert, M. Chartier, J. Fermé, L. Gaudard, A. Gillibert, M. Lewitowicz, M.H. Moscatello, N.A. Orr, E. Plagnol, C. Ricault, A.C.C. Villari, and Yang Yong Feng. A cyclotron as a high resolution mass spectrometer for fast secondary ions. *Nuclear Instruments and Methods in Physics Research Section A: Accelerators, Spectrometers, Detectors and Associated Equipment*, 350(1-2):235–243, 10 1994. doi:10.1016/0168-9002(94)91170-3.
  - [111] M. Mukherjee, D. Beck, K. Blaum, G. Bollen, J. Dilling, S. George, F. Herfurth, A. Herlert, A. Kellerbauer, H. J. Kluge, S. Schwarz, L. Schweikhard, and C. Yazidjian. ISOLTRAP: An on-line Penning trap for mass spectrometry on short-lived nuclides. *The European Physical Journal A* 2008 35:1, 35(1):1–29, 2 2008. URL: <https://link.springer.com/article/10.1140/epja/i2007-10528-9>, doi:10.1140/EPJA/I2007-10528-9.
  - [112] J. Dilling, R. Baartman, P. Bricault, M. Brodeur, L. Blomeley, F. Buchinger, J. Crawford, J.R. Crespo López-Urrutia, P. Delheij, M. Froese, G.P. Gwinner, Z. Ke, J.K.P. Lee, R.B. Moore, V. Ryjkov, G. Sikler, M. Smith, J. Ullrich, and J. Vaz. Mass measurements on highly charged radioactive ions, a new approach to high precision with TITAN. *International Journal of Mass Spectrometry*, 251(2-3):198–203, 4 2006. doi:10.1016/j.ijms.2006.01.044.

- [113] T. Eronen, V. S. Kolhinen, V. V. Elomaa, D. Gorelov, U. Hager, J. Hakala, A. Jokinen, A. Kankainen, P. Karvonen, S. Kopecky, I. D. Moore, H. Penttilä, S. Rahaman, S. Rinta-Antila, J. Rissanen, A. Saastamoinen, J. Szerypo, C. Weber, and J. Äystö. JYFLTRAP: a Penning trap for precision mass spectroscopy and isobaric purification. *The European Physical Journal A*, 48(4):46, 4 2012. [doi:10.1140/epja/i2012-12046-1](https://doi.org/10.1140/epja/i2012-12046-1).
- [114] R. Ringle, P. Schury, T. Sun, G. Bollen, D. Davies, J. Huikari, E. Kwan, D.J. Morrissey, A. Prinke, J. Savory, S. Schwarz, and C. Sumithrarachchi. Precision mass measurements with LEBIT at MSU. *International Journal of Mass Spectrometry*, 251(2-3):300–306, 4 2006. [doi:10.1016/j.ijms.2006.02.011](https://doi.org/10.1016/j.ijms.2006.02.011).
- [115] O. Kaleja, B. Andelić, O. Bezrodnova, K. Blaum, M. Block, S. Chenmarev, P. Chhetri, C. Droese, Ch. E. Düllmann, M. Eibach, S. Eliseev, J. Even, P. Filianin, F. Giacoppo, S. Götz, Yu. Gusev, M. J. Gutiérrez, F. P. Heßberger, N. Kalantar-Nayestanaki, J. J. W. van de Laar, M. Laatiaoui, S. Lohse, N. Martynova, E. Minaya Ramirez, A. K. Mistry, T. Murböck, Yu. Novikov, S. Raeder, D. Rodríguez, F. Schneider, L. Schweikhard, P. G. Thirolf, and A. Yakushev. Direct high-precision mass spectrometry of superheavy elements with SHIPTRAP. *Physical Review C*, 106(5):054325, 11 2022. [doi:10.1103/PhysRevC.106.054325](https://doi.org/10.1103/PhysRevC.106.054325).
- [116] M. Rosenbusch, M. Wada, S. Chen, A. Takamine, S. Iimura, D. Hou, W. Xian, S. Yan, P. Schury, Y. Hirayama, Y. Ito, H. Ishiyama, S. Kimura, T. Kojima, J. Lee, J. Liu, S. Michimasa, H. Miyatake, J.Y. Moon, M. Mukai, S. Naimi, S. Nishimura, T. Niwase, T. Sonoda, Y.X. Watanabe, and H. Wollnik. The new MRTOF mass spectrograph following the ZeroDegree spectrometer at RIKEN’s RIBF facility. *Nuclear Instruments and Methods in Physics Research Section A: Accelerators, Spectrometers, Detectors and Associated Equipment*, 1047:167824, 2 2023. [doi:10.1016/j.nima.2022.167824](https://doi.org/10.1016/j.nima.2022.167824).
- [117] G. Savard, St. Becker, G. Bollen, H.-J. Kluge, R.B. Moore, Th. Otto, L. Schweikhard, H. Stolzenberg, and U. Wiess. A new cooling technique for heavy ions in a Penning trap. *Physics Letters A*, 158(5):247–252, 9 1991. URL: <https://linkinghub.elsevier.com/retrieve/pii/0375960191910082>, [doi:10.1016/0375-9601\(91\)91008-2](https://doi.org/10.1016/0375-9601(91)91008-2).
- [118] Lowell S. Brown and Gerald Gabrielse. Geonium theory: Physics of a single electron or ion in a Penning trap. *Reviews of Modern Physics*, 58(1):233–311, 1 1986. [doi:10.1103/RevModPhys.58.233](https://doi.org/10.1103/RevModPhys.58.233).
- [119] G. Gräff, H. Kalinowsky, and J. Traut. A direct determination of the proton electron mass ratio. *Zeitschrift für Physik A: Atoms and Nuclei*, 297:35–39, 3 1980. [doi:10.1007/BF01414243](https://doi.org/10.1007/BF01414243).
- [120] M. König, G. Bollen, H.-J. Kluge, T. Otto, and J. Szerypo. Quadrupole excitation of stored ion motion at the true cyclotron frequency. *International Journal of Mass Spectrometry and Ion Processes*, 142:95–116, 3 1995. [doi:10.1016/0168-1176\(95\)04146-C](https://doi.org/10.1016/0168-1176(95)04146-C).

- [121] S. George, S. Baruah, B. Blank, K. Blaum, M. Breitenfeldt, U. Hager, F. Herfurth, A. Herlert, A. Kellerbauer, H.-J. Kluge, M. Kretzschmar, D. Lunney, R. Savreux, S. Schwarz, L. Schweikhard, and C. Yazidjian. Ramsey Method of Separated Oscillatory Fields for High-Precision Penning Trap Mass Spectrometry. *Physical Review Letters*, 98(16):162501, 4 2007. doi:[10.1103/PhysRevLett.98.162501](https://doi.org/10.1103/PhysRevLett.98.162501).
- [122] S. George, K. Blaum, F. Herfurth, A. Herlert, M. Kretzschmar, S. Nagy, S. Schwarz, L. Schweikhard, and C. Yazidjian. The Ramsey method in high-precision mass spectrometry with Penning traps: Experimental results. *International Journal of Mass Spectrometry*, 264(2-3):110–121, 7 2007. doi:[10.1016/j.ijms.2007.04.003](https://doi.org/10.1016/j.ijms.2007.04.003).
- [123] T. Day Goodacre, A. V. Afanasjev, A. E. Barzakh, L. Nies, B. A. Marsh, S. Sels, U. C. Perera, P. Ring, F. Wienholtz, A. N. Andreyev, P. Van Duppen, N. A. Althubiti, B. Andel, D. Atanasov, R. S. Augusto, J. Billowes, K. Blaum, T. E. Cocolios, J. G. Cubiss, G. J. Farooq-Smith, D. V. Fedorov, V. N. Fedosseev, K. T. Flanagan, L. P. Gaffney, L. Ghys, A. Gottberg, M. Huyse, S. Kreim, P. Kunz, D. Lunney, K. M. Lynch, V. Manea, Y. Martinez Palenzuela, T. M. Medonca, P. L. Molkanov, M. Mougeot, J. P. Ramos, M. Rosenbusch, R. E. Rossel, S. Rothe, L. Schweikhard, M. D. Seliverstov, P. Spagnoletti, C. Van Beveren, M. Veinhard, E. Verstraelen, A. Welker, K. Wendt, R. N. Wolf, A. Zadornaya, and K. Zuber. Charge radii, moments, and masses of mercury isotopes across the N=126 shell closure. *Physical Review C*, 104:054322, 11 2021. URL: <https://journals.aps.org/prc/abstract/10.1103/PhysRevC.104.054322>, doi:[10.1103/PHYSREVC.104.054322](https://doi.org/10.1103/PHYSREVC.104.054322)/FIGURES/12/MEDIUM.
- [124] S. Eliseev, K. Blaum, M. Block, C. Droese, M. Goncharov, E. Minaya Ramirez, D. A. Nesterenko, Yu N. Novikov, and L. Schweikhard. Phase-imaging ion-cyclotron-resonance measurements for short-lived nuclides. *Physical Review Letters*, 2013. doi:[10.1103/PhysRevLett.110.082501](https://doi.org/10.1103/PhysRevLett.110.082501).
- [125] S. Eliseev, K. Blaum, M. Block, A. Dörr, C. Droese, T. Eronen, M. Goncharov, M. Höcker, J. Ketter, E. Minaya Ramirez, D. A. Nesterenko, Yu. N. Novikov, and L. Schweikhard. A phase-imaging technique for cyclotron-frequency measurements. *Applied Physics B*, 114:107–128, 1 2014. URL: <http://link.springer.com/10.1007/s00340-013-5621-0>, doi:[10.1007/s00340-013-5621-0](https://doi.org/10.1007/s00340-013-5621-0).
- [126] A. E. Cameron and D. F. Eggers. An Ion “Velocitron”. *Review of Scientific Instruments*, 19(9):605–607, 9 1948. doi:[10.1063/1.1741336](https://doi.org/10.1063/1.1741336).
- [127] B.A. Mamyurin, V.I. Karataev, D.V. Shmikk, and V.A. Zagulin. The mass-reflectron, a new nonmagnetic time-of-flight mass spectrometer with high resolution. *Zh. Eksp. Teor. Fiz*, 64:82–89, 1973.
- [128] Werner Tretner. An electrostatic mass spectroscope. *Vacuum*, 10:31–34, 2 1960. doi:[10.1016/0042-207X\(60\)90104-4](https://doi.org/10.1016/0042-207X(60)90104-4).

- [129] H. Wollnik and M. Przewloka. Time-of-flight mass spectrometers with multiply reflected ion trajectories. *International Journal of Mass Spectrometry and Ion Processes*, 96(3):267–274, 4 1990. doi:[10.1016/0168-1176\(90\)85127-N](https://doi.org/10.1016/0168-1176(90)85127-N).
- [130] D. Zajfman, O. Heber, L. Vejby-Christensen, I. Ben-Itzhak, M. Rappaport, R. Fishman, and M. Dahan. Electrostatic bottle for long-time storage of fast ion beams. *Physical Review A*, 55(3):R1577–R1580, 3 1997. doi:[10.1103/PhysRevA.55.R1577](https://doi.org/10.1103/PhysRevA.55.R1577).
- [131] R. N. Wolf, D. Beck, K. Blaum, Ch. Böhm, Ch. Borgmann, M. Breitenfeldt, N. Chamel, S. Goriely, F. Herfurth, M. Kowalska, S. Kreim, D. Lunney, V. Manea, E. Minaya Ramirez, S. Naimi, D. Neidherr, M. Rosenbusch, L. Schweikhard, J. Stanja, F. Wienholtz, and K. Zuber. Plumbing Neutron Stars to New Depths with the Binding Energy of the Exotic Nuclide  $^{82}\text{Zn}$ . *Physical Review Letters*, 110:041101, 1 2013. URL: <https://link.aps.org/doi/10.1103/PhysRevLett.110.041101>, doi:[10.1103/PhysRevLett.110.041101](https://doi.org/10.1103/PhysRevLett.110.041101).
- [132] M. Au, M. Athanasakis-Kaklamanakis, L. Nies, J. Ballof, R. Berger, K. Chrysalidis, P. Fischer, R. Heinke, J. Johnson, U. Köster, D. Leimbach, B. Marsh, M. Mougeot, B. Reich, J. Reilly, E. Reis, M. Schlaich, Ch. Schweiger, L. Schweikhard, S. Stegemann, J. Wessolek, F. Wienholtz, S.G. Wilkins, W. Wojtaczka, Ch.E. Düllmann, and S. Rothe. In-source and in-trap formation of molecular ions in the actinide mass range at CERN-ISOLDE. *Nuclear Instruments and Methods in Physics Research Section B: Beam Interactions with Materials and Atoms*, 541:375–379, 8 2023. URL: <https://linkinghub.elsevier.com/retrieve/pii/S0168583X23002112>, doi:[10.1016/j.nimb.2023.05.015](https://doi.org/10.1016/j.nimb.2023.05.015).
- [133] R. N. Wolf, F. Wienholtz, D. Atanasov, D. Beck, K. Blaum, Ch Borgmann, F. Herfurth, M. Kowalska, S. Kreim, Yu A. Litvinov, D. Lunney, V. Manea, D. Neidherr, M. Rosenbusch, L. Schweikhard, J. Stanja, and K. Zuber. ISOLTRAP’s multi-reflection time-of-flight mass separator/spectrometer. *International Journal of Mass Spectrometry*, 349-350(1):123–133, 9 2013. doi:[10.1016/J.IJMS.2013.03.020](https://doi.org/10.1016/J.IJMS.2013.03.020).
- [134] T. Dickel, W.R. Plaß, A. Becker, U. Czok, H. Geissel, E. Haettner, C. Jesch, W. Kinsel, M. Petrick, C. Scheidenberger, A. Simon, and M.I. Yavor. A high-performance multiple-reflection time-of-flight mass spectrometer and isobar separator for the research with exotic nuclei. *Nuclear Instruments and Methods in Physics Research Section A: Accelerators, Spectrometers, Detectors and Associated Equipment*, 777:172–188, 3 2015. doi:[10.1016/j.nima.2014.12.094](https://doi.org/10.1016/j.nima.2014.12.094).
- [135] M.P. Reiter, S. Ayet San Andrés, J. Bergmann, T. Dickel, J. Dilling, A. Jacobs, A.A. Kwiatkowski, W.R. Plaß, C. Scheidenberger, D. Short, C. Will, C. Babcock, E. Dunling, A. Finlay, C. Hornung, C. Jesch, R. Klawitter, B. Kootte, D. Lascar, E. Leistenschneider, T. Murböck, S.F. Paul, and M. Yavor. Commissioning and performance of TITAN’s Multiple-Reflection Time-of-Flight Mass-Spectrometer and isobar separator. *Nuclear Instruments and Methods in Physics Research Section*

- A: Accelerators, Spectrometers, Detectors and Associated Equipment*, 1018:165823, 12 2021. doi:[10.1016/j.nima.2021.165823](https://doi.org/10.1016/j.nima.2021.165823).
- [136] Heikki Penttilä, Olga Beliuskina, Laetitia Canete, Antoine de Roubin, Tommi Eronen, Marjut Hukkanen, Anu Kankainen, Iain Moore, Dmitrii Nesterenko, Philippos Papadakis, Ilkka Pohjalainen, Mikael Reponen, Sami Rinta-Antila, Jan Sarén, Juha Uusitalo, Markus Vilén, and Ville Virtanen. Radioactive ion beam manipulation at the IGISOL-4 facility. *EPJ Web of Conferences*, 239:17002, 9 2020. doi:[10.1051/epjconf/202023917002](https://doi.org/10.1051/epjconf/202023917002).
- [137] M. Rosenbusch, P. Ascher, D. Atanasov, C. Barbieri, D. Beck, K. Blaum, Ch. Borgmann, M. Breitenfeldt, R. B. Cakirli, A. Cipollone, S. George, F. Herfurth, M. Kowalska, S. Kreim, D. Lunney, V. Manea, P. Navrátil, D. Neidherr, L. Schweikhard, V. Somà, J. Stanja, F. Wienholtz, R. N. Wolf, and K. Zuber. Probing the  $N = 32$  Shell Closure below the Magic Proton Number  $Z = 20$ : Mass Measurements of the Exotic Isotopes  $^{52,53}\text{K}$ . *Phys. Rev. Lett.*, 114:202501, May 2015. URL: <https://link.aps.org/doi/10.1103/PhysRevLett.114.202501>, doi:[10.1103/PhysRevLett.114.202501](https://doi.org/10.1103/PhysRevLett.114.202501).
- [138] S. Sels, P. Fischer, H. Heylen, V. Lagaki, S. Lechner, F.M. Maier, P. Plattner, M. Rosenbusch, F. Wienholtz, R.N. Wolf, W. Nörtershäuser, L. Schweikhard, and S. Malbrunot-Ettenauer. First steps in the development of the Multi Ion Reflection Apparatus for Collinear Laser Spectroscopy. *Nuclear Instruments and Methods in Physics Research Section B: Beam Interactions with Materials and Atoms*, 463:310–314, 1 2020. doi:[10.1016/j.nimb.2019.04.076](https://doi.org/10.1016/j.nimb.2019.04.076).
- [139] V. Lagaki, H. Heylen, I. Belosevic, P. Fischer, C. Kanitz, S. Lechner, F.M. Maier, W. Nörtershäuser, P. Plattner, M. Rosenbusch, S. Sels, L. Schweikhard, M. Vilen, F. Wienholtz, R.N. Wolf, and S. Malbrunot-Ettenauer. An accuracy benchmark of the MIRACLS apparatus: Conventional, single-passage collinear laser spectroscopy inside a MR-ToF device. *Nuclear Instruments and Methods in Physics Research Section A: Accelerators, Spectrometers, Detectors and Associated Equipment*, 1014:165663, 10 2021. doi:[10.1016/j.nima.2021.165663](https://doi.org/10.1016/j.nima.2021.165663).
- [140] F. M. Maier, M. Vilen, I. Belosevic, F. Buchinger, C. Kanitz, S. Lechner, E. Leitschneider, W. Nörtershäuser, P. Plattner, L. Schweikhard, S. Sels, F. Wienholtz, and S. Malbrunot-Ettenauer. Simulation studies of a 30-keV MR-ToF device for highly sensitive collinear laser spectroscopy. *Nuclear Instruments and Methods in Physics Research Section A: Accelerators, Spectrometers, Detectors and Associated Equipment*, 1048:167927, 3 2023. doi:[10.1016/J.NIMA.2022.167927](https://doi.org/10.1016/J.NIMA.2022.167927).
- [141] Robert N. Wolf, Gerrit Marx, Marco Rosenbusch, and Lutz Schweikhard. Static-mirror ion capture and time focusing for electrostatic ion-beam traps and multi-reflection time-of-flight mass analyzers by use of an in-trap potential lift. *International Journal of Mass Spectrometry*, 313:8–14, 3 2012. doi:[10.1016/j.ijms.2011.12.006](https://doi.org/10.1016/j.ijms.2011.12.006).
- [142] D. Zajfman, D. Strasser, O. Heber, S. Goldberg, A. Diner, and M.L. Rappaport. Dynamics of stored ions in an electrostatic ion beam trap. *Nuclear Instruments and*

*Methods in Physics Research Section A: Accelerators, Spectrometers, Detectors and Associated Equipment*, 532(1-2):196–202, 10 2004. doi:[10.1016/j.nima.2004.06.045](https://doi.org/10.1016/j.nima.2004.06.045).

- [143] F. M. Maier, F. Buchinger, L. Croquette, P. Fischer, H. Heylen, F. Hummer, C. Kanitz, A. A. Kwiatkowski, V. Lagaki, S. Lechner, E. Leistenschneider, G. Neyens, P. Plattner, A. Roitman, M. Rosenbusch, L. Schweikhard, S. Sels, M. Vilen, F. Wienholtz, and S. Malbrunot-Ettenauer. Increased Beam Energy as a Pathway Towards a Highly Selective and High-Flux MR-ToF Mass Separator. *Accepted to Nucl. Instr. Meth. A*, 2023.
- [144] St. Becker, G. Bollen, F. Kern, H.-J. Kluge, R.B. Moore, G. Savard, L. Schweikhard, and H. Stolzenberg. Mass measurements of very high accuracy by time-of-flight ion cyclotron resonance of ions injected into a penning trap. *International Journal of Mass Spectrometry and Ion Processes*, 99:53–77, 10 1990. URL: <https://linkinghub.elsevier.com/retrieve/pii/016811769085021S>, doi:[10.1016/0168-1176\(90\)85021-S](https://doi.org/10.1016/0168-1176(90)85021-S).
- [145] H. Stolzenberg, St. Becker, G. Bollen, F. Kern, H.-J. Kluge, Th. Otto, G. Savard, L. Schweikhard, G. Audi, and R. B. Moore. Accurate mass determination of short-lived isotopes by a tandem Penning-trap mass spectrometer. *Physical Review Letters*, 65:3104–3107, 12 1990. URL: <https://link.aps.org/doi/10.1103/PhysRevLett.65.3104>, doi:[10.1103/PhysRevLett.65.3104](https://doi.org/10.1103/PhysRevLett.65.3104).
- [146] F. Herfurth, J. Dilling, A. Kellerbauer, G. Bollen, S. Henry, H.-J. Kluge, E. Lamour, D. Lunney, R.B. Moore, C. Scheidenberger, S. Schwarz, G. Sikler, and J. Szerypo. A linear radiofrequency ion trap for accumulation, bunching, and emittance improvement of radioactive ion beams. *Nuclear Instruments and Methods in Physics Research Section A: Accelerators, Spectrometers, Detectors and Associated Equipment*, 469(2):254–275, 2001. URL: <https://www.sciencedirect.com/science/article/pii/S0168900201001681>, doi:[10.1016/S0168-9002\(01\)00168-1](https://doi.org/10.1016/S0168-9002(01)00168-1).
- [147] R. N. Wolf, D. Beck, K. Blaum, Ch Böhm, Ch Borgmann, M. Breitenfeldt, F. Herfurth, A. Herlert, M. Kowalska, S. Kreim, D. Lunney, S. Naimi, D. Neidherr, M. Rosenbusch, L. Schweikhard, J. Stanja, F. Wienholtz, and K. Zuber. On-line separation of short-lived nuclei by a multi-reflection time-of-flight device. *Nuclear Instruments and Methods in Physics Research Section A: Accelerators, Spectrometers, Detectors and Associated Equipment*, 686:82–90, 9 2012. doi:[10.1016/J.NIMA.2012.05.067](https://doi.org/10.1016/J.NIMA.2012.05.067).
- [148] Robert N. Wolf, Gerrit Marx, Marco Rosenbusch, and Lutz Schweikhard. Static-mirror ion capture and time focusing for electrostatic ion-beam traps and multi-reflection time-of-flight mass analyzers by use of an in-trap potential lift. *International Journal of Mass Spectrometry*, 313:8–14, 2012. URL: <https://www.sciencedirect.com/science/article/pii/S1387380611004775>, doi:[10.1016/j.ijms.2011.12.006](https://doi.org/10.1016/j.ijms.2011.12.006).
- [149] F. Wienholtz, S. Kreim, M. Rosenbusch, L. Schweikhard, and R. N. Wolf. Mass-selective ion ejection from multi-reflection time-of-flight devices via a

- pulsed in-trap lift. *International Journal of Mass Spectrometry*, 421:285–293, 2017. URL: <https://www.sciencedirect.com/science/article/pii/S1387380617301987>, doi:10.1016/j.ijms.2017.07.016.
- [150] H. Raimbault-Hartmann, D. Beck, G. Bollen, M. König, H.-J. Kluge, E. Schark, J. Stein, S. Schwarz, and J. Szerypo. A cylindrical Penning trap for capture, mass selective cooling, and bunching of radioactive ion beams. *Nuclear Instruments and Methods in Physics Research Section B: Beam Interactions with Materials and Atoms*, 126(1):378–382, 1997. International Conference on Electromagnetic Isotope Separators and Techniques Related to Their Applications. URL: <https://www.sciencedirect.com/science/article/pii/S0168583X96010671>, doi:10.1016/S0168-583X(96)01067-1.
- [151] H. Schnatz, G. Bollen, P. Dabkiewicz, P. Egelhof, F. Kern, H. Kalinowsky, L. Schweikhard, H. Stolzenberg, and H.-J. Kluge. In-flight capture of ions into a penning trap. *Nuclear Instruments and Methods in Physics Research Section A: Accelerators, Spectrometers, Detectors and Associated Equipment*, 251:17–20, 10 1986. URL: <https://linkinghub.elsevier.com/retrieve/pii/0168900286911459>, doi:10.1016/0168-9002(86)91145-9.
- [152] D. Beck, K. Blaum, G. Bollen, P. Delahaye, S. George, C. Guénaut, F. Herfurth, A. Herlert, D. Lunney, L. Schweikhard, and C. Yazidjian. Electric and magnetic field optimization procedure for Penning trap mass spectrometers. *Nuclear Instruments and Methods in Physics Research Section A: Accelerators, Spectrometers, Detectors and Associated Equipment*, 598(2):635–641, 1 2009. doi:10.1016/j.nima.2008.09.019.
- [153] A. Kellerbauer, K. Blaum, G. Bollen, F. Herfurth, H. J. Kluge, M. Kuckein, E. Sauvan, C. Scheidenberger, and L. Schweikhard. From direct to absolute mass measurements: A study of the accuracy of ISOLTRAP. *European Physical Journal D*, 22(1):53–64, 1 2003. doi:10.1140/epjd/e2002-00222-0.
- [154] D. Fink, J. Barea, D. Beck, K. Blaum, Ch Böhm, Ch Borgmann, M. Breitenfeldt, F. Herfurth, A. Herlert, J. Kotila, M. Kowalska, S. Kreim, D. Lunney, S. Naimi, M. Rosenbusch, S. Schwarz, L. Schweikhard, F. Šimkovic, J. Stanja, and K. Zuber. Q value and half-lives for the double- $\beta$ decay nuclide Pd110. *Physical Review Letters*, 108(6):062502, 2 2012. URL: <https://journals-aps-org.ezproxy.cern.ch/prl/abstract/10.1103/PhysRevLett.108.062502>, doi:10.1103/PHYSREVLETT.108.062502/FIGURES/3/MEDIUM.
- [155] Ch. Schweiger, C. M. König, J. R. Crespo López-Urrutia, M. Door, H. Dorrer, Ch. E. Düllmann, S. Eliseev, P. Filianin, W. Huang, K. Kromer, P. Micke, M. Müller, D. Renisch, A. Rischka, R. X. Schüssler, and K. Blaum. Production of highly charged ions of rare species by laser-induced desorption inside an electron beam ion trap. *Review of Scientific Instruments*, 90(12):123201, 12 2019. URL: <https://aip.scitation.org/doi/abs/10.1063/1.5128331>, doi:10.1063/1.5128331.
- [156] A. Rischka, H. Cakir, M. Door, P. Filianin, Z. Harman, W. J. Huang, P. Indelicato, C. H. Keitel, C. M. König, K. Kromer, M. Müller, Y. N. Novikov,

- R. X. Schüssler, Ch. Schweiger, S. Eliseev, and K. Blaum. Mass-Difference Measurements on Heavy Nuclides with an  $eV/c^2$  Accuracy in the PENTATRAP Spectrometer. *Physical Review Letters*, 124(11):113001, 3 2020. URL: <https://journals.aps.org/prl/abstract/10.1103/PhysRevLett.124.113001>, doi: 10.1103/PHYSREVLETT.124.113001/FIGURES/2/MEDIUM.
- [157] M. Lindinger, St. Becker, G. Bollen, K. Dasgupta, R. Jertz, H.-J. Kluge, L. Schweikhard, M. Vogel, and K. Lützenkischen. Cluster isobars for high-precision mass spectrometry. *Zeitschrift für Physik D Atoms, Molecules and Clusters*, 20(1):441–443, Mar 1991. doi:10.1007/BF01544032.
- [158] K. Blaum, G. Bollen, F. Herfurth, A. Kellerbauer, H.-J. Kluge, M. Kuckein, E. Sauvan, C. Scheidenberger, and L. Schweikhard. Carbon clusters for absolute mass measurements at ISOLTRAP. *The European Physical Journal A*, 15(1):245–248, Sep 2002. doi:10.1140/epja/i2001-10262-4.
- [159] K. Blaum, G. Huber, H.-J. Kluge, and L. Schweikhard. Laser desorption/ionization cluster studies for calibration in mass spectrometry. *The European Physical Journal D - Atomic, Molecular, Optical and Plasma Physics*, 24(1):145–148, Jun 2003. doi:10.1140/epjd/e2003-00131-8.
- [160] A. Kellerbauer, K. Blaum, G. Bollen, F. Herfurth, H.-J. Kluge, M. Kuckein, E. Sauvan, C. Scheidenberger, and L. Schweikhard. Carbon Cluster Ions For a Study of the Accuracy of ISOLTRAP. *Hyperfine Interactions*, 146:307–312, 2003. doi:10.1007/978-94-007-0946-1\\_47.
- [161] C. Scheidenberger, G. Bollen, F. Herfurth, A. Kellerbauer, H.-J. Kluge, M. Koizumi, S. Schwarz, and L. Schweikhard. Production and trapping of carbon clusters for absolute mass measurements at ISOLTRAP. *Nuclear Physics A*, 701:574–578, 2002. doi:10.1016/S0375-9474(01)01647-5.
- [162] Vuk Uskoković. A historical review of glassy carbon: Synthesis, structure, properties and applications. *Carbon Trends*, 5:100116, 10 2021. doi:10.1016/J.CARTRE.2021.100116.
- [163] Paul Fischer and Lutz Schweikhard. Disentangling polycationic fullerenes produced from glassy carbon with multireflection time-of-flight mass spectrometry. *Phys. Rev. Res.*, 4:043187, Dec 2022. URL: <https://link.aps.org/doi/10.1103/PhysRevResearch.4.043187>, doi:10.1103/PhysRevResearch.4.043187.
- [164] F. Wienholtz, K. Blaum, J. Kartheim, D. Lunney, S. Malbrunot-Ettenauer, V. Manea, M. Mougeot, L. Schweikhard, T. Steinsberger, and R. N. Wolf. Improved stability of multi-reflection time-of-flight mass spectrometers through passive and active voltage stabilization. *Nuclear Instruments and Methods in Physics Research Section B: Beam Interactions with Materials and Atoms*, 463:348–356, 1 2020. doi:10.1016/J.NIMB.2019.04.061.
- [165] Paul Fischer and Lutz Schweikhard. Multiple active voltage stabilizations for multi-reflection time-of-flight mass spectrometry. *Review of Scientific Instruments*,

- 92(6):063203, 6 2021. URL: <https://aip.scitation.org/doi/abs/10.1063/5.0050568>, doi:10.1063/5.0050568.
- [166] Lukas Nies. ISOLTRAP MR-ToF MS analysis software, GitHub repository. URL: <https://github.com/lnies/lEval>.
- [167] Guido Van Rossum and Fred L. Drake. *Python 3 Reference Manual*. CreateSpace, Scotts Valley, CA, 2009.
- [168] Rene Brun and Fons Rademakers. ROOT — An object oriented data analysis framework. *Nuclear Instruments and Methods in Physics Research Section A: Accelerators, Spectrometers, Detectors and Associated Equipment*, 389(1-2):81–86, 4 1997. URL: <https://www.sciencedirect.com/science/article/pii/S016890029700048X>, doi:10.1016/S0168-9002(97)00048-X.
- [169] Paul Fischer, Stefan Knauer, Gerrit Marx, and Lutz Schweikhard. Non-isobaric time-of-flight correction for isobar resolving in MR-ToF mass spectrometry. *International Journal of Mass Spectrometry*, 432:44–51, 9 2018. doi:10.1016/j.ijms.2018.07.004.
- [170] Samuel Ayet San Andrés, Christine Hornung, Jens Ebert, Wolfgang R. Plaß, Timo Dickel, Hans Geissel, Christoph Scheidenberger, Julian Bergmann, Florian Greiner, Emma Haettner, Christian Jesch, Wayne Lippert, Israel Mardor, Ivan Miskun, Zygmunt Patyk, Stephane Pietri, Alexander Pihktelev, Sivaji Purushothaman, Moritz P. Reiter, Ann-Kathrin Rink, Helmut Weick, Mikhail I. Yavor, Soumya Bagchi, Volha Charviakova, Paul Constantin, Marcel Diwisch, Andrew Finlay, Satbir Kaur, Ronja Knöbel, Johannes Lang, Bo Mei, Iain D. Moore, Jan-Hendrik Otto, Ilkka Pohjalainen, Andrej Prochazka, Christophe Rappold, Maya Takechi, Yoshiki K. Tanaka, John S. Winfield, and Xiaodong Xu. High-resolution, accurate multiple-reflection time-of-flight mass spectrometry for short-lived, exotic nuclei of a few events in their ground and low-lying isomeric states. *Physical Review C*, 99(6):064313, 6 2019. doi:10.1103/PhysRevC.99.064313.
- [171] M. Rosenbusch, S. Kemnitz, R. Schneider, L. Schweikhard, R. Tschiersch, and R. N. Wolf. Towards systematic investigations of space-charge phenomena in multi-reflection ion traps. *AIP Conf. Proc.*, 1521(1):53–62, 03 2013. doi:10.1063/1.4796061.
- [172] Wouter Verkerke and David Kirkby. The RooFit toolkit for data modeling. *arXiv:physics/0306116 [physics.data-an]*, 2003. URL: <https://arxiv.org/abs/physics/0306116>, arXiv:physics/0306116, doi:10.48550/arXiv.physics/0306116.
- [173] S. Purushothaman, S. Ayet San Andrés, J. Bergmann, T. Dickel, J. Ebert, H. Geissel, C. Hornung, W. R. Plaß, C. Rappold, C. Scheidenberger, Y. K. Tanaka, and M. I. Yavor. Hyper-EMG: A new probability distribution function composed of Exponentially Modified Gaussian distributions to analyze asymmetric peak shapes in high-resolution time-of-flight mass spectrometry. *International Journal of Mass Spectrometry*, 421:245–254, 10 2017. doi:10.1016/J.IJMS.2017.07.014.

- [174] X.F. Yang, S.J. Wang, S.G. Wilkins, and R.F. Garcia Ruiz. Laser spectroscopy for the study of exotic nuclei. *Progress in Particle and Nuclear Physics*, 129:104005, 3 2023. doi:[10.1016/j.ppnp.2022.104005](https://doi.org/10.1016/j.ppnp.2022.104005).
- [175] R. Neugart, J. Billowes, M. L. Bissell, K. Blaum, B. Cheal, K. T. Flanagan, G. Neyens, W. Nörtershäuser, and D. T. Yordanov. Collinear laser spectroscopy at ISOLDE: new methods and highlights. *Journal of Physics G: Nuclear and Particle Physics*, 44:064002, 4 2017. URL: <https://iopscience.iop.org/article/10.1088/1361-6471/aa6642><https://iopscience.iop.org/article/10.1088/1361-6471/aa6642/meta>, doi:[10.1088/1361-6471/AA6642](https://doi.org/10.1088/1361-6471/AA6642).
- [176] D. Winzen, V. Hannen, M. Bussmann, A. Buß, C. Egelkamp, L. Eidam, Z. Huang, D. Kiefer, S. Klammes, Th. Kühl, M. Loeser, X. Ma, W. Nörtershäuser, H.-W. Ortjohann, R. Sánchez, M. Siebold, Th. Stöhlker, J. Ullmann, J. Vollbrecht, Th. Walther, H. Wang, Ch. Weinheimer, and D. F. A. Winters. Laser spectroscopy of the  $^2S_{1/2}-^2P_{1/2}$ ,  $^2P_{3/2}$  transitions in stored and cooled relativistic  $C^{3+}$  ions. *Scientific Reports*, 11(1):9370, Apr 2021. doi:[10.1038/s41598-021-88926-w](https://doi.org/10.1038/s41598-021-88926-w).
- [177] R. F. Garcia Ruiz, C. Gorges, M. Bissell, K. Blaum, W. Gins, H. Heylen, K. Koenig, S. Kaufmann, M. Kowalska, J. Krämer, P. Lievens, S. Malbrunot-Ettenauer, R. Neugart, G. Neyens, W. Nörtershäuser, D. T. Yordanov, and X. F. Yang. Development of a sensitive setup for laser spectroscopy studies of very exotic calcium isotopes. *Journal of Physics G: Nuclear and Particle Physics*, 44:044003, 4 2017. doi:[10.1088/1361-6471/aa5a24](https://doi.org/10.1088/1361-6471/aa5a24).
- [178] R. Neugart, W. Klempt, and K. Wendt. Collisional ionization as a sensitive detection scheme in collinear laser-fast-beam spectroscopy. *Nuclear Instruments and Methods in Physics Research Section B: Beam Interactions with Materials and Atoms*, 17:354–359, 11 1986. doi:[10.1016/0168-583X\(86\)90125-4](https://doi.org/10.1016/0168-583X(86)90125-4).
- [179] K. Marinova, W. Geithner, M. Kowalska, K. Blaum, S. Kappertz, M. Keim, S. Kloos, G. Kotrotsios, P. Lievens, R. Neugart, H. Simon, and S. Wilbert. Charge radii of neon isotopes across the *sd* neutron shell. *Phys. Rev. C*, 84:034313, Sep 2011. URL: <https://link.aps.org/doi/10.1103/PhysRevC.84.034313>, doi:[10.1103/PhysRevC.84.034313](https://doi.org/10.1103/PhysRevC.84.034313).
- [180] Judith A. Halstead and Robert R. Reeves. Determination of the lifetime of the mercury  $6^3P_1$  state. *Journal of Quantitative Spectroscopy and Radiative Transfer*, 28:289–296, 10 1982. doi:[10.1016/0022-4073\(82\)90029-2](https://doi.org/10.1016/0022-4073(82)90029-2).
- [181] Reinhard Heinke, Mia Au, Cyril Bernerd, Katerina Chrysalidis, Thomas E. Colosios, Valentin N. Fedosseev, Isabel Hendriks, Asar A.H. Jaradat, Magdalena Kaja, Tom Kieck, Tobias Kron, Ralitsa Mancheva, Bruce A. Marsh, Stefano Marzari, Sebastian Raeder, Sebastian Rothe, Dominik Studer, Felix Weber, and Klaus Wendt. First on-line application of the high-resolution spectroscopy laser ion source PI-LIST at ISOLDE. *Nuclear Instruments and Methods in Physics Research Section B: Beam Interactions with Materials and Atoms*, 541:8–12, 8 2023. URL:

<https://linkinghub.elsevier.com/retrieve/pii/S0168583X23001945>, doi:  
10.1016/j.nimb.2023.04.057.

- [182] T.E. Cocolios, H.H. Al Suradi, J. Billowes, I. Budinčević, R.P. de Groote, S. De Schepper, V.N. Fedosseev, K.T. Flanagan, S. Franchoo, R.F. Garcia Ruiz, H. Heylen, F. Le Blanc, K.M. Lynch, B.A. Marsh, P.J.R. Mason, G. Neyens, J. Papuga, T.J. Procter, M.M. Rajabali, R.E. Rossel, S. Rothe, G.S. Simpson, A.J. Smith, I. Strashnov, H.H. Stroke, D. Verney, P.M. Walker, K.D.A. Wendt, and R.T. Wood. The Collinear Resonance Ionization Spectroscopy (CRIS) experimental setup at CERN-ISOLDE. *Nuclear Instruments and Methods in Physics Research Section B: Beam Interactions with Materials and Atoms*, 317:565–569, 12 2013. doi:10.1016/j.nimb.2013.05.088.
- [183] D. B. Newell, F. Cabiati, J. Fischer, K. Fujii, S. G. Karshenboim, H. S. Margolis, E. de Mirandés., P. J. Mohr, F. Nez, K. Pachucki, T. J. Quinn, B. N. Taylor, M. Wang, B. M. Wood, and Z. Zhang. The CODATA 2017 values of  $h$ ,  $e$ ,  $k$ , and  $N_A$  for the revision of the SI. *Metrologia*, 55:L13–L16, 4 2018. URL: <https://iopscience.iop.org/article/10.1088/1681-7575/aa950a>, doi:10.1088/1681-7575/aa950a.

## 7 Cumulative thesis articles

### 7.1 Author contributions

**Article I:** Charge radii, moments, and masses of mercury isotopes across the  $N = 126$  shell closure

T. Day Goodacre, A. V. Afanasjev, A. E. Barzakh, L. Nies, B. A. Marsh, S. Sels, U. C. Perera, P. Ring, F. Wienholtz, A. N. Andreyev, P. Van Duppen, N. A. Althubiti, B. Andel, D. Atanasov, R. S. Augusto, J. Billowes, K. Blaum, T. E. Cocolios, J. G. Cubiss, G. J. Farooq-Smith, D. V. Fedorov, V. N. Fedosseev, K. T. Flanagan, L. P. Gaffney, L. Ghys, A. Gottberg, M. Huyse, S. Kreim, P. Kunz, D. Lunney, K. M. Lynch, V. Manea, Y. Martinez Palenzuela, T. M. Medonca, P. L. Molkanov, M. Mougeot, J. P. Ramos, M. Rosenbusch, R. E. Rossel, S. Rothe, L. Schweikhard, M. D. Seliverstov, P. Spagnoletti, C. Van Beveren, M. Veinhard, E. Verstraelen, A. Welker, K. Wendt, R. N. Wolf, A. Zadornaya, and K. Zuber

Phys. Rev. C **104**, 054322 (2021)

<https://doi.org/10.1103/PhysRevC.104.054322>

The experiment was performed by T.D.G., A.E.B., B.A.M., S.S., F.W., A.N.A., P.V.D., N.A.A., B.A., D.A., J.B., T.E.C., J.G.C., G.J.F.-S., D.V.F., V.N.F., K.T.F., L.P.G., L.G., M.H., D.L., K.M.L., V.M., Y.M.P., T.M.M., P.L.M., J.P.R., M.R., R.E.R., S.R., M.D.S., P.S., C.V.B., M.V., E.V., A.W., R.N.W., and A.Z. The data was analyzed by T.D.G., A.V.A., A.E.B., L.N., and F.W. The manuscript was prepared by T.D.G., A.V.A., A.E.B., L.N., and F.W. Funding and supervision were provided by K.B., L.S., K.W., and K.Z. The manuscript was edited by all co-authors.

**Article II:** Isomeric excitation energy for  $^{99}\text{In}^m$  from mass spectrometry reveals constant trend next to doubly magic  $^{100}\text{Sn}$

L. Nies, D. Atanasov, M. Athanasakis-Kaklamanakis, M. Au, K. Blaum, J. Dobaczewski, J. Kartheim, I. Kulikov, Yu. A. Litvinov, D. Lunney, V. Manea, T. Miyagi, M. Mougeot, L. Schweikhard, A. Schwenk, K. Sieja, and F. Wienholtz

Phys. Rev. Lett. **131** 022502 (2023)

<https://doi.org/10.1103/PhysRevLett.131.022502>

The experiment was conducted by M.A.-K., M.Au, D.A., K.B., I.K., Yu.A.L., D.L., V.M., M.M., L.N., and F.W. The theoretical calculations were performed by J.D., T.M., A.S., and K. S. The manuscript was prepared by L.N., and was edited by all co-authors.

**Article III:** Shape coexistence in  $^{79}\text{Zn}^m$  near doubly-magic  $^{78}\text{Ni}$  confirmed

L. Nies, L. Canete, D. D. Dao, Giraud, A. Kankainen, D. Lunney, F. Nowacki, B. Bastin, M. Stryczyk, P. Ascher, K. Blaum, R. B. Cakirli, T. Eronen, P. Fischer, M. Flayol, V. Girard Alcindor, A. Herlert, A. Jokinen, A. Khanam, U. Köster, D. Lange, I. D. Moore, M. Müller, M. Mougeot, D.A. Nesterenko, F. de Oliveira, H. Penttilä, C. Petrone, I.

Pohjalainen, A. De Roubin, V. Rubchenya, Ch. Schweiger, L. Schweikhard, M. Vilen, and J. Äystö, submitted (2023)

The JYFLTRAP experiment was conducted by L.C, S.G, A.K, B.B, P.A, T.E, V.G.A., A.J., A.K, I.D.M, D.A.N, F.D.O., H.P., C.P., I.P., A.D.R., V.R., M.V., and J.Ä. The ISOLTRAP experiment was conducted by L.N., R.B.C., P.F., M.F., A.H., D.La., M.Mü., M.M., Ch.S., and was conceived by U.K. The theoretical calculations were performed by D.D.D. and F.N. Funding and supervision were provided, in parts, by K.B. and L.S. The Manuscript was prepared by L.N., D.D.D., A.K., D.Lu., F.N., and M.S. All authors contributed to the editing of the manuscript.

Confirmed by:

Genf, den

Lukas Nies

Greifswald, den

Lutz Schweikhard

## 7.2 Charge radii, moments, and masses of mercury isotopes across the $N = 126$ shell closure



# Charge radii, moments, and masses of mercury isotopes across the $N = 126$ shell closure

T. Day Goodacre<sup>1,2,3,\*</sup>, A. V. Afanasjev<sup>4</sup>, A. E. Barzakh<sup>5</sup>, L. Nies<sup>2,6</sup>, B. A. Marsh<sup>2</sup>, S. Sels<sup>2,7</sup>, U. C. Perera<sup>4</sup>, P. Ring<sup>8</sup>, F. Wienholtz<sup>2,6,†</sup>, A. N. Andreyev<sup>9,10</sup>, P. Van Duppen<sup>7</sup>, N. A. Althubiti<sup>1,11</sup>, B. Andel<sup>7,12</sup>, D. Atanasov<sup>13,‡</sup>, R. S. Augusto<sup>3</sup>, J. Billowes<sup>1</sup>, K. Blaum<sup>13</sup>, T. E. Cocolios<sup>1,7</sup>, J. G. Cubiss<sup>9</sup>, G. J. Farooq-Smith<sup>1,7,§</sup>, D. V. Fedorov<sup>13,¶</sup>, V. N. Fedosseev<sup>2</sup>, K. T. Flanagan<sup>1,14</sup>, L. P. Gaffney<sup>7,15,||</sup>, L. Ghys<sup>7,16</sup>, A. Gottberg<sup>3,17</sup>, M. Huyse<sup>7</sup>, S. Kreim<sup>2,13</sup>, P. Kunz<sup>3,18</sup>, D. Lunney<sup>19,¶</sup>, K. M. Lynch<sup>1,2</sup>, V. Manea<sup>13,¶</sup>, Y. Martinez Palenzuela<sup>2,7</sup>, T. M. Medonca<sup>2</sup>, P. L. Molkanov<sup>5</sup>, M. Mougeot<sup>2</sup>, J. P. Ramos<sup>2,\*\*</sup>, M. Rosenbusch<sup>6,††</sup>, R. E. Rossel<sup>2,20</sup>, S. Rothe<sup>2</sup>, L. Schweikhard<sup>6</sup>, M. D. Seliverstov<sup>5</sup>, P. Spagnoletti<sup>15</sup>, C. Van Beveren<sup>7</sup>, M. Veinhard<sup>2</sup>, E. Verstraelen<sup>7</sup>, A. Welker<sup>2,21</sup>, K. Wendt<sup>20</sup>, R. N. Wolf<sup>6,13,‡‡</sup>, A. Zadornaya<sup>7</sup> and K. Zuber<sup>21</sup>

<sup>1</sup>Department of Physics and Astronomy, School of Natural Science, The University of Manchester, Manchester M13 9PL, United Kingdom

<sup>2</sup>CERN, CH-1211 Geneva 23, Switzerland

<sup>3</sup>TRIUMF, Vancouver V6T 2A3, Canada

<sup>4</sup>Department of Physics and Astronomy, Mississippi State University, Mississippi 39762, USA

<sup>5</sup>Petersburg Nuclear Physics Institute, NRC Kurchatov Institute, Gatchina 188300, Russia

<sup>6</sup>Institut für Physik, Universität Greifswald, D-17487 Greifswald, Germany

<sup>7</sup>KU Leuven, Instituut voor Kern- en Stralingsfysica, B-3001 Leuven, Belgium

<sup>8</sup>Fakultät für Physik, Technische Universität München, D-85748 Garching, Germany

<sup>9</sup>Department of Physics, University of York, York, YO10 5DD, United Kingdom

<sup>10</sup>Advanced Science Research Center (ASRC), Japan Atomic Energy Agency (JAEA), Tokai-mura, Japan

<sup>11</sup>Physics Department, Faculty of Science, Jouf University, Aljouf, Saudi Arabia

<sup>12</sup>Department of Nuclear Physics and Biophysics, Comenius University in Bratislava, 84248 Bratislava, Slovakia

<sup>13</sup>Max-Planck-Institut für Kernphysik, Saupfercheckweg 1, D-69117 Heidelberg, Germany

<sup>14</sup>The Photon Science Institute, The University of Manchester, Manchester M13 9PL, United Kingdom

<sup>15</sup>School of Computing, Engineering, and Physical Sciences, University of the West of Scotland, Paisley PA1 2BE, United Kingdom

<sup>16</sup>Belgian Nuclear Research Center SCK CEN, Boeretang 200, B-2400 Mol, Belgium

<sup>17</sup>Department of Physics and Astronomy, University of Victoria, Victoria, British Columbia V8W 2Y2, Canada

<sup>18</sup>Department of Physics, Simon Fraser University, Burnaby, British Columbia V5A 1S6, Canada

<sup>19</sup>CSNSM-IN2P3, Université de Paris Sud, Orsay, France

<sup>20</sup>Institut für Physik, Johannes Gutenberg-Universität, D-55099 Mainz, Germany

<sup>21</sup>Institut für Kern- und Teilchenphysik, Technische Universität Dresden, Dresden D-01069, Germany



(Received 4 August 2021; accepted 20 October 2021; published 30 November 2021)

Combining laser spectroscopy in a Versatile Arc Discharge and Laser Ion Source (VADLIS) with Penning-trap mass spectrometry at the CERN-ISOLDE facility, this work reports on mean-square charge radii of neutron-rich mercury isotopes across the  $N = 126$  shell closure, the electromagnetic moments of  $^{207}\text{Hg}$ , and more precise mass values of  $^{206-208}\text{Hg}$ . The odd-even staggering (OES) of the mean square charge radii and the kink at

\*tdaygoodacre@triumf.ca

†Present address: Institut für Kernphysik, Technische Universität Darmstadt, D-64289 Darmstadt, Germany.

‡Present address: CERN, 1211, Geneva 23, Switzerland.

§Present address: Department of Oncology Physics, Edinburgh Cancer Centre, Western General Hospital, Edinburgh EH4 2XU, United Kingdom.

¶Present address: Department of Physics, University of Liverpool, Liverpool L69 7ZE, United Kingdom.

||Present address: Université Paris-Saclay, CNRS/IN2P3, IJCLab, 91405 Orsay, France.

\*\*Present address: SCK CEN, Boeretang 200, 2400 Mol, Belgium.

††Present address: Wako Nuclear Science Center (WNSC), Institute of Particle and Nuclear Studies (IPNS), High Energy Accelerator Research Organization (KEK), Wako, Saitama 351-0198, Japan.

‡‡Present address: ARC Centre of Excellence for Engineered Quantum Systems, School of Physics, The University of Sydney, NSW 2006, Australia.

Published by the American Physical Society under the terms of the [Creative Commons Attribution 4.0 International](#) license. Further distribution of this work must maintain attribution to the author(s) and the published article's title, journal citation, and DOI.

$N = 126$  are analyzed within the framework of covariant density functional theory (CDFT), with comparisons between different functionals to investigate the dependence of the results on the underlying single-particle structure. The observed features are defined predominantly in the particle-hole channel in CDFT, since both are present in the calculations without pairing. However, the magnitude of the kink is still affected by the occupation of the  $\nu 1i_{11/2}$  and  $\nu 2g_{9/2}$  orbitals with a dependence on the relative energies as well as pairing.

DOI: [10.1103/PhysRevC.104.054322](https://doi.org/10.1103/PhysRevC.104.054322)

## I. INTRODUCTION

The kink in the relative mean square charge radii ( $\delta\langle r^2 \rangle$ ) at the  $N = 126$  shell closure has long been considered as a benchmark for testing theoretical calculations. Traditionally the lead isotopic chain was employed [1–5], but new experimental results in this region that reveal the systematics of other isotopic chains [6–9], mass measurements, and odd-even staggering (OES) in charge radii offer the opportunity to broaden this benchmark. The droplet model is unable to reproduce this kink because of the absence of single-particle degrees of freedom [10]. Early nonrelativistic mean field approaches were also incapable of reproducing a kink at  $^{208}\text{Pb}$  [11], while, conversely, relativistic mean field approaches were demonstrated to be successful in doing so [2].

Two alternative modifications were suggested to correct this deficiency in nonrelativistic models. The first relies on the modification of the spin-orbit interaction, either through a fitting procedure (see Refs. [3,12]) or via the introduction of a density dependence (see Refs. [13,14]). This leads to a reasonable reproduction of the experimental isotope shifts (see Refs. [3,15]). The second approach (employing so-called Fayans functionals) introduces gradient terms into the pairing and surface terms of the functional [4,16,17]. This significantly improves the general description of experimental data; however, discrepancies are still apparent in the lead and tin isotopic chains [18]. Moreover, pairing becomes a dominant contributor to the kink and OES [18], in contradiction with the results obtained in relativistic Hartree-Bogoliubov (RHB) calculations with the DD-ME2 functional and nonrelativistic Hartree-Fock-Bogoliubov (NR-HFB) calculations with the M3Py-P6a functional presented in Ref. [9].

This work is an in-depth follow-up to Ref. [9], which reported on the  $\delta\langle r^2 \rangle$  of mercury isotopes across  $N = 126$  and employed these results, together with existing lead data, to compare RHB and NR-HFB approaches. A new OES mechanism was additionally suggested, related to the staggering in the occupation of the different neutron orbitals in odd- and even- $A$  nuclei and facilitated by particle-vibration coupling (PVC) in odd- $A$  nuclei. Here we report on the magnetic-dipole and electric-quadrupole moments of  $^{207}\text{Hg}$ , new and improved mass measurements of  $^{206-208}\text{Hg}$ , and a detailed theoretical study within the RHB framework to better understand the kinks and OES in lead and mercury isotopes. Multiple state-of-the-art covariant energy density functionals (CEDFs) are employed (NL3\* [19], DD-PC1 [20], DD-ME2 [21], and DD-ME $\delta$  [22]) to assess the dependence of the theoretical results on the underlying single-particle structure. The global performance of these functionals in describing ground state properties such as masses and charge radii of even-even nuclei has been tested in Refs. [23,24].

This article is arranged as follows. The experimental techniques are presented in Sec. II. The radiogenic production of  $^{207,208}\text{Hg}$  in a molten lead target is discussed in Sec. III. Experimental results on mean square charge radii, magnetic-dipole and electric-quadrupole moments and masses are summarized in Sec. IV. The discussion of experimental results is presented in Sec. V. A theoretical formalism and theoretical analysis of the kinks and OES in charge radii are presented in Sec. VI, together with their dependence on the underlying single-particle structure and pairing and a comparison of experimental and calculated binding energies. Finally, we give a brief summary in Sec. VII.

## II. EXPERIMENTAL TECHNIQUE

The neutron-rich mercury isotopes were studied at the ISOLDE facility [25] as part of a wider experimental campaign which investigated both ends of the isotopic chain [9,26,27]. The mercury nuclei were produced using the Isotope Separator On-Line (ISOL) method [28,29] and studied via in-source resonance ionization spectroscopy [30,31] as depicted in Fig. 1(a).

A molten lead target (thickness 170 g/cm<sup>2</sup>) was bombarded with 1.4-GeV protons, resulting in a cocktail of reaction products which effused via a temperature controlled chimney [32] into the anode volume of a Versatile Arc Discharge and Laser Ion Source (VADLIS) [33]. The target and ion source were biased at 30 kV and laser light from the ISOLDE Resonance Ionization Laser Ion Source (RILIS) [34] was directed into the anode volume for multistep resonance ionization [35] of the mercury isotopes. A  $\{\lambda_1 | \lambda_2 | \lambda_3\} = \{254 \text{ nm} | 313 \text{ nm} | 532 \text{ nm}\}$  ionization scheme [36] was applied, with the first (254 nm) resonant transition used to investigate the hyperfine structure (hfs) and isotope shifts in the  $5d^{10}6s^2 \ ^1S_0 \rightarrow 5d^{10}6s6p \ ^3P_1^\circ$  atomic transition.

The ions were accelerated by the electric field resulting from the grounded extraction electrode depicted in Fig. 1(a) and Fig. 1(b) to form a 30-keV radioactive ion beam (RIB). The ISOLDE General Purpose Separator [25] was employed for mass separation before the RIB was directed to either a Faraday cup for direct ion current measurement or to the ISOLTRAP radio frequency quadrupole cooler-buncher (RFQ C-B) [37]. Downstream of the RFQ C-B, the RIB was injected into the Multi-Reflection Time-of-Flight Mass Spectrometer (MR-ToF MS) [38] for either isobaric separation and subsequent detection [39] or for mass measurements, either by measuring the time of flight of the ions [40] or by utilizing the downstream Penning traps [41].

The lead target–VADLIS combination was required to avoid the overwhelming isobaric francium contamination present on masses  $A = 207, 208$  when employing a standard

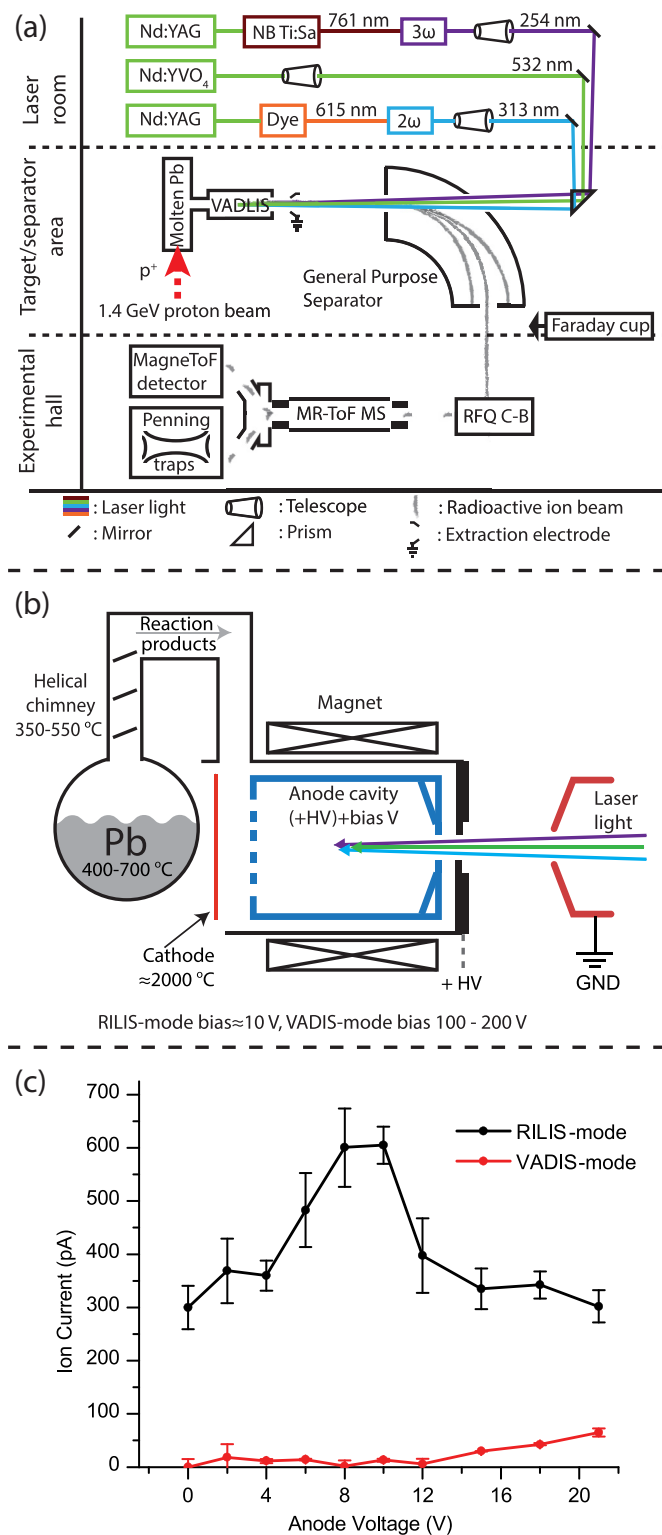


FIG. 1. (a) Overview of the experimental setup for the production and study of mercury isotopes. (b) Schematic of a VADLIS coupled to a molten lead target via a temperature controlled chimney. (c) The variation in the RILIS-mode and VADIS-mode ion currents on mass  $A = 197$  for differing anode bias voltages. See text for additional details and the definition of acronyms.

UC<sub>x</sub> target with a hot cavity surface ion source for the laser light-atom interaction region [42]. Alternative approaches

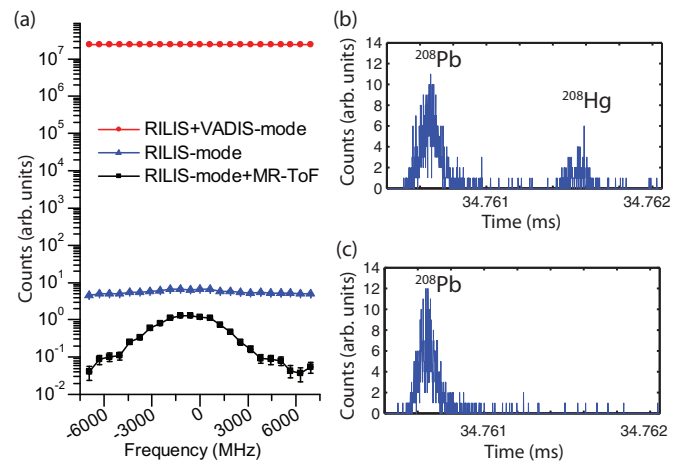


FIG. 2. (a) Ion rate on mass  $A = 208$  measured by the MR-ToF MS detector for a given frequency tripled laser frequency. The RILIS+VADIS-mode is dominated by VADIS ionized <sup>208</sup>Pb; the count rate was estimated based on Faraday cup measurements. Further discussion is in the text. (b) and (c) Time-of-flight spectra on mass  $A = 208$ , measured downstream of the MR-ToF MS with the VADLIS in RILIS-mode and the lasers on resonance and off-resonance, respectively. The y axis scales of (b) and (c) are identical.

have struggled to suppress certain isotopes of francium, and would additionally be expected to result in a factor of  $\approx 20$  reduction of the signal of interest [43,44].

A schematic of the VADLIS is presented in Fig. 1(b) together with the relative bias of the components. In the standard Versatile Arc Discharge Ion Source (VADIS)-mode of operation, atoms and molecules are ionized by electrons that are emitted from the  $\approx 2000$  °C cathode and accelerated into the anode volume by a relative anode voltage of 100–200 V [45]. The selective RILIS-mode of operation was employed for this experiment, where the anode voltage is optimized for laser-ion extraction while maintaining it below what is required for significant electron impact ionization [33]. Figure 1(c) presents the online optimization of the RILIS-mode with radiogenically produced <sup>197</sup>Hg. The RILIS-mode and VADIS-mode related signals were separated by blocking and unblocking the laser light exciting the 254-nm transition. A clear maximum is visible with a near-negligible background with the anode voltage set to  $\approx 8$  V. The alternative, applying the RILIS lasers with a 100–200 V anode bias (termed RILIS+VADIS-mode), would have resulted in significant isobaric contamination and a reduced signal-to-noise ratio as a result of the competing ionization processes.

The benefits of combining the RILIS-mode of operation with the ISOLTRAP MR-ToF MS are highlighted in Fig. 2(a). Operating in RILIS-mode reduced the isobaric <sup>208</sup>Pb background by seven orders of magnitude compared with RILIS+VADIS-mode. This enabled the MR-ToF MS to be employed for selective detection and for determining the mass of <sup>208</sup>Hg. Time-of-flight spectra recorded on and off resonance with the MR-ToF MS are shown in Figs. 2(b) and 2(c), respectively. By applying time gates in the ToF spectra, it was possible to separate the <sup>208</sup>Hg signal from the remaining isobaric contamination.

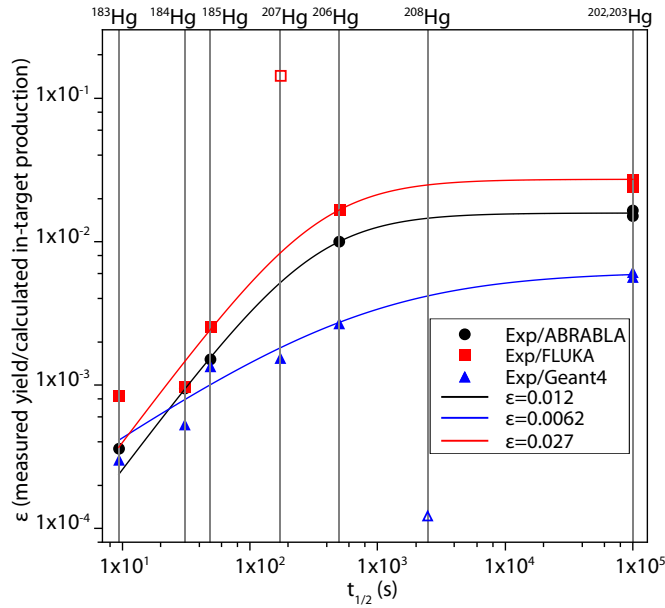


FIG. 3. Ionization and release efficiency ( $\epsilon$ ) as a function of the half-life of mercury isotopes from a molten lead target. The results from ABRABLA, FLUKA, and GEANT4 simulations are compared. See text for details.

### III. RADIOGENIC PRODUCTION OF $^{207,208}\text{Hg}$ IN A MOLTEN LEAD TARGET

Considering the natural lead ( $^{206-208}\text{Pb}$ ) target material used for this experiment, the creation of mercury isotopes with  $N \leq 126$  is comparatively well understood as the result of spallation reactions induced by the incident 1.4 GeV proton beam. However, when going beyond  $N = 126$  ( $^{206}\text{Hg}$ ) the production mechanism changes, and a range of other processes may become relevant [46,47] including secondary reactions induced by the light and energetic products of the primary spallation reactions. The production of  $^{207}\text{Hg}$  via  $^{208}\text{Pb}(n, 2p)^{207}\text{Hg}$  is a good example of such a process, and was first reported at an ISOL facility in Ref. [48]. The mechanism for producing  $^{208}\text{Hg}$  is significantly more exotic, as evidenced by a factor of 2400 decrease in the measured ion rate between  $^{207}\text{Hg}$  and  $^{208}\text{Hg}$ . There are a number of potential production channels including  $^{208}\text{Pb}(t, 3p)^{208}\text{Hg}$ ,  $^{208}\text{Pb}(\alpha, 4p)^{208}\text{Hg}$ , or reactions with radiogenically produced  $^{209}\text{Pb}$  ( $t_{1/2} \approx 3$  h) or  $^{210}\text{Pb}$  ( $t_{1/2} \approx 22$  y) which build up within the target during the experiment.

The in-target production of mercury isotopes was calculated via ABRABLA [49,50], FLUKA [51,52], and GEANT4 [53–55] simulations. The results are assessed by considering the isotope specific extraction and ionization efficiencies ( $\epsilon$ ), determined by dividing the measured yield by the calculated in-target production. Figure 3 presents the relationship between  $\epsilon$  and half-life for the mercury isotopes measured with the MR-ToF MS during this experimental campaign. For  $^{202}\text{Hg}$  (stable) and  $^{203}\text{Hg}$  ( $t_{1/2} \approx 47$  days) the half-lives are set at  $1 \times 10^5$  s to facilitate their inclusion. The data are fitted using Eq. (4) from Ref. [42], with the hollow data points omitted from the fits to enable them to converge.

As expected,  $\epsilon$  generally increases with increasing half-life, and stabilizes at a point where the half-life is sufficiently long compared to the release time.

All of the results broadly agree with an extraction and ionization efficiency of approximately 1% for sufficiently long-lived isotopes. ABRABLA [49] is not capable of reproducing the secondary reactions required for the production of  $^{207,208}\text{Hg}$ , however, as it is commonly used for calculating in-target production, it is useful for benchmarking the other codes for this application. FLUKA [52] was found to reproduce some  $^{207}\text{Hg}$  production, though based on Fig. 3 the rate appears to be underestimated. The GEANT4 (release 10.7) simulations employing the Liege (QGSP\_INCLXX\_HP) model [54] combined with the native deexcitation code were the most successful in reproducing both  $^{207}\text{Hg}$  and  $^{208}\text{Hg}$  production, though with an apparent overestimation of the latter. Discrepancies with the Geant4 results may be a consequence of the necessity to scale from the simulation of a reduced density target, which was required to enable a feasible simulation time.

While  $^{208}\text{Hg}$  production was not present in the FLUKA results, the simulations presented the possibility to investigate the  $^{208}\text{Pb}(t, 3p)^{208}\text{Hg}$  channel. The results for tritium production (using FLUKA 2021.0) were convoluted with cross-section data from TENDL17 [56] over a 40–200 MeV interval. This resulted in an in-target production rate of 110 atoms/ $\mu\text{C}$  for  $^{208}\text{Hg}$ , significantly below the estimated rate of  $\approx 56\,000$  atoms/ $\mu\text{C}$  calculated considering a 1% extraction and ionization efficiency. This suggests that  $^{208}\text{Pb}(t, 3p)^{208}\text{Hg}$  reactions only contribute to a fraction of the observed  $^{208}\text{Hg}$  yields. Based on this, we tentatively conclude that the observed  $^{208}\text{Hg}$  production is the result of a combination of multiple reaction channels.

### IV. EXPERIMENTAL RESULTS

#### A. Laser spectroscopy of mercury isotopes across $N = 126$

Mean square charge radii and magnetic-dipole and electric-quadrupole moments were studied via the measurement of isotope shifts and hfs in the 254-nm transition. Sample spectra are presented in Fig. 4(a), with the (substate weighted) centroids indicated with solid black lines.

Reference scans of  $^{198}\text{Hg}$  were taken periodically to monitor the stability of the experimental setup, with a 10 h interval. Multiple measurements of the hfs of each isotope were taken ( $2 \times ^{202,203}\text{Hg}$ ,  $3 \times ^{206,207}\text{Hg}$ ,  $5 \times ^{208}\text{Hg}$ ) and the fitting of the resulting spectra was cross-checked using multiple software packages: ORIGIN 2016 with a chi-squared minimization [57] performed with a Levenberg-Marquardt algorithm [58,59], the SATLAS open source Python package [60] and a similar program written in ROOT [61]. The results are presented in Table I, together with literature data ( $^{202,203,206}\text{Hg}$ ) for comparison. Relative mean square charge radii and magnetic-dipole and electric-quadrupole moments were extracted from the spectra by applying standard methods; these are summarized in Appendix A.

The nuclear spin of  $^{207}\text{Hg}$  could not be determined unambiguously because the spectroscopic transition is between

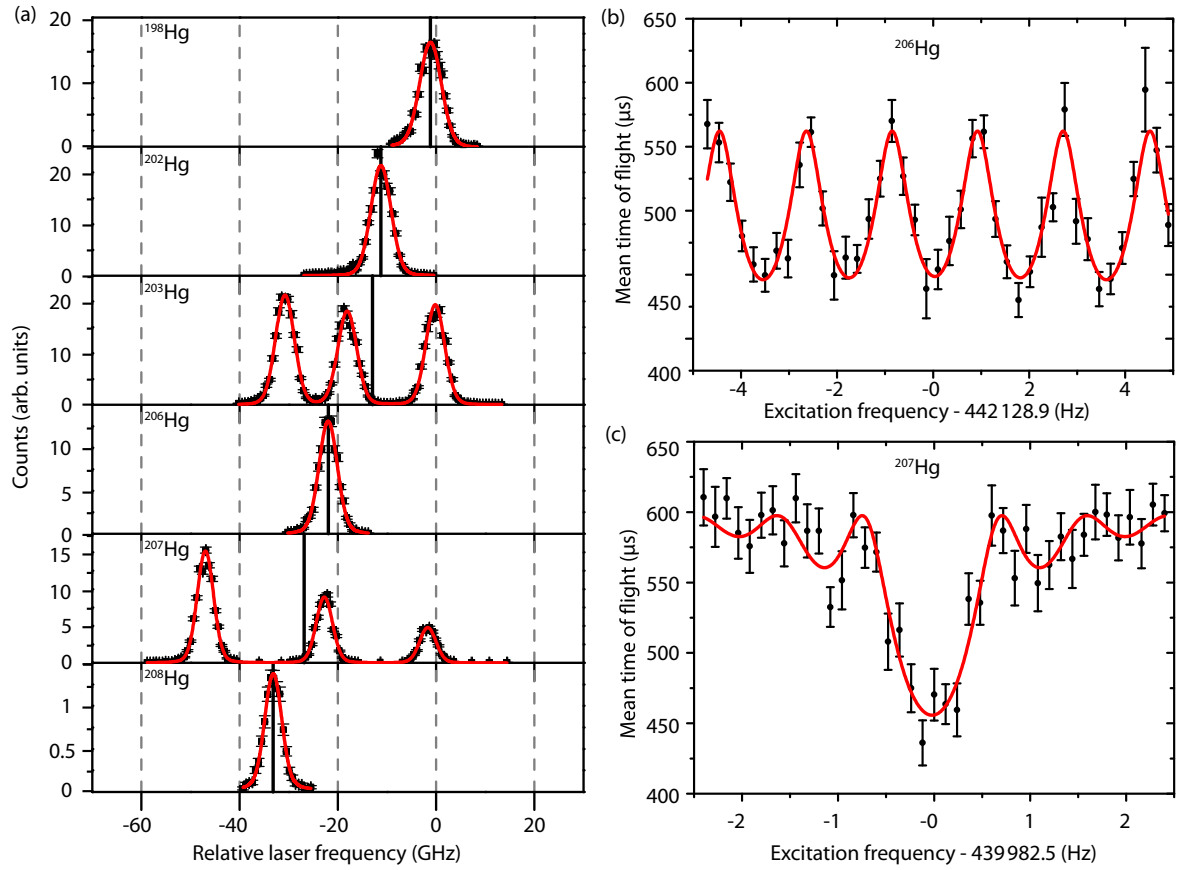


FIG. 4. (a) Hyperfine structure spectra of the measured isotopes; the (substate weighted) centroids are indicated with solid black lines. The y axis represents the number of “counts per shot” from the RFQ C-B. (b) and (c) Sample plots of the measured time-of-flight ion-cyclotron resonances. (b) Measurement of  $^{206}\text{Hg}$  using a Ramsey-type excitation scheme with an excitation time of  $2 \times 60$  ms separated by 480 ms. (c) Measurement of  $^{207}\text{Hg}$  using a single-pulse excitation scheme with an excitation time of 1.2 s.

atomic states with electronic spins  $J = 0$  and  $J = 1$ .  $I^\pi = 9/2^+$  was assumed for the analysis of the  $^{207}\text{Hg}$  measurements based on Refs. [48,64]. The extracted isotope shifts for  $^{202,203}\text{Hg}$  are in good agreement with literature. The same is true for the neutron deficient isotopes that were remeasured during this experimental campaign [26,27]. The 500-MHz discrepancy between the  $\delta\nu^{A,198}$  value of [65] and this work is discussed in [66]. The general agreement of the extracted

$\delta\nu^{A,198}$  and hyperfine  $a$  and  $b$  factors with the previously published literature values further validates the method of in-source resonance ionization spectroscopy with a VADLIS ion source.

### B. Mass spectrometry of $^{206-208}\text{Hg}$

The masses of  $^{206-208}\text{Hg}$  were measured, employing different techniques with respect to earlier experiments that are

TABLE I. Extracted isotope shifts in the 254-nm line with respect to  $^{198}\text{Hg}$ , hyperfine  $a$  and  $b$  factors of the  $5d^{10}6s6p\ ^3P_1^\circ$  state, and literature values recalculated from the compilations of [62,63]. The spin assignment of  $^{207}\text{Hg}$  is discussed in the text. Statistical uncertainties are listed in parentheses and the systematic uncertainties related to  $F_{254}$  and  $M$  are listed in curly brackets.

Isotope $A$	$I^\pi$	$\delta\nu^{A,198}$ (MHz)	$a$ (MHz)	$b$ (MHz)	$\delta\langle r^2 \rangle^{A,198}$ (fm <sup>2</sup> )	$\mu$ ( $\mu_N$ )	$Q_s$ ( $b$ )	Ref.
202	0	-10 100(180) -10 102.4(4.2)			0.197(3){14} 0.1973(2){152}			This work & [9] [62]
203	$5/2^-$	-11 870(200) -11 750(180)	5070(90) 4991.33(4)	-20(250) -249.2(3)	0.232(5){17} 0.2296(35){180}	0.843(15) 0.8300(7)	0.03(35) 0.40(4)	This work & [9] [62,63]
206	0	-20 930(160) -20 420(80)			0.409(3){30} 0.3987(16){308}			This work & [9] [62]
207	$(9/2^+)$	-25 790(190)	-4500(60)	530(250)	0.503(4){38}	-1.373(20)	-0.73(37)	This work & [9]
208	0	-32 030(160)			0.625(3){47}			This work & [9]

TABLE II. Mass-measurement results for the mercury isotopes, given either as the ratio  $R$  of cyclotron frequencies from ToF-ICR or as the  $C_{\text{ToF}}$  from the MR-ToF MS. The computed mass excess values  $M_{\text{exc}}$  from this work are compared to the literature values found in [67]. Additionally, half-lives  $T_{1/2}$  from [67] are given as well as the reference ions that were used to extract the mass values. The mass excesses are given in terms of energy divided by the square of the speed of light  $c_0$ .

Isotope	$T_{1/2}$ (min)	Ref. ions	$C_{\text{ToF}}$	$R$	$M_{\text{exc, ISOLTRAP}}$ (keV/ $c_0^2$ )	$M_{\text{exc, AME20}}$ (keV/ $c_0^2$ )	$ \Delta_{\text{TRAP-AME20}} $ (keV/ $c_0^2$ )
$^{206}\text{Hg}$	8.32(7)	$^{133}\text{Cs}^+$		1.549 807 228 2(661)	-20 932.1(82)	-20 946(20)	13(22)
$^{207}\text{Hg}$	2.9(2)	$^{133}\text{Cs}^+$		1.557 367 639 6(489)	-16 446.2(6.1)	-16 487(30)	41(31)
$^{208}\text{Hg}$	42(5)	$^{208}\text{Pb}^+$ , $^{133}\text{Cs}^+$	0.500 108 969(255)		-13 279(20)	-13 270(30)	9(36)

referenced in the AME2020 [67]. A short outline of the time-of-flight methods that were used in our experiment can be found in Appendix B. A summary of the measured values is presented in Table II and a comparison with the AME2020 is shown in Fig. 5.

The atomic mass of  $^{206}\text{Hg}$  was previously deduced from  $\alpha$ -decay measurements [68]. Our measurements of  $^{206}\text{Hg}$ , using the time-of-flight ion-cyclotron-resonance (ToF-ICR) technique, represent the first direct determination of the mass of this nucleus. For the ToF-ICR measurements in a Penning trap, two excitation schemes were employed: a single pulse excitation of 400 ms, as well as a Ramsey-type scheme [69], presented in Fig. 4(b), where two excitation pulses of 60 ms were applied, separated by a waiting time of 480 ms.

The masses of  $^{207}\text{Hg}$  and  $^{208}\text{Hg}$  have been determined previously by storage-ring measurements at GSI using Schottky mass spectrometry [70–72]. In the present experiment, ToF-ICR measurements were performed for  $^{207}\text{Hg}$  with a single-pulse excitation of 1.2 s [see Fig. 4(c)]. For  $^{208}\text{Hg}$ , the hyperfine structure was measured in five different laser scans, using ISOLTRAP’s MR-ToF MS as mass separator and ion counter. Mass data were extracted from the scans by summing individual binned data per scan step into a single histogram, resulting in one histogram per scan. The ToF distributions corresponding to singly charged ions of the isotope of interest,  $^{208}\text{Hg}^+$ , and to an online reference ion,  $^{208}\text{Pb}^+$ , were aligned as outlined in [73] and fitted by employing an unbinned maximum-likelihood estimation where the fit

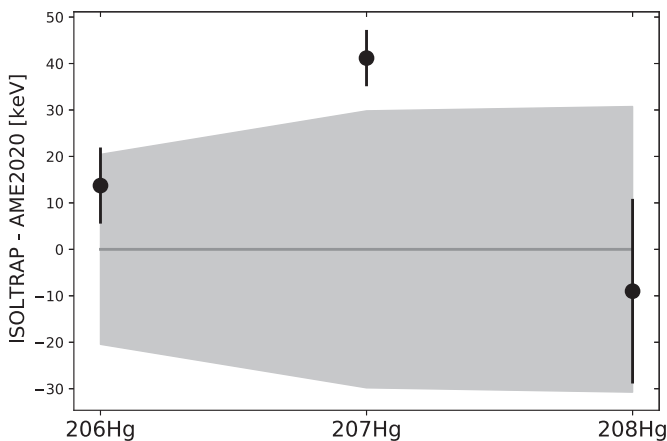


FIG. 5. Difference between the ISOLTRAP mass measurements of this work and the corresponding AME20 values (black), including the AME20 error band (grey).

function was constructed as an exponential-Gaussian hybrid (EGH) to account for the tails of the ToF distributions towards longer flight times. The mass was extracted by calculating the average  $C_{\text{ToF}}$  of the five scans, using the  $^{208}\text{Pb}^+$  present in the RIB and  $^{133}\text{Cs}^+$  from an offline ion source as reference ions. The results we report are in general agreement with the literature and improve upon the precision.

## V. DISCUSSION

### A. Magnetic moment of $^{207}\text{Hg}$

A value of  $g(^{207}\text{Hg}) = -0.305(6)$  was deduced based on the results presented in Table I. The  $g$  factors of the  $\nu g_{9/2}$  isotones  $^{209}\text{Pb}$  and  $^{211}\text{Po}$  are plotted in Fig. 6 together with the Schmidt value, the energies of the first excited  $2^+$  states  $[E(2^+)^{-2}]$  of the  $N = 126$  cores, and  $g(^{210}\text{Bi})$  calculated from the measured magnetic moments of the  $5^-$ ,  $7^-$ , and  $9^-$  isomeric states [74,75] using the additivity relation and assuming a pure  $[\pi h_{9/2} \otimes \nu g_{9/2}]$  configuration for these states. The inverse square of  $E(2^+)$  is of particular relevance due to its approximate proportionality to the second-order perturbation theory correction [76,77].

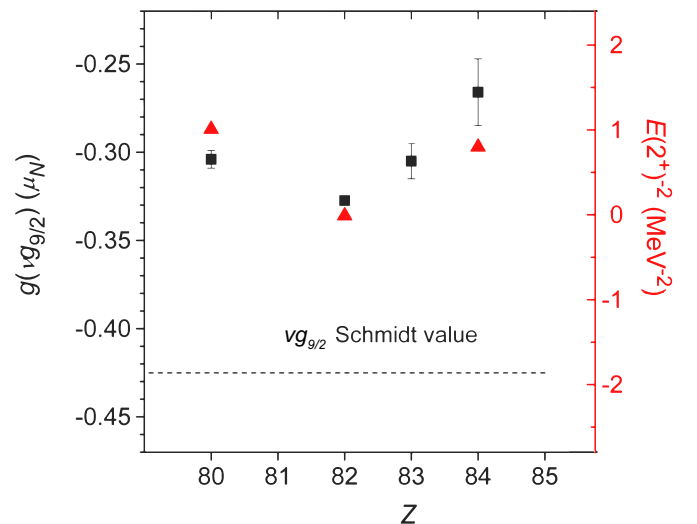


FIG. 6. Squares: experimental  $g$  factors for  $N = 127$  isotones ( $\nu g_{9/2}$  [74,75,78,79] and this work). The  $g$  factor of  $^{210}\text{Bi}$  is deduced from measurements of isomer states; see text for details. Dashed line shows the Schmidt value for the  $\nu g_{9/2}$  shell. Triangles:  $E(2^+)^{-2}$  values of the corresponding  $N = 126$  even-even nuclei (see the corresponding scale on the right-hand side of the figure) experimental data from [80].

The experimentally determined  $g$  factors differ significantly from the Schmidt value  $g_{\text{Schmidt}} = -0.425$  and there is a noticeable  $Z$  dependence. The deviation of the  $g$  factor of the magic  $^{209}\text{Pb}$  isotope was explained in non relativistic [81,82] and relativistic [83] approaches by taking into account corrections for the meson exchange current and first- and second-order core polarization (CP). The configuration admixture contributing to the magnetic dipole moment in the first-order of perturbation theory corresponds to a particle-hole excitation from an orbit  $j = l + 1/2$  to its spin-orbit partner  $j = l - 1/2$  (CP1 correction [84]). In the second order of perturbation theory, the most important magnetic moment correction stems from the odd-particle coupling with the lowest  $2^+$  excitation of the core (CP2 correction [76,77]). In the vicinity of the doubly magic  $^{208}\text{Pb}$ , the most important  $Z$ -dependent CP1 correction corresponds to the proton  $(h_{11/2}^{-1}h_{9/2})$  particle-hole excitation. A corresponding increase in the occupancy of the  $\pi h_{9/2}$  orbital with the increase of  $Z$ , reduces the probability of proton  $(h_{11/2}^{-1}h_{9/2})$  core excitations, thereby decreasing the magnitude of the CP1 correction. The opposite is apparent in Fig. 6, where the deviation from the Schmidt value increases between  $^{209}_{82}\text{Pb}$  and  $^{211}_{84}\text{Po}$ , thus CP1 corrections do not appear to be the dominant driver for the  $g$ -factor  $Z$  dependence. Additionally, meson exchange corrections have been shown to have a weak  $A$  dependence in the vicinity of  $^{208}\text{Pb}$  [77,85]. It could then be suggested that CP2 corrections are primarily responsible for the  $Z$  dependence of the discrepancy with the Schmidt value.

The same mechanism (particle-quadrupole-vibration coupling) was used to explain the magnetic moment evolution in the vicinity of the magic numbers [76,77]. This explanation is supported by the apparent correspondence of the energies of the first excited  $2^+$  states of the  $N = 126$  cores and the  $g$  factors of the  $N = 127$  isotones in Fig. 6. Considering that  $E(2^+, ^{208}\text{Pb}) \approx 4.1$  MeV,  $E(2^+, ^{206}\text{Hg}) \approx 1.1$  MeV, and  $E(2^+, ^{210}\text{Po}) \approx 1.2$  MeV [80], the admixture of the  $(2^+, \nu i_{13/2})_{9/2+}$  should be larger for  $^{207}\text{Hg}$  and  $^{211}\text{Po}$  than for  $^{209}\text{Pb}$ , resulting in an increased CP2 correction. It is worth noting that this interpretation indicates the importance of particle-vibration coupling in the description of the ground-state properties of the odd- $A$  nuclei in the vicinity of shell closure. This same mechanism proves to be decisive for explanation of the charge radii behavior in this region of the chart of the nuclides (see Sec. VI).

### B. Quadrupole moment of $^{207}\text{Hg}$

Quadrupole moments near the closed proton and neutron shells have a predominantly single-particle nature and are usually well described by the shell-model formula:

$$Q = -e_{\text{eff}} \frac{2j-1}{2j+1} \langle r^2 \rangle_j, \quad (1)$$

where  $j$  is the spin of the odd particle,  $\langle r^2 \rangle_j$  is its mean square radius, and  $e_{\text{eff}}$  is an effective charge. Taking  $\langle r^2 \rangle_j$  from Ref. [86], one obtains  $e_{\text{eff}}(^{207}\text{Hg}; \nu 2g_{9/2}) = 2.4(13)e$ . This neutron effective charge is noticeably larger than the value of the “universal” neutron  $e_{\text{eff}} = 0.95e$  which describes fairly well the measured quadrupole moments for all closed-shell  $\pm 1$  nuclear states in the vicinity of  $^{208}\text{Pb}$  [87]. This points

to the rapid increase of a quadrupole core polarization when moving away from the magic  $Z = 82$ , similar to that observed for the proton  $e_{\text{eff}}$  when moving away from the magic  $N = 126$  [87].

## VI. THEORETICAL INTERPRETATION

### A. Theoretical framework and the details of the calculations

A theoretical interpretation of experimental data is performed within the framework of covariant density functional theory [88] using the RHB computer code for spherical nuclei first employed in Ref. [9]. This code enables the blocking of selected single-particle orbitals and allows for fully self-consistent calculations of the ground and excited states in even-even and odd- $A$  spherical nuclei. In the pairing channel, the RHB code employs a separable version of the Gogny pairing [89] with the pairing strength defined in Ref. [23].

Several restrictions/constraints are employed in the present paper. First, we consider only spherical nuclei, i.e., nuclei for which  $\langle \beta_2^2 \rangle^{1/2} < 0.1$  where  $\langle \beta_2^2 \rangle^{1/2}$  is the mean-square deformation deduced from experimental  $\delta \langle r^2 \rangle$  using the droplet model (see Refs. [90,91]). This restriction corresponds to  $N \geq 116$  and  $N \geq 121$  for lead and mercury isotopes, respectively, and it was already used in our earlier paper [9].

Second, two different procedures labeled as “LES” and “EGS” are used for the blocking in odd- $A$  nuclei, and the results of the respective calculations are labeled by these abbreviations. In the LES (lowest in energy solution) procedure, the lowest in energy configuration is used, which is similar to all earlier calculations of OES in nonrelativistic DFTs [4,17]. In the EGS (experimental ground state) procedure, the configuration with the spin and parity of the blocked state corresponding to those of the experimental ground state is employed, although it is not necessarily the lowest in energy. The need for this procedure is due to the following considerations. First, the nodal structure of the wave functions and neutron radius of the single-neutron orbital depend on its quantum numbers such as total and orbital angular momenta (see Refs. [3,5,92]). Thus, the occupation of different neutron single-particle states impacts the resulting charge radii (see Refs. [3,5] and the discussion of Fig. 7(a) below). Second, the structure of the experimental ground states in odd- $A$  nuclei is reproduced globally only in approximately 40% of the nuclei in the nonrelativistic and relativistic DFTs [93,94].<sup>1</sup>

If there is a mismatch in the structure of experimental and calculated ground states, the impact of the blocked orbital on the physical observable of interest (charge radius, deformations, binding, etc.) in odd- $A$  nuclei is expected to deviate from the value observed in experiment. The consequences of this mismatch exist for the deformations of one-quasiparticle states (see Ref. [94]), odd-even staggerings in charge radii (see Ref. [9]), and binding energies (see Ref. [97]). Note that the latter are used to define pairing indicators. In such a situation it is safer to use the blocked solution with the structure

<sup>1</sup>The inclusion of particle-vibrational coupling increases the accuracy of the description of the single-particle configurations in odd- $A$  nuclei (see Refs. [95,96]).

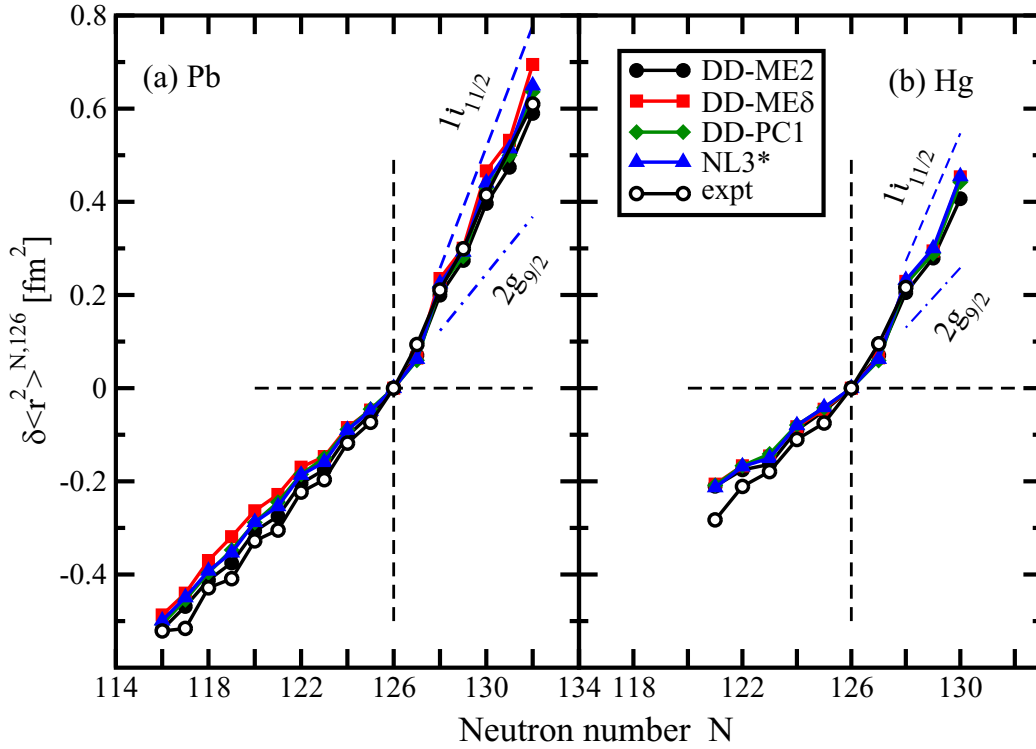


FIG. 7. The  $\delta \langle r^2 \rangle^{N,126}$  values of the Pb and Hg isotopes obtained in the RHB calculations with indicated CEDFs. The experimental data are taken from Refs. [9,62,78]. The  $\delta \langle r^2 \rangle^{N,126}$  values, obtained in the calculations with CEDF NL3\* without pairing under the condition that either only  $\nu 1i_{11/2}$  or only  $\nu 2g_{9/2}$  orbitals are occupied in the  $N > 126$  nuclei, are shown by blue dashed and dash-dotted lines, respectively.

corresponding to the experimental ground state (even if it leads to an excited solution) for the description of charge radii since a moderate shift in the energy of a single-particle state has negligible effect on its neutron single-particle rms radius  $\langle r^2 \rangle_{sp}$ .

### B. Charge radii and related indicators

The charge radii were calculated from the corresponding point proton radii as

$$r_{ch} = \sqrt{\langle r^2 \rangle + 0.64} \text{ fm}, \quad (2)$$

where  $\langle r^2 \rangle$  stands for the mean square radius of the proton density distribution and the factor 0.64 accounts for the finite size of the proton.

Three indicators are commonly used to facilitate the quantitative comparison of the experimental results with those from theoretical calculations. The first is differential mean-square charge radius,<sup>2</sup>

$$\delta \langle r^2 \rangle^{N,N'} = \langle r^2 \rangle(N) - \langle r^2 \rangle(N') = r_{ch}^2(N) - r_{ch}^2(N'), \quad (3)$$

where  $N'$  is the neutron number of the reference nucleus.

The second one is the  $\xi_{\text{even}}$  indicator

$$\xi_{\text{even}} = \frac{\delta \langle r^2 \rangle^{128,126}}{\delta \langle r^2 \rangle^{126,124}}, \quad (4)$$

<sup>2</sup>This quantity is frequently written as a function of mass number  $A$ . However, we prefer to define it as a function of neutron number  $N$  since this allows to see the behavior of the  $\delta \langle r^2 \rangle^{N,N'}$  curves at neutron shell closures for different isotopic chains.

introduced in Ref. [8,66]. It provides a quantitative measure of the change of the slope (i.e.,  $\delta \langle r^2 \rangle^{N,126}/\delta N$ ) of differential charge radii as a function of neutron number  $N$  at  $N = 126$ . The applicability of  $\xi_{\text{even}}$  is restricted by the limited availability of the data for the  $N = 128$  isotones because for  $84 \leq Z \leq 88$  they have half-lives ( $t_{1/2}$ )  $< 300 \mu\text{s}$  [98] which limits the potential for laser spectroscopy measurements. Thus, in these cases the  $\xi_{\text{even}}$  indicator is replaced by

$$\xi_{\text{even}}^* = \frac{2}{N_0 - 126} \frac{\delta \langle r^2 \rangle^{N_0,126}}{\delta \langle r^2 \rangle^{126,124}}, \quad (5)$$

where  $N_0$  is the lowest even neutron number at  $N > 126$  with measured isotopic shift:  $N_0 = 132$  for  $^{84}\text{Po}$  [6,99],  $^{85}\text{At}$  [100],  $^{86}\text{Rn}$  [90,101],  $^{87}\text{Fr}$  [102–104],  $^{88}\text{Ra}$  [105], and  $N_0 = 138$  for  $^{89}\text{Ac}$  [106]. For the  $^{82}\text{Pb}$  and  $^{83}\text{Bi}$  isotopes, the data for the nuclei with  $N = 124, 126, 128$  were taken from [78] and [8], respectively. Note that for the Bi and Pb isotopes, for which the  $N = 128$  data are available,  $\frac{2}{N_0-126} \delta \langle r^2 \rangle^{N_0,126} \approx \delta \langle r^2 \rangle^{128,126}$  ( $N_0 = 130$  for Bi and  $N_0 = 132$  for Pb) since differential radii increase nearly linearly for the  $N > 126$  nuclei under study.

The third is the three-point indicator

$$\begin{aligned} \Delta \langle r^2 \rangle^{(3)}(N) &= \frac{1}{2} [\langle r^2 \rangle(N-1) + \langle r^2 \rangle(N+1) - 2\langle r^2 \rangle(N)] \\ &= \frac{1}{2} [r_{ch}^2(N-1) + r_{ch}^2(N+1) - 2r_{ch}^2(N)] \end{aligned} \quad (6)$$

which quantifies OES in charge radii.

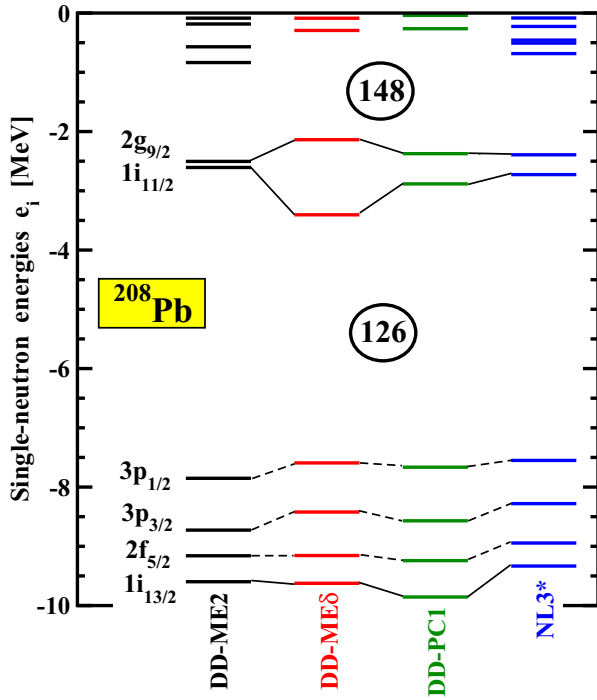


FIG. 8. The energies of neutron single-particle states at spherical shape in  $^{208}\text{Pb}$  obtained in the calculations without pairing with the indicated CEDFs. Solid and dashed connecting lines are used for positive- and negative-parity states. Spherical gaps are indicated.

### C. The kink in charge radii and its relation to underlying single-particle structure and pairing

The differential charge radii of the Pb and Hg isotopes are shown in Fig. 7. One can see that all of the employed CEDFs generate a kink at  $N = 126$  and that the best description is provided by the CEDF DD-ME2. Thus, it is important to understand which physical features determine the differences between the functionals. For that we look at the energies of the neutron single-particle states and their occupation probabilities.

The energies of neutron single-particle states obtained in the  $^{208}\text{Pb}$  nucleus with the employed CEDFs are shown in Fig. 8. One can see close similarities in the predictions of the energies and relative positions of the  $2f_{5/2}$ ,  $3p_{3/2}$ , and  $3p_{1/2}$  states occupied in the  $N \leq 126$  nuclei. In contrast, the differences are more pronounced for the  $1i_{11/2}$  and  $2g_{9/2}$  orbitals located above the  $N = 126$  shell closure. In all functionals, the  $1i_{11/2}$  orbital is the lowest in energy<sup>3</sup> but the energy gap between these two orbitals strongly depends on the functional. It is smallest in DD-ME2, gets larger in NL3\* and DD-PC1, and becomes extremely large in DD-ME $\delta$ . Because of this feature, and the fact that the kink in charge radii at  $N = 126$  is defined by the interplay of the occupation of these two orbitals, we focus our discussion on the  $N > 126$  nuclei.

Let us analyze the slope of differential radii defined as  $\delta\langle r^2 \rangle^{N,N'}/\delta N$ . Note that in such an analysis we consider only even-even nuclei. The results of the calculations without pairing indicate that this slope is almost the same for  $N < 126$ <sup>4</sup> and  $N > 126$  nuclei when only the  $2g_{9/2}$  states are occupied above  $N = 126$  [see Fig. 7(a) for Pb isotopes and Fig. 7(b) for Hg isotopes]. As a consequence, there would be either no kink or a very small kink in the charge radii at  $N = 126$ . However, the situation drastically changes when only  $1i_{11/2}$  states are occupied above  $N = 126$ . This leads to a substantial increase of the  $\delta\langle r^2 \rangle^{N,N'}/\delta N$  slope and as a result to a creation of large kink in the charge radii at  $N = 126$ . This is related to the fact that the neutron  $1i_{11/2}$  orbital is the  $n = 1$  orbital which overlaps more strongly with the majority of the proton orbitals than the  $n = 2$  neutron  $2g_{9/2}$  orbital [5]. As a consequence, it provides a larger pull of the  $1i_{11/2}$  neutron states on proton orbitals via the symmetry energy. This is despite the fact that in  $^{208}\text{Pb}$  the rms radius of the neutron  $1i_{11/2}$  orbital (for example,  $r_{\text{ch}} = 6.4131$  fm in DD-ME2) is smaller than that of the neutron  $2g_{9/2}$  one (for example,  $r_{\text{ch}} = 7.0227$  fm in DD-ME2) by  $\approx 0.6$  fm in all employed CEDFs.

The inclusion of pairing modifies the situation in the  $N > 126$  nuclei in such a way that both of these orbitals become partially occupied [see Fig. 9(a)]. Note that we consider a cumulative occupation probability  $v_{\text{state}}^2$  which provides information on the filling of a given  $j$  subshell:  $v_{\text{state}}^2$  could take any value between 0 (unoccupied subshell) and  $2j + 1$  (fully occupied  $j$  subshell). Pairing also leads to a partial occupation of the single-particle states located above the  $N = 148$  gap (see Fig. 8), but their occupation probabilities are relatively small because of the presence of this gap. Thus, for the sake of simplicity we focus our discussion on the interplay of the occupation of the  $2g_{9/2}$  and  $1i_{11/2}$  states and the consequences of this interplay on the  $\delta\langle r^2 \rangle^{N,N'}/\delta N$  slope.

The large energy gap of 1.27 MeV between the  $2g_{9/2}$  and  $1i_{11/2}$  states in the DD-ME $\delta$  functional (see Fig. 8) is responsible for a predominant occupation of the lower lying  $1i_{11/2}$  states [see Fig. 9(a)]. Considering the  $N = 134$  nucleus as an example, the eight neutrons outside of the  $N = 126$  shell closure are located almost entirely in the  $1i_{11/2}$  subshell ( $v_{1i_{11/2}}^2 \approx 7.1$ ) with only a small portion occupying  $2g_{9/2}$  ( $v_{2g_{9/2}}^2 \approx 0.5$ ).

This leads to a large  $\delta\langle r^2 \rangle^{N,N'}/\delta N$  slope (see Fig. 7). Note that this slope is the largest among the considered functionals and it is not far away from the one obtained in the calculations without pairing, when only the  $1i_{11/2}$  states are occupied in the nuclei with  $N > 126$  (see Fig. 7). The reduction of the gap between the  $2g_{9/2}$  and  $1i_{11/2}$  orbitals in the DD-PC1, NL3\* and, especially, DD-ME2 functionals [see Figs. 8 and 9(b)] is responsible for a decrease of the difference in the occupation of these orbitals (see Fig. 9). For these three functionals, the eight neutrons outside of the  $N = 126$  shell closure in the  $N = 134$  nucleus are still located predominantly in the  $1i_{11/2}$  subshell

<sup>3</sup>The order of these two orbitals is inverted in the majority of nonrelativistic functionals (see Refs. [3,5]) and in many of them this creates a problem in the description of the kink in charge radii at  $N = 126$ .

<sup>4</sup>The averaged slopes for the  $N < 126$  nuclei are almost the same in the calculations with and without pairing (see Ref. [92] for details).

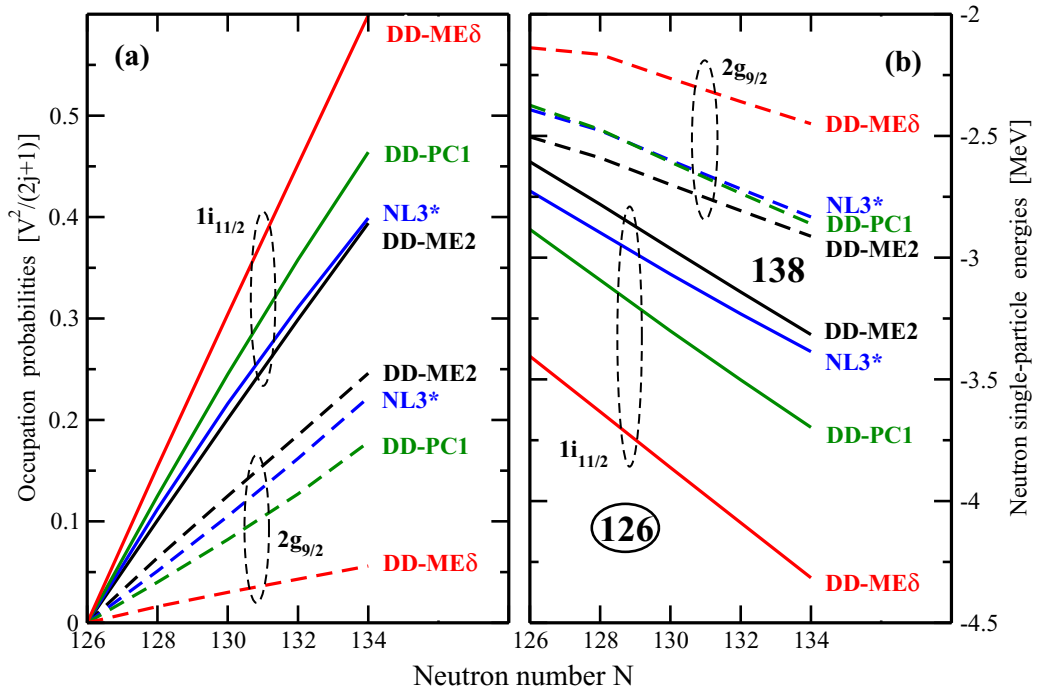


FIG. 9. (a) The evolution of the cumulative occupation probabilities  $v^2_{\text{state}}$  of the neutron  $2g_{9/2}$  and  $1i_{11/2}$  orbitals as a function of neutron number in the  $N \geq 126$  Pb nuclei for the indicated CEDFs. (b) The evolution of the energies of these single-particle states as a function of neutron number. Note that both types of physical quantities are calculated in canonical basis. The neutron shell closure at  $N = 126$  and the energy gap between the  $2g_{9/2}$  and  $1i_{11/2}$  orbitals at  $N = 138$  are indicated. Note that this figure is based on the results of the calculations of even-even nuclei. Dashed ellipses envelope the states with the same structure.

( $v^2_{1i_{11/2}} \approx 4.7$ ) but with a significant portion also found in  $2g_{9/2}$  ( $v^2_{2g_{9/2}} \approx 2.5$ ). This leads a reduction of the  $\delta \langle r^2 \rangle^{N,N'} / \delta N$  slope as compared with the case of the DD-ME $\delta$  functional. One can see in Fig. 7 that the experimental  $\delta \langle r^2 \rangle^{N,N'} / \delta N$  slope in the  $N > 126$  nuclei is reproduced with comparable accuracy by the DD-ME2, NL3\*, and DD-PC1 functionals. Note that with increasing neutron number  $N$  the single-particle states become more bound, but for a given functional, the relative energies of the  $2g_{9/2}$  and  $1i_{11/2}$  states change only slightly [see Fig. 9(b)]. As a consequence, the occupation probabilities of the single-particle states behave as almost linear functions of neutron number [see Fig. 9(a)].

The magnitude of the kink in charge radii at  $N = 126$  is better quantified by the  $\xi_{\text{even}}$  and  $\xi_{\text{even}}^*$  indicators defined in Eqs. (4) and (5), respectively. Experimentally available values of these indicators (for both even-even and odd nuclei) and calculated (only for even-even nuclei) are compared in Fig. 10. Mercury is the first element below  $Z = 82$  and only the second even- $Z$  element for which  $\xi_{\text{even}}$  is experimentally determined; the kink in the mercury charge radii is of a similar magnitude to that of lead. Only experimental  $\xi_{\text{even}}^*$  indicators are available for  $Z > 83$  nuclei. Note that experimental  $\xi_{\text{even}}$  and  $\xi_{\text{even}}^*$  indicators form a smooth curve which indicates that neither addition nor subtraction of proton(s) from the  $Z = 82$  nuclei affects drastically a kink in charge radii at  $N = 126$ . Figure 10 clearly shows that the best reproduction of this trend is achieved by the CEDF DD-ME2. Other functionals (including the Fayans  $\text{Fy}(\Delta r)$  functional) deviate somewhat from experimental data.

This analysis clearly indicates that the evolution of charge radii with neutron and proton numbers is sensitive to the details of underlying single-particle structure and the occupation probabilities of these states. Note that the latter depends on the

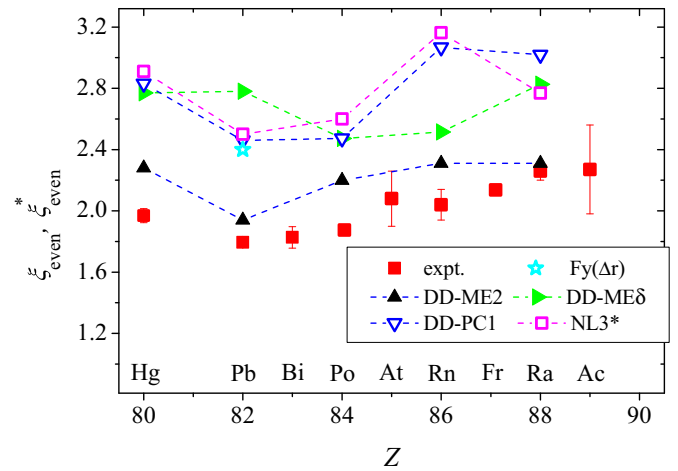


FIG. 10. Experimental and calculated  $\xi_{\text{even}}$  (for  $Z \leq 83$ ) and  $\xi_{\text{even}}^*$  (for  $Z \geq 84$ ) indicators. Note that the calculated results are presented only for even-even nuclei. The experimental values are determined using Eqs. (4) and (5), using data from [8,9,62,78] and the references listed in the explanation of Eq. (5), while the calculated ones are from the charge radii defined in the present paper and in Ref. [23], which is publicly available at Ref. [107]. The  $\xi_{\text{even}}(\text{Pb})$  value for Fayans  $\text{Fy}(\Delta r)$  functional was extracted from the data presented in Ref. [18].

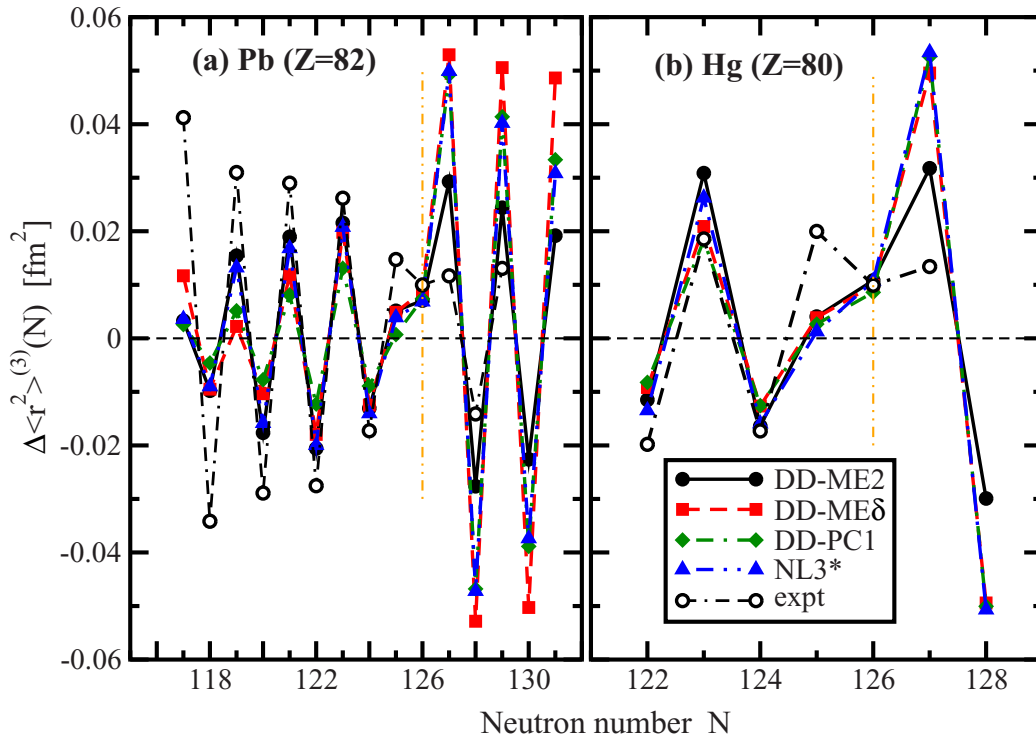


FIG. 11. Comparison of experimental and theoretical  $\Delta\langle r^2 \rangle^{(3)}(N)$  values for isotopes of lead (a) and mercury (b), respectively. The EGS procedure is employed in odd- $A$  nuclei. Experimental data are taken from Refs. [9,62,108]. Vertical orange dot-dot-dashed lines indicate  $N = 126$ .

type of pairing interaction employed in the calculations and its strength. It also indicates that the magnitude of the kink in charge radii at  $N = 126$  depends on the relative balance of the occupation of the  $2g_{9/2}$  and  $1i_{11/2}$  orbitals. In general, the substantial occupation of the  $1i_{11/2}$  orbital and the kink can be obtained even when the  $2g_{9/2}$  orbital is located lower in energy than the  $1i_{11/2}$  orbital (but still within its vicinity). This, for example, takes place in the nonrelativistic HFB (NR-HFB) calculations with the semirealistic M3Y-P6a interaction, the spin-orbit properties of which were modified [13] to improve the description of the charge radii of proton-magic nuclei [13–15]. However, these calculations underestimate the kink. A similar situation exists in the Skyrme DFT calculations with the SLy4mod functional presented in Ref. [5].

#### D. Odd-even staggering in charge radii

It was shown in Ref. [9] both in the RHB calculations with DD-ME2 and in the NR-HFB studies with semirealistic M3Y-P6a interaction that OES in charge radii is best reproduced when the EGS procedure is applied in odd- $A$  nuclei. In contrast, the experimental OES is significantly underestimated when the LES procedure is used in odd- $A$  nuclei in the RHB framework for all nuclei under study and for  $N < 126$  nuclei in the NR-HFB approach. The same behavior is observed also in the results of RHB calculations with CEDFs DD-ME $\delta$ , DD-PC1, and NL3\*, the results of which are shown in Fig. 11. This figure shows also that there is some dependence of the magnitude of the  $\Delta\langle r^2 \rangle^{(3)}(N)$  values on the employed func-

tional, which comes from the differences in the energies of the single-particle states and their occupations (see Figs. 8 and 9).

Particle-vibration coupling (PVC) plays a critical role in the emergence of such significant OES in charge radii because it leads to the nucleonic configuration with the blocked state corresponding to the experimental ground state (see Ref. [9] for details). Let us illustrate that with the case of the  $N > 126$  Pb nuclei. In the odd- $A$  isotopes, the PVC coupling lowers the  $2g_{9/2}$  state below the  $1i_{11/2}$  state, making it the ground state despite the fact that at the mean field level (as well as in even-even nuclei) the energy of the  $2g_{9/2}$  state is higher than that of the  $1i_{11/2}$  state (see Fig. 5 of Ref. [95]). Although these results were obtained with NL3\*, a comparable effect of PVC on relative energies of these states is expected in other functionals. However, the feasibility of such a scenario also crucially depends on the relative energies of the single-particle orbitals of interest at the mean field level. For example, if the energy gap between the  $2g_{9/2}$  and  $1i_{11/2}$  states is too large [like in the case of the DD-ME $\delta$  functional; see Figs. 8 and 9(b)], the impact of the PVC would most likely not be enough to make the  $2g_{9/2}$  state as a ground state. This functional, however, suffers from some significant deficiencies in the  $Z > 82$  region which probably are the consequences of the overly large energy gap between these two states. For example, it does not predict octupole deformed actinides [109] and predicts fission barriers in superheavy nuclei which are too small to make them relatively stable [110]. One has to keep in mind, however, that the interaction DD-ME $\delta$  is different from the other interactions discussed here. It is the most microscopic one among considered functionals: only four

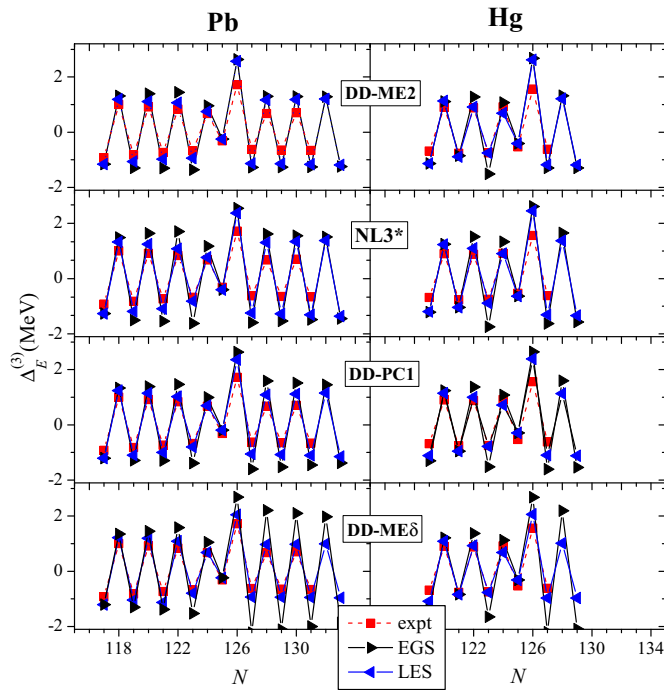


FIG. 12. Experimental and calculated odd-even staggerings in binding energies  $\Delta_E^{(3)}$  of the Pb and Hg isotopes under study. The calculated results are defined for the EGS and LES procedures in odd-A nuclei.

parameters at the saturation density are fitted to finite nuclei and the full density dependence of the parameters is derived from *ab initio* calculations. In contrast, the other interactions contain an additional two (NL3\*), four (DD-ME2), or six (DD-PC1) phenomenological parameters for the fine-tuning of the density dependence.

### E. Binding energies and $\Delta_E^{(3)}$ indicators

Empirical approaches considering binding energies can help with understanding the interplay between nucleons. With the exception of the DD-ME $\delta$  functional, there is a good agreement between the calculated and the experimental binding energies for both lead and mercury isotopes. For  $^{198-214}\text{Pb}$  and  $^{201-208}\text{Hg}$  nuclei, the rms deviations from experiment are 1.3 and 0.6 MeV for NL3\* CEDF, 1.3 and 1.1 MeV for DD-ME2, 1.8 and 2.1 MeV for DD-PC1, and 4.0 and 3.9 MeV for DD-ME $\delta$ , respectively. To highlight the odd-even staggering of binding energies along the isotopic chains, an indicator in the form of

$$\Delta_E^{(3)}(Z, N) = \frac{1}{2}[B(Z, N-1) - 2B(Z, N) + B(Z, N+1)] \quad (7)$$

was used. Here  $B(N, Z)$  is the binding energy for a nucleus with proton number  $Z$  and neutron number  $N$ . The odd-even staggerings in the binding energies<sup>5</sup>  $\Delta_E^{(3)}$  are reproduced reasonably well (see Fig. 12), especially when the LES are used

in odd-A nuclei. The level of agreement is comparable with that provided by the Fayans  $Fy(\Delta r)$  functionals in Ref. [17].

Figure 12 also illustrates the challenges faced by all existing theories. Polarization effects in deformation/radial density distributions and pairing depend on the blocked state in odd-A nuclei. Thus, on the one hand, the  $\Delta_E^{(3)}$  indicators are distorted by incorrect polarizations effects when a wrong (as compared with experiment) state is used for the ground state of an odd-A nucleus. The related uncertainties in binding energies due to polarization effects in the pairing channel are on the level of 150 keV, and those due to deformation/radial density distribution polarization effects are more difficult to estimate but are expected typically to be less than 100 keV. On the other hand, large theoretical uncertainties in the predictions of single-particle energies (see Refs. [94–96] and Fig. 8) reveal themselves when the  $\Delta_E^{(3)}$  indicators are defined using the EGS procedure in odd-A nuclei. This is especially pronounced in the calculations for the  $N > 126$  nuclei with the DD-ME $\delta$  functional (see Fig. 12) which is characterized by a large energy gap between the  $2g_{9/2}$  and  $1i_{11/2}$  subshells (see Fig. 8). Comparing these uncertainties, it is safer to use the LES procedure in the definition of the  $\Delta_E^{(3)}$  indicators and their association with pairing indicators (see detailed discussion in Ref. [97]). Note that the calculations somewhat overestimate experimental  $\Delta_E^{(3)}$  indicators. The PVC provides additional binding (on the level of few 100 keV) to the ground states of odd-A nuclei. Thus, its inclusion into the calculations is expected to decrease the calculated  $\Delta_E^{(3)}$  and, as a consequence, to improve the description of experimental data.

## VII. CONCLUSION

The kink in the  $\delta\langle r^2 \rangle$  systematics of the mercury isotopic chain has been analyzed considering a variety of dimensionless parameters and employed in the comparison of the results of a range of covariant energy density functionals. The results of mass measurements of  $^{206-208}\text{Hg}$  are presented, which improve upon the precision of previously measured values. The observed  $Z$  dependence of the  $g$  factors of  $I = 9/2$ ,  $N = 127$  isotones is interpreted as the result of CP2 corrections. The magnitude of the extracted neutron effective charge for  $^{207}\text{Hg}$  suggests a rapidly increasing quadrupole core polarization when moving away from the  $Z = 82$  proton shell.

The theoretical analysis of charge radii and related indicators in the Pb and Hg isotopic chains has been performed within the RHB framework using several CEDFs characterized by different single-particle properties. This analysis supports the conclusion that the kink at  $N = 126$  in  $\delta\langle r^2 \rangle^{N,N'}$  originates from the occupation of the  $\nu 1i_{11/2}$  orbital located above the  $N = 126$  shell gap. The pairing effect does not play a critical role here since the kink is present also in the calculations without pairing. This is in contrast to nonrelativistic Skyrme and Fayans functionals, in which the pairing becomes a dominant contributor to the kink and OES [18]. However,

<sup>5</sup>This quantity is frequently used as a pairing indicator. However, in no way should it be considered as a clean measure of pair-

ing correlations since it is polluted by time-odd mean fields and particle-vibration coupling in odd-A nuclei (see detailed discussion in Ref. [97]).

the pairing plays an important role in defining the magnitude of the kink, which depends on the balance of the occupation of the  $1i_{11/2}$  and  $2g_{9/2}$  orbitals. This balance sensitively depends on the relative energies of these two orbitals. The DD-ME2 functional provides the best description of kinks at  $N = 126$  not only in the Pb and Hg isotopes but also in all isotopic chains for which experimental data is available. A reasonable description of OES in charge radii has been achieved with all employed functionals. This confirms a new mechanism of OES suggested in Ref. [9] which is related to the staggering in the occupation of neutron orbitals between odd and even isotopes facilitated by PVC in odd-mass nuclei.

### ACKNOWLEDGMENTS

This project has received funding through the European Union's Seventh Framework Programme for Research and Technological Development under Grants Agreement No. 267194 (COFUND), No. 262010 (ENSAR), No. 289191 (LA<sup>3</sup>NET), and No. 267216 (PEGASUS). This project has received funding from the European Union's Horizon 2020 research and innovation program Grant Agreement No. 654002 (ENSAR2). This material is based upon work supported by the U.S. Department of Energy, Office of Science, Office of Nuclear Physics under Award No. DE-SC0013037, and by the Deutsche Forschungsgemeinschaft (DFG, German Research Foundation) under Germany's Excellence Strategy EXC-2094-390783311, ORIGINS. S.S. acknowledges a SB Ph.D. grant from the former Belgian Agency for Innovation by Science and Technology (IWT), now incorporated in FWO-Vlaanderen. This work was supported by the RFBR according to the research project No. 19-02-00005; the ERC Consolidator Grant No. 648381; the IUAP-Belgian State Science Policy (BRIX network P7/12), FWO-Vlaanderen (Belgium) and GOA's 10/010 and 10/05 and starting grant STG 15/031 from KU Leuven; the Science and Technology Facilities Council Consolidated Grants No. ST/F012071/1, No. ST/P003885/1, and No. ST/R004056/1, Continuation Grant No. ST/J000159/1 and Ernest Rutherford Grant No. ST/L002868/1; the Slovak Research and Development Agency, Contract No. APVV-14-0524; the French IN2P3; the BMBF (German Federal Ministry for Education and Research) Grants No. 05P12HGCI1, No. 05P15HGCI1, No. 05E18CHA, and No. 05P18HGCI1.

### APPENDIX A: NUCLEAR OBSERVABLES IN THE HYPERFINE STRUCTURE

Nuclear observables were extracted from the experimentally measured hfs through the application of standard methods [90]. The substate weighted centroid  $\nu_0$  and the hyperfine  $a$  and  $b$  parameters were extracted from the fitted spectra, where the shift  $\Delta\nu^F$  of the state  $F$  of the hyperfine multiplet from  $\nu_0$  is given as

$$\Delta\nu^F = a \frac{K}{2} + b \frac{\frac{3}{4}K(K+1) - I(I+1)J(J+1)}{2(2I-1)(2J-1)IJ}, \quad (\text{A1})$$

where  $K = [F(F+1) - I(I+1) - J(J-1)]$ ,  $I$  is the nuclear spin, and  $J$  is the atomic angular momentum. The extraction of  $\nu_0$  enabled the calculation of  $\delta\nu^{A,A'}$ , the isotope

shift between  $A$  the isotope under investigation and  $A'$  a reference isotope.  $\delta\langle r^2 \rangle^{A,A'}$ , the change in the mean square charge radius of  $A$  with respect  $A'$  was extracted as

$$\delta\nu^{A,A'} = F_\lambda K(Z) \delta\langle r^2 \rangle^{A,A'} + M \times \frac{A - A'}{AA'}, \quad (\text{A2})$$

where for the spectroscopic transition  $F_{254\text{nm}} = -55.36 \text{ GHz fm}^{-2}$  [62],  $K(Z=80) = 0.931$  (taking into account [111,112]) is a calculable correction factor, and  $M$  is the mass shift factor representing the sum of the normal mass shift ( $M_{\text{NMS}}$ ) and the specific mass shift ( $M(Z=80) = (1 \pm 0.5) \times M_{\text{NMS}}$  [62]).

The magnetic moments  $\mu_A$  were calculated as

$$\mu_A = \mu_{\text{ref}} \times \frac{I_A}{I_{\text{ref}}} \times \frac{a_A}{a_{\text{ref}}} \times (1 + {}^{\text{ref}}\Delta^A), \quad (\text{A3})$$

where the isomer  $^{199\text{m}}\text{Hg}$  ( $I = 13/2$ ) was used as a reference nucleus with  $\mu(^{199\text{m}}\text{Hg}) = -1.0147(8) \mu_N$  [113] and  $a(^{199\text{m}}\text{Hg}) = -2298.3(2) \text{ MHz}$  [113]. An additional correction for the hyperfine anomaly (HFA) is included for the  $\mu$  values presented in Table I. Moskowitz and Lombardi [114] demonstrated that for mercury isotopes the “Bohr-Weisskopf” component ( ${}^{A_1}\Delta_{\text{BW}}^{A_2}$ ) [115] is dominant, thus the “Breit-Rosenthal” component ( ${}^{A_1}\Delta_{\text{BR}}^{A_2}$ ) [116] can be ignored. The following relation between the magnetic moments and the HFA, the so-called Moskowitz-Lombardi (ML) rule was used, determining  ${}^{A_1}\Delta_{\text{BW}}^{A_2}$  [115]:

$${}^{A_1}\Delta_{\text{BW}}^{A_2} = \pm \alpha \times \left( \frac{1}{\mu_1} - \frac{1}{\mu_2} \right), \quad I = l \pm \frac{1}{2}, \quad (\text{A4})$$

where  $\alpha = 1 \times 10^{-2}$  and  $l$  is the orbital momentum of the last neutron. The ML rule was verified later by the microscopic theory [117]. The application of the ML rule to estimate the Bohr-Weisskopf correction of the magnetic moment of  $^{207}\text{Hg}$  is justified based on the successful reproduction of the experimental HFA by this rule for neutron single-particle states in mercury nuclei across a rather large range of masses [114].

For previously measured isotopes and isomers the maximum deviation of the experimental  ${}^{A_1}\Delta_{\text{BW}}^{A_2}$  from the ML calculation is equal to  $2 \times 10^{-3}$ . Correspondingly, we conservatively estimated the error of the ML prediction for  $^{207}\Delta_{\text{BW}}^{199}$  as  $5 \times 10^{-3}$ . The uncertainty of this correction was estimated based on the omitted  ${}^{A_1}\Delta_{\text{BR}}^{A_2}$  correction. It was shown in [118] that  ${}^{A_1}\Delta_{\text{BR}}^{A_2}$  is proportional to  $\delta\langle r^2 \rangle^{A_1,A_2}$ . Thus  $^{207}\Delta_{\text{BR}}^{199}$  for  $^{207}\text{Hg}$  can be estimated by scaling the calculated  $^{201}\Delta_{\text{BR}}^{199}$  [119]. It should be noted that  $^{205}\Delta_{\text{BR}}^{203}$  for thallium isotopes, calculated in [119] by solving the one-electron Dirac equation, practically coincides with that calculated in [118] by the Dirac-Fock approach. Taking into account the independence of the  ${}^{A_1}\Delta_{\text{BR}}^{A_2}$  correction on the details of the atomic calculations and the uncertainty of  $\delta\langle r^2 \rangle$ , we estimate the uncertainty of this correction as 10%.

The spectroscopic quadrupole moments  $Q_s^A$  were calculated using the relation

$$Q_s^A = \frac{b_A}{b_{^{201}\text{Hg}}} Q_s^{^{201}\text{Hg}}, \quad (\text{A5})$$

where  $Q_s^{201\text{Hg}} = 0.387(6)$  b (from [120]) and  $b_{201\text{Hg}} = -280.107(5)$  MHz [121]. The results are presented in Table I.

## APPENDIX B: MASS SPECTROMETRY METHODS

The mass measurements were performed with the ISOLTRAP mass spectrometer [122]. As described in parts above, the setup consists of four ion traps for beam preparation and mass measurements. First, a linear radio-frequency quadrupole trap was used to accumulate, cool, and bunch the quasicontinuous radioactive ion beam delivered by ISOLDE [37]. Using a pulsed drift tube, the energy of the bunched beam is then reduced from the initial 30 keV to 3.2 keV.

Ions are captured by the Multi-Reflection Time-of-Flight Mass Spectrometer/Mass Separator (MR-ToF MS) [38] using the in-trap lift electrode [123], following this, they undergo a certain number of revolutions in-between the mirror electrodes of the device. Here, the time of flight is given as  $t = a\sqrt{m} + b$ , where  $a$  and  $b$  are device-dependent parameters. Due to the mass dependence of the trapped ions moving at the same kinetic energy, the different isobaric species separate in time-of-flight. In mass spectrometry mode, the MR-ToF MS can be used to determine the mass of the ion of interest by using well known reference masses to account for the calibration parameters  $a$  and  $b$ . This is done by expressing the mass  $m$  using the so-called  $C_{\text{ToF}}$  value [40]:

$$m^{1/2} = C_{\text{ToF}}(m_1^{1/2} - m_2^{1/2}) + \frac{1}{2}(m_1^{1/2} + m_2^{1/2}), \quad (\text{B1})$$

where  $m_1, m_2$  and  $t_1, t_2$  are the masses and times of flight of the two reference species, respectively, and  $C_{\text{ToF}} = (2t - t_1 -$

$t_2)/[2(t_1 - t_2)]$ . An example of a time-of-flight spectrum is presented in Figs. 2(b) and 2(c).

In mass-separation mode, the MR-ToF MS selectively ejects the ions of interest towards the Penning traps located downstream of the setup. In the so-called preparation Penning trap, the ions are captured and cooled using a mass-selective buffer-gas method to improve beam emittance [124] and to further reduce contamination. Subsequently, the ions are ejected and recaptured in the precision Penning trap in which the high precision mass measurement is performed. In the present measurement, this is achieved by employing the time-of-flight ion cyclotron resonance (ToF-ICR) technique, which determines the cyclotron frequency of the trapped ions by scanning the frequency of an applied quadrupolar electric field [125]. This frequency can be written as  $\omega_c = \frac{qB}{m}$ , where  $q$  is the electric charge of the ion,  $B$  is the magnetic field, and  $m$  is the ion mass. By performing cross-reference measurements with known mass calibrants, the mass  $m$  of the ion of interest can be extracted by comparing its cyclotron frequency with that of a well-known mass. Expressed as a frequency ratio

$$R = \frac{\omega_{c,\text{ref}}}{\omega_c} = \frac{m}{m_{\text{ref}}}, \quad (\text{B2})$$

the magnetic field and the charge cancel out. For the atomic mass, the electron mass is added to the measured ion mass. The ionization energy is negligible.

Expressing the ion masses in MR-ToF MS and ToF-ICR measurements via the  $C_{\text{ToF}}$  value and the frequency ratio  $R$ , respectively, facilitates an easy recalculation of the mass of interest in case one of the employed reference masses is measured more precisely in the future.

- 
- [1] N. Tajima, P. Bonche, H. Flocard, P. H. Heenen, and M. S. Weiss, Self-consistent calculation of charge radii of Pb isotopes, *Nucl. Phys. A* **551**, 434 (1993).
  - [2] M. Sharma, G. Lalazissis, and P. Ring, Anomaly in the charge radii of Pb isotopes, *Phys. Lett. B* **317**, 9 (1993).
  - [3] P.-G. Reinhard and H. Flocard, Nuclear effective forces and isotope shifts, *Nucl. Phys. A* **584**, 467 (1995).
  - [4] S. Fayans, S. Tolokonnikov, E. Trykov, and D. Zawischa, Nuclear isotope shifts within the local energy-density functional approach, *Nucl. Phys. A* **676**, 49 (2000).
  - [5] P. M. Goddard, P. D. Stevenson, and A. Rios, Charge Radius Isotope Shift Across the  $N = 126$  Shell Gap, *Phys. Rev. Lett.* **110**, 032503 (2013).
  - [6] T. E. Cocolios, W. Dexters, M. D. Seliverstov, A. N. Andreyev, S. Antalic, A. E. Barzakh, B. Bastin, J. Buscher, I. G. Darby, D. V. Fedorov, V. N. Fedosseev, K. T. Flanagan, S. Franchoo, S. Fritzsche, G. Huber, M. Huyse, M. Keupers, U. Koster, Y. Kudryavtsev, E. Mane, B. A. Marsh, P. L. Molkanov, R. D. Page, A. M. Sjoedin, I. Stefan, J. VandeWalle, P. VanDuppen, M. Venhart, S. G. Zemlyanoy, M. Bender, and P. H. Heenen, Early Onset of Ground State Deformation in Neutron Deficient Polonium Isotopes, *Phys. Rev. Lett.* **106**, 052503 (2011).
  - [7] G. J. Farooq-Smith, T. E. Cocolios, J. Billowes, M. L. Bissell, I. Budinčević, T. Day Goodacre, R. P. de Groote, V. N. Fedosseev, K. T. Flanagan, S. Franchoo, R. F. Garcia Ruiz, H. Heylen, R. Li, K. M. Lynch, B. A. Marsh, G. Neyens, R. E. Rossel, S. Rothe, H. H. Stroke, K. D. A. Wendt *et al.*, Laser and decay spectroscopy of the short-lived isotope  $^{214}\text{Fr}$  in the vicinity of the  $N = 126$  shell closure, *Phys. Rev. C* **94**, 054305 (2016).
  - [8] A. E. Barzakh, D. V. Fedorov, V. S. Ivanov, P. L. Molkanov, F. V. Moroz, S. Y. Orlov, V. N. Panteleev, M. D. Seliverstov, and Y. M. Volkov, Shell effect in the mean square charge radii and magnetic moments of bismuth isotopes near  $N = 126$ , *Phys. Rev. C* **97**, 014322 (2018).
  - [9] T. Day Goodacre, A. V. Afanasjev, A. E. Barzakh, B. A. Marsh, S. Sels, P. Ring, H. Nakada, A. N. Andreyev, P. Van Duppen, N. A. Althubiti, B. Andel, D. Atanasov, J. Billowes, K. Blaum, T. E. Cocolios, J. G. Cubiss, G. J. Farooq-Smith, D. V. Fedorov, V. N. Fedosseev, K. T. Flanagan *et al.*, Laser Spectroscopy of Neutron-Rich  $^{207,208}\text{Hg}$  Isotopes: Illuminating the Kink and Odd-Even Staggering in Charge Radii across the  $N = 126$  Shell Closure, *Phys. Rev. Lett.* **126**, 032502 (2021).
  - [10] W. Myers and K.-H. Schmidt, An update on droplet-model charge distributions, *Nucl. Phys. A* **410**, 61 (1983).
  - [11] R. C. Thompson, A. Hanser, K. Bekk, G. Meisel, and D. Frölich, High resolution measurements of isotope shifts in lead, *Z. Phys. A* **305**, 89 (1982).
  - [12] M. M. Sharma, G. Lalazissis, J. König, and P. Ring, Isospin Dependence of the Spin-Orbit Force and

- Effective Nuclear Potentials, *Phys. Rev. Lett.* **74**, 3744 (1995).
- [13] H. Nakada, Further evidence for three-nucleon spin-orbit interaction in isotope shifts of nuclei with magic proton numbers, *Phys. Rev. C* **92**, 044307 (2015).
- [14] H. Nakada and T. Inakura, Effects of three-nucleon spin-orbit interaction on isotope shifts of Pb nuclei, *Phys. Rev. C* **91**, 021302(R) (2015).
- [15] H. Nakada, Irregularities in nuclear radii at magic numbers, *Phys. Rev. C* **100**, 044310 (2019).
- [16] S. Fayans, E. Trykov, and D. Zawischa, Influence of effective spin-orbit interaction on the collective states of nuclei, *Nucl. Phys. A* **568**, 523 (1994).
- [17] P.-G. Reinhard and W. Nazarewicz, Toward a global description of nuclear charge radii: Exploring the Fayans energy density functional, *Phys. Rev. C* **95**, 064328 (2017).
- [18] C. Gorges, L. V. Rodriguez, D. L. Balabanski, M. L. Bissell, K. Blaum, B. Cheal, R. F. GarciaRuiz, G. Georgiev, W. Gins, H. Heylen, A. Kanellakopoulos, S. Kaufmann, M. Kowalska, V. Lagaki, S. Lechner, B. Maass, S. Malbrunot-Ettenauer, W. Nazarewicz, R. Neugart, G. Neyens, W. Nortershauser, P. G. Reinhard, S. Sailer, R. Sanchez, S. Schmidt, L. Wehner, C. Wraith, L. Xie, Z. Y. Xu, X. F. Yang, and D. T. Yordanov, Laser Spectroscopy of Neutron-Rich Tin Isotopes: A Discontinuity in Charge Radii across the  $N = 82$  Shell Closure, *Phys. Rev. Lett.* **122**, 192502 (2019).
- [19] G. A. Lalazissis, S. Karatzikos, R. Fossion, D. P. Arteaga, A. V. Afanasjev, and P. Ring, The effective force NL3 revisited, *Phys. Lett. B* **671**, 36 (2009).
- [20] T. Nikšić, D. Vretenar, and P. Ring, Relativistic nuclear energy density functionals: Adjusting parameters to binding energies, *Phys. Rev. C* **78**, 034318 (2008).
- [21] G. A. Lalazissis, T. Nikšić, D. Vretenar, and P. Ring, New relativistic mean-field interaction with density-dependent meson-nucleon couplings, *Phys. Rev. C* **71**, 024312 (2005).
- [22] X. Roca-Maza, X. Viñas, M. Centelles, P. Ring, and P. Schuck, Relativistic mean-field interaction with density-dependent meson-nucleon vertices based on microscopical calculations, *Phys. Rev. C* **84**, 054309 (2011).
- [23] S. E. Agbemava, A. Afanasjev, D. Ray, and P. Ring, Global performance of covariant energy density functionals: Ground state observables of even-even nuclei and the estimate of theoretical uncertainties, *Phys. Rev. C* **89**, 054320 (2014).
- [24] A. V. Afanasjev and S. E. Agbemava, Covariant energy density functionals: Nuclear matter constraints and global ground state properties, *Phys. Rev. C* **93**, 054310 (2016).
- [25] R. Catherall, W. Andreatza, M. Breitenfeldt, A. Dorsival, G. Focker, T. Gharsa, G. T.J., J.-L. Grenard, F. Locci, P. Martins, S. Marzari, J. Schipper, A. Shornikov, and T. Stora, The ISOLDE facility, *J. Phys. G: Nucl. Part. Phys.* **44**, 094002 (2017).
- [26] B. A. Marsh, T. Day Goodacre, S. Sels, Y. Tsunoda, B. Andel, A. N. Andreyev, N. A. Althubiti, D. Atanasov, A. E. Barzakh, J. Billowes, K. Blaum, T. E. Cocolios, J. G. Cubiss, J. Dobaczewski, G. J. Farooq-Smith, D. V. Fedorov, V. N. Fedosseev, K. T. Flanagan, L. P. Gaffney, L. Ghys *et al.*, Characterization of the shape-staggering effect in mercury nuclei, *Nat. Phys.* **14**, 1163 (2018).
- [27] S. Sels, T. Day Goodacre, B. A. Marsh, A. Pastore, W. Ryssens, Y. Tsunoda, N. Althubiti, B. Andel, A. N. Andreyev, D. Atanasov, A. E. Barzakh, M. Bender, J. Billowes, K. Blaum, T. E. Cocolios, J. G. Cubiss, J. Dobaczewski, G. J. Farooq-Smith, D. V. Fedorov, V. N. Fedosseev *et al.*, Shape staggering of midshell mercury isotopes from in-source laser spectroscopy compared with density-functional-theory and Monte Carlo shell-model calculations, *Phys. Rev. C* **99**, 044306 (2019).
- [28] O. Kofoed-Hansen and K. O. Nielsen, Short-lived krypton isotopes and their daughter substances, *Phys. Rev.* **82**, 96 (1951).
- [29] Y. Blumenfeld, T. Nilsson, and P. Van Duppen, Facilities and methods for radioactive ion beam production, *Phys. Scr.* **T152**, 014023 (2013).
- [30] G. D. Alkhazov, A. E. Barzakh, V. P. Denisov, K. A. Mezilev, Y. N. Novikov, V. N. Panteleyev, A. V. Popov, E. P. Sudentas, V. S. Letokhov, V. I. Mishin, V. N. Fedoseyev, S. V. Andreyev, D. S. Vedeneyev, and A. D. Zyuzikov, A new highly efficient method of atomic spectroscopy for nuclides far from stability, *Nucl. Instrum. Methods Phys. Res., Sect. B* **69**, 517 (1992).
- [31] B. A. Marsh, B. Andel, A. N. Andreyev, S. Antalic, D. Atanasov, A. E. Barzakh, B. Bastin, C. Borgmann, L. Capponi, T. E. Cocolios, T. Day Goodacre, M. Dehairs, X. Derkx, H. De Witte, D. V. Fedorov, V. N. Fedosseev, G. J. Focker, D. A. Fink, K. T. Flanagan, S. Franchoo *et al.*, New developments of the in-source spectroscopy method at RILIS/ISOLDE, *Nucl. Instrum. Methods Phys. Res., Sect. B* **317**, 550 (2013).
- [32] J. Lettry, R. Catherall, G. Cyvoct, P. Drumm, A. Evensen, M. Lindroos, O. Jonsson, E. Kugler, J. Obert, J. Putaux, J. Sauvage, K. Schindl, H. Ravn, and E. Wildner, Release from ISOLDE molten metal targets under pulsed proton beam conditions, *Nucl. Instrum. Methods Phys. Res., Sect. B* **126**, 170 (1997).
- [33] T. Day Goodacre, J. Billowes, R. Catherall, T. E. Cocolios, B. Crepieux, D. V. Fedorov, V. Fedosseev, L. P. Gaffney, T. Giles, A. Gottberg, K. M. Lynch, B. A. Marsh, T. M. Mendonça, J. P. Ramos, R. E. Rossel, S. Rothe, S. Sels, C. Sotty, T. Stora, C. Van Beveren *et al.*, Blurring the boundaries between ion sources: The application of the RILIS inside a FEBIAD type ion source at ISOLDE, *Nucl. Instrum. Methods Phys. Res., Sect. B* **376**, 39 (2016).
- [34] V. Fedosseev, K. Chrysalidis, T. Day Goodacre, B. Marsh, S. Rothe, C. Seiffert, and K. Wendt, Ion beam production and study of radioactive isotopes with the laser ion source at ISOLDE, *J. Phys. G: Nucl. Part. Phys.* **44**, 084006 (2017).
- [35] V. Letokhov, *Laser Photoionization Spectroscopy*, 1st ed. (Academic, London, 1987), p. 357.
- [36] T. Day Goodacre, J. Billowes, K. Chrysalidis, D. V. Fedorov, V. N. Fedosseev, B. A. Marsh, P. L. Molkanov, R. E. Rossel, S. Rothe, C. Seiffert, and K. D. A. Wendt, RILIS-ionized mercury and tellurium beams at ISOLDE CERN, *Hyperfine Interact.* **238**, 41 (2017).
- [37] F. Herfurth, J. Dilling, A. Kellerbauer, G. Bollen, S. Henry, H. J. Kluge, E. Lamour, D. Lunney, R. B. Moore, C. Scheidenberger, S. Schwarz, G. Sikler, and J. Szerypo, A linear radiofrequency ion trap for accumulation, bunching, and emittance improvement of radioactive ion beams, *Nucl. Instrum. Methods Phys. Res., Sect. A* **469**, 254 (2001).
- [38] R. Wolf, F. Wienholtz, D. Atanasov, D. Beck, K. Blaum, C. Borgmann, F. Herfurth, M. Kowalska, S. Kreim, Y. A. Litvinov, D. Lunney, V. Manea, D. Neidherr, M. Rosenbusch, L. Schweikhard, J. Stanja, and K. Zuber, ISOLTRAP's multi-reflection time-of-flight mass separator/spectrometer, *Int. J. Mass Spectrom.* **349-350**, 123 (2013).

- [39] R. N. Wolf, D. Beck, K. Blaum, C. Böhm, C. Borgmann, M. Breitenfeldt, F. Herfurth, A. Herlert, M. Kowalska, S. Kreim, D. Lunney, S. Naimi, D. Neidherr, M. Rosenbusch, L. Schweikhard, J. Stanja, F. Wienholtz, and K. Zuber, On-line separation of short-lived nuclei by a multi-reflection time-of-flight device, *Nucl. Instrum. Methods Phys. Res., Sect. A* **686**, 82 (2012).
- [40] F. Wienholtz, D. Beck, K. Blaum, C. Borgmann, M. Breitenfeldt, R. B. Cakirli, S. George, F. Herfurth, J. D. Holt, M. Kowalska, S. Kreim, D. Lunney, V. Manea, J. Menéndez, D. Neidherr, M. Rosenbusch, L. Schweikhard, A. Schwenk, J. Simonis, J. Stanja *et al.*, Masses of exotic calcium isotopes pin down nuclear forces, *Nature (London)* **498**, 346 (2013).
- [41] R. N. Wolf, D. Beck, K. Blaum, C. Böhm, C. Borgmann, M. Breitenfeldt, N. Chamel, S. Goriely, F. Herfurth, M. Kowalska, S. Kreim, D. Lunney, V. Manea, E. Minaya Ramirez, S. Naimi, D. Neidherr, M. Rosenbusch, L. Schweikhard, J. Stanja, F. Wienholtz *et al.*, Plumbing Neutron Stars to New Depths with the Binding Energy of the Exotic Nuclide  $^{82}\text{Zn}$ , *Phys. Rev. Lett.* **110**, 041101 (2013).
- [42] S. Lukić, F. Gevaert, A. Kelić, M. Ricciardi, K. Schmidt, and O. Yordanov, Systematic comparison of ISOLDE-SC yields with calculated in-target production rates, *Nucl. Instrum. Methods Phys. Res., Sect. A* **565**, 784 (2006).
- [43] D. A. Fink, T. E. Cocolios, A. N. Andreyev, S. Antalic, A. E. Barzakh, B. Bastin, D. V. Fedorov, V. N. Fedosseev, K. T. Flanagan, L. Ghys, A. Gottberg, M. Huyse, N. Imai, T. Kron, N. Lemesne, K. M. Lynch, B. A. Marsh, D. Pauwels, E. Rapisarda, S. D. Richter, R. E. Rossel, S. Rothe, M. D. Seliverstov, A. M. Sjödin, C. Van Beveren, P. Van Duppen, and K. D. A. Wendt, In-Source Laser Spectroscopy with the Laser Ion Source and Trap: First Direct Study of the Ground-State Properties of  $^{217,219}\text{Po}$ , *Phys. Rev. X* **5**, 011018 (2015).
- [44] D. A. Fink, S. D. Richter, K. Blaum, R. Catherall, B. Crepieux, V. N. Fedosseev, A. Gottberg, T. Kron, B. A. Marsh, C. Mattolat, S. Raeder, R. E. Rossel, S. Rothe, F. Schwellnus, M. D. Seliverstov, M. Sjödin, T. Stora, P. Suominen, and K. D. A. Wendt, On-line implementation and first operation of the Laser Ion Source and Trap at ISOLDE/CERN, *Nucl. Instrum. Methods Phys. Res., Sect. B* **344**, 83 (2015).
- [45] L. Penescu, R. Catherall, J. Lettry, and T. Stora, Development of high efficiency Versatile Arc Discharge Ion Source at CERN ISOLDE, *Rev. Sci. Instrum.* **81**, 02A906 (2010).
- [46] Y. Tall, S. Cormon, M. Fallot, Y. Foucher, A. Guertin, T. Kirchner, L. Zanini, M. Andersson, K. Berg, H. Frånberg, F. Gröschel, E. Manfrin, W. Wagner, M. Wohlmuther, P. Everaerts, U. Köster, H. Ravn, E. Noah Messomo, C. Jost, and Y. Kojima, Volatile Elements Production Rates in a Proton-Irradiated Molten Lead-Bismuth Target, in *International Conference on Nuclear Data for Science and Technology ND2007* (EDP Sciences, Les Ulis, France, 2007).
- [47] J. Rodríguez-Sánchez, J. Benlliure, I. Vidaña, H. Lenske, C. Scheidenberger, J. Vargas, H. Alvarez-Pol, J. Atkinson, T. Aumann, Y. Ayyad, S. Beceiro-Novo, K. Boretzky, M. Caamaño, E. Casarejos, D. Cortina-Gil, P. Díaz Fernández, A. Estrade, H. Geissel, E. Haettner, A. Kelić-Heil *et al.*, Study of  $\Delta$  excitations in medium-mass nuclei with peripheral heavy ion charge-exchange reactions, *Phys. Lett. B* **807**, 135565 (2020).
- [48] B. Jonson, O. Nielsen, L. Westgaard, and J. Zylicz, The decay  $^{207}\text{Hg}$  to  $^{207}\text{Tl}$ , in *4th International Conference on Nuclei Far from Stability* (Helsingør, Denmark, 1981), pp. 640–643.
- [49] J.-J. Gaimard and K.-H. Schmidt, A reexamination of the abrasion-ablation model for the description of the nuclear fragmentation reaction, *Nucl. Phys. A* **531**, 709 (1991).
- [50] A. Junghans, M. de Jong, H.-G. Clerc, A. Ignatyuk, G. Kudyaev, and K.-H. Schmidt, Projectile-fragment yields as a probe for the collective enhancement in the nuclear level density, *Nucl. Phys. A* **629**, 635 (1998).
- [51] A. Ferrari, P. R. Sala, A. Fasso, and J. Ranft, FLUKA: A multi-particle transport code, CERN Technical Report No. CERN-2005-010, 2005.
- [52] T. Böhlen, F. Cerutti, M. Chin, A. Fassò, A. Ferrari, P. Ortega, A. Mairani, P. Sala, G. Smirnov, and V. Vlachoudis, The FLUKA code: Developments and challenges for high energy and medical applications, *Nucl. Data Sheets* **120**, 211 (2014).
- [53] S. Agostinelli, J. Allison, K. Amako, J. Apostolakis, H. Araujo, P. Arce, M. Asai, D. Axen, S. Banerjee, G. Barrand, F. Behner, L. Bellagamba, J. Boudreau, L. Broglia, A. Brunengo, H. Burkhardt, S. Chauvie, J. Chuma, R. Chytracsek, G. Cooperman *et al.*, Geant4—a simulation toolkit, *Nucl. Instrum. Methods Phys. Res., Sect. A* **506**, 250 (2003).
- [54] J. Allison, K. Amako, J. Apostolakis, P. Arce, M. Asai, T. Aso, E. Bagli, A. Bagulya, S. Banerjee, G. Barrand, B. Beck, A. Bogdanov, D. Brandt, J. Brown, H. Burkhardt, P. Canal, D. Cano-Ott, S. Chauvie, K. Cho, G. Cirrone *et al.*, Recent developments in Geant4, *Nucl. Instrum. Methods Phys. Res., Sect. A* **835**, 186 (2016).
- [55] F. H. Garcia, C. Andreoiu, and P. Kunz, Calculation of in-target production rates for isotope beam production at TRIUMF, *Nucl. Instrum. Methods Phys. Res., Sect. B* **412**, 174 (2017).
- [56] A. Koning and D. Rochman, Modern nuclear data evaluation with the TALYS code system, *Nucl. Data Sheets* **113**, 2841 (2012).
- [57] OriginLab, manual, 15.5.3 Theory of Nonlinear Curve Fitting.
- [58] K. Levenberg, A method for the solution of certain non-linear problems in least squares, *Q. Appl. Math.* **2**, 164 (1944).
- [59] D. Marquardt, An algorithm for least-squares estimation of nonlinear parameters, *J. Soc. Ind. Appl. Math.* **11**, 431 (1963).
- [60] W. Gins, R. P. de Groote, M. L. Bissell, C. Granados Buitrago, R. Ferrer, K. M. Lynch, G. Neyens, and S. Sels, Analysis of counting data: Development of the SATLAS Python package, *Comput. Phys. Commun.* **222**, 286 (2018).
- [61] R. Brun and F. Rademakers, ROOT - An object oriented data analysis framework, *Nucl. Instrum. Methods Phys. Res., Sect. A* **389**, 81 (1997).
- [62] G. Ulm, S. K. Bhattacharjee, P. Dabkiewicz, G. Huber, H. J. Kluge, T. Köhl, H. Lochmann, E. W. Otten, K. Wendt, S. A. Ahmad, W. Klempt, and R. Neugart, Isotope shift of  $^{182}\text{Hg}$  and an update of nuclear moments and charge radii in the isotope range  $^{181}\text{Hg} - ^{206}\text{Hg}$ , *Z. Phys. A* **325**, 247 (1986).
- [63] J. Bonn, G. Huber, H. J. Kluge, and E. W. Otten, Spins, moments and charge radii in the isotopic series  $^{181}\text{Hg} - ^{191}\text{Hg}$ , *Z. Phys. A* **276**, 203 (1976).
- [64] T. L. Tang, B. P. Kay, C. R. Hoffman, J. P. Schiffer, D. K. Sharp, L. P. Gaffney, S. J. Freeman, M. R. Mumpower, A. Arokiaraj, E. F. Baader, P. A. Butler, W. N. Catford, G. de Angelis, F. Flavigny, M. D. Gott, E. T. Gregor, J. Konkli, M. Labiche, I. H. Lazarus, P. T. MacGregor *et al.*, First

- Exploration of Neutron Shell Structure below Lead and beyond  $N = 126$ , *Phys. Rev. Lett.* **124**, 062502 (2020).
- [65] P. Dabkiewicz, Laserspektroskopische bestimmung der formisomerie in  $^{185}\text{Hg}$  und der isotopieverschiebung von  $^{206}\text{Hg}$ , Ph.D. thesis, The Johannes Gutenberg University of Mainz, 1980, Chaps. 6 and 7.
- [66] T. Day Goodacre, Developments of the ISOLDE RILIS for Radioactive Ion Beam Production and the Results Of Their Application in the Study of Exotic Mercury Isotopes, Ph.D. thesis, The University of Manchester, 2016, Chap. 11.
- [67] M. Wang, W. Huang, F. Kondev, G. Audi, and S. Naimi, The AME 2020 atomic mass evaluation (II). Tables, graphs and references\*, *Chin. Phys. C* **45**, 030003 (2021).
- [68] P. Kauranen, Alpha branching in the decay of  $^{210}\text{Pb}$  and  $^{210}\text{Bi}$ , a new mercury isotope  $^{206}\text{Hg}$ , *Ann. Acad. Sci. Fenn., Ser. A VI* **96**, 30 (1962).
- [69] S. George, S. Baruah, B. Blank, K. Blaum, M. Breitenfeldt, U. Hager, F. Herfurth, A. Herlert, A. Kellerbauer, H.-J. Kluge, M. Kretschmar, D. Lunney, R. Savreux, S. Schwarz, L. Schweikhard, and C. Yazidjian, Ramsey Method of Separated Oscillatory Fields for High-Precision Penning Trap Mass Spectrometry, *Phys. Rev. Lett.* **98**, 162501 (2007).
- [70] L. Chen, Investigation of Stored Neutron-Rich Nuclides in the Element Range of Pt-U with the FRS-ESR Facility at 360–400 MeV/u, Ph.D. thesis, Justus-Liebig-Universität, 2008, Chap. 4.
- [71] L. Chen, Y. A. Litvinov, W. R. Plass, K. Beckert, P. Beller, F. Bosch, D. Boutin, L. Caceres, R. B. Cakirli, J. J. Carroll, R. F. Casten, R. S. Chakrawarthy, D. M. Cullen, I. J. Cullen, B. Franzke, H. Geissel, J. Gerl, M. Gorska, G. A. Jones, A. Kishada, R. Knobel, C. Kozhuharov, S. A. Litvinov, Z. Liu, S. Mandal, F. Montes, G. Munzenberg, F. Nolden, T. Ohtsubo, Z. Patyk, Z. Podolyak, R. Propri, S. Rigby, N. Saito, T. Saito, C. Scheidenberger, M. Shindo, M. Steck, P. Ugorowski, P. M. Walker, S. Williams, H. Weick, M. Winkler, H. J. Wollersheim, and T. Yamaguchi, Schottky Mass Measurement of the  $^{208}\text{Hg}$  Isotope: Implication for the Proton-Neutron Interaction Strength around Doubly Magic  $^{208}\text{Pb}$ , *Phys. Rev. Lett.* **102**, 122503 (2009).
- [72] L. Chen, W. R. Plass, H. Geissel, R. Knöbel, C. Kozhuharov, Y. A. Litvinov, Z. Patyk, C. Scheidenberger, K. Siegień-Iwaniuk, B. Sun, H. Weick, K. Beckert, P. Beller, F. Bosch, D. Boutin, L. Caceres, J. J. Carroll, D. M. Cullen, I. J. Cullen, B. Franzke *et al.*, New results on mass measurements of stored neutron-rich nuclides in the element range from Pt to U with the FRS-ESR facility at 360–400 MeV/u, *Nucl. Phys. A* **882**, 71 (2012).
- [73] P. Fischer, S. Knauer, G. Marx, and L. Schweikhard, Non-isobaric time-of-flight correction for isobar resolving in mr-tof mass spectrometry, *Int. J. Mass Spectrom.* **432**, 44 (2018).
- [74] C. V. K. Baba, T. Faestermann, D. B. Fossan, and D. Proetel, Magnetic Moments of the  $7^-$  and  $5^-$  ( $\pi g_{9/2}$ ,  $\nu g_{9/2}$ ) States in  $^{210}\text{Bi}$ , *Phys. Rev. Lett.* **29**, 496 (1972).
- [75] M. R. Pearson, P. Campbell, K. Leerunnavarat, J. Billowes, I. S. Grant, M. Keim, J. Kilgallon, I. D. Moore, R. Neugart, M. Neuroth, S. Wilbert, and the ISOLDE Collaboration, Nuclear moments and charge radii of bismuth isotopes, *J. Phys. G: Nucl. Part. Phys.* **26**, 1829 (2000).
- [76] K. Heyde, Nuclear moments as a test of shell-model and collective model descriptions of the nucleus, *Hyperfine Interact.* **75**, 67 (1992).
- [77] A. Arima and H. Sagawa, The effect of particle-vibration coupling due to the collective  $2^+$  state on the magnetic moments of Tl-isotopes, *Phys. Lett. B* **173**, 351 (1986).
- [78] M. Anselment, W. Faubel, S. Göring, A. Hanser, G. Meisel, H. Rebel, and G. Schatz, The odd-even staggering of the nuclear charge radii of Pb isotopes, *Nucl. Phys. A* **451**, 471 (1986).
- [79] M. D. Seliverstov, T. E. Cocolios, W. Dexters, A. N. Andreyev, S. Antalic, A. E. Barzakh, B. Bastin, J. Buscher, I. G. Darby, D. V. Fedorov, V. N. Fedosseev, K. T. Flanagan, S. Franchoo, G. Huber, M. Huyse, M. Keupers, U. Koster, Y. Kudryavtsev, B. A. Marsh, P. L. Molkanov, R. D. Page, A. M. Sjodin, I. Stefan, P. VanDuppen, M. Venhart, and S. G. Zemlyanov, Electromagnetic moments of odd-A  $^{193-203,211}\text{Po}$  isotopes, *Phys. Rev. C* **89**, 034323 (2014).
- [80] B. Pritychenko, M. Birch, B. Singh, and M. Horoi, Tables of E2 transition probabilities from the first  $2^+$  states in even-even nuclei, *At. Data Nucl. Data Tables* **107**, 1 (2016).
- [81] A. Arima, K. Shimizu, W. Bentz, and H. Hyuga, Nuclear Magnetic Properties and Gamow-teller Transitions, in *Advances in Nuclear Physics Volume 18*, edited by J. Negele and E. Vogt (1987), pp. 1–106.
- [82] A. Arima and L. J. Huang-Lin, Magnetic dipole transitions in the vicinity of  $^{208}\text{Pb}$ , *Phys. Lett. B* **41**, 429 (1972).
- [83] J. Li, J. X. Wei, J. N. Hu, P. Ring, and J. Meng, Relativistic description of magnetic moments in nuclei with doubly closed shells plus or minus one nucleon, *Phys. Rev. C* **88**, 064307 (2013).
- [84] A. Arima and H. Horie, Configuration mixing and magnetic moments of odd nuclei, *Prog. Theor. Phys.* **12**, 623 (1954).
- [85] I. Towner, F. Khanna, and O. Häusser, Magnetic moments in  $N = 126$  isotones and core polarisation blocking, *Nucl. Phys. A* **277**, 285 (1977).
- [86] H. Sagawa and A. Arima, Static and dynamic quadrupole moments of high-spin isomers in the Pb-region, *Phys. Lett. B* **202**, 15 (1988).
- [87] G. Neyens, Nuclear magnetic and quadrupole moments for nuclear structure research on exotic nuclei, *Rep. Prog. Phys.* **66**, 633 (2003).
- [88] D. Vretenar, A. V. Afanasjev, G. Lalazissis, and P. Ring, Relativistic Hartree-Bogoliubov theory: Static and dynamic aspects of exotic nuclear structure, *Phys. Rep.* **409**, 101 (2005).
- [89] Y. Tian, Z. Ma, and P. Ring, A finite range pairing force for density functional theory in superfluid nuclei, *Phys. Lett. B* **676**, 44 (2009).
- [90] E. Otten, Nuclear Radii and Moments of Unstable Isotopes, in *Treatise on Heavy Ion Science* (Springer, Boston, 1989), pp. 517–638.
- [91] D. Berdichevsky and F. Tondeur, Nuclear core densities, isotope shifts, and the parametrization of the droplet model, *Z. Phys. A* **322**, 141 (1985).
- [92] U. Perera, A. V. Afanasjev, and P. Ring, Charge radii in covariant density functional theory: a global view, *arXiv:2108.02245* [nucl-th].
- [93] L. Bonneau, P. Quentin, and P. Möller, Global microscopic calculations of ground-state spins and parities for odd-mass nuclei, *Phys. Rev. C* **76**, 024320 (2007).
- [94] A. V. Afanasjev and S. Shawaqfeh, Deformed one-quasiparticle states in covariant density functional theory, *Phys. Lett. B* **706**, 177 (2011).
- [95] E. V. Litvinova and A. V. Afanasjev, Dynamics of nuclear single-particle structure in covariant theory of

- particle-vibration coupling: From light to superheavy nuclei, *Phys. Rev. C* **84**, 014305 (2011).
- [96] A. V. Afanasjev and E. Litvinova, Impact of collective vibrations on quasiparticle states of open-shell odd-mass nuclei and possible interference with the tensor force, *Phys. Rev. C* **92**, 044317 (2015).
- [97] S. Teeti and A. V. Afanasjev, Global study of separable pairing interaction in covariant density functional theory, *Phys. Rev. C* **103**, 034310 (2021).
- [98] G. Audi, F. Kondev, M. Wang, W. Huang, and S. Naimi, The NUBASE2016 evaluation of nuclear properties, *Chin. Phys. C* **41**, 030001 (2017).
- [99] D. Kowalewska, K. Bekk, S. Göring, A. Hanser, W. Kalber, G. Meisel, and H. Rebel, Isotope shifts and hyperfine structure in polonium isotopes by atomic-beam laser spectroscopy, *Phys. Rev. A* **44**, R1442(R) (1991).
- [100] A. E. Barzakh, J. G. Cubiss, A. N. Andreyev, M. D. Seliverstov, B. Andel, S. Antalic, P. Ascher, D. Atanasov, D. Beck, J. Bieroń, K. Blaum, C. Borgmann, M. Breitenfeldt, L. Capponi, T. E. Cocolios, T. Day Goodacre, X. Derkx, H. De Witte, J. Elseviers, D. V. Fedorov *et al.*, Inverse odd-even staggering in nuclear charge radii and possible octupole collectivity in  $^{217,218,219}\text{At}$  revealed by in-source laser spectroscopy, *Phys. Rev. C* **99**, 054317 (2019).
- [101] W. Borchers, R. Neugart, E. W. Otten, H. T. Duong, G. Ulm, and K. Wendt, Hyperfine structure and isotope shift investigations in  $^{202-222}\text{Rn}$  for the study of nuclear structure beyond  $Z = 82$ , *Hyperfine Interact.* **34**, 25 (1987).
- [102] I. Budinčević, J. Billowes, M. L. Bissell, T. E. Cocolios, R. P. de Groote, S. De Schepper, V. N. Fedosseev, K. T. Flanagan, S. Franchoo, R. F. Garcia Ruiz, H. Heylen, K. M. Lynch, B. A. Marsh, G. Neyens, T. J. Procter, R. E. Rossel, S. Rothe, I. Strashnov, H. H. Stroke, and K. D. A. Wendt, Laser spectroscopy of francium isotopes at the borders of the region of reflection asymmetry, *Phys. Rev. C* **90**, 014317 (2014).
- [103] A. Coc, C. Thibault, F. Touchard, H. T. Duong, P. Juncar, S. Liberman, J. Pinard, J. Lermé, J. L. Vialle, S. Büttgenbach, A. C. Mueller, and A. Pesnelle, Hyperfine structures and isotope shifts of  $^{207-213,220-228}\text{Fr}$ : Possible evidence of octupolar deformation, *Phys. Lett. B* **163**, 66 (1985).
- [104] V. A. Dzuba, W. R. Johnson, and M. S. Safronova, Calculation of isotope shifts for cesium and francium, *Phys. Rev. A* **72**, 022503 (2005).
- [105] L. W. Wansbeek, S. Schlessler, B. K. Sahoo, A. E. L. Dieperink, C. J. G. Onderwater, and R. G. E. Timmermans, Charge radii of radium isotopes, *Phys. Rev. C* **86**, 015503 (2012).
- [106] R. Ferrer, A. Barzakh, B. Bastin, R. Beerwerth, M. Block, P. Creemers, H. Grawe, R. de Groote, P. Delahaye, X. Fléchar, S. Franchoo, S. Fritzsche, L. P. Gaffney, L. Ghys, W. Gins, C. Granados, R. Heinke, L. Hijazi, M. Huyse, T. Kron *et al.*, Towards high-resolution laser ionization spectroscopy of the heaviest elements in supersonic gas jet expansion, *Nat. Commun.* **8**, 14520 (2017).
- [107] Mass Explorer: DFT mass tables at <http://massexplorer.frib.msu.edu/content/DFTMassTables.html>.
- [108] M. Anselment, K. Bekk, A. Hanser, H. Hoeffgen, G. Meisel, S. Göring, H. Rebel, and G. Schatz, Charge radii and moments of tin nuclei by laser spectroscopy, *Phys. Rev. C* **34**, 1052 (1986).
- [109] S. E. Agbemava, A. V. Afanasjev, and P. Ring, Octupole deformation in the ground states of even-even nuclei: A global analysis within the covariant density functional theory, *Phys. Rev. C* **93**, 044304 (2016).
- [110] S. E. Agbemava, A. V. Afanasjev, D. Ray, and P. Ring, Assessing theoretical uncertainties in fission barriers of superheavy nuclei, *Phys. Rev. C* **95**, 054324 (2017).
- [111] G. Torbom, B. Fricke, and A. Rosén, State-dependent volume isotope shifts of low-lying states of group-IIa and -IIb elements, *Phys. Rev. A* **31**, 2038 (1985).
- [112] G. Fricke and K. Heilig, *Nuclear Charge Radii*, 1st ed., edited by H. Schopper, Landolt-Börnstein Group I, Elementary Particles, Nuclei and Atoms (Springer-Verlag, Berlin, 2004), Vol. 20, pp. 1–419.
- [113] R. J. Reimann and M. N. McDermott, Precision magnetic moment determinations for 43-min  $^{199\text{m}}\text{Hg}$  and other isomers of mercury, *Phys. Rev. C* **7**, 2065 (1973).
- [114] P. Moskowitz and M. Lombardi, Distribution of nuclear magnetization in mercury isotopes, *Phys. Lett. B* **46**, 334 (1973).
- [115] A. Bohr and V. Weisskopf, The Influence of nuclear structure on the hyperfine structure of heavy elements, *Phys. Rev.* **77**, 94 (1950).
- [116] J. Rosenthal and G. Breit, The isotope shift in hyperfine structure, *Phys. Rev.* **41**, 459 (1932).
- [117] T. Fujita and A. Arima, Magnetic hyperfine structure of muonic and electronic atoms, *Nucl. Phys. A* **254**, 513 (1975).
- [118] A.-M. Mårtensson-Pendrill, Magnetic Moment Distributions in Tl Nuclei, *Phys. Rev. Lett.* **74**, 2184 (1995).
- [119] H. Rosenberg and H. Stroke, Effect of a diffuse nuclear charge distribution on the hyperfine-structure interaction, *Phys. Rev. A* **5**, 1992 (1972).
- [120] J. Bieroń, P. Pykkö, and P. Jönsson, Nuclear quadrupole moment of  $^{201}\text{Hg}$ , *Phys. Rev. A* **71**, 012502 (2005).
- [121] R. Kohler, Detection of double resonance by frequency change: Application to  $^{201}\text{Hg}$ , *Phys. Rev.* **121**, 1104 (1961).
- [122] M. Mukherjee, D. Beck, K. Blaum, G. Bollen, J. Dilling, S. George, F. Herfurth, A. Herlert, A. Kellerbauer, H. J. Kluge, S. Schwarz, L. Schweikhard, and C. Yazidjian, Isoltrap: An on-line penning trap for mass spectrometry on short-lived nuclides, *Eur. Phys. J. A* **35**, 1 (2008).
- [123] R. N. Wolf, G. Marx, M. Rosenbusch, and L. Schweikhard, Static-mirror ion capture and time focusing for electrostatic ion-beam traps and multi-reflection time-of-flight mass analyzers by use of an in-trap potential lift, *Int. J. Mass Spectrom.* **313**, 8 (2012).
- [124] G. Savard, S. Becker, G. Bollen, H.-J. Kluge, R. Moore, T. Otto, L. Schweikhard, H. Stolzenberg, and U. Wiess, A new cooling technique for heavy ions in a Penning trap, *Phys. Lett. A* **158**, 247 (1991).
- [125] M. König, G. Bollen, H.-J. Kluge, T. Otto, and J. Szerypo, Quadrupole excitation of stored ion motion at the true cyclotron frequency, *Int. J. Mass Spectrom. Ion Processes* **142**, 95 (1995).

### 7.3 Isomeric excitation energy for $^{99}\text{In}^m$ from mass spectrometry reveals constant trend next to doubly magic $^{100}\text{Sn}$



# Isomeric Excitation Energy for $^{99}\text{In}^m$ from Mass Spectrometry Reveals Constant Trend Next to Doubly Magic $^{100}\text{Sn}$

L. Nies<sup>1,2,\*</sup>, D. Atanasov<sup>1,†</sup>, M. Athanasakis-Kaklamanakis<sup>1,3</sup>, M. Au<sup>1,4</sup>, K. Blaum<sup>5</sup>, J. Dobaczewski<sup>6,7</sup>, B. S. Hu<sup>8</sup>, J. D. Holt<sup>8,9</sup>, J. Karthein<sup>10</sup>, I. Kulikov<sup>11</sup>, Yu. A. Litvinov<sup>11,12</sup>, D. Lunney<sup>13</sup>, V. Manea<sup>13</sup>, T. Miyagi<sup>14,12,5</sup>, M. Mougeot<sup>1,5,‡</sup>, L. Schweikhard<sup>2</sup>, A. Schwenk<sup>14,12,5</sup>, K. Sieja<sup>15</sup>, and F. Wienholtz<sup>14</sup>

<sup>1</sup>European Organization for Nuclear Research (CERN), 1211 Geneva 23, Switzerland

<sup>2</sup>Institut für Physik, Universität Greifswald, 17487 Greifswald, Germany

<sup>3</sup>KU Leuven, Instituut voor Kern- en Stralingsfysica, B-3001 Leuven, Belgium

<sup>4</sup>Johannes Gutenberg-Universität Mainz, 55128 Mainz, Germany

<sup>5</sup>Max-Planck-Institut für Kernphysik, 69117 Heidelberg, Germany

<sup>6</sup>School of Physics, Engineering and Technology, University of York, Heslington, York YO10 5DD, United Kingdom

<sup>7</sup>Institute of Theoretical Physics, Faculty of Physics, University of Warsaw,

Warsaw, ul. Pasteura 5, PL-02-093 Warsaw, Poland

<sup>8</sup>TRIUMF, TRIUMF 4004 Wesbrook Mall, Vancouver, British Columbia V6T 2A3, Canada

<sup>9</sup>Department of Physics, McGill University, Montréal, Quebec H3A 2T8, Canada

<sup>10</sup>Massachusetts Institute of Technology, Cambridge, Massachusetts 02139, USA

<sup>11</sup>GSI Helmholtzzentrum für Schwerionenforschung GmbH, 64291 Darmstadt, Germany

<sup>12</sup>ExtreMe Matter Institute EMMI, GSI Helmholtzzentrum für Schwerionenforschung GmbH, 64291 Darmstadt, Germany

<sup>13</sup>Université Paris-Saclay, CNRS/IN2P3, IJCLab, 91405 Orsay, France

<sup>14</sup>Institut für Kernphysik, Technische Universität Darmstadt, 64289 Darmstadt, Germany

<sup>15</sup>IPHC, CNRS/IN2P3 et Université de Strasbourg, F-67037 Strasbourg, France



(Received 2 February 2023; revised 10 April 2023; accepted 2 June 2023; published 14 July 2023)

The excitation energy of the  $1/2^-$  isomer in  $^{99}\text{In}$  at  $N = 50$  is measured to be 671(37) keV and the mass uncertainty of the  $9/2^+$  ground state is significantly reduced using the ISOLTRAP mass spectrometer at ISOLDE/CERN. The measurements exploit a major improvement in the resolution of the multireflection time-of-flight mass spectrometer. The results reveal an intriguing constancy of the  $1/2^-$  isomer excitation energies in neutron-deficient indium that persists down to the  $N = 50$  shell closure, even when all neutrons are removed from the valence shell. This trend is used to test large-scale shell model, *ab initio*, and density functional theory calculations. The models have difficulties describing both the isomer excitation energies and ground-state electromagnetic moments along the indium chain.

DOI: [10.1103/PhysRevLett.131.022502](https://doi.org/10.1103/PhysRevLett.131.022502)

Considerable experimental and theoretical efforts have concentrated on the region around  $^{100}\text{Sn}$  [1], the heaviest known self-conjugate and doubly magic nucleus ( $N = Z = 50$ ), including decay spectroscopy [2–9], laser spectroscopy [10–12], Coulomb excitation studies [13–15], and mass measurements [16–19]. The similar valence orbitals that the protons and neutrons occupy are expected to enhance the effect of proton-neutron pairing, while the proximity of the double shell closure and proton drip line make it a unique laboratory to test our understanding of the strong interaction. However, core-excitation effects, i.e., the promotion of nucleons across shell gaps, can complicate

the single- or few-particle picture even near shell closures, making accurate theoretical predictions difficult.

Theoretical approaches to calculate the properties of neutron-deficient nuclei near  $^{100}\text{Sn}$  are computationally costly due to the large configuration space required. Nevertheless, the large-scale shell model (LSSM), the Monte Carlo shell model, and *ab initio* approaches have been successfully used in the tin region to describe, e.g.,  $\beta$ -decay rates, quadrupole collectivity, and the enhanced magicity in  $^{132}\text{Sn}$  [4,20–24].

In the indium isotopic chain, the single proton hole below the  $Z = 50$  shell closure provides insight into the effective proton-neutron interaction. Mass measurements of the ground states in  $^{99}\text{In}$  and  $^{100}\text{In}$  were recently used to test *ab initio* calculations extended to a medium-mass odd- $Z$  isotopic chain [18], thus providing valuable input for shell-model coupled-cluster (CCSM) calculations [25]. Moreover, recent results from laser spectroscopy revealed

Published by the American Physical Society under the terms of the Creative Commons Attribution 4.0 International license. Further distribution of this work must maintain attribution to the author(s) and the published article's title, journal citation, and DOI.

the emergence of nuclear collectivity in neutron-rich indium isotopes, with the  $9/2^+$  ground state abruptly departing the single-particle limit below  $N = 82$  [10].

Nuclear isomers are particularly important for nuclear-structure studies [26] and their long lifetimes allow access to a broader range of experimental techniques. Measurements on the  $N = 50$  isomer are an important milestone because they will reveal the effects of completely removing neutron excitations from the valence space, especially compared to  $N = 82$ . Its excitation energy will provide direct access to the energy difference between the configurations in which the proton hole occupies the  $\pi g_{9/2}$  orbital (ground state) and  $\pi p_{1/2}$  orbital (isomer).

In this Letter, we present measurements of the isomeric excitation energies in neutron-deficient indium isotopes, including the first determination of the excitation energy of  $^{99}\text{In}^m$  at the  $N = 50$  shell closure. The experimental results are compared to state-of-the-art LSSM [27] and density functional theory (DFT) [28] calculations, as well as to *ab initio* calculations using the valence-space in-medium similarity renormalization group (VS-ISMGRG) [29,30] and the CCSM method [31]. Advances in these methods are not only of interest for nuclear shell structure investigations but are also frequently used in metrology, atomic physics, and quantum chemistry [32–34].

The neutron-deficient indium isotopes were produced at the ISOLDE radioactive ion beam facility at CERN [35,36] by impinging a 1.4 GeV proton beam onto a thick lanthanum carbide target. Elements produced by fission, spallation, and fragmentation diffused out of the heated target into a hot tantalum tube, where they were ionized by the hot surface and through an element-selective two-step laser scheme provided by ISOLDE-RILIS [37]. The radioactive ion beam was then extracted at 30 keV, mass separated, and delivered to the ISOLTRAP experiment [38]. There it was cooled and bunched in a linear radio-frequency quadrupole cooler and buncher (RFQ-cb) [39]. The bunched beam was then sent at 3.2 keV to the multireflection time-of-flight mass spectrometer (MR-TOF MS) [40]. After capturing the bunches using the in-trap lift technique and storage of a few tens of milliseconds, the beam was ejected [41] and analyzed by single-ion counting with a time-of-flight detector. For calibration and optimization,  $^{85}\text{Rb}^+$  and  $^{133}\text{Cs}^+$  ions from an offline source were used.

The mass  $m$  of the ion of interest is extracted from its measured time of flight  $t$ , compared to two reference masses  $m_1$  and  $m_2$  with flight times  $t_1$  and  $t_2$ , respectively,  $\sqrt{m} = C_{\text{TOF}}\Delta_{\text{Ref}} + \Sigma_{\text{Ref}}/2$ , where  $\Delta_{\text{Ref}} = \sqrt{m_1} - \sqrt{m_2}$ ,  $\Sigma_{\text{Ref}} = \sqrt{m_1} + \sqrt{m_2}$ , and  $C_{\text{TOF}} = (2t - t_1 - t_2)/[2(t_1 - t_2)]$  [42]. The excitation energy  $E = [(\Delta t/t_0)^2 + 2\Delta t/t_0]m_0c^2$  of an isomeric state can be directly related to the TOF difference  $\Delta t$  with respect to its ground state of mass  $m_0$  and TOF  $t_0$ , with  $c$  being the speed of light.

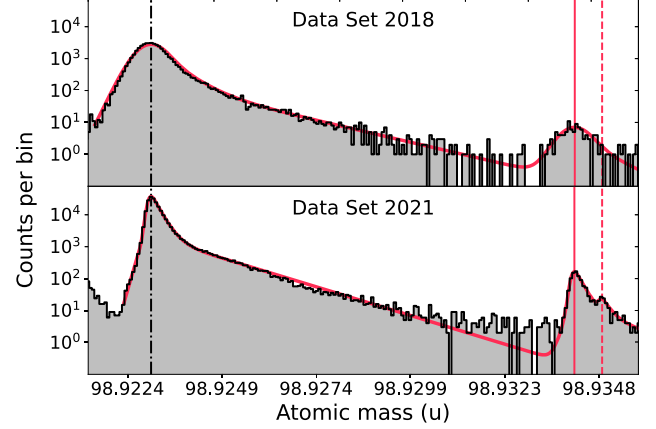


FIG. 1. Time-of-flight spectrum for the  $m/q = 99$  beam in the MR-TOF MS with a hyperEMG fit [45] (red) to the data (see text for explanation). The top panel shows the 2018 dataset before the device improvements, and the lower panel shows the dataset from this Letter. The black (dash-dotted) line highlights the TOF for the strontium fluoride molecule. The vertical red lines show the ground state TOF (solid) and isomeric state TOF (dashed) of  $^{99}\text{In}$ . The bin size is  $\sim 73 \mu\text{u}$ .

To achieve the resolving power  $R = t_0/(\Delta t_{\text{FWHM}})$  necessary to separate the indium isomers, the capabilities of the MR-TOF MS were greatly enhanced. An extended active and passive multi-mirror voltage stabilization system based on Refs. [43,44] was implemented, which reduced  $\Delta t_{\text{FWHM}}$ . This not only allowed stable continuous operation of the device for more than 70 hours but also a much higher number of revolutions, between 1500 and 3000, increasing  $t_0$ . Furthermore, the initial ion-bunch emittance was optimized by synchronizing the experimental cycle to the 50-Hz AC power line and by fine-tuning the RFQ-cb ejection with respect to its radio-frequency field.

Figure 1 shows the TOF spectrum for the ISOLDE beam with mass-to-charge ratio  $m/q = 99$  compared with the dataset from Ref. [18] to highlight the performance improvement. Surface-ionized contamination (here  $^{80}\text{Sr}^{19}\text{F}^+$ ) was identified by calculating its mass  $m$  from its observed flight time  $t$  and comparing it to the known values of potential isotopes and molecules in the mass region. Indium was identified by its TOF and RILIS laser on-off tests. With an average proton current of  $2.0 \mu\text{A}$  and about  $3 \times 10^{13}$  protons per pulse, roughly four  $^{99}\text{In}^+$  ions per second were extracted from the target on average. The ground-state-to-isomer ratio was determined to be 13:1, resulting in less than 0.3 isomers per second delivered to the spectrometer.

TOF drifts were eliminated by calculating time-rolling averages of the reference  $\text{SrF}^+$  molecule, thus quantifying the drifts and allowing to correct the TOF spectrum during the experiment, similar to Ref. [46]. For the TOF of 50 ns thus obtained for the indium ions, the resulting TOF widths of  $\Delta t_{\text{FWHM}} \approx 50 \text{ ns}$  allowed a mass resolving power of

TABLE I. Mass-measurement results for the indium isotopes given as  $C_{\text{TOF}}$  values (with mass excess calculated) for the ground states and as TOF difference  $\Delta t$  to the reference mass (with excitation energy calculated) for the isomeric states. Spin assignments  $J^\pi$ , half-lives, and reference masses are taken from the AME2020 [48] while the literature values marked with an asterisk are taken from Mougeot *et al.* [18]. Values marked with # are extrapolated or assigned from systematics. The uncertainties given for the mass excesses and the excitation energies correspond to statistical, followed by systematic uncertainties.

A	$J^\pi$	Half-life	Ref. ions	$C_{\text{TOF}}$ or $\Delta t$ (ns)	Mass excess or exc. energy (keV)	
					This Letter	Literature
99	$9/2^+\#$	3.11(6) s	$^{80}\text{Sr}^{19}\text{F}^+$ , $^{133}\text{Cs}^+$	$0.499\,646\,429(355)_{\text{stat}}(270)_{\text{syst}}$	$-61\,431(12)_{\text{stat}}(8)_{\text{syst}}$	$-61\,429(77)^*$
	$1/2^-\#$	1 s#	$^{99}\text{gsIn}^+$	$174(9)_{\text{stat}}(4)_{\text{syst}}$	$671(33)_{\text{stat}}(16)_{\text{syst}}$	$400\#(150\#)$
100	$6^+\#$	5.62(6) s	$^{81}\text{Sr}^{19}\text{F}^+$ , $^{85}\text{Rb}^+$	$0.499\,690\,777(350)_{\text{stat}}(156)_{\text{syst}}$	$-64\,191(11)_{\text{stat}}(5)_{\text{syst}}$	$-64\,178.1(22)^*$
101	$9/2^+\#$	15.1(11) s	$^{82}\text{Sr}^{19}\text{F}^+$ , $^{133}\text{Cs}^+$	$0.499\,677\,661(69)_{\text{stat}}(99)_{\text{syst}}$	$-68\,552.6(93)_{\text{stat}}(28)_{\text{syst}}$	$-68\,545.4(47)^*$
	$1/2^-\#$	10 s#	$^{101}\text{gsIn}^+$	$169.3(35)_{\text{stat}}(17)_{\text{syst}}$	$658(14)_{\text{stat}}(7)_{\text{syst}}$	$668(10.8)^*$

$5 \times 10^5$ , an improvement factor of 2.5 compared to our previous experiment [18]. The improvement helps not only the direct measurement of nuclear isomers and the isobaric purification for Penning-trap measurements but also increases long-term operation stability.

To extract the ground-state  $C_{\text{TOF}}$  value and the excitation energy of the isomeric state, a simultaneous fit of  $^{80}\text{Sr}^{19}\text{F}^+$  and both  $^{99}\text{In}^+$  states was performed. Because of the asymmetric nature of the TOF distribution, a multi-component exponentially modified Gaussian probability density function (“hyperEMG”) [45] was used. This approach captures most of the tailing towards longer TOF, while small deviations from the model in the tail showed no influence on the mean of the Gaussian contribution to the fit, i.e., the extracted absolute TOF values.

To study systematic effects on the data evaluation method, radioactive ion beams were taken for  $99 \leq m/q \leq 101$ . The results are listed in Table I. The contaminant  $\text{SrF}^+$  served as the first reference to determine the  $C_{\text{TOF}}$  values, while  $^{133}\text{Cs}^+$  from an offline ion source was used as the second reference. The relative production rates of the two indium states were similar along the investigated chain, suggesting, in combination with laser spectroscopy data [47], a  $9/2^+$  and  $1/2^-$  spin assignment to the ground and isomeric states, respectively. This is furthermore supported by a recent gamma-spectroscopy experiment of  $^{99}\text{In}$  [9], which assigns spin  $9/2^+$  to the dominantly produced state. The mass measurement results are in excellent agreement with previous studies [16–19], improving the precision of our former  $^{99}\text{In}$  ground-state mass measurement by a factor of 5. Notably, the enhanced MR-TOF MS now achieved a similar precision as the Penning-trap experiment from [18].

In the simplest shell-model picture the ground and isomeric states are formed by a proton hole in the  $\pi g_{9/2}$  and the  $\pi p_{1/2}$  shells, respectively, determining the spins and parities of the two states. The evolution of their binding energies with neutron number, presented in Fig. 2, is influenced by the filling of the  $\nu d_{5/2}$  and  $\nu g_{7/2}$  neutron

shells. The  $Z = 50$  shell gap is formed between the  $9/2^+$  states in indium and the  $5/2^+$  states in antimony, also shown in Fig. 2. The present measurements extend the data down to  $N = 50$ . Although the experimental binding energies of the two states are not linear with neutron number, the splitting between the two states is almost constant (including that of  $^{99}\text{In}$ , determined in this work to be about 670 keV), only changing at the  $N = 64$  subshell closure. This is intriguing, considering the large variation in neutron number between  $N = 50$  and  $N = 64$ .

To investigate the origin of this constant trend, we performed LSSM calculations with the effective interaction above a  $^{88}\text{Sr}$  core employed previously to obtain  $\beta$ -decay half-lives around  $N = 82$  [49,50]. To study neutron-deficient indium isotopes, the single-particle energies were adjusted to reproduce the spectrum of  $^{91}\text{Zr}$ , while the  $V_{g_{9/2}-g_{7/2}} T = 0$  proton-neutron monopole interaction was made more attractive (by  $-600$  keV) to match the observed shell evolution between  $^{91}\text{Zr}$  and  $^{101}\text{Sn}$ . The calculations

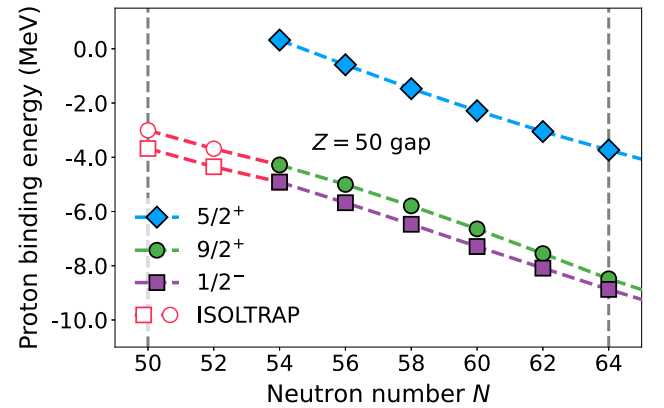


FIG. 2. Proton binding energies for nuclear states of the indium ( $Z = 49$ , green and purple) and antimony ( $Z = 51$ , blue) isotopic chains. Data taken from Ref. [48] (solid symbols) and this work (open symbols, red). The vertical dashed lines indicate the spherical shell closure at  $N = 50$  and the subshell closure at  $N = 64$ .

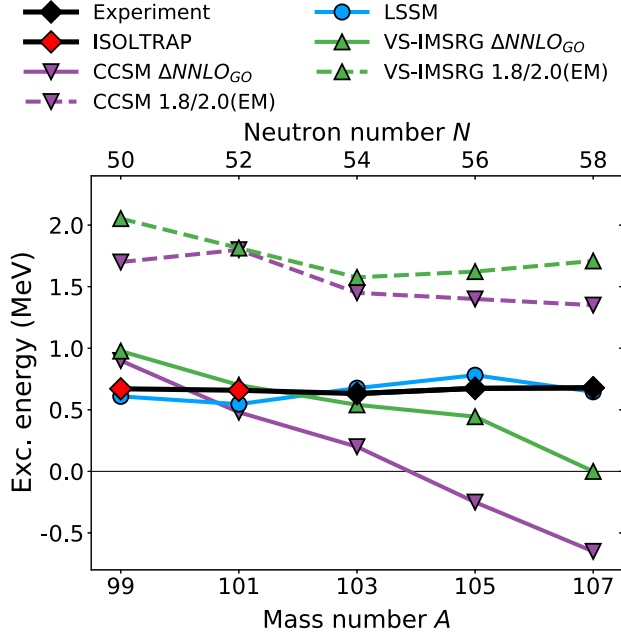


FIG. 3. Excitation energies for the  $1/2^-$  states in odd-even neutron-deficient indium isotopes compared to large-scale shell model and *ab initio* calculations. The CCSM results are taken from [25].

were performed using the Strasbourg shell-model codes Antoine and NATHAN [27,51], maximally allowing for 4-particle–4-hole excitations for both neutrons and protons across the  $N = Z = 50$  gap (3-particle–3-hole for  $A = 105, 107$ ). The excitation energies are converged within 50 keV in all nuclei. The resulting energy splitting, shown in blue in Fig. 3, is very close to the experimental results.

The LSSM predicts states with very similar proton orbital occupation across the indium chain. The neutrons above  $N = 50$  are located predominantly in the  $\nu d_{5/2}$  and  $\nu g_{7/2}$  orbitals, having little effect on the proton occupancy. The results indicate that the attractive monopole interaction between the  $\pi g_{9/2}$  and the  $\nu g_{7/2}$  nucleons is roughly compensated by the sum of the likewise attractive  $T = 0$   $\pi p_{1/2} - \nu d_{5/2}$  and  $\pi p_{1/2} - \nu g_{7/2}$  monopoles, which is likely the reason for the similar energy splittings of the two states. The slight variations of the  $1/2^-$  energy may further relate to modifications of the relative population of neutron orbitals along the isotopic chain. This complex picture makes the excitation energy of the  $1/2^-$  isomeric state an interesting benchmark for *ab initio* methods, which have only recently been applied to this region [18,22,25].

Thus, we present *ab initio* calculations using the VS-IMSRG and also compare to the CCSM results of Ref. [25], using the 1.8/2.0(EM) [52,53] and  $\Delta\text{NNLO}_{GO}$  interactions [54]. The VS-IMSRG calculations are performed in a 15 major-shell harmonic oscillator (HO) space. For the three-nucleon matrix elements, an additional  $E_{3\text{max}}$  truncation is required, defined as the sum of three-body HO

principal quantum numbers. Here we use  $E_{3\text{max}} = 24$  which is sufficiently large in the  $A \sim 100$  region [55] to achieve converged results. To explicitly capture the effect of excitations across the  $N = Z = 50$  gap, both the proton and neutron  $1p_{1/2}$ ,  $1p_{3/2}$ ,  $1d_{5/2}$ ,  $0g_{7/2}$ , and  $0g_{9/2}$  spaces were decoupled above a  $^{88}\text{Se}$  core using the multishell approach of Ref. [56]. While the full valence-space diagonalization is impossible, up to 5-particle–5-hole excitations across the  $N = Z = 50$  gap were included. We observed that the excitation energies are converged to  $\approx 70$  keV with respect to the particle-hole truncation.

As shown in Fig. 3, the two employed interactions result in similar energy-splitting trends for both the VS-IMSRG and CCSM methods. The  $\Delta\text{NNLO}_{GO}$  interaction tends to be more accurate at the expense of a linear decrease of excitation energy with  $N$  leading to an inversion, which is at odds with the data. On the other hand, the 1.8/2.0(EM) interaction reproduces the rather flat trend of the splitting better and does not result in any state inversion, but overpredicts the magnitude of the splitting.

The state crossing in  $^{107}\text{In}$  from the calculations with  $\Delta\text{NNLO}_{GO}$  can be understood by comparing the diagonal monopole matrix elements of the  $\Delta\text{NNLO}_{GO}$  and 1.8/2.0 (EM) valence-space interactions. Similar to what is found in the LSSM calculations, the flatness of the excitation energies for the 1.8/2.0 (EM) interaction results from the relevant monopole matrix elements and the balanced occupancy of  $\nu g_{7/2}$  and  $\nu d_{5/2}$ . This similarity is reinforced by the observation that both interactions reproduce the energy splitting  $\nu g_{7/2} - \nu d_{5/2}$  of the single-neutron state in  $^{101}\text{Sn}$  [57] within 100 keV. Although the relevant matrix elements are almost the same for 1.8/2.0 (EM) and  $\Delta\text{NNLO}_{GO}$ , the weaker  $\nu p_{3/2} - \nu g_{7/2}$  monopole repulsion of the latter reduces the mixing between  $\nu g_{7/2}$  and  $\nu d_{5/2}$ , leading to a larger  $\nu g_{7/2} - \nu d_{5/2}$  splitting. In this case, the filled  $\nu g_{7/2}$  configuration leads to a linear decrease.

For a broader view, in Fig. 4 we show the energy splitting across the full indium chain with recent nuclear moment measurements from Ref. [10], compared to theoretical calculations. (Note that for Ref. [10], the VS-IMSRG calculations were performed in a different valence space than the results shown in Fig. 3, leading to a slightly different energy splitting for  $A \leq 107$ .) In addition, we extend the DFT calculations of Ref. [10] to  $N = 50$ . Those were performed within the Hartree-Fock approximation for both protons and neutrons and thus they stagger with  $N$  owing to occupying consecutive individual single-particle deformed neutron orbitals. The complementary data show another remarkable constancy: that of the magnetic dipole moments of the  $9/2^+$  ground state which are significantly lower than those expected in the single-particle configuration (the so-called Schmidt limit [58]), except for the value at the  $N = 82$  closed shell. The excitation energy at  $N = 82$ , similar to  $N = 50$ , stays rather constant. From the VS-IMSRG calculations, this can be explained by the

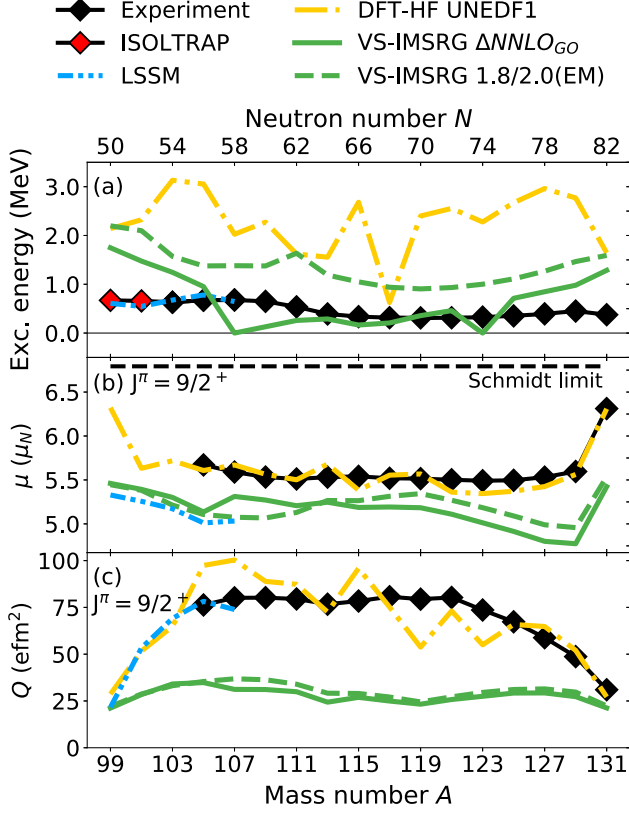


FIG. 4. Isomer excitation energies (a) and ground-state electromagnetic moments (b) and (c) of odd-even indium isotopes, compared to theoretical calculations. The experimental data are from [59] (black) and this work (red) for the excitation energies and from [10] for the moments. Both DFT-HF and VS-IMSRG calculations are from [10] and are extended in this work to reach  $N = 50$ .

monopole strengths, which are almost the same at  $N = 50$  and  $N = 82$ , and are only weakly dependent on the number of neutrons.

While the differences between the excitation energy measurements and the DFT calculations are quite large for the density functional UNEDF1 [60] used here, a rather constant trend remains at the same level as the *ab initio* results [see Fig. 4(a)]. We note that in the DFT calculations, the isomer excitation energy is directly related to the strength of the spin-orbit interaction (see the discussion of the analogous excitation energy in silver isotopes [12]). Therefore, the measurements presented in this Letter provide an important anchor point for future global readjustments of nuclear density functionals.

By including time-odd fields, the DFT approach accurately reproduces the  $9/2^+$  dipole moments  $\mu$ . In contrast, the LSSM and VS-IMSRG calculations underestimate the absolute value but reproduce the general trend well [see Fig. 4(b)]. The sudden increase of the magnetic moment at  $N = 82$  is well described by the DFT calculations, which

predict a similar occurrence at  $N = 50$ . Intriguingly, the LSSM and *ab initio* calculations show a much smoother evolution towards  $N = 50$ . While the excitation energy is flat at  $N = 82$  due to the cancellation of the monopoles in the VS-IMSRG calculations, the  $9/2^+$  dipole moments are much more sensitive to the neutron configuration.

The DFT and LSSM calculations reproduce the quadrupole moments  $Q$  reasonably well, while the VS-IMSRG describes neither the absolute values nor the trend [see Fig. 4(c)]. This is most likely due to collective effects that are not fully captured when calculating the E2 matrix elements at the IMSRG(2) level [61].

In summary, the excitation energy of the  $1/2^-$  isomer in  $^{99}\text{In}$  has been measured for the first time, thanks to significant upgrades of the ISOLTRAP MR-TOF MS at ISOLDE/CERN. The systematics of the isomer excitation energy now reach the crucial  $N = 50$  shell closure, confirming its constancy—even with no neutrons left in the valence shell. The shell model and the *ab initio* calculations using the 1.8/2.0(EM) interaction describe the constancy with the compensation of the monopole proton-neutron interactions, via a balanced occupation of the valence neutron orbitals. The  $\Delta\text{NNLO}_{GO}$  interaction results in a different occupation and leads to a linear decrease with neutron number, at odds with the experiment. Examining the electromagnetic moments of the  $9/2^+$  ground states and including DFT calculations in the comparisons, we find that all models struggle to describe both energy and electromagnetic observables consistently. Measurements of nuclear moments of the  $1/2^-$  and  $9/2^+$  states down to  $N = 50$  are needed to further benchmark the trends predicted by the calculations, as well as future theoretical developments.

We thank the ISOLDE technical group and the ISOLDE Collaboration for their support. We acknowledge the support of the German Max Planck Society, the French Institut National de Physique Nucléaire et de Physique des Particules (IN2P3), the European Research Council (ERC) under the European Union's Horizon 2020 research and innovation programme (Grant Agreements No. 682841 'ASTRUM', 654002 'ENSAR2', 101020842 'EUSTRONG', and 861198 'LISA'), as well as the German Federal Ministry of Education and Research (BMBF; Grants No. 05P18HGCIA, 05P21HGCII, and 05P21RDFNB). L.N. acknowledges support from the Wolfgang Gentner Programme of the German Federal Ministry of Education and Research (Grant No. 13E18CHA). This work was partially supported by the STFC Grants No. ST/P003885/1 and No. ST/V001035/1, by the Polish National Science Centre under Contract No. 2018/31/B/ST2/02220, and by a Leverhulme Trust Research Project Grant. The VS-IMSRG computations were in part performed with an allocation of computing resources at the Jülich Supercomputing Center and with an allocation of computing resources on Cedar at WestGrid

and Compute Canada using `imsrg++` [62] and `KSHELL` [63] codes. We acknowledge the CSC-IT Center for Science Ltd., Finland, for allocating computational resources. This project was partly undertaken on the Viking Cluster, which is a high-performance computing facility provided by the University of York. We are grateful for computational support from the University of York High Performance Computing service, Viking, and the Research Computing team. The experiment was conducted by M. A.-K., M. Au, D. A., K. B., I. K., Yu. A. L., D. L., V. M., M. M., L. N., and F. W. The theoretical calculations were performed by J. D., B. S. H., J. D. H, T. M., A. S., and K. S. All authors contributed to the preparation of the manuscript.

\*Lukas.Nies@cern.ch

†Present address: LP2i Bordeaux, UMR5797, Université de Bordeaux, CNRS, France.

‡Present address: University of Jyväskylä, Department of Physics, Accelerator laboratory, P.O. Box 35(YFL), FI-40014, Finland.

- [1] T. Faestermann, M. Górski, and H. Grawe, The structure of  $^{100}\text{Sn}$  and neighbouring nuclei, *Prog. Part. Nucl. Phys.* **69**, 85 (2013).
- [2] I. G. Darby, R. K. Grzywacz, J. C. Batchelder, C. R. Bingham, L. Cartegni, C. J. Gross, M. Hjorth-Jensen, D. T. Joss, S. N. Liddick, W. Nazarewicz, S. Padgett, R. D. Page, T. Papenbrock, M. M. Rajabali, J. Rotureau, and K. P. Rykaczewski, Orbital Dependent Nucleonic Pairing in the Lightest Known Isotopes of Tin, *Phys. Rev. Lett.* **105**, 162502 (2010).
- [3] G. Lorusso *et al.*,  $\beta$ -delayed proton emission in the  $^{100}\text{Sn}$  region, *Phys. Rev. C* **86**, 014313 (2012).
- [4] C. B. Hinke *et al.*, Superaligned Gamow–Teller decay of the doubly magic nucleus  $^{100}\text{Sn}$ , *Nature (London)* **486**, 341 (2012).
- [5] J. Park *et al.*,  $\beta$  decays of the heaviest  $N = Z - 1$  nuclei and proton instability of  $^{97}\text{In}$ , *Phys. Rev. C* **97**, 051301 (2018).
- [6] K. Auranen *et al.*, Superaligned  $\alpha$  Decay to Doubly Magic  $^{100}\text{Sn}$ , *Phys. Rev. Lett.* **121**, 182501 (2018).
- [7] D. Lubos *et al.*, Improved Value for the Gamow–Teller Strength of the  $^{100}\text{Sn}$  Beta Decay, *Phys. Rev. Lett.* **122**, 222502 (2019).
- [8] J. Park *et al.*, New and comprehensive  $\beta$ - and  $\beta p$ -decay spectroscopy results in the vicinity of  $^{100}\text{Sn}$ , *Phys. Rev. C* **99**, 034313 (2019).
- [9] J. Park *et al.*, Spectroscopy of  $^{99}\text{Cd}$  and  $^{101}\text{In}$  from  $\beta$  decays of  $^{99}\text{In}$  and  $^{101}\text{Sn}$ , *Phys. Rev. C* **102**, 014304 (2020).
- [10] A. R. Vernon *et al.*, Nuclear moments of indium isotopes reveal abrupt change at magic number 82, *Nature (London)* **607**, 260 (2022).
- [11] X. Yang, S. Wang, S. Wilkins, and R. G. Ruiz, Laser spectroscopy for the study of exotic nuclei, *Prog. Part. Nucl. Phys.* **129**, 104005 (2023).
- [12] R. de Groote *et al.*, Measurements of Binding Energies and Electromagnetic Moments of Silver Isotopes—A Complementary Benchmark of Density Functional Theory (to be published).
- [13] C. Vaman *et al.*,  $Z = 50$  Shell Gap near  $^{100}\text{Sn}$  from Intermediate-Energy Coulomb Excitations in Even-Mass  $^{106-112}\text{Sn}$  Isotopes, *Phys. Rev. Lett.* **99**, 162501 (2007).
- [14] V. M. Bader, A. Gade, D. Weisshaar, B. A. Brown, T. Baugher, D. Bazin, J. S. Berryman, A. Ekström, M. Hjorth-Jensen, S. R. Stroberg, W. B. Walters, K. Wimmer, and R. Winkler, Quadrupole collectivity in neutron-deficient Sn nuclei:  $^{104}\text{Sn}$  and the role of proton excitations, *Phys. Rev. C* **88**, 051301(R) (2013).
- [15] G. Guastalla *et al.*, Coulomb Excitation of  $^{104}\text{Sn}$  and the Strength of the  $^{100}\text{Sn}$  Shell Closure, *Phys. Rev. Lett.* **110**, 172501 (2013).
- [16] X. Xu *et al.*, Masses of ground and isomeric states of  $^{101}\text{In}$  and configuration-dependent shell evolution in odd- $A$  indium isotopes, *Phys. Rev. C* **100**, 051303(R) (2019).
- [17] C. Hornung *et al.*, Isomer studies in the vicinity of the doubly-magic nucleus  $^{100}\text{Sn}$ : Observation of a new low-lying isomeric state in  $^{97}\text{Ag}$ , *Phys. Lett. B* **802**, 135200 (2020).
- [18] M. Mougeot *et al.*, Mass measurements of  $^{99-101}\text{In}$  challenge *ab initio* nuclear theory of the nuclide  $^{100}\text{Sn}$ , *Nat. Phys.* **17**, 1099 (2021).
- [19] Y. M. Xing *et al.*, Isochronous mass measurements of neutron-deficient nuclei from  $^{112}\text{Sn}$  projectile fragmentation, *Phys. Rev. C* **107**, 014304 (2023).
- [20] L. Coraggio, A. Covello, A. Gargano, N. Itaco, and T. T. S. Kuo, Shell-model study of quadrupole collectivity in light tin isotopes, *Phys. Rev. C* **91**, 041301(R) (2015).
- [21] T. Togashi, Y. Tsunoda, T. Otsuka, N. Shimizu, and M. Honma, Novel Shape Evolution in Sn Isotopes from Magic Numbers 50 to 82, *Phys. Rev. Lett.* **121**, 062501 (2018).
- [22] T. D. Morris, J. Simonis, S. R. Stroberg, C. Stumpf, G. Hagen, J. D. Holt, G. R. Jansen, T. Papenbrock, R. Roth, and A. Schwenk, Structure of the Lightest Tin Isotopes, *Phys. Rev. Lett.* **120**, 152503 (2018).
- [23] P. Gysbers, G. Hagen, J. D. Holt, G. R. Jansen, T. D. Morris, P. Navrátil, T. Papenbrock, S. Quaglioni, A. Schwenk, S. R. Stroberg, and K. A. Wendt, Discrepancy between experimental and theoretical  $\beta$ -decay rates resolved from first principles, *Nat. Phys.* **15**, 428 (2019).
- [24] A. P. Zuker, Quadrupole dominance in the light Sn and in the Cd isotopes, *Phys. Rev. C* **103**, 024322 (2021).
- [25] Z. H. Sun, G. Hagen, G. R. Jansen, and T. Papenbrock, Effective shell-model interaction for nuclei “southeast” of  $^{100}\text{Sn}$ , *Phys. Rev. C* **104**, 064310 (2021).
- [26] A. Jain, B. Maheshwari, and A. Goel, *Nuclear Isomers: A Primer* (Springer International Publishing, New York, 2021).
- [27] E. Caurier, G. Martínez-Pinedo, F. Nowacki, A. Poves, and A. P. Zuker, The shell model as a unified view of nuclear structure, *Rev. Mod. Phys.* **77**, 427 (2005).
- [28] N. Schunck, ed., *Energy Density Functional Methods for Atomic Nuclei* (IOP Publishing, Bristol, 2019).
- [29] S. R. Stroberg, A. Calci, H. Hergert, J. D. Holt, S. K. Bogner, R. Roth, and A. Schwenk, A Nucleus-Dependent Valence-Space Approach to Nuclear Structure, *Phys. Rev. Lett.* **118**, 032502 (2017).

- [30] S. R. Stroberg, H. Hergert, S. K. Bogner, and J. D. Holt, Nonempirical interactions for the nuclear shell model: An update, *Annu. Rev. Nucl. Part. Sci.* **69**, 307 (2019).
- [31] Z. H. Sun, T. D. Morris, G. Hagen, G. R. Jansen, and T. Papenbrock, Shell-model coupled-cluster method for open-shell nuclei, *Phys. Rev. C* **98**, 054320 (2018).
- [32] S. Patra, M. Germann, J.-P. Karr, M. Haidar, L. Hilico, V. I. Korobov, F. M. J. Cozijn, K. S. E. Eikema, W. Ubachs, and J. C. J. Koelmeij, Proton-electron mass ratio from laser spectroscopy of  $\text{HD}^+$  at the part-per-trillion level, *Science* **369**, 1238 (2020).
- [33] R. X. Schüssler *et al.*, Detection of metastable electronic states by penning trap mass spectrometry, *Nature (London)* **581**, 42 (2020).
- [34] R. J. Bartlett and M. Musiał, Coupled-cluster theory in quantum chemistry, *Rev. Mod. Phys.* **79**, 291 (2007).
- [35] M. J. G. Borge and K. Blaum, Focus on exotic beams at ISOLDE: A laboratory portrait, *J. Phys. G* **45**, 010301 (2017).
- [36] R. Catherall, W. Andreatza, M. Breitenfeldt, A. Dorsival, G. J. Focker, T. P. Gharsa, G. T. J. J.-L. Grenard, F. Locci, P. Martins, S. Marzari, J. Schipper, A. Shornikov, and T. Stora, The ISOLDE facility, *J. Phys. G* **44**, 094002 (2017).
- [37] V. Fedosseev, K. Chrysalidis, T. D. Goodacre, B. Marsh, S. Rothe, C. Seiffert, and K. Wendt, Ion beam production and study of radioactive isotopes with the laser ion source at ISOLDE, *J. Phys. G* **44**, 084006 (2017).
- [38] M. Mukherjee, D. Beck, K. Blaum, G. Bollen, J. Dilling, S. George, F. Herfurth, A. Herlert, A. Kellerbauer, H.-J. Kluge, S. Schwarz, L. Schweikhard, and C. Yazidjian, ISOLTRAP: An on-line Penning trap for mass spectrometry on short-lived nuclides, *Eur. Phys. J. A* **35**, 1 (2008).
- [39] F. Herfurth, J. Dilling, A. Kellerbauer, G. Bollen, S. Henry, H.-J. Kluge, E. Lamour, D. Lunney, R. Moore, C. Scheidenberger, S. Schwarz, G. Sikler, and J. Szerypo, A linear radiofrequency ion trap for accumulation, bunching, and emittance improvement of radioactive ion beams, *Nucl. Instrum. Methods Phys. Res., Sect. A* **469**, 254 (2001).
- [40] R. Wolf, F. Wienholtz, D. Atanasov, D. Beck, K. Blaum, C. Borgmann, F. Herfurth, M. Kowalska, S. Kreim, Y. A. Litvinov, D. Lunney, V. Manea, D. Neidherr, M. Rosenbusch, L. Schweikhard, J. Stanja, and K. Zuber, ISOLTRAP's multi-reflection time-of-flight mass separator/spectrometer, *Int. J. Mass Spectrom.* **349–350**, 123 (2013).
- [41] F. Wienholtz, S. Kreim, M. Rosenbusch, L. Schweikhard, and R. Wolf, Mass-selective ion ejection from multi-reflection time-of-flight devices via a pulsed in-trap lift, *Int. J. Mass Spectrom.* **421**, 285 (2017).
- [42] F. Wienholtz *et al.*, Masses of exotic calcium isotopes pin down nuclear forces, *Nature (London)* **498**, 346 (2013).
- [43] F. Wienholtz, K. Blaum, J. Kartheim, D. Lunney, S. Malbrunot-Ettenauer, V. Manea, M. Mougeot, L. Schweikhard, T. Steinsberger, and R. Wolf, Improved stability of multi-reflection time-of-flight mass spectrometers through passive and active voltage stabilization, *Nucl. Instrum. Methods Phys. Res., Sect. B* **463**, 348 (2020).
- [44] P. Fischer and L. Schweikhard, Multiple active voltage stabilizations for multi-reflection time-of-flight mass spectrometry, *Rev. Sci. Instrum.* **92**, 063203 (2021).
- [45] S. Purushothaman, S. Ayet San Andrés, J. Bergmann, T. Dickel, J. Ebert, H. Geissel, C. Hornung, W. Plaß, C. Rappold, C. Scheidenberger, Y. Tanaka, and M. Yavor, Hyper-EMG: A new probability distribution function composed of exponentially modified Gaussian distributions to analyze asymmetric peak shapes in high-resolution time-of-flight mass spectrometry, *Int. J. Mass Spectrom.* **421**, 245 (2017).
- [46] P. Fischer, S. Knauer, G. Marx, and L. Schweikhard, Non-isobaric time-of-flight correction for isobar resolving in MR-ToF mass spectrometry, *Int. J. Mass Spectrom.* **432**, 44 (2018).
- [47] J. Eberz, U. Dinger, G. Huber, H. Lochmann, R. Menges, R. Neugart, R. Kirchner, O. Klepper, T. Kühl, D. Marx, G. Ulm, and K. Wendt, Spins, moments and mean square charge radii of  $104\text{--}127\text{In}$  determined by laser spectroscopy, *Nucl. Phys. A* **464**, 9 (1987).
- [48] M. Wang, W. Huang, F. Kondev, G. Audi, and S. Naimi, The AME 2020 atomic mass evaluation (II). Tables, graphs and references, *Chin. Phys. C* **45**, 030003 (2021).
- [49] F. Naqvi *et al.*, Isomer spectroscopy of  $^{127}\text{Cd}$ , *Phys. Rev. C* **82**, 034323 (2010).
- [50] Q. Zhi, E. Caurier, J. J. Cuenca-García, K. Langanke, G. Martínez-Pinedo, and K. Sieja, Shell-model half-lives including first-forbidden contributions for  $r$ -process waiting-point nuclei, *Phys. Rev. C* **87**, 025803 (2013).
- [51] E. Caurier and F. Nowacki, Present status of shell model techniques, *Acta Phys. Pol. B* **30**, 705 (1999), <https://www.actaphys.uj.edu.pl/R/30/3/705/pdf>.
- [52] K. Hebeler, S. K. Bogner, R. J. Furnstahl, A. Nogga, and A. Schwenk, Improved nuclear matter calculations from chiral low-momentum interactions, *Phys. Rev. C* **83**, 031301(R) (2011).
- [53] J. Simonis, S. R. Stroberg, K. Hebeler, J. D. Holt, and A. Schwenk, Saturation with chiral interactions and consequences for finite nuclei, *Phys. Rev. C* **96**, 014303 (2017).
- [54] W. G. Jiang, A. Ekström, C. Forssén, G. Hagen, G. R. Jansen, and T. Papenbrock, Accurate bulk properties of nuclei from  $A = 2$  to  $\infty$  from potentials with  $\Delta$  isobars, *Phys. Rev. C* **102**, 054301 (2020).
- [55] T. Miyagi, S. R. Stroberg, P. Navrátil, K. Hebeler, and J. D. Holt, Converged *ab initio* calculations of heavy nuclei, *Phys. Rev. C* **105**, 014302 (2022).
- [56] T. Miyagi, S. R. Stroberg, J. D. Holt, and N. Shimizu, *Ab initio* multishell valence-space Hamiltonians and the island of inversion, *Phys. Rev. C* **102**, 034320 (2020).
- [57] D. Seweryniak, M. P. Carpenter, S. Gros, A. A. Hecht, N. Hoteling, R. V. F. Janssens, T. L. Khoo, T. Lauritsen, C. J. Lister, G. Lotay, D. Peterson, A. P. Robinson, W. B. Walters, X. Wang, P. J. Woods, and S. Zhu, Single-Neutron States in  $^{101}\text{Sn}$ , *Phys. Rev. Lett.* **99**, 022504 (2007).
- [58] G. Neyens, Nuclear magnetic and quadrupole moments for nuclear structure research on exotic nuclei, *Rep. Prog. Phys.* **66**, 633 (2003).

- [59] From ENSDF database as of January 26th, 2022. Version available at <http://www.nndc.bnl.gov/ensarchivals/> (2022).
- [60] M. Kortelainen, J. McDonnell, W. Nazarewicz, P.-G. Reinhard, J. Sarich, N. Schunck, M. V. Stoitsov, and S. M. Wild, Nuclear energy density optimization: Large deformations, *Phys. Rev. C* **85**, 024304 (2012).
- [61] S. R. Stroberg, J. Henderson, G. Hackman, P. Ruotsalainen, G. Hagen, and J. D. Holt, Systematics of  $E2$  strength in the  $sd$  shell with the valence-space in-medium similarity renormalization group, *Phys. Rev. C* **105**, 034333 (2022).
- [62] S. R. Stroberg, <https://github.com/ragnarstroberg/imsrg>.
- [63] N. Shimizu, T. Mizusaki, Y. Utsuno, and Y. Tsunoda, Thick-restart block Lanczos method for large-scale shell-model calculations, *Comput. Phys. Commun.* **244**, 372 (2019).

#### 7.4 Further evidence for shape coexistence in $^{79}\text{Zn}^m$ near doubly-magic $^{78}\text{Ni}$



# Further evidence for shape coexistence in $^{79}\text{Zn}^m$ near doubly-magic $^{78}\text{Ni}$

L. Nies,<sup>1,2,\*</sup> L. Canete,<sup>3,4</sup> D. D. Dao,<sup>5</sup> S. Giraud,<sup>6,†</sup> A. Kankainen,<sup>3,‡</sup> D. Lunney,<sup>7</sup> F. Nowacki,<sup>5</sup>  
 B. Bastin,<sup>6</sup> M. Stryczyk,<sup>3</sup> P. Ascher,<sup>8</sup> K. Blaum,<sup>9</sup> R. B. Cakirli,<sup>10</sup> T. Eronen,<sup>3</sup> P. Fischer,<sup>2</sup> M. Flayol,<sup>8</sup>  
 V. Girard Alcindor,<sup>6</sup> A. Herlert,<sup>11</sup> A. Jokinen,<sup>3</sup> A. Khanam,<sup>3,12,13</sup> U. Köster,<sup>1,14</sup> D. Lange,<sup>9</sup> I. D. Moore,<sup>3</sup>  
 M. Müller,<sup>9</sup> M. Mougéot,<sup>3,9</sup> D.A. Nesterenko,<sup>3</sup> F. de Oliveira,<sup>6</sup> H. Penttilä,<sup>3</sup> C. Petrone,<sup>15</sup> I. Pohjalainen,<sup>3</sup>  
 A. de Roubin,<sup>3,§</sup> V. Rubchenya,<sup>3,¶</sup> Ch. Schweiger,<sup>9</sup> L. Schweikhard,<sup>2</sup> M. Vilen,<sup>3</sup> and J. Äystö<sup>3</sup>

<sup>1</sup>European Organization for Nuclear Research (CERN), Meyrin, 1211 Geneva, Switzerland

<sup>2</sup>Institut für Physik, Universität Greifswald, 17487 Greifswald, Germany

<sup>3</sup>University of Jyväskylä, Department of Physics, Accelerator laboratory,  
 P.O. Box 35(YFL) FI-40014 University of Jyväskylä, Finland

<sup>4</sup>Department of Physics, University of Surrey, Guildford, GU2 7X5, United Kingdom

<sup>5</sup>Université de Strasbourg, CNRS, IPHC UMR 7178, F-67000 Strasbourg, France

<sup>6</sup>GANIL, Bd Henri Becquerel, BP 55027, F-14076 Caen Cedex 5, France

<sup>7</sup>Université Paris-Saclay, CNRS/IN2P3, IJCLab, 91405 Orsay, France

<sup>8</sup>Université de Bordeaux, CNRS/IN2P3—Université, CNRS/IN2P3,  
 LP2I Bordeaux, UMR 5797, F-33170 Gradignan, France

<sup>9</sup>Max-Planck-Institut für Kernphysik, 69117 Heidelberg, Germany

<sup>10</sup>Department of Physics, Istanbul University, Istanbul 34134, Turkey

<sup>11</sup>FAIR GmbH, Planckstraße 1, 64291 Darmstadt, Germany

<sup>12</sup>Department of Applied Physics, Aalto University, P.O. Box 15100, FI-00076 Aalto, Finland

<sup>13</sup>Department of Physics, University of Helsinki, P.O. Box 43, FI-00014 Helsinki, Finland

<sup>14</sup>Institut Laue-Langevin, 38000 Grenoble, France

<sup>15</sup>IFIN-HH, P.O. Box MG-6, 077125 Bucharest-Magurele, Romania

(Dated: July 24, 2023)

Isomers close to the doubly-magic  $^{78}\text{Ni}$  ( $Z = 28$ ,  $N = 50$ ) provide essential information on the shell evolution and shape coexistence near the  $Z = 28$  and  $N = 50$  double shell closure. We report the excitation energy measurement of the  $1/2^+$  isomer in  $^{79}\text{Zn}_{49}$  through independent high-precision mass measurements with the JYFLTRAP double Penning trap and with the ISOLTRAP Multi-Reflection Time-of-Flight Mass Spectrometer. We unambiguously place the  $1/2^+$  isomer at 942(10) keV, slightly below the  $5/2^+$  state at 983(3) keV. With the use of state-of-the-art shell-model diagonalizations, complemented with Discrete Non Orthogonal shell-model calculations, we find low-lying deformed intruder states, similar to other  $N = 49$  isotones. The  $1/2^+$  isomer is interpreted as the band-head of a low-lying deformed structure akin to a predicted low-lying deformed band in  $^{80}\text{Zn}$ , and points to shape coexistence in  $^{79,80}\text{Zn}$  similar to the one observed in  $^{78}\text{Ni}$ . The results make a strong case for confirming the claim of shape coexistence in this key region of the nuclear chart.

The atomic nucleus, a conglomerate of protons and neutrons, is a complex many-body system with unique features. The nuclear shell model has successfully described various nuclear properties, including the emergence of shell closures [1] and magic numbers [2].

Similar to the atomic shell, nuclei can be excited, resulting in a dense level structure. Ground and excited states can show different shapes resulting from the microscopic wave function [3]. Deformed excited states often emerge near closed shells, where the excitation of multiple nucleons across the shell gap can be energetically favorable, leading to deformation through the increased number of particles found in the valence space [4]. While typically the coexistence of ground states and deformed excited states at low energies are observed, shape inversion can appear when the ground state becomes deformed in coexistence with a spherical excited state [4–6]

Research on shape coexistence close to the doubly-magic nucleus  $^{78}\text{Ni}_{50}$  has gained momentum only recently [7]. Low-lying intruder states, often indicators of

shape coexistence, have been studied in  $N = 49$  isotones through transfer-reaction experiments [8–11]. First evidence supporting shape coexistence, such as the claimed discovery of a  $0_2^+$  intruder state in  $^{80}\text{Ge}_{48}$  from Ref. [12], could, however, not be confirmed in subsequent experiments [13, 14].

More recently, the doubly-magic nature of  $^{78}\text{Ni}$  was supported through the measurement of its  $E(2_1^+)$  value [15], as well as  $\gamma$ -ray spectroscopy [16] and mass spectrometry of  $^{79}\text{Cu}_{50}$  [17], reinforcing the persistence of the  $Z = 28$  gap. The potential appearance of shape coexistence in  $^{78}\text{Ni}$  is furthermore theorized to be a pathway into a new island of inversion at  $N = 50$  [18].

The isomer in  $^{79}\text{Zn}_{49}$ , a long-lived nuclear state, provides a unique opportunity to further study the interplay between the single-particle and collective degrees of freedom in the close vicinity of  $^{78}\text{Ni}$ . The first spectroscopy of  $^{79}\text{Zn}$  from (d,p) transfer reactions found evidence for the presence of intruder states and tentatively assigned a spin-parity of  $1/2^+$  to the isomeric state with an excita-

tion energy of 1100(150) keV, as well as a close-lying  $5/2^+$  state with 983(3) keV [19], leaving the exact state ordering uncertain. The spin-parity was confirmed for the  $9/2^+$  ground and the  $1/2^+$  isomeric states through magnetic moment measurements from collinear laser spectroscopy [20, 21]. More significantly, these works found a large isomer shift in the charge radius but could not connect this increase to a deformation unambiguously.

Recent studies have shown that shape changes may be linked to multiple particle-hole excitations of both protons and neutrons [22–26]. However, a precise and accurate excitation energy measurement of the  $1/2^+$  isomer to confirm claims of shape coexistence in  $^{79}\text{Zn}$  is missing from the above-mentioned work. Such measurement will unambiguously determine the state ordering, validate the particle-hole excitation character, and benchmark the binding energy predictions of the employed shell-model interactions near  $^{78}\text{Ni}$ .

While the ground-state mass of  $^{79}\text{Zn}$  is precisely known [27–29] via mass measurements, the uncertainty on the excitation energy from the transfer-reaction experiment is rather large. Given the importance of shape coexistence in the immediate vicinity of  $^{78}\text{Ni}$ , we present two independent high-precision mass spectrometry experiments of the isomer  $^{79}\text{Zn}^m$  using the JYFLTRAP double Penning trap [30] at the Ion Guide Isotope Separator On-Line (IGISOL) facility [31] in Jyväskylä (Finland), and the Multi-Reflection Time-of-Flight Mass Spectrometer (MR-ToF MS) of ISOLTRAP [32] at ISOLDE/CERN [33] (Switzerland). The experiments were performed at different facilities and with different techniques to ensure the isomer's production and the accuracy of its excitation energy. The results are interpreted by large-scale shell model calculations, utilizing the valence space of interactions used in Refs. [17, 18, 20, 21]. While offering a more detailed and accurate picture of the nuclear structure in this critical region, the calculations highlight the relative fragility of the doubly-magic shell strength.

*For the Penning-trap measurements*, the ions of interest were produced via proton-induced fission using 35-MeV protons from the K130 cyclotron impinging onto a  $15\text{ mg cm}^{-2}$  thick  $^{nat}\text{U}$  target at IGISOL. The reaction products were stopped and thermalized in the helium gas cell of the fission ion guide [35], leaving a large fraction of the products singly charged. The ions were extracted from the chamber with a sextupole ion guide [36] and accelerated to 30 keV. A  $55^\circ$  dipole magnet was used to mass-separate the ions based on their mass-to-charge ratio  $m/q$ . The mass-separated beam was then stopped in a radiofrequency quadrupole cooler and buncher (RFQ-cb) [37] and released as ion bunches into the double Penning trap JYFLTRAP [30]. In the first trap, either the ground- or isomeric-state ions of  $^{79}\text{Zn}$  were selected using mass-selective buffer-gas cooling [38]. The selected ions were transferred to the second

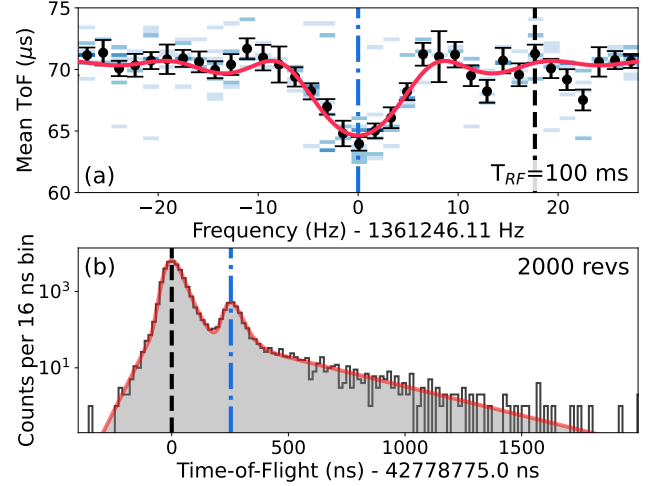


FIG. 1. (a) Example of ToF-ICR spectra for the  $1/2^+$  state in  $^{79}\text{Zn}^+$ . Colored bins indicate the number of detected ions. Darker shades correspond to more ions and lighter shades to fewer ions. The solid red line represents the fit to the data points (black) using the model from Ref. [39]. The cyclotron frequencies are indicated with a vertical black dashed line for the ground state (not present in this spectrum) and a vertical blue dash-dotted line for the isomer. (b) Time-of-Flight spectrum for the MR-ToF MS data. The ToF of the ground state is indicated by a vertical black dashed line, and the ToF of the isomer by a vertical blue dash-dotted line. The solid red line represents the fit to the data using the model from Ref. [40].

trap, where the high-precision mass measurements were performed using the Time-of-Flight Ion Cyclotron Resonance (ToF-ICR) method [39]. The cyclotron resonance frequency  $\nu_c = qB/(2\pi m)$  of the  $1/2^+$  state in  $^{79}\text{Zn}^+$  was measured using a 100 ms pulse of quadrupolar rf excitation. The ToF-ICR spectrum is shown in Fig. 1(a).

The magnetic field strength  $B$  was determined using  $^{84}\text{Kr}^+$  as a mass reference with  $m(^{84}\text{Kr})=83.9114977271(41)\text{ u}$  [34]. The mass of the  $1/2^+$  state in  $^{79}\text{Zn}$  was obtained from the measured frequency ratio  $r = \nu_{c,\text{ref}}/\nu_c$  between the  $^{84}\text{Kr}^+$  reference ions and the isomeric-state ions of  $^{79}\text{Zn}^+$  as  $m = r(m_{\text{ref}} - m_e) + m_e$ , where  $m_{\text{ref}}$  is the mass of the reference ion and  $m_e$  is the electron mass. Two sources of systematic uncertainties were taken into account in the analysis, the fluctuation of the magnetic field being  $8.18 \times 10^{-12} \times \Delta t \text{ min}^{-1}$  [41], where  $\Delta t$  represents the time between two reference measurements, and mass-dependent uncertainties being  $2.2 \times 10^{-10} \times (m - m_{\text{ref}})/\text{u}$  [42].

*For the MR-ToF MS measurements*, neutron-rich zinc isotopes were produced at the isotope separation online facility ISOLDE at CERN [33] by impinging a 1.4-GeV proton beam onto a solid tungsten block to generate an intense spallation neutron flux [43]. The zinc isotopes were then produced through neutron-induced fission pro-

TABLE I. Frequency ratio  $r$  or time-of-flight difference  $\Delta t$ , mass-excess values ME, and excitation energy of the isomer  $E$  determined in this work. The values for  $J^\pi$  and  $T_{1/2}$  are from Ref. [20],  $\text{ME}_{\text{lit}}$  is deduced from Ref. [34], in combination with the excitation energy reported in [19].  $^{84}\text{Kr}^+$  from [34] was used as a reference for the ToF-ICR measurements, while  $^{79}\text{Zn}^+$  in its ground state from [27–29] was used for the MR-ToF MS measurements.

Nuclide	$J^\pi$	$T_{1/2}$	Method	$r$ or $\Delta t$	ME (keV)	$\text{ME}_{\text{lit}}$ (keV)	Diff. (keV)	$E$ (keV)
$^{79}\text{Zn}^m$	$1/2^+$	$> 200$ ms	ToF-ICR	$0.940796186(144)$	$-52490(12)$	$-52330(150)$	$-160(150)$	$942(12)$
			MR-ToF MS	$274.2(40)$ ns	$-52489(14)$		$-159(150)$	$943(14)$

cesses in an adjacent thick uranium carbide target. Using the tungsten converter resulted in reduced production of isobaric neutron-deficient nuclides. The radioactive fission products then diffused through the target material into a cold quartz transfer line [44, 45] which further eliminated contamination of surface-ionized elements, e.g. Ga, Rb, and Sr [46]. The remaining radioactive species were then ionized by the Resonance Ionization Laser Ion Source (RILIS) [47], using an element-selective three-step ionization scheme for zinc. The ion beam was then mass-separated using the general-purpose mass-separator dipole magnet, removing non-isobaric contamination, before being sent to the ISOLTRAP mass spectrometer [32].

The quasi-continuous ion beam was cooled and bunched in a linear RFQ-cb [48] with a storage time of 10 ms before being captured in the MR-ToF MS [49] using the in-trap lift method [50]. After trapping times of up to 43 ms, the ion bunch was ejected onto a single-ion counting detector using the same in-trap lift.

The excitation energy of the isomeric state  $E = [(\Delta t/t_0)^2 + 2\Delta t/t_0] m_0 c^2$  is related to the time-of-flight difference  $\Delta t$  to its ground state with mass  $m_0$ , the absolute flight time of the ground state  $t_0$ , and the speed of light in vacuum  $c$ . For long flight times, where  $\Delta t \ll t_0$ , this reduces to  $E \approx 2\Delta t/t_0 \times m_0 c^2$ . Figure 1 (b) shows the ToF spectrum for the MR-ToF MS data. Zinc was delivered from ISOLDE as a pure beam, thus only the ground state (black dashed line) and the isomeric state (blue dash-dotted line) of  $^{79}\text{Zn}$  were present in the spectrum. A mass resolving power  $R = t_0/2\Delta t_{\text{FWHM}} = 300\,000$  was reached, sufficient to resolve the two states. The asymmetric peak shape was fitted with a multi-component exponentially modified Gaussian [40] to extract the absolute ToF  $t_0 = 4\,277\,871(2)$  ns of the ground state and the ToF difference  $\Delta t = 274(4)$  ns between the two states. The excitation energy was then calculated using the ground state mass with  $\text{ME}_{\text{lit}} = -53\,432.1(18)$  keV, which we calculated as the weighted mean of the results from Refs. [27–29]. The excitation energy was measured for different ion loads to account for ion-ion interactions during the storage time in the MR-ToF MS [51, 52].

The results of the two independent measurements are summarized in Tab. I. The extracted excitation energies of the isomer agree very well, resulting in a weighted mean of  $942(10)$  keV. The isomer energy is lower than

$1100(150)$  keV as given in the NUBASE 2020 evaluation [53], which is based on the transfer reaction experiment from Ref. [19]. Our value is significantly more precise and unambiguously sets the isomeric state below the  $5/2^+$  state located at  $983(3)$  keV. We note that the result agrees with the value  $943(3)$  keV, obtained from the beta-decay spectroscopy of  $^{79}\text{Cu}$  [54]. Here, we confirm the existence of the isomer and provide a direct measure of its excitation energy.

To interpret the present experimental data, shell-model calculations with the PFSDG-U interaction [15, 18] were performed for  $^{79,80}\text{Zn}$ . The valence space is spanned across the full  $pf$  shell for protons and full  $sdg$  shell for neutrons, with  $^{60}\text{Ca}$  as an inert core. This interaction has been successfully used in the  $^{78}\text{Ni}$  region to describe, among others, the two-neutron separation energies  $S_{2n}$  along the zinc isotopic chain [17], as well as the magnetic  $g$ -factor in  $^{79}\text{Zn}$  [21].

The calculated excitation energies for  $^{79}\text{Zn}$  (Tab. II) are in good agreement with the experimental results with  $1/2^+$  and  $5/2^+$  at 0.83 MeV and 0.94 MeV, respectively. We find that the two low-lying excited states in  $^{79}\text{Zn}$  show a one-particle-two-hole configuration, consistent with other  $N = 49$  isotones [8–11]. While the  $s_{1/2}$  and  $d_{5/2}$  orbitals lie together at the neutron Fermi surface in the vicinity of  $^{78}\text{Ni}$ , the correlated  $N = 50$  neutron gap  $S_N(^{81}\text{Zn}) - S_N(^{80}\text{Zn})$ , calculated from the present theoretical values, remains sizeable at about 4.0 MeV and is in agreement with the effective single-particle energies of Ref. [6] and with the experimental value provided in Ref. [34]. These states usually recover enough correlation energy (total energy minus monopole part) to compensate for their energy gap loss. This is observed in our calculations shown in Tab. II, where the total correlation energy is extracted. The excited  $1/2^+$  and  $5/2^+$  states recover correlation energy on the order of  $\sim 6.5$  MeV – 6.9 MeV compared to the  $9/2^+$  the ground state.

The low excitation energy of these two states can be understood as the balance between an average of 1.3 neutrons excited across the shell gap with respect to the ground state ( $\sim 5.5$  MeV) and the correlation energies ( $\sim 6.5$  MeV – 6.9 MeV) which compensate and result in very low-lying excitation energies for these one-particle-two-holes states.

An inspection of the partial occupancies of the first to

TABLE II. Occupation of orbitals in the full proton  $pf$  and neutron  $sdg$  valence space for low-lying states in  $^{79,80}\text{Zn}$  and  $^{78}\text{Ni}$  (the latter taken from Ref. [18]).  $E_{\text{exp}}$  and  $E_{\text{theo}}$  (in MeV) are the experimental and theoretical excitation energies.  $E_{\text{corr}}$  and  $E_{\text{corr}}^*$  (in MeV) are the total correlation energy and the correlation energy difference of an excited state with respect to its ground state.  $n^\nu$  and  $n^\pi$  are the average number of particle-hole excitations for the proton and neutron shells.

Nuclide	$J^\pi$	$E_{\text{exp}}$	$E_{\text{theo}}$	$E_{\text{corr}}$	$E_{\text{corr}}^*$	$n^\nu$	$\nu_{g9/2}$	$\nu_{d5/2}$	$\nu_{s1/2}$	$\nu_{g7/2}$	$\nu_{d3/2}$	$n^\pi$	$\pi_{f7/2}$	$\pi_{f5/2}$	$\pi_{p3/2}$	$\pi_{p1/2}$
$^{79}\text{Zn}$	$9/2^+$	0.0	0.0	-11.72	-	0.53	8.47	0.27	0.04	0.18	0.04	2.49	7.51	1.79	0.50	0.20
	$1/2^+$	0.94	0.83	-18.59	-6.87	1.84	7.17	0.81	0.54	0.34	0.15	2.82	7.18	1.45	0.95	0.42
	$5/2^+$	0.98	0.94	-18.23	-6.51	1.82	7.18	1.06	0.31	0.33	0.12	2.79	7.20	1.51	0.87	0.41
$^{80}\text{Zn}$	$0_1^+$	0.0	0.0	-10.80	-	0.49	9.50	0.23	0.03	0.19	0.04	2.48	7.52	1.90	0.44	0.14
	$0_2^+$	-	2.16	-17.12	-6.32	2.74	7.26	1.20	0.71	0.52	0.31	3.08	6.92	1.33	1.28	0.47
$^{78}\text{Ni}$	$0_1^+$	0.0	0.0	-8.00	-	0.38	9.62	0.12	0.02	0.20	0.04	0.57	7.44	0.38	0.15	0.04
	$0_2^+$	-	2.65	-24.09	-16.09	2.70	7.30	1.11	0.81	0.43	0.35	2.35	5.65	0.98	0.94	0.43

excited states (see Tab. II) reveals strong neutron mixing for the orbitals above  $N = 50$ , as well as different proton occupancies with respect to the ground state, invalidating the spherical single particle-hole nature of these states and rather suggesting a deformed shape. This neutron mixing and proton reshuffling is visualized in Fig. 2, where the occupancy differences of the excited states with respect to their ground states are plotted.

The structure of the excited states can be interpreted within the Discrete Non-Orthogonal shell-model (DNO-SM) method, newly developed in Ref. [55] and applied recently in Refs. [56, 57]. This approach expands the shell-model wave functions in the deformed Hartree-Fock basis rather than the usual spherical m-scheme basis. This allows the extraction of the corresponding deformation amplitudes of a given state in the  $(\beta, \gamma)$  plane.

Figure 3 (top panel) depicts such expansion for the ground state and the first two excited states of  $^{79}\text{Zn}$ . Two clear patterns emerge: in the ground state, the main components of the wave function tend towards the low-deformation region with a small  $\beta$  value, while for the excited states, the wave functions are more fragmented and have, on average, a larger deformation. Also, we find the clustering of the wave-function components consistent with the deformation parameters  $\beta \approx 0.15$  (ground state) and  $\beta \approx 0.22$  (isomeric state), deduced from the nuclear charge radius in Ref. [20]. Moreover, the DNO-SM calculations reveal that both  $1/2^+$  and  $5/2^+$  states belong to the same rotational structure, which is characterized by the  $K = 1/2$  components of 100% and 96%, respectively (see K-component extraction in Refs. [55, 57]).

To probe further into the deformed character of the low-lying states in  $^{79}\text{Zn}$ , we have complemented the calculations with the investigation of  $^{80}\text{Zn}$ . We find two low-lying  $0^+$  states: the spherical ground-state and an excited deformed state of two-particle-two-hole nature at 2.16 MeV (see Tab. II). Again, a larger correlation energy ( $\sim 6.3$  MeV) is observed for the excited  $0^+$  state on the same order of magnitude as those of the deformed intruder states in  $^{79}\text{Zn}$ , indicating the same deformation nature of these states. Figure 3 shows the wave function

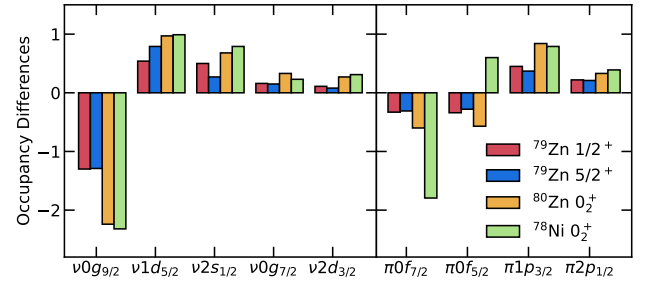


FIG. 2. Occupancy differences between excited states in  $^{79,80}\text{Zn}$ , and  $^{78}\text{Ni}$  with their respective ground states. The data for  $^{78}\text{Ni}$  is taken from [18].

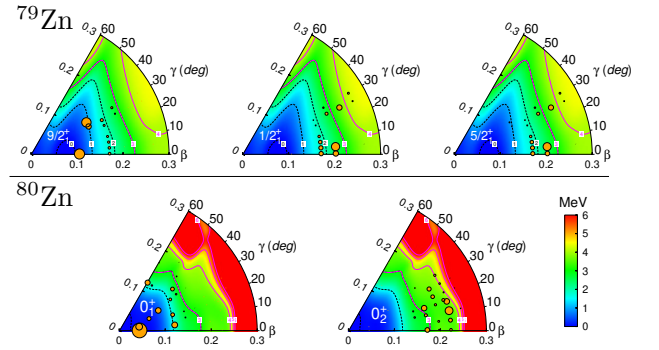


FIG. 3. DNO-SM expansions in the  $(\beta, \gamma)$  plane (using the same energy scale) for low-lying states in  $^{79}\text{Zn}$  ( $9/2_1^+$ ,  $1/2_1^+$  and  $5/2_1^+$  in upper panel) and  $^{80}\text{Zn}$  ( $0_1^+$  and  $0_2^+$  in lower panel). The radius of circles represents the normalized probability of finding a deformation of  $(\beta, \gamma)$  in the corresponding state.

expansions for these two  $0^+$  states (bottom panel). There is a clear similarity between the spherical ground states for  $^{79}\text{Zn}(9/2^+)/^{80}\text{Zn}(0_1^+)$  and the deformed excited states for  $^{79}\text{Zn}(1/2^+, 5/2^+)/^{80}\text{Zn}(0_2^+)$ , advocating for the deformed nature of the observed isomer in  $^{79}\text{Zn}$ , as well as its  $5/2^+$  companion.

Finally, the present shape coexistence discussed for  $^{79,80}\text{Zn}$  can be put in perspective with the shape coexis-

tence recently observed and discussed for  $^{78}\text{Ni}$  [15, 18]: the deformed intruder  $0_2^+$  of  $^{78}\text{Ni}$  has 2.7 neutron p-h excitations on average, in remarkable agreement with present values quoted in Tab. II for  $0_2^+$  of  $^{80}\text{Zn}$ . Both  $0_2^+$  states have  $\sim 2.4 - 3$  protons on average in the  $f_{5/2}, p_{3/2}, p_{1/2}$  shells, leading to close collective structures. Therefore, the shape coexistence in  $^{78}\text{Ni}$  and in the presented  $^{79-80}\text{Zn}$  reveal striking similarities.

To summarize, we have established the level ordering and determined the excitation energy of the isomer in  $^{79}\text{Zn}$  by means of high-precision mass spectrometry. Two measurements were performed independently, using different production methods and measurement techniques at different radioactive ion beam facilities. We show unambiguously that the  $1/2^+$  isomeric state with 942(10) keV lies below the  $5/2^+$  state with 983(3) keV. The new DNO-SM calculations tool provides the theoretical analysis, predicting the occurrence of low-lying deformed intruder states. The  $1/2^+$  isomer is interpreted as the band-head of a low-lying deformed structure of the same nature as a predicted low-lying deformed band in  $^{80}\text{Zn}$ . These findings confirm shape coexistence in  $^{79,80}\text{Zn}$ , similar to the one observed in  $^{78}\text{Ni}$ .

We thank the ISOLDE technical group and the ISOLDE Collaboration for their support. We acknowledge the support of the German Max Planck Society, the French Institut National de Physique Nucléaire et de Physique des Particules (IN2P3), the European Research Council (ERC) under the European Union's Horizon 2020 research and innovation programme (Grant Agreements No. 682841 'ASTRUM', 654002 'ENSAR2', and 101020842 'EUSTRONG'), as well as the German Federal Ministry of Education and Research (BMBF; Grants No. 05P18HGCIA, 05P21HGCII, and 05P21RDFNB). L.N. acknowledges support from the Wolfgang Gentner Programme of the German Federal Ministry of Education and Research (Grant No. 13E18CHA). This work has been supported by the Academy of Finland under the Finnish Centre of Excellence Program (Nuclear and Accelerator Based Physics Research at JYFL 2012-2017), and under Academy of Finland grants No. 275389, 284516, 312544, 295207, and 306980. We acknowledge the support of the European Union's Horizon 2020 research and innovation program grant agreement No 654002 (ENSAR2) and No. 771036 (ERC CoG MAIDEN). We thank for the bilateral mobility grant from the Institut Français in Finland, the Embassy of France in Finland, the French Ministry of Higher Education and Research, and the Finnish Society of Science and Letters. We are grateful for the mobility support from PICS MITICANS (Manipulation of Ions in Traps and Ion sources for Atomic and Nuclear Spectroscopy). S.G. thanks for the mobility grant from the EDPSIME. F. N and D. D. D. acknowledge the financial support of CNRS/IN2P3, France, via ABI-CONFI master projet.

The JYFLTRAP experiment was conducted by L.C,

S.G, A.K, B.B, P.A, T.E, V.G.A., A.J., A.K, I.D.M, D.A.N, F.D.O., H.P., C.P., I.P., A.D.R., V.R., M.V., and J.Ä. The ISOLTRAP experiment was conducted by L.N., R.B.C., P.F., M.F., A.H., D.La., M.Mü., M.M., Ch.S., and was conceived by U.K. The theoretical calculations were performed by D.D.D. and F.N. Funding and supervision were provided, in parts, by K.B. and L.S. The Manuscript was prepared by L.N., D.D.D., A.K., D.Lu., F.N., and M.S. All authors contributed to the editing of the manuscript.

---

\* Lukas.Nies@cern.ch

† Present address: Facility for Rare Isotope Beams, Michigan State University, East Lansing, Michigan 48824, USA

‡ anu.kankainen@jyu.fi

§ Present address: KU Leuven, Instituut voor Kern- en Stralingsfysica, B-3001 Leuven, Belgium

¶ Deceased.

- [1] M. G. Mayer, On Closed Shells in Nuclei. II, Phys. Rev. **75**, 1969 (1949).
- [2] O. Haxel, J. H. D. Jensen, and H. E. Suess, On the "Magic Numbers" in Nuclear Structure, Phys. Rev. **75**, 1766 (1949).
- [3] A. Jain, B. Maheshwari, and A. Goel, *Nuclear Isomers: A Primer* (Springer International Publishing, 2021).
- [4] K. Heyde and J. L. Wood, Shape coexistence in atomic nuclei, Rev. Mod. Phys. **83**, 1467 (2011).
- [5] T. J. Gray, J. M. Allmond, Z. Xu, T. T. King, R. S. Lubna, H. L. Crawford, V. Tripathi, B. P. Crider, R. Grzywacz, S. N. Liddick, A. O. Macchiavelli, T. Miyagi, A. Poves, A. Andalib, E. Argo, C. Benetti, S. Bhattacharya, C. M. Campbell, M. P. Carpenter, J. Chan, A. Chester, J. Christie, B. R. Clark, I. Cox, A. A. Doetsch, J. Dopfer, J. G. Duarte, P. Fallon, A. Frotscher, T. Gaballah, J. T. Harke, J. Heideman, H. Huegen, J. D. Holt, R. Jain, N. Kitamura, K. Kolos, F. G. Kondev, A. Laminack, B. Longfellow, S. Luitel, M. Madurga, R. Mahajan, M. J. Mogannam, C. Morse, S. Neupane, A. Nowicki, T. H. Ogunbaku, W.-J. Ong, C. Porzio, C. J. Prokop, B. C. Rasco, E. K. Ronning, E. Rubino, T. J. Ruland, K. P. Rykaczewski, L. Schaedig, D. Seweryniak, K. Siegl, M. Singh, A. E. Stuchbery, S. L. Tabor, T. L. Tang, T. Wheeler, J. A. Winger, and J. L. Wood, Microsecond Isomer at the N=20 Island of Shape Inversion Observed at FRIB, Phys. Rev. Lett. **130**, 242501 (2023).
- [6] F. Nowacki, A. Obertelli, and A. Poves, The neutron-rich edge of the nuclear landscape: Experiment and theory., Prog. Part. Nucl. Phys. **120**, 103866 (2021), arXiv:2104.06238 [nucl-th].
- [7] P. E. Garrett, M. Zielińska, and E. Clément, An experimental view on shape coexistence in nuclei, Prog. in Part. and Nucl. Phys. **124**, 103931 (2022).
- [8] S. Ahn, D. W. Bardayan, K. L. Jones, A. S. Adekola, G. Arbanas, J. C. Blackmon, K. Y. Chae, K. A. Chipps, J. A. Cizewski, S. Hardy, M. E. Howard, R. L. Kozub, B. Manning, M. Matoš, C. D. Nesaraja, P. D. O'Malley, S. D. Pain, W. A. Peters, S. T. Pittman, B. C. Rasco,

- M. S. Smith, and I. Spassova, Direct neutron capture cross section on  $^{80}\text{Ge}$  and probing shape coexistence in neutron-rich nuclei, *Phys. Rev. C* **100**, 044613 (2019).
- [9] L. A. Montestruque, M. Cobian-Rozak, G. Szaloky, J. Zumbro, and S. Darden, Study of the  $^{77,79,81,83}\text{Se}$  level structure with the  $^{76,78,80,82}\text{Se}(d,p)$  reaction, *Nucl. Phys. A* **305**, 29 (1978).
- [10] N. A. Detorie, P. L. Jolivet, C. P. Browne, and A. A. Rollefson, Nuclear structure information for states in  $^{85}\text{Kr}$  from the  $^{84}\text{Kr}(d,p)$  and  $^{84}\text{Kr}(\vec{d},p)$  reactions, *Phys. Rev. C* **18**, 991 (1978).
- [11] B. Burks, R. Anderson, T. Clegg, E. Ludwig, B. Karp, and Y. Aoki, A DWBA analysis of the  $^{86}\text{Sr}(d,p)^{87}\text{Sr}$  reaction and implications for a  $^{87}\text{Rb}$  solar neutrino detector, *Nucl. Phys. A* **457**, 337 (1986).
- [12] A. Gottardo, D. Verney, C. Delafosse, F. Ibrahim, B. Roussière, C. Sotty, S. Roccia, C. Andreoiu, C. Costache, M.-C. Delattre, I. Deloncle, A. Etilé, S. Franchoo, C. Gaulard, J. Guillot, M. Lebois, M. MacCormick, N. Marginean, R. Marginean, I. Matea, C. Mihai, I. Mitu, L. Olivier, C. Portail, L. Qi, L. Stan, D. Testov, J. Wilson, and D. T. Yordanov, First Evidence of Shape Coexistence in the  $^{78}\text{Ni}$  Region: Intruder  $0_2^+$  State in  $^{80}\text{Ge}$ , *Phys. Rev. Lett.* **116**, 182501 (2016).
- [13] F. H. Garcia, C. Andreoiu, G. C. Ball, A. Bell, A. B. Garnsworthy, F. Nowacki, C. M. Petrache, A. Poves, K. Whitmore, F. A. Ali, N. Bernier, S. S. Bhattacharjee, M. Bowry, R. J. Coleman, I. Dillmann, I. Djianto, A. M. Forney, M. Gascoine, G. Hackman, K. G. Leach, A. N. Murphy, C. R. Natzke, B. Olaizola, K. Ortner, E. E. Peters, M. M. Rajabali, K. Raymond, C. E. Svensson, R. Umashankar, J. Williams, and D. Yates, Absence of Low-Energy Shape Coexistence in  $^{80}\text{Ge}$ : The Nonobservation of a Proposed Excited  $0_2^+$  Level at 639 keV, *Phys. Rev. Lett.* **125**, 172501 (2020).
- [14] S. Sekal, L. M. Fraile, R. Lică, M. J. G. Borge, W. B. Walters, A. Aprahamian, C. Benchouk, C. Bernards, J. A. Briz, B. Bucher, C. J. Chiara, Z. Dlouhý, I. Gheorghe, D. G. Ghiță, P. Hoff, J. Jolie, U. Köster, W. Kurcewicz, H. Mach, N. Mărginean, R. Mărginean, Z. Meliani, B. Olaizola, V. Pazyi, J. M. Régis, M. Rudigier, T. Sava, G. S. Simpson, M. Stănoiu, and L. Stroe, Low-spin states in  $^{80}\text{Ge}$  populated in the  $\beta$  decay of the  $^{80}\text{Ga}$   $3^-$  isomer, *Phys. Rev. C* **104**, 024317 (2021).
- [15] R. Taniuchi, C. Santamaria, P. Doornenbal, A. Obertelli, K. Yoneda, G. Authelet, H. Baba, D. Calvet, F. Châteaueu, A. Corsi, A. Delbart, J.-M. Gheller, A. Gillibert, J. D. Holt, T. Isobe, V. Lapoux, M. Matsushita, J. Menéndez, S. Momiyama, T. Motobayashi, M. Niikura, F. Nowacki, K. Ogata, H. Otsu, T. Otsuka, C. Péron, S. Péru, A. Peyaud, E. C. Pollacco, A. Poves, J.-Y. Roussé, H. Sakurai, A. Schwenk, Y. Shiga, J. Simonis, S. R. Stroberg, S. Takeuchi, Y. Tsunoda, T. Uesaka, H. Wang, F. Browne, L. X. Chung, Z. Dombardi, S. Franchoo, F. Giacoppo, A. Gottardo, K. Hadyńska-Klęk, Z. Korkulu, S. Koyama, Y. Kubota, J. Lee, M. Lettmann, C. Louchart, R. Lozeva, K. Matsui, T. Miyazaki, S. Nishimura, L. Olivier, S. Ota, Z. Patel, E. Şahin, C. Shand, P.-A. Söderström, I. Stefan, D. Steppenbeck, T. Sumikama, D. Suzuki, Z. Vajta, V. Werner, J. Wu, and Z. Y. Xu,  $^{78}\text{Ni}$  revealed as a doubly magic stronghold against nuclear deformation, *Nature* **569**, 53 (2019).
- [16] L. Olivier, S. Franchoo, M. Niikura, Z. Vajta, D. Sohlér, P. Doornenbal, A. Obertelli, Y. Tsunoda, T. Otsuka, G. Authelet, H. Baba, D. Calvet, F. Châteaueu, A. Corsi, A. Delbart, J.-M. Gheller, A. Gillibert, T. Isobe, V. Lapoux, M. Matsushita, S. Momiyama, T. Motobayashi, H. Otsu, C. Péron, A. Peyaud, E. C. Pollacco, J.-Y. Roussé, H. Sakurai, C. Santamaria, M. Sasano, Y. Shiga, S. Takeuchi, R. Taniuchi, T. Uesaka, H. Wang, K. Yoneda, F. Browne, L. X. Chung, Z. Dombardi, F. Flavigny, F. Giacoppo, A. Gottardo, K. Hadyńska-Klęk, Z. Korkulu, S. Koyama, Y. Kubota, J. Lee, M. Lettmann, C. Louchart, R. Lozeva, K. Matsui, T. Miyazaki, S. Nishimura, K. Ogata, S. Ota, Z. Patel, E. Şahin, C. Shand, P.-A. Söderström, I. Stefan, D. Steppenbeck, T. Sumikama, D. Suzuki, V. Werner, J. Wu, and Z. Xu, Persistence of the  $Z = 28$  Shell Gap Around  $^{78}\text{Ni}$ : First Spectroscopy of  $^{79}\text{Cu}$ , *Phys. Rev. Lett.* **119**, 192501 (2017).
- [17] A. Welker, N. A. S. Althubiti, D. Atanasov, K. Blaum, T. E. Cocolios, F. Herfurth, S. Kreim, D. Lunney, V. Manea, M. Mougeot, D. Neidherr, F. Nowacki, A. Poves, M. Rosenbusch, L. Schweikhard, F. Wienholtz, R. N. Wolf, and K. Zuber, Binding Energy of  $^{79}\text{Cu}$ : Probing the Structure of the Doubly Magic  $^{78}\text{Ni}$  from Only One Proton Away, *Phys. Rev. Lett.* **119**, 192502 (2017).
- [18] F. Nowacki, A. Poves, E. Caurier, and B. Bounthong, Shape Coexistence in  $^{78}\text{Ni}$  as the Portal to the Fifth Island of Inversion, *Phys. Rev. Lett.* **117**, 272501 (2016).
- [19] R. Orlandi, D. Mücher, R. Raabe, A. Jungclaus, S. D. Pain, V. Bildstein, R. Chapman, G. de Angelis, J. G. Johansen, P. Van Duppen, A. N. Andreyev, S. Bottoni, T. E. Cocolios, H. De Witte, J. Diriken, J. Elseviers, F. Flavigny, L. P. Gaffney, R. Gernhäuser, A. Gottardo, M. Huyse, A. Illana, J. Konki, T. Kröll, R. Krücken, J. F. Lane, V. Liberati, B. Marsh, K. Nowak, F. Nowacki, J. Pakarinen, E. Rapisarda, F. Recchia, P. Reiter, T. Roger, E. Şahin, M. Seidlitz, K. Sieja, J. F. Smith, J. J. Valiente Dobón, M. von Schmid, D. Voulot, N. Warr, F. K. Wenander, and K. Wimmer, Single-neutron orbits near  $^{78}\text{Ni}$ : Spectroscopy of the  $N=49$  isotope  $^{79}\text{Zn}$ , *Phys. Lett. B* **740**, 298 (2015).
- [20] X. F. Yang, C. Wraith, L. Xie, C. Babcock, J. Billowes, M. L. Bissell, K. Blaum, B. Cheal, K. T. Flanagan, R. F. Garcia Ruiz, W. Gins, C. Gorges, L. K. Grob, H. Heylen, S. Kaufmann, M. Kowalska, J. Kraemer, S. Malbrunot-Ettenauer, R. Neugart, G. Neyens, W. Nörtershäuser, J. Papuga, R. Sánchez, and D. T. Yordanov, Isomer Shift and Magnetic Moment of the Long-Lived  $1/2^+$  Isomer in  $^{79}\text{Zn}_{49}$ : Signature of Shape Coexistence near  $^{78}\text{Ni}$ , *Phys. Rev. Lett.* **116**, 182502 (2016).
- [21] C. Wraith, X. F. Yang, L. Xie, C. Babcock, J. Bieroń, J. Billowes, M. L. Bissell, K. Blaum, B. Cheal, L. Filippin, R. F. Garcia Ruiz, W. Gins, L. K. Grob, G. Gaigalas, M. Godefroid, C. Gorges, H. Heylen, M. Honma, P. Jönsson, S. Kaufmann, M. Kowalska, J. Krämer, S. Malbrunot-Ettenauer, R. Neugart, G. Neyens, W. Nörtershäuser, F. Nowacki, T. Otsuka, J. Papuga, R. Sánchez, Y. Tsunoda, and D. T. Yordanov, Evolution of nuclear structure in neutron-rich odd-Zn isotopes and isomers, *Phys. Lett. B* **771**, 385 (2017).
- [22] A. Morales, G. Benzoni, H. Watanabe, Y. Tsunoda, T. Otsuka, S. Nishimura, F. Browne, R. Daido, P. Doornenbal, Y. Fang, G. Lorusso, Z. Patel, S. Rice, L. Sinclair, P.-A. Söderström, T. Sumikama, J. Wu, Z. Xu, A. Yagi, R. Yokoyama, H. Baba, R. Avigo, F. Bello Gar-

- rote, N. Blasi, A. Bracco, F. Camera, S. Ceruti, F. Crespi, G. de Angelis, M.-C. Delattre, Z. Dombradi, A. Gottardo, T. Isobe, I. Kojouharov, N. Kurz, I. Kuti, K. Matsui, B. Melon, D. Mengoni, T. Miyazaki, V. Modamio-Hoybjor, S. Momiyama, D. Napoli, M. Niikura, R. Orlandi, H. Sakurai, E. Sahin, D. Sohler, H. Schaffner, R. Taniuchi, J. Taprogge, Z. Vajta, J. Valiente-Dobón, O. Wieland, and M. Yalcinkaya, Type II shell evolution in  $A=70$  isobars from the  $N \geq 40$  island of inversion, *Phys. Lett. B* **765**, 328 (2017).
- [23] S. Leoni, B. Fornal, N. Mărginean, M. Sferrazza, Y. Tsunoda, T. Otsuka, G. Bocchi, F. C. L. Crespi, A. Bracco, S. Aydin, M. Boromiza, D. Bucurescu, N. Cieplicka-Oryńczak, C. Costache, S. Călinescu, N. Florea, D. G. Ghiță, T. Glodariu, A. Ionescu, L. Iskra, M. Krzysiek, R. Mărginean, C. Mihai, R. E. Mihai, A. Mitu, A. Negret, C. R. Niță, A. Olăcel, A. Oprea, S. Pascu, P. Petkov, C. Petrone, G. Porzio, A. Șerban, C. Sotty, L. Stan, I. Știru, L. Stroe, R. Șuvăilă, S. Toma, A. Turturică, S. Ujeniuc, and C. A. Ur, Multifaceted quadruplet of low-lying spin-zero states in  $^{66}\text{Ni}$ : Emergence of shape isomerism in light nuclei, *Phys. Rev. Lett.* **118**, 162502 (2017).
- [24] M. Stryjczyk, Y. Tsunoda, I. G. Darby, H. De Witte, J. Diriken, D. V. Fedorov, V. N. Fedosseev, L. M. Fraile, M. Huyse, U. Köster, B. A. Marsh, T. Otsuka, D. Pauwels, L. Popescu, D. Radulov, M. D. Seliverstov, A. M. Sjödin, P. Van den Bergh, P. Van Duppen, M. Venhart, W. B. Walters, and K. Wimmer,  $\beta^-$  decay study of the  $^{66}\text{Mn}$ – $^{66}\text{Fe}$ – $^{66}\text{Co}$ – $^{66}\text{Ni}$  decay chain, *Phys. Rev. C* **98**, 064326 (2018).
- [25] S. Sels, T. Day Goodacre, B. A. Marsh, A. Pastore, W. Ryssens, Y. Tsunoda, N. Althubiti, B. Andel, A. N. Andreyev, D. Atanasov, A. E. Barzakh, M. Bender, J. Billowes, K. Blaum, T. E. Cocolios, J. G. Cubiss, J. Dobaczewski, G. J. Farooq-Smith, D. V. Fedorov, V. N. Fedosseev, K. T. Flanagan, L. P. Gaffney, L. Ghys, P.-H. Heenen, M. Huyse, S. Kreim, D. Lunney, K. M. Lynch, V. Manea, Y. Martinez Palenzuela, T. M. Medonca, P. L. Molkanov, T. Otsuka, J. P. Ramos, R. E. Rossel, S. Rothe, L. Schweikhard, M. D. Seliverstov, P. Spagnoletti, C. Van Beveren, P. Van Duppen, M. Weinhard, E. Verstraelen, A. Welker, K. Wendt, F. Wienholtz, R. N. Wolf, and A. Zadornaya, Shape staggering of midshell mercury isotopes from in-source laser spectroscopy compared with density-functional-theory and Monte Carlo shell-model calculations, *Phys. Rev. C* **99**, 044306 (2019).
- [26] B. Olaizola, L. M. Fraile, H. Mach, F. Nowacki, A. Poves, A. Aprahamian, J. A. Briz, J. Cal-González, D. Ghiță, U. Köster, W. Kurcewicz, S. R. Leshner, D. Pauwels, E. Picado, D. Radulov, G. S. Simpson, and J. M. Udías, Properties of low-lying states in  $^{65}\text{Co}$  from lifetime measurements, *Phys. Rev. C* **99**, 024321 (2019).
- [27] J. Hakala, S. Rahaman, V.-V. Elomaa, T. Eronen, U. Hager, A. Jokinen, A. Kankainen, I. D. Moore, H. Penttilä, S. Rinta-Antila, J. Rissanen, A. Saastamoinen, T. Sonoda, C. Weber, and J. Äystö, Evolution of the  $N = 50$  Shell Gap Energy towards  $^{78}\text{Ni}$ , *Phys. Rev. Lett.* **101**, 052502 (2008).
- [28] S. Baruah, G. Audi, K. Blaum, M. Dworschak, S. George, C. Guénaut, U. Hager, F. Herfurth, A. Herlert, A. Kellerbauer, H.-J. Kluge, D. Lunney, H. Schatz, L. Schweikhard, and C. Yazidjian, Mass Measurements beyond the Major  $r$ -Process Waiting Point  $^{80}\text{Zn}$ , *Phys. Rev. Lett.* **101**, 262501 (2008).
- [29] S. Giraudo, L. Canete, B. Bastin, A. Kankainen, A. Fantina, F. Gulminelli, P. Ascher, T. Eronen, V. Girard-Alcindor, A. Jokinen, A. Khanam, I. Moore, D. Nesterenko, F. de Oliveira Santos, H. Penttilä, C. Petrone, I. Pohjalainen, A. De Roubin, V. Rubchenya, M. Vilen, and J. Äystö, Mass measurements towards doubly magic  $^{78}\text{Ni}$ : Hydrodynamics versus nuclear mass contribution in core-collapse supernovae, *Phys. Lett. B* **833**, 137309 (2022).
- [30] T. Eronen, V. Kolhinen, V.-V. Elomaa, D. Gorelov, U. Hager, J. Hakala, A. Jokinen, A. Kankainen, P. Karvonen, S. Kopecky, I. D. Moore, H. Penttilä, S. Rahaman, S. Rinta-Antila, J. Rissanen, A. Saastamoinen, J. Szerypo, C. Weber, and J. Äystö, JYFLTRAP: a Penning trap for precision mass spectroscopy and isobaric purification, *Eur. Phys. J. A* **48**, 46 (2012).
- [31] I. Moore, T. Eronen, D. Gorelov, J. Hakala, A. Jokinen, A. Kankainen, V. Kolhinen, J. Koponen, H. Penttilä, I. Pohjalainen, M. Reponen, J. Rissanen, A. Saastamoinen, S. Rinta-Antila, V. Sonnenschein, and J. Äystö, Towards commissioning the new IGISOL-4 facility, *Nucl. Instrum. Methods. Phys. Res. B* **317**, 208 (2013), xVIth International Conference on ElectroMagnetic Isotope Separators and Techniques Related to their Applications, December 2–7, 2012 at Matsue, Japan.
- [32] M. Mukherjee, D. Beck, K. Blaum, G. Bollen, J. Dilling, S. George, F. Herfurth, A. Herlert, A. Kellerbauer, H.-J. Kluge, S. Schwarz, L. Schweikhard, and C. Yazidjian, ISOLTRAP: An on-line Penning trap for mass spectrometry on short-lived nuclides, *Eur. Phys. J. A* **35**, 1 (2008).
- [33] R. Catherall, W. Andraza, M. Breitenfeldt, A. Dorsival, G. J. Focker, T. P. Gharsa, G. T. J. J.-L. Grenard, F. Locci, P. Martins, S. Marzari, J. Schipper, A. Shornikov, and T. Stora, The ISOLDE facility, *J. Phys. G Nucl. Part. Phys.* **44**, 094002 (2017).
- [34] M. Wang, W. Huang, F. Kondev, G. Audi, and S. Naimi, The AME 2020 atomic mass evaluation (II). Tables, graphs and references\*, *Chin. Phys. C* **45**, 030003 (2021).
- [35] Al-Adili, A., Jansson, K., Lantz, M., Solders, A., Gorelov, D., Gustavsson, C., Mattera, A., Moore, I., Prokofiev, A. V., Rakopoulos, V., Penttilä, H., Tarrío, D., Wiberg, S., Österlund, M., and Pomp, S., Simulations of the fission-product stopping efficiency in IGISOL, *Eur. Phys. J. A* **51**, 59 (2015).
- [36] P. Karvonen, I. Moore, T. Sonoda, T. Kessler, H. Penttilä, K. Peräjärvi, P. Ronkanen, and J. Äystö, A sextupole ion beam guide to improve the efficiency and beam quality at IGISOL, *Nucl. Instrum. Methods Phys. Res. B* **266**, 4794 (2008).
- [37] A. Nieminen, J. Huikari, A. Jokinen, J. Äystö, P. Campbell, and E. Cochrane, Beam cooler for low-energy radioactive ions, *Nucl. Instrum. Methods Phys. Res. A* **469**, 244 (2001).
- [38] G. Savard, S. Becker, G. Bollen, H.-J. Kluge, R. Moore, T. Otto, L. Schweikhard, H. Stolzenberg, and U. Wiess, A new cooling technique for heavy ions in a Penning trap, *Phys. Lett. A* **158**, 247 (1991).
- [39] M. König, G. Bollen, H.-J. Kluge, T. Otto, and J. Szerypo, Quadrupole excitation of stored ion motion at the true cyclotron frequency, *Int. J. Mass Spectrom.* **142**, 95 (1995).
- [40] S. Purushothaman, S. Ayet San Andrés, J. Bergmann,

- T. Dickel, J. Ebert, H. Geissel, C. Hornung, W. Plaß, C. Rappold, C. Scheidenberger, Y. Tanaka, and M. Yavor, Hyper-EMG: A new probability distribution function composed of Exponentially Modified Gaussian distributions to analyze asymmetric peak shapes in high-resolution time-of-flight mass spectrometry, *Int. J. Mass. Spectrom.* **421**, 245 (2017).
- [41] L. Canete, A. Kankainen, T. Eronen, D. Gorelov, J. Hakala, A. Jokinen, V. S. Kolhinen, J. Koponen, I. D. Moore, J. Reinikainen, and S. Rinta-Antila, High-precision mass measurements of  $^{25}\text{Al}$  and  $^{30}\text{P}$  at JYFLTRAP, *Eur. Phys. J. A* **52**, 124 (2016).
- [42] L. Canete, *High precision mass measurements for nuclear astrophysics*, Ph.D. thesis, University of Jyväskylä (2019).
- [43] R. Luis, J. G. Marques, T. Stora, P. Vaz, and L. Zanini, Optimization studies of the CERN-ISOLDE neutron converter and fission target system, *Eur. Phys. J. A* **48**, 90 (2012).
- [44] E. Bouquerel, R. Catherall, M. Eller, J. Lettry, S. Marzari, T. Stora, and ISOLDE Collaboration, Purification of a Zn radioactive ion beam by alkali suppression in a quartz line target prototype, *Eur. Phys. J.: Spec. Top.* **150**, 277 (2007).
- [45] E. Bouquerel, R. Catherall, M. Eller, J. Lettry, S. Marzari, and T. Stora, Beam purification by selective trapping in the transfer line of an ISOL target unit, *Nucl. Instrum. Methods Phys. Res. B* **266**, 4298 (2008), proceedings of the XVth International Conference on Electromagnetic Isotope Separators and Techniques Related to their Applications.
- [46] U. Köster, O. Arndt, E. Bouquerel, V. Fedoseyev, H. Fränberg, A. Joinet, C. Jost, I. Kerkines, R. Kirchner, and T. T. Collaboration, Progress in ISOL target-ion source systems, *Nucl. Instrum. Methods Phys. Res. B* **266**, 4229 (2008), proceedings of the XVth International Conference on Electromagnetic Isotope Separators and Techniques Related to their Applications.
- [47] V. Fedosseev, K. Chrysalidis, T. D. Goodacre, B. Marsh, S. Rothe, C. Seiffert, and K. Wendt, Ion beam production and study of radioactive isotopes with the laser ion source at ISOLDE, *J. Phys. G Nucl. Part. Phys.* **44**, 084006 (2017).
- [48] F. Herfurth *et al.*, A linear radiofrequency ion trap for accumulation, bunching, and emittance improvement of radioactive ion beams, *Nucl. Instrum. Methods Phys. Res. A* **469**, 254 (2001).
- [49] R. Wolf, F. Wienholtz, D. Atanasov, D. Beck, K. Blaum, C. Borgmann, F. Herfurth, M. Kowalska, S. Kreim, Y. A. Litvinov, D. Lunney, V. Manea, D. Neidherr, M. Rosenbusch, L. Schweikhard, J. Stanja, and K. Zuber, ISOLTRAP's multi-reflection time-of-flight mass separator/spectrometer, *Int. J. Mass. Spectrom.* **349-350**, 123 (2013), 100 years of Mass Spectrometry.
- [50] R. N. Wolf, G. Marx, M. Rosenbusch, and L. Schweikhard, Static-mirror ion capture and time focusing for electrostatic ion-beam traps and multi-reflection time-of-flight mass analyzers by use of an in-trap potential lift, *Int. J. Mass. Spectrom.* **313**, 8 (2012).
- [51] M. Rosenbusch, S. Kemnitz, R. Schneider, L. Schweikhard, R. Tschiersch, and R. N. Wolf, Towards systematic investigations of space-charge phenomena in multi-reflection ion traps, *AIP Conf. Proc.* **1521**, 53 (2013).
- [52] F. Maier, F. Buchinger, L. Croquette, P. Fischer, H. Heylen, F. Hummer, C. Kanitz, A. Kwiatkowski, V. Lagaki, S. Lechner, E. Leistenschneider, G. Neyens, P. Plattner, A. Roitman, M. Rosenbusch, L. Schweikhard, S. Sels, M. Vilen, F. Wienholtz, and S. Malbrunot-Ettenauer, Increased Beam Energy as a Pathway Towards a Highly Selective and High-Flux MR-ToF Mass Separator, *Nucl. Instrum. Methods Phys. Res. A*, accepted (2023).
- [53] F. Kondev, M. Wang, W. Huang, S. Naimi, and G. Audi, The NUBASE2020 evaluation of nuclear physics properties, *Chin. Phys. C* **45**, 030001 (2021).
- [54] M.-C. Delattre, *Étude de la structure à basse énergie de  $^{79}\text{Zn}$  par décroissance  $\beta$  et  $\beta$ -n de  $^{79}\text{Cu}$  et  $^{80}\text{Cu}$* , Ph.D. thesis, Université Paris-Saclay (2016).
- [55] D. D. Dao and F. Nowacki, Nuclear structure within a discrete nonorthogonal shell model approach: New frontiers, *Phys. Rev. C* **105**, 054314 (2022).
- [56] M. Rocchini, P. E. Garrett, M. Zielińska, S. M. Lenzi, D. D. Dao, F. Nowacki, V. Bildstein, A. D. MacLean, B. Olaizola, Z. T. Ahmed, C. Andreoiu, A. Babu, G. C. Ball, S. S. Bhattacharjee, H. Bidaman, C. Cheng, R. Coleman, I. Dillmann, A. B. Garnsworthy, S. Gillespie, C. J. Griffin, G. F. Grinyer, G. Hackman, M. Hanley, A. Illana, S. Jones, A. T. Laffoley, K. G. Leach, R. S. Lubna, J. McAfee, C. Natzke, S. Pannu, C. Paxman, C. Porzio, A. J. Radich, M. M. Rajabali, F. Sarazin, K. Schwarz, S. Shadrick, S. Sharma, J. Suh, C. E. Svensson, D. Yates, and T. Zidar, First Evidence of Axial Shape Asymmetry and Configuration Coexistence in  $^{74}\text{Zn}$ : Suggestion for a Northern Extension of the  $N = 40$  Island of Inversion, *Phys. Rev. Lett.* **130**, 122502 (2023).
- [57] K. Rezyunkina, D. D. Dao, G. Duchêne, J. Dudouet, F. Nowacki, E. Clément, A. Lemasson, C. Andreoiu, A. Astier, G. de Angelis, G. de France, C. Delafosse, I. Deloncle, F. Didierjean, Z. Dombradi, C. Ducoin, A. Gadea, A. Gottardo, D. Guinet, B. Jacquot, P. Jones, T. Konstantinopoulos, I. Kuti, A. Korichi, S. M. Lenzi, G. Li, F. Le Blanc, C. Lizarazo, R. Lozeva, G. Maquart, B. Million, C. Michelagnoli, D. R. Napoli, A. Navin, R. M. Pérez-Vidal, C. M. Petrache, N. Pietralla, D. Ralet, M. Ramdhane, M. Rejmund, O. Stezowski, C. Schmitt, D. Sohler, and D. Verney, Structure of  $^{83}\text{As}$ ,  $^{85}\text{As}$ , and  $^{87}\text{As}$ : From semimagicity to  $\gamma$  softness, *Phys. Rev. C* **106**, 014320 (2022).

## 8 Eigenständigkeitserklärung

Hiermit erkläre ich, dass diese Arbeit bisher von mir weder an der Mathematisch-Naturwissenschaftlichen Fakultät der Universität Greifswald noch einer anderen wissenschaftlichen Einrichtung zum Zwecke der Promotion eingereicht wurde.

Ferner erkläre ich, dass ich diese Arbeit selbstständig verfasst und keine anderen als die darin angegebenen Hilfsmittel und Hilfen benutzt und keine Textabschnitte eines Dritten ohne Kennzeichnung übernommen habe.

Genf, den

Lukas Nies



## 9 Peer-reviewed publications

2023

1. **Further evidence for shape coexistence in  $^{79}\text{Zn}^m$  near doubly-magic  $^{78}\text{Ni}$**   
**L. Nies**, L. Canete, D. D. Dao, S. Giraud, A. Kankainen, D. Lunney, F. Nowacki, B. Bastin, M. Stryczyk, P. Ascher, K. Blaum, R. B. Cakirli, T. Eronen, P. Fischer, M. Flayol, V. Girard Alcindor, A. Herlert, A. Jokinen, A. Khanam, U. Köster, D. Lange, I. D. Moore, M. Müller, M. Mougeot, D. A. Nesterenko, F. de Oliveira, H. Penttil, C. Petrone, I. Pohjalainen, A. De Roubin, V. Rubchenya, Ch. Schweiger, L. Schweikhard, M. Vilen, and J. Äystö  
submitted (2023)
2. **Isomeric excitation energy for  $^{99}\text{In}^m$  from mass spectrometry reveals constant trend next to doubly magic  $^{100}\text{Sn}$**   
**L. Nies**, D. Atanasov, M. Athanasakis-Kaklamanakis, M. Au, K. Blaum, J. Dobaczewski, B. S. Hu, J. D. Holt, J. Kartheim, I. Kulikov, Yu. A. Litvinov, D. Lunney, V. Manea, T. Miyagi, M. Mougeot, L. Schweikhard, A. Schwenk, K. Sieja, and F. Wienholtz  
Phys. Rev. Lett. **131**, 022502 (2023)  
<https://doi.org/10.1103/PhysRevLett.131.022502>
3. **Charge radii, moments, and masses of mercury isotopes across the  $N = 126$  shell closure**  
M. Au, M. Athanasakis-Kaklamanakis, **L. Nies**, R. Heinke, K. Chrysalidis, U. Köster, P. Kunz, B. Marsh, M. Mougeot, L. Schweikhard, S. Stegemann, Y. Vila Gracia, Ch. E. Düllmann, and S. Rothe  
Phys. Rev. C **107**, 064604 (2023)  
<https://doi.org/10.1103/PhysRevC.107.064604>
4. **In-source and in-trap formation of molecular ions in the actinide mass range at CERN-ISOLDE**  
M. Au, M. Athanasakis-Kaklamanakis, **L. Nies**, J. Ballof, R. Berger, K. Chrysalidis, P. Fischer, R. Heinke, J. Johnson, U. Köster, D. Leimbach, B. Marsh, M. Mougeot, B. Reich, J. Reilly, E. Reis, M. Schlaich, Ch. Schweiger, L. Schweikhard, S. Stegemann, J. Wessolek, F. Wienholtz, S.G. Wilkins, W. Wojtaczka, Ch.E. Düllmann, and S. Rothe  
Nucl. Instrum. Methods.: B **541**, Pages 375-379 (2023) <https://doi.org/10.1016/j.nimb.2023.05.015>
5. **Experimental setup for Weak Interaction Studies with Radioactive ion-beams WISArD**  
D. Atanasov, F. Cresto, **L. Nies**, M. Pomorski, M. Versteegen, P. Alfaut, V. Araujo-Escalona, P. Ascher, B. Blank, L. Daudin, D. Guillet, X. Fléchar, and S. Rothe

J. Ha, A. Husson, M. Gerbaux, J. Giovinozzo, S. Grévy, T. Kurtukian-Nieto, L. Leterrier, R. Lica, E. Liénard, C. Mihai, C. Neacsu, A. Ortega-Moral, G. Pascovici, M. Roche, N. Severijns, S. Vanlangendonck, A. Welker, and D. Zákoucký

Nucl. Instrum. Methods.: A **1050**, 168159 (2023)

<https://doi.org/10.1016/j.nima.2023.168159>

## 2021

### 6. Charge radii, moments, and masses of mercury isotopes across the $N = 126$ shell closure

T. Day Goodacre, A. V. Afanasjev, A. E. Barzakh, **L. Nies**, A. Marsh, S. Sels, U. C. Perera, P. Ring, F. Wienholtz, A. N. Andreyev, P. Van Duppen, N. A. Althubiti, B. Andel, D. Atanasov, R. S. Augusto, J. Billowes, K. Blaum, T. E. Cocolios, J. G. Cubiss, G. J. Farooq-Smith, D. V. Fedorov, V. N. Fedosseev, K. T. Flanagan, L. P. Gaffney, L. Ghys, A. Gottberg, M. Huyse, S. Kreim, P. Kunz, D. Lunney, K. M. Lynch, V. Manea, Y. Martinez Palenzuela, T. M. Medonca, P. L. Molkanov, M. Mougeot, J. P. Ramos, M. Rosenbusch, R. E. Rossel, S. Rothe, L. Schweikhard, M. D. Seliverstov, P. Spagnoletti, C. Van Beveren, M. Veinhard, E. Verstraelen, A. Welker, K. Wendt, R. N. Wolf, A. Zadvornaya, and K. Zuber

Phys. Rev. C **104**, 054322 (2021)

<https://doi.org/10.1103/PhysRevC.104.054322>

## 2019

### 7. Scalar current limit from the beta-neutrino correlation: the WIS-**ArD** experiment

V. Araujo-Escalona, P. Alfaut, P. Ascher, D. Atanasov, B. Blank, L. Daudin, X. Fléhard, M. Gerbaux, J. Giovinozzo, S. Grévy, T. Kurtukian Nieto, E. Liénard, **L. Nies**, G. Quémener, M. Roche, N. Severijns, S. Vanlangendonck, M. Versteegen, P. Wagenknecht and D. Zákoucký

J. Phys.: Conf. Ser. **1308** 012003 (2018)

<https://doi.org/10.1088/1742-6596/1308/1/012003>

## 10 Acknowledgments

A thesis work like this can, of course, not be done by one person alone but rather is a collaborative effort. While I wrote the introductory chapters in the Spring and early Summer of 2023, the reported contents, especially the publications, were enabled by technical, experimental, and theoretical work dating back to 2015 and earlier, many of which were performed while I was still in high school and college, ignorant about the nuclear shell model and high-precision mass spectrometry.

First and foremost, I have to thank my parents and family, without their support and encouragement, I would not be the person I am today. Even from afar at times, Hwidahm, hayatim, has been an unwavering companion, listening to my endless complaints about work, physics, and life in general. Without you, this part of my life could have been dull and monotone.

Before I continue, I must thank my former colleagues and friends from the University of Gießen, my alma mater, where I enjoyed an excellent physics education, during which I was able to study abroad and visit CERN as a summer student in 2018. In particular, Dr. Hans-Georg Zaunick and René Schubert have taught me to work independently in the lab and tackle new problems creatively.

As a summer student at CERN, I was wholeheartedly welcomed by Dr. Dinko Atanasov and Dr. Victoria Araujo-Escalona, who have become not only colleagues but, more importantly, friends. To both of you, I wish only the best for your future.

One of the main reasons I started as a Ph.D. student at CERN was thanks to Frank Wienholtz, who back then proposed and enabled me to join the ISOLTRAP collaboration. He was the main person to consult for advice on all lab-related questions and will be, as far as I can tell, for the foreseeable future. For getting me into all this, thank you ;)

Every Ph.D. student needs a supervisor, and Prof. Dr. Lutz Schweikhard has filled this position true to its meaning. Many problems can arise when the student and his supervisor are separated by 1300km; I did not face many. Lutz, thank you for always being available for advice and counsel, for reading and proofreading, no matter the time of day, and for quick responses. I know supervising from afar is not ideal, but you managed it as good as it can get, and for this, I thank you a lot.

Being a student at a university usually involves attending lectures, living close by, and generally feeling connected to the institution. For a CERN Ph.D. student, these things are difficult to accomplish, especially when the university is a two-hour plane and a three-hour train ride away and a global pandemic is taking place. Everything bureaucracy-related could easily have been a nightmare. It never became one, thanks to Iris-Diana Passow, who made my studentship at the university as seamless as possible, and I am very grateful for this. Also, many thanks to Dr. Paul Fischer for similar reasons and for helping out whenever person-power was in a shortage.

At this point, I have to thank the German Federal Ministry of Education and Research (grant no. 13E18CHA), BMBF, through which most of my stay at CERN was financed,

being a holder of a Wolfgang-Gentner Stipend. For the successful application to this program I would like to thank Prof. Dr. David Hertzog, PD Dr. Sören Lange, and Prof. Dr. Lutz Schweikard for their support, as well as Dr. Michael Hauschild and Dr. Dominik Dannheim for managing the program at CERN.

At ISOLDE, I would like to thank my local supervisors Prof. Dr. Gerda Neyens, followed by Prof. Dr. Sean Freeman, for their support in the collaboration. At ISOLTRAP, Dr. Maxime Mougeot taught me everything I know about ion traps, for which I am very grateful. I have to thank him, Prof. Dr. David Lunney, and Dr. Vladimir Manea for teaching me nuclear physics and enabling the science-rich character of this thesis.

At the Max-Planck Institute for Nuclear Physics in Heidelberg, I (and many others) owe big thanks to Prof. Dr. Klaus Blaum for supporting our work at ISOLDE in every possible way. Klaus, I thank you and Gabi Weese a lot for keeping things afloat.

Furthermore, I would like to thank all my colleagues and friends at ISOLDE for being the absolute best, especially Liss, Tim, Peter, Mia, Simon, Franziska, and Michail, the ISOLDE operators for keeping the machine running, the ISOLDE target group for doing their best in producing “gold from lead”, Katerina and Reinhard for running RILIS during unofficial experiments and for helping out with the ISOLTRAP laser system, and to numerous others not mentioned by name.

Finally, I want to thank Maxime, Liss, Lutz, and Sebastian for proofreading this manuscript.

# A Appendix

## A.1 Note on the atomic mass unit

As shown in Section 2.2.1, the atomic mass is usually presented as the mass excess (see Eq. (2.7)) in terms of energy in kiloelectronvolt. The accepted non-SI unit commonly used is the unified atomic mass unit  $u$ , equivalent to one Dalton  $Da$  or “1/12 of the mass of a free carbon 12 atom, at rest and in its ground state” [38]. As all atomic masses are measured as frequency ratios or time-of-flight differences using one or two well-known reference masses, a conversion from atomic mass in units of the unified atomic mass unit  $u$  to energy in keV using  $E = mc^2$  has to be made. This includes using the mass of  $u$  in kg, which is not exactly defined in the SI but consists of several different measured quantities.

Prior to 2018, the mass of  $1 u = \frac{1}{12}m(^{12}\text{C}) = m_u$  was determined through it’s connection to the molar mass  $M(^{12}\text{C})$  of carbon-12 and the Avogadro constant  $N_A$

$$M(^{12}\text{C}) = m(^{12}\text{C})N_A = 0.012 \text{ kg mol}^{-1}, \quad (\text{A.1})$$

where the definition of the Avogadro constant relied on the number of atoms in one mole of carbon-12, making the value  $M(^{12}\text{C})$  exact. The relative standard uncertainty on  $N_A$  through experiments prior 2018 was  $10^{-8}$  [183].

With the redefinition of the international system of units (SI) in 2018 [38], a number of fundamental observables are now exact physical constants, among them the Avogadro constant, effectively breaking the link between carbon-12 and the molar mass. These

**Table A.1:** Reprinted table from the 9<sup>th</sup> Brochure of the SI [38] for the seven defining base constants and some selected derived values. The base constants are exact by definition.

Defining constant	Symbol	Value and unit
hyperfine transition frequency of Cs	$\Delta\nu_{\text{Cs}}$	9 192 631 770 Hz
speed of light in vacuum	$c$	299 792 458 m s <sup>-1</sup>
Planck constant	$h$	$6.626\,070\,15 \times 10^{-34}$ J s
elementary charge	$e$	$1.602\,176\,634 \times 10^{-19}$ C
Boltzmann constant	$k$	$1.380\,649 \times 10^{-23}$ J K <sup>-1</sup>
Avogadro constant	$N_A$	$6.022\,140\,76 \times 10^{23}$ mol <sup>-1</sup>
luminous efficacy	$K_{\text{cd}}$	683 lm W <sup>-1</sup>
Accepted non-SI units		
energy	eV	1.602 176 634 J
mass	Da	$1.660\,539\,066\,60(50) \times 10^{-27}$ kg
molar mass of <sup>12</sup> C	$M(^{12}\text{C})$	11.999 999 995 8(36) g mol <sup>-1</sup>

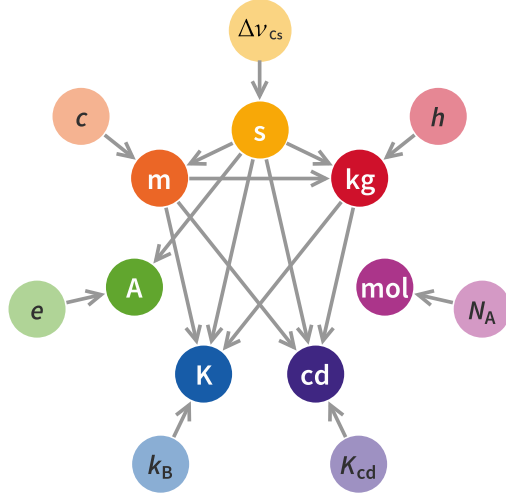


**Figure A.1:** Relations of the base units with physical constants in the 2018 redefinition of the SI units. Graphic reprinted from Emilio Pisanty, [CC BY-SA 4.0](#), via Wikimedia Commons.

physical constants are the input for the seven base units as shown in table Table A.1 and Fig. A.1. This means that the molar mass of carbon-12 is not exact anymore, with a numerical value differing from  $12 \text{ g mol}^{-1}$  in the order of  $10^{-10}$  (see Table A.1).

Using the relative atomic mass of the electron  $A_r(e)$  and the electron's rest mass  $m_e$ , the atomic mass constant is written as

$$m_u = \frac{1}{12} m(^{12}\text{C}) = \frac{m_e}{A_r(e)} = \frac{2hR_\infty}{A_r(e)\alpha^2 c}, \quad (\text{A.2})$$

where  $h$  and  $c$  are now exact,  $R_\infty$  is the Rydberg constant known to  $10^{-12}$  relative uncertainty from the 1S-2S laser spectroscopy in the hydrogen atom,  $\alpha$  is the hyperfine constant known to  $10^{-10}$  relative uncertainty from electron g-factor and atom recoil measurements, and  $A_r(e)$  is known to  $10^{-11}$  relative uncertainty from spin-precession and cyclotron-frequency measurements of  $^{12}\text{C}^{5+}$  in a Penning trap [35]. Now being exact, the relative uncertainty of  $10^{-8}$  on  $h$  does not contribute to the overall relative uncertainty of  $u$  anymore, decreasing the uncertainty effectively by a factor of 40 to  $10^{-10}$ .

The ATOMIC MASS EVALUATION (AME) is usually representing the atomic mass  $M(N, Z)$  and its uncertainty in units of  $\mu u$ , the mass excess  $ME(N, Z) = M(N, Z) - Au$  in keV, and the binding energy per nucleon  $E_B/A = [ZM(^1\text{H}) + NM(n) - M(N, Z)]/A$  in keV [2]. In the past, due to the relative uncertainty on the conversion of  $u$  to keV, the precision on  $ME(N, Z)$  for some nuclides was worse than the same value expressed in  $u$ . With the 2018 SI redefinition and the ever-improving measurement precision of some fundamental constants, the mass excess given in keV is now at the same level of precision as the corresponding value given in  $u$  [39].



